Phosphors for Lighting Applications

A thesis submitted for the degree of
Doctor of Philosophy

by

Xiao Yan

Wolfson Centre for Materials Processing

Brunel University

July 2012

Acknowledgement

There was continuous help and support from many people since the very beginning of this work. Firstly, I wish to thank my supervisor Prof. Jack Silver for his kind advice and patient guidance through my whole experience of the PhD study in the Wolfson Centre, Brunel University. Prof. Robert Withnall assisted a lot with his vast knowledge and experience in upconversion phosphors and Raman spectroscopy. I would also like to thank Dr Terry Ireland for his kind help on almost every aspect of my work at the beginning of my PhD life.

I would like to express my appreciations to all my colleagues and friends in the Wolfson Centre for their help and support, especially to our kind SRI Manager, Dr Fiona Cotterill for her perfect managing work and making everything available in a convenient way. I wish to thank the staff from the Experimental Techiniques Centre (ETC) at Brunel University, including Dr Alan Reynolds, Dr Nita Verma and Dr Lorna Anguilano. Due to their help and expertise, I could make full use of the state of the art equipment to get fruitful results. I would also like to thank Dr George Fern for the help with TEM and XRD.

Specially, I would like to thank Prof. Yali Li, Dr Feng Hou and Dr Wenhui Song for your kind help on my application for this PhD studentship as well as the CSC scholarship. I wish to thank Dr Ning Wang and Lei Zhao. It was not easy for me to start and get used to my new life here if not for your kind help and support.

Last but not least I would like to thank my family in China. This thesis could not have been done without their continuous support and encouragement.

Abstract

Trivalent rare earth cations (RE^{3+}) activated nanometre-sized Y_2O_2S and Gd_2O_2S phosphors were prepared by converting hydroxycarbonate precursor powders during a firing process. The precursors were prepared using the urea homoprecipitation method. The choice of host crystal and dopant were optimised to meet the specific requirements for practical applications in the field of lighting, X-ray detection, and displays. Parameters that affect the luminescent properties of the resulting phosphors, such as doping concentration, excitation mechanism, firing temperature, and host lattice were investigated.

Tb^{3+} and Er^{3+} co-doped Y_2O_2S and Gd_2O_2S were studied for their upconversion properties under 632.8 nm red laser excitation. The intensities of UC emission were affected by both doping concentration and host lattices. Tb^{3+} and Er^{3+} co-doped Y_2O_2S was found to show strong downconversion from Tb^{3+} and upconversion from Er^{3+}. The presence of the Er^{3+} cations directly affects the Tb^{3+} down-converting properties by acting as centres for energy transfer. The possible energy transfer between Gd^{3+} and Er^{3+} should be responsible for the different trend of Er^{3+} upconversion intensity in Y_2O_2S and Gd_2O_2S. It has been established that the Tb^{3+} and Er^{3+} co-doped system is superior than the Yb^{3+} and Er^{3+} co-doped one. In the latter system the presence of Yb^{3+} reduces the efficiency of both upconversion and downconversion emission under red laser excitation. These phosphors show potential applications in the security and anti-fraud field.

The novel ZnS:Mn QDs were prepared and successfully incorporated into GaN based photonic crystal (PC) holes to efficiently produce white light. The crystal structure and luminescent properties of the ZnS:Mn QDs were investigated as well as the factors affecting the filling rate. $Zn_{1-x}Cd_xS$:Mn QDs were also investigated. The addition of Cd cations leads to a red shift in the PL excitation spectra of the $Zn_{1-x}Cd_xS$:Mn QDs. The crystal structures and surface properties were also affected by the presence of Cd. Monodisperse PbS QDs with particle size of ~5 nm has been obtained using a similar aqueous reaction method.

Table of Contents

List of Figures

List of Tables

Chapter 1 An introduction to phosphors and an overview of phosphor areas relevant to the work described in this thesis

1.1 Phosphors and luminescence

Luminescent materials, also known as phosphors, can absorb energy from the incident radiation and emit light after a series of energy transfer processes. The emissions usually fall into the visible region but also could be invisible, such as ultraviolet [1-3] or infrared light [1, 4-8]. Although the last decade has witnessed an increasingly extensive research interest and great progress on organic phosphors for light emitting diodes (OLED) [9-12], the subject of this thesis centres on phosphors that are novel solid inorganic compounds. To meet the demands for various applications, phosphors are usually in the form of powders with specific requirements on particle size distribution and morphology [13]. Usually, larger crystals (4 to 5 μm) of high quality are required [14] since the quantum efficiencies are generally higher in crystals than in amorphous hosts [15].

Luminescent materials have found wide application in many fields in recent years. Major traditional applications include lighting and emissive display devices [13, 16-19], amplifiers in optical communication [20, 21] and lasers [2, 22-24]. In addition, phosphors also find applications in X-ray detector systems [25-35] and scintillators [30, 36-39]. Developments on the phosphors for these novel applications are well documented in many reviews and books [18, 36, 37, 40-44]. Most recently, phosphors have found applications in new areas such as solar cells [45-48] and white-light-emitting LEDs [19, 49-51] due to increasing concern on energy efficiency [52].

Luminescence, the electromagnetic radiation from phosphors with appropriate excitation, was first termed in 1888 by the German physicist Eilhard Wiedemann to characterize light emission not originating from a rise in temperature [53]. The so-called ‘cold light’ is in obvious contrast to incandescence, which is light emitted by a substance as a result of heating. Luminescence can be

distinguished depending on the excitation source (Table 1.1). In this work the focus will be on the first four forms of luminescence since all the other forms of luminescence are not currently used in lighting or display applications. Many materials have been developed for Photoluminescence (PL), Cathodoluminescence (CL), X-ray luminescence (XL) and Electroluminescence (EL) in the fields of both inorganic and organic phosphors.

Table 1.1 Different forms of luminescence.

Luminescence type	Excitation source	Applications
photoluminescence (PL)	photons	fluorescent lamps
cathodoluminescence (CL)	electron beams	TV sets, monitors
X-ray luminescence (XL)	X-rays	scintillators
electroluminescence (EL)	electric current	LEDs
chemoluminescence	chemical reaction energy	analytical chemistry
bioluminescence	biochemical reaction energy	analytical chemistry
sonoluminescence	ultrasound	—
triboluminescence	mechanical energy	—
fractoluminescence	fracture in certain crystals	—
piezoluminescence	pressure on certain solids	—

Luminescence can also be divided into phosphorescence and fluorescence by the difference in decay time. Fluorescence denotes an emission of short decay time, ~10^{-9} to 10^{-7} s, while phosphorescence is used to denote the emission of a much longer decay time, from a few minutes up to several hours. In quantum theory, in a fluorescence process, transitions arise from the singlet excited state where the electron does not change its spin direction. However, sometimes under the appropriate conditions a spin-flip could happen and a lower triplet excited state is created, which is the case in a phosphorescence process. Transitions from a triplet excited state is forbidden by the selection rules and have to wait for a long time until the electron spin flips back. Thus phosphorescence is usually of low intensity compared with fluorescence and could last for a while after the removal of the excitation source.

A typical human eye can only respond to the visible light between roughly 380 nm and 780 nm (see Figure 1.1) and generally has its maximum sensitivity at around 555 nm [54]. Thus, the phosphors that have emissions in the visible range are the ones of most commercial importance. Several terms are used to define the properties of phosphors for practical applications in lighting and displays. These include: quantum efficiency, colour coordinates and colour temperature and these terms are explained in the following section.

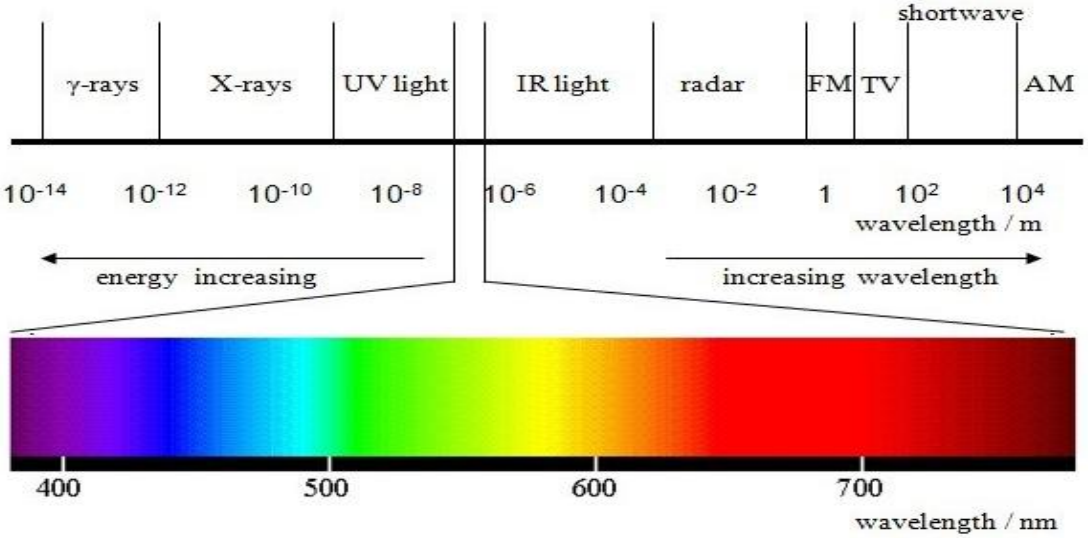

Figure 1.1 The electromagnetic spectrum.

Quantum yield (QY) is defined as the ratio of the number of the emitted photons to the number of the absorbed photons:

$$\mathrm{QY} = \frac{\mathrm{n(emitted\ photons)}}{\mathrm{n(absorbed\ photons)}} \qquad (1)$$

The maximum quantum yield of PL is usually 1.0 but due to energy loss in the energy transfer processes between absorption and emission it is usually less than this. However, in one special area this is not true: in quantum cutting (a process in which phosphors are capable of emitting more than one photon after absorption of a single high-energy photon) where Pr^{3+} activated fluorides [55-57] and oxides [58-60] have been observed to give QY values greater than 1. Piper *et al* [57] reported a quantum yield of 140% for 185nm UV excitation in YF_3:Pr^{3+} at room temperature. Quantum cutting can also be observed from ion pairs. A well-

investigated example is that of Gd^{3+}-Eu^{3+} dual ions [61-65]. Quantum yields of up to 190% ($LiGdF_4$:Eu) [62, 64] and 194% (BaF_2:Gd, Eu) [65] have been reported. Quantum yields in CL (number of CL photons/incident electron) are much higher (~10^3) due to a different excitation mechanism: the luminescence centre is predominantly excited by the recombination of electron-hole pairs (excitons) that are generated by the incident electrons.

In emissive displays, all colours are obtained by mixing the three primary colours of red, green, and blue at appropriate ratios. The chromaticity of a colour can be indicated in colour space which is defined according to the convention of the International Commission on Illumination (CIE) in a normalised two-dimensional coordinate system [66]. The 1931 CIE colour space together with the SMPTE (Society of Motion Picture and Television Engineers) colour triangle is illustrated in Figure 1.2. The ideal phosphors for displays should have high colour saturation, which means their respective colour coordinates should be positioned as close as to the borders of the SMPTE colour triangle as possible.

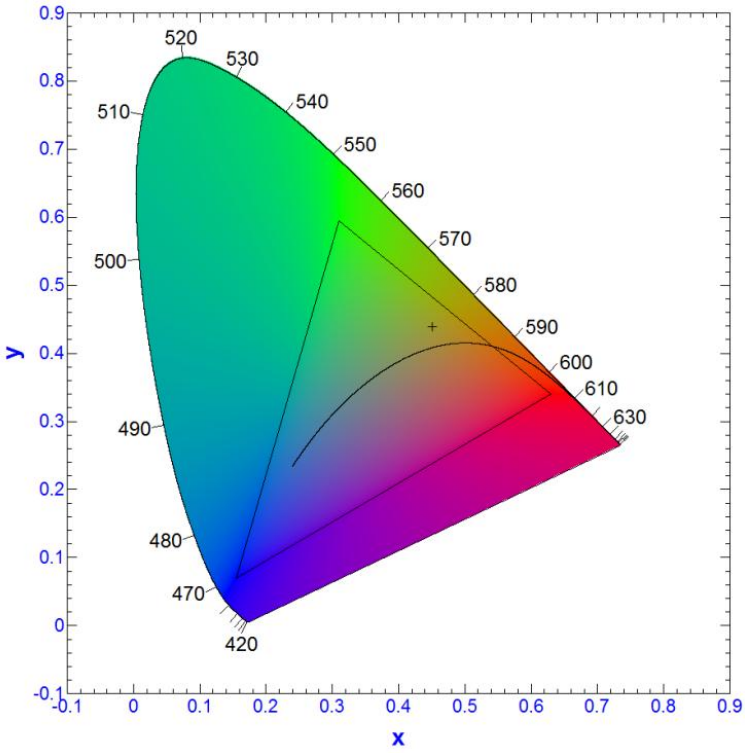

Figure 1.2 The 1931 CIE colour space and the SMPTE colour triangle. Also shown is the locus of the colour of the black-body radiator.

The colour temperature is introduced to characterize the colour of emitted light, which is defined by the absolute temperature of an ideal black-body radiator that has the same colour as that of the light source. The locus of the colour of the black body radiator is also given in Figure 1.2. Meaningful colour temperatures are those from emitters that lie on this locus. Light emissions from materials with CIE coordinates close to the line have colour temperatures that are called correlated colour temperatures (CCT). The CCT is defined as the temperature of the Planckian radiator whose perceived colour most closely resembles that of a given stimulus at the same brightness and under specified viewing conditions [67]. Some examples of the colour temperatures of natural and artificial light sources are presented in Table 1.2.

Table 1.2 Colour temperatures of several common light sources

Light source	Colour temperature/K
blue sky	15000–20000
LCD or CRT screen	6500-9000
daylight	6500
moonlight	4100-4150
halogen incandescent lamps	3000
ordinary incandescent lamps	2800
high-pressure sodium lamps	2000
candle flame	2000
sunset/sunrise	1850
match flame	1700

A high luminous efficacy (LE) is required for lighting applications. The calculation method is given by the following equation, where *P(λ)* denotes the spectral power distribution of the radiant energy and *V(λ)* denotes the spectral luminous efficiency for the human eye (Figure 1.3).

$$\mathrm{LE} = \int_{380}^{780} \mathrm{P}(\lambda)\,\mathrm{V}(\lambda)\mathrm{d}\lambda \ \ (\mathrm{lm}\cdot\mathrm{W}^{-1}) \qquad (2)$$

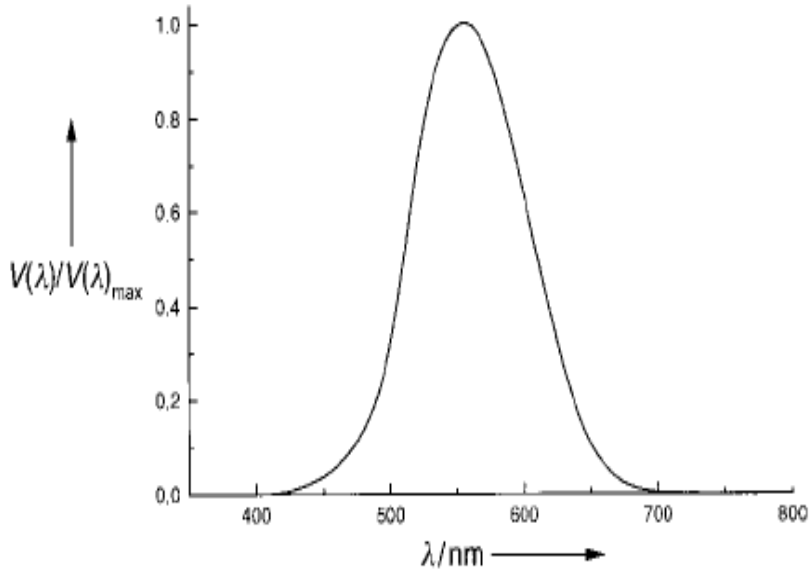

Figure 1.3 Normalised luminous efficiency for the human eye as a function of wavelength [40].

The colour rendering index (CRI) is introduced to quantitatively measure the ability of a light source to reproduce the colour of the object illuminated by the light source. It is defined by the CIE as ‘effect of an illuminant on the colour appearance of objects by conscious or subconscious comparison with their colour appearance under a reference illuminant’. A black-body radiator, such as the sun or a incandescent lamp, is defined to have a CRI of 100. The CRI of a light source is calculated by comparing the colour difference between the reflection spectra of the selected test colours obtained by the irradiation of the investigated light source and the reflection spectra when irradiated by a black-body radiator. The larger the difference is, the lower the CRI. So a line emitter of single emission line has a CRI of 0 because not all colours could be displayed under such a light source. It’s worth noting that no valid comparisons could be made using only the CRI between light sources with considerably different colour temperatures because the perceived colours under reference light sources vary for different colour temperatures.

1.2 Absorption, excitation, and emission

Luminescence can only be observed after phosphors absorb an appropriate incident radiation. Absorption can occur either at the luminescent centre or at any place in the host lattice. If it is in the host lattice it is followed by an energy transfer to the luminescent centre before emission can occur. In general, high-energy excitation such as accelerated electron beams, γ-rays, and X-rays always excited the host lattice. The luminescent centre can only be directly excited by the lower-energy excitation, such as UV light, visible light or IR light.

Figure 1.4 presents a schematic absorption spectrum of Y_2O_3:Eu^{3+}, which is used as an example to explain the absorption process in phosphors [68]. The absorption band before 230 nm is due to the host lattice and the one at 250 nm due to Eu^{3+}-O^{2-} charge transfer transition while the narrow lines are transitions within the $4f^6$ configuration of Eu^{3+}.

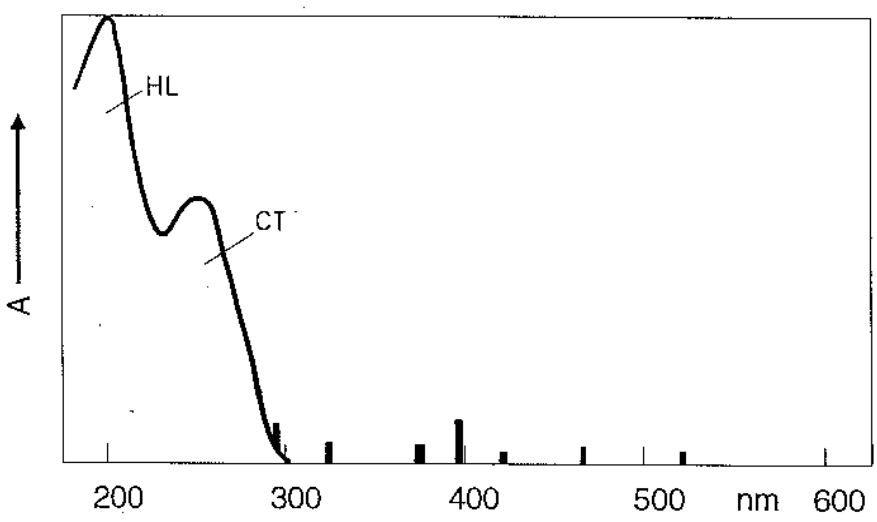

Figure 1.4 Schematic absorption diagram of Y_2O_3:Eu^{3+} [68]. HL and CT indicate absorptions due to the Y_2O_3 host lattice and the Eu^{3+}-O^{2-} charge transfer transition, respectively.

The configurational coordinate diagram was proposed to explain the luminescence process. Figure 1.5 shows a configurational coordinate diagram, in which the potential energy E is plotted as a function of the configurational coordinate R, where R represents the distance between the luminescence centre

and its coordinate neighbour. Optical transitions are represented vertically in the configurational coordinate diagram since they are electronic and occur rapidly compared to nuclear motions. The ground state and excited state are shown in the form of parabolic potential wells. The luminescence centre is prompted from its ground state to an excited state after absorbing energy E_{ab}. The luminescence centres tend to stay in the minimum energy points of the excited state before a possible optical transition can happen. The difference between E_{ab} and the emission energy E_m is called the Stokes shift, denoted ΔE_s. It's also shown in Figure 1.5, where there is a shift of ΔR between the minimum energy point of the ground state and excited state because the chemical bond in the excited state is different from that in the ground state.

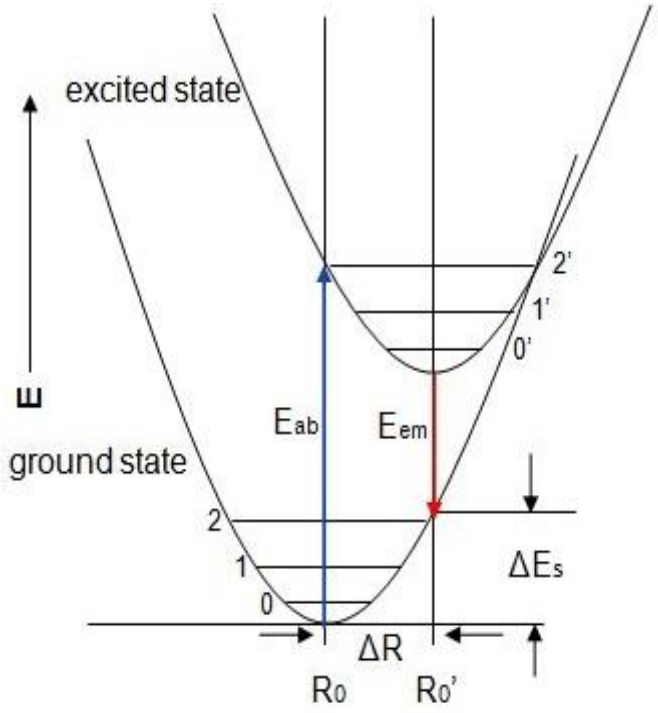

Figure 1.5 Configurational coordinate diagram. The vibrational states are shown in number.

Figure 1.6 and Figure 1.7 show the excitation and emission spectra of $Y_2O_2S:Pr^{3+}$ nanometre sized phosphor particles as examples. More details of the energy transfer process will be discussed for each specific phosphor in the following sections. The excitation spectrum of $Y_2O_2S:Pr^{3+}$ consists of two broad and strong bands centred at about 264 nm and 304 nm, respectively (Figure 1.6). The relatively weak band centred at 264 nm is due to the excitation of the Y_2O_2S

host lattice and this energy would be partially transferred to the Pr^{3+}, while the strong one at 304 nm corresponds to the excitation associated with the Pr^{3+} [69].

Figure 1.7 shows the emission spectra of $Y_2O_2S:Pr^{3+}$ nanometre sized phosphor particles with 254nm UV excitation. The strong emission line at 514nm corresponds to the electric dipole transition of $^3P_0 \rightarrow {}^3H_4$. Other emission lines at 549nm, 641nm, 670nm, and 770nm can be attributed to transitions from $^3P_0$ to $^3H_5$, $^3H_6$, $^3F_2$ and $^3F_4$, respectively.

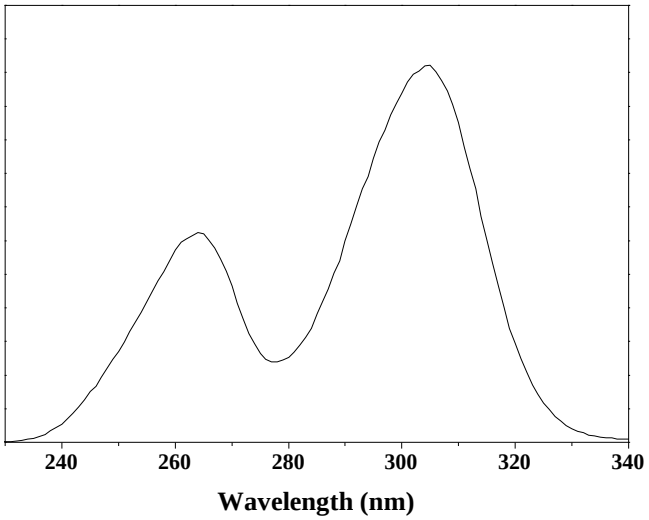

Figure 1.6 Excitation spectrum of $Y_2O_2S:Pr^{3+}$ nanosized phosphors.

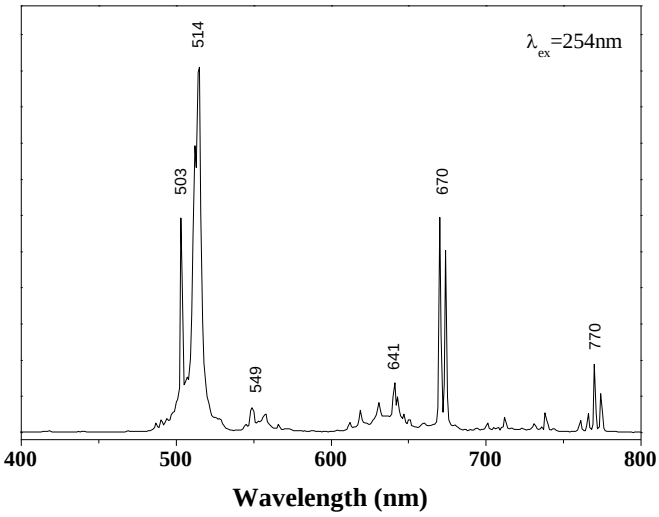

Figure 1.7 Emission spectrum of $Y_2O_2S:Pr^{3+}$ nanosized phosphors.

1.3 Activators and host crystals

Most phosphors consist of two components: a host lattice and an activator. Activators are deliberately introduced impurities and function as the luminescent centre in the host crystal. Rare earth elements can play an important role in both sides. The electronic structures and optical properties of the rare earth ions used in our work, such as Dy^{3+}, Pr^{3+}, Eu^{3+}, Er^{3+}, and Tb^{3+} are described in the following section as well as the Y_2O_2S and Gd_2O_2S host lattices. All the elements that have been employed in the host lattice and/or as activator are given in the periodic table of the 'lighting' elements [40].

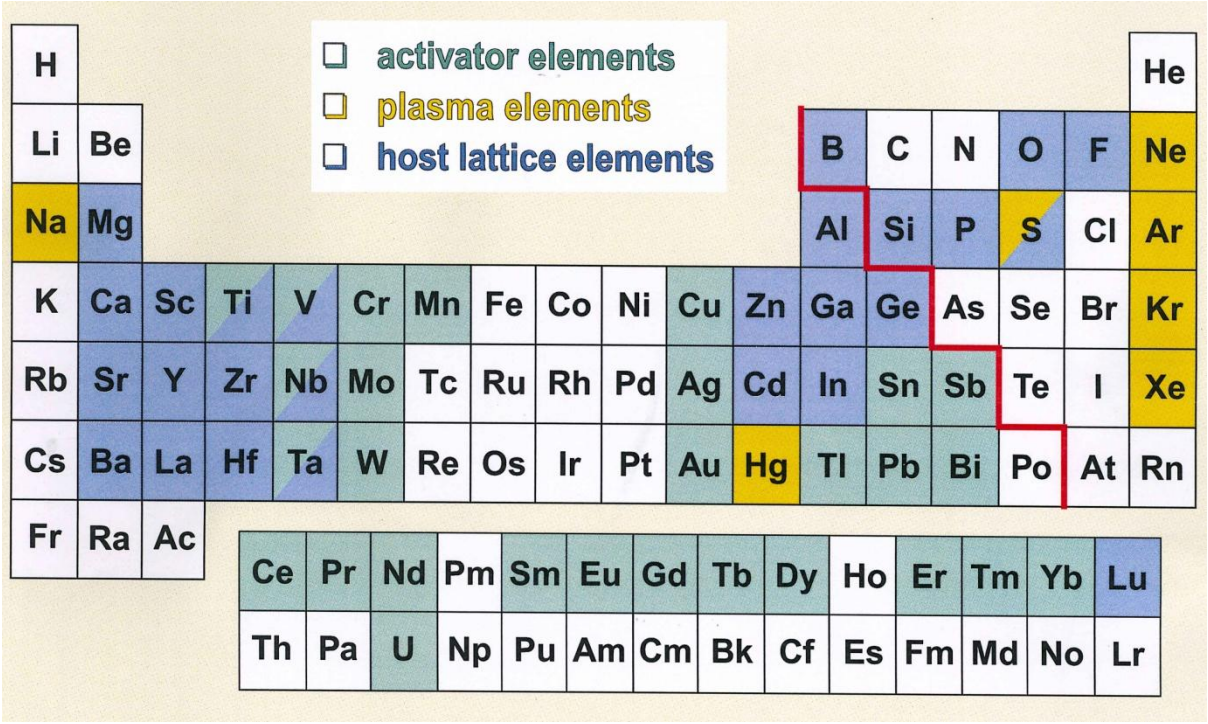

Figure 1.8 Periodic table of the 'lighting' elements [40].

Generally the rare earth elements consist of the lanthanide elements from La (atomic number 57) to Lu (atomic number 71), often Sc (atomic number 21) and Y (atomic number 39) are included. These elements benefit from their characteristic incompletely filled 4f shell and exhibit unique optic, electric and magnetic properties. In the rare earth elements, the 4f electrons are shielded from the surroundings by the $5s^2$ and $5p^6$ electrons. Therefore the optical transitions within the 4f configuration are hardly influenced by the environmental or crystal electric field. The energy levels of 4f electrons of the trivalent rare earth ions

(RE^{3+}) have been extensively investigated by Dieke [70] and other researchers [71]. Figure 1.9 shows the Dieke diagram in which the energy states were determined experimentally by considering the optical spectra of individual ions incorporated in $LaCl_3$ crystals. Light-emitting levels are indicated by semicircles below the bars. The width of the energy state bars gives the order of magnitude of the crystal field splitting, which is very small. Since the 4f electrons hardly interact with the environmental electric field the diagram is applicable to ions in almost any host lattices. The maximum variation of the energy states is very confined and is at most of the order of several hundred cm^{-1}.

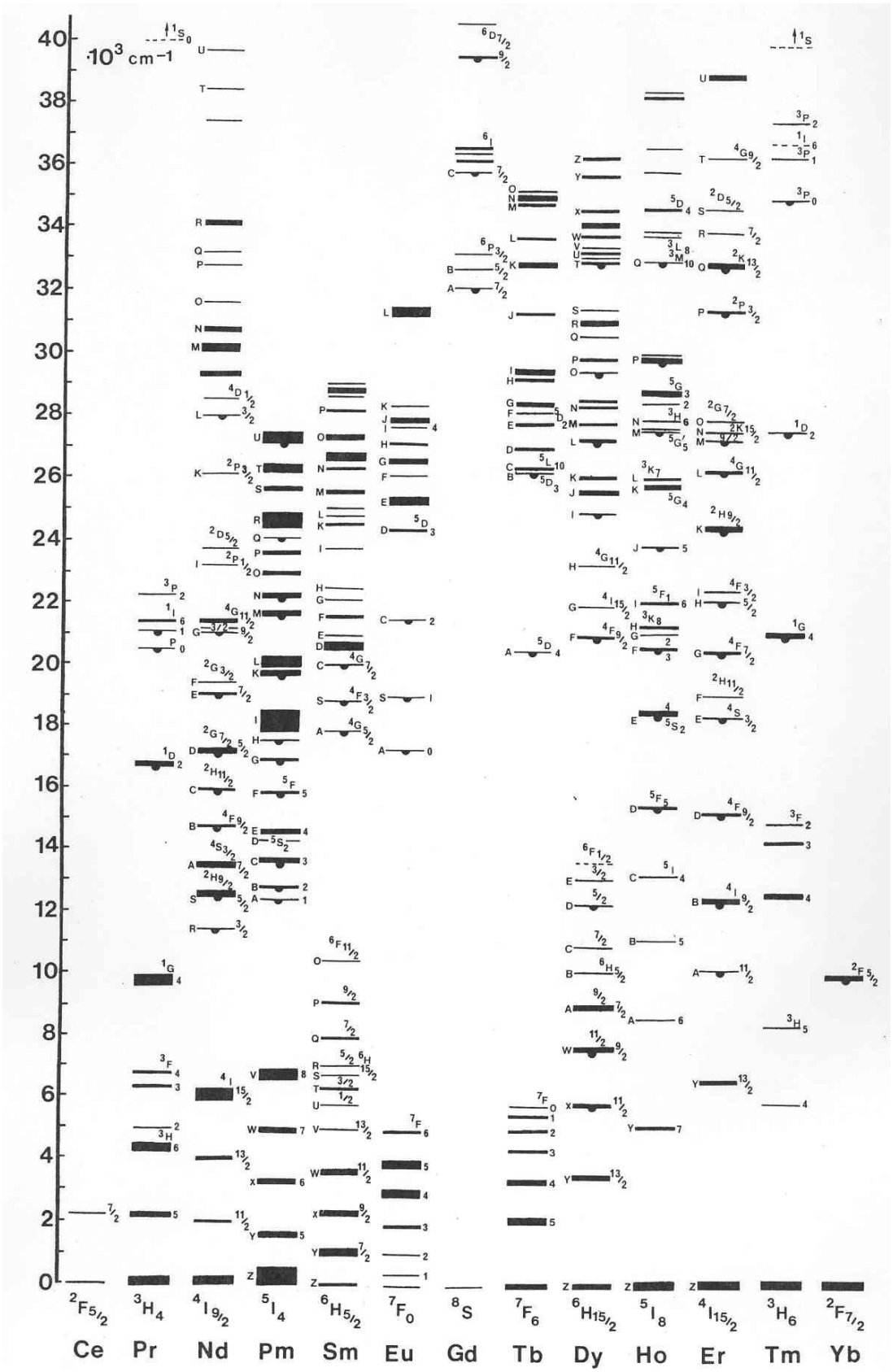

Figure 1.9 Energy levels of RE^{3+} ions [71].

1.3.1 Electronic structure and optical properties of RE^{3+} ions

The characteristic electronic structures of RE^{3+} ions arises from the gradual filling of the 4f orbitals from La^{3+} ($4f^0$) to Lu^{3+} ($4f^{14}$) (Table 1.3), except for Sc^{3+} and Y^{3+}, which are not optically active because both have no energy levels that can induce excitation and luminescence processes in or near the visible region. As mentioned above, the 4f electrons are well shielded from the surroundings. Thus the life time of the excited state of RE^{3+} ions is long (ms) and emission transitions yield sharp lines in the spectra.

Table 1.3 Electronic structures of RE^{3+} ions (except for Sc^{3+} and Y^{3+}).

Atomic number	Element symbol	Configuration RE^{3+}	Ground state of RE^{3+}
57	La	[Xe]	$^1S_0$
58	Ce	[Xe]$4f^1$	$^2F_{5/2}$
59	Pr	[Xe]$4f^2$	$^3H_4$
60	Nd	[Xe]$4f^3$	$^4I_{9/2}$
61	Pm	[Xe]$4f^4$	$^5I_4$
62	Sm	[Xe]$4f^5$	$^6H_{5/2}$
63	Eu	[Xe]$4f^6$	$^7F_0$
64	Gd	[Xe]$4f^7$	$^8S_{7/2}$
65	Tb	[Xe]$4f^8$	$^7F_6$
66	Dy	[Xe]$4f^9$	$^6H_{15/2}$
67	Ho	[Xe]$4f^{10}$	$^5I_8$
68	Er	[Xe]$4f^{11}$	$^4I_{15/2}$
69	Tm	[Xe]$4f^{12}$	$^3H_6$
70	Yb	[Xe]$4f^{13}$	$^2F_{7/2}$
71	Lu	[Xe]$4f^{14}$	$^1S_0$

The optical properties of the RE^{3+} ions used in our work, such as Pr^{3+}, Eu^{3+}, Tb^{3+}, Dy^{3+}, and Er^{3+}, are discussed in the following section.

- Pr^{3+}

The emission colour from Pr^{3+} ion depends on the host crystals. Pr^{3+} activated Y_2O_2S, Gd_2O_2S, and La_2O_2S emit a green emission under cathode-ray or UV excitation [29, 69, 72]. This is due to the electrical dipole transitions of $^3P_0 \rightarrow {}^3H_J$ (J=4, 5, 6) and $^3P_0 \rightarrow {}^3F_2$ and $^3P_0 \rightarrow {}^3F_4$. A strong single red emission band of $^1D_2 \rightarrow {}^3H_4$ transition has been observed from Pr^{3+} activated $CaTiO_3$ [73], which results from the $^3P_0$ to $^1D_2$ non-radiative relaxation caused by the downshift of the

4f-5d band due to a covalency effect. The low-lying $Pr^{3+}/Ti^{4+} \leftrightarrow Pr^{4+}/Ti^{3+}$ charge transfer state (CTS) has also been proposed to explain the $^3P_0$ to $^1D_2$ non-radiative quenching [74]. The decay time of the $^3P_0$ to ^3H_J or ^3F_J emission is ~10^{-5} s, which is short for a RE^{3+} ion (~ms).

Pr^{3+} is also well known for its quantum cutting effect, which was discovered in the 1960s and has been the source of new research interest in recent years [55-57, 60, 61, 63-65]. When the 4f5d levels are situated above the $^1S_0$ level, a high-energy UV photon can be absorbed by a parity-allowed and spin-allowed 4f→5d transition. The energy is subsequently transferred to the rather stable $^1S_0$ energy state through non-radiative relaxation, from where several emissions in the visible region are possible. More details about the quantum cutting effect and recent progress can be found in reviews for further interest [52, 61].

- Eu^{3+}

Eu^{3+} ions activated phosphors emit bright red light. Eu^{3+} has been incorporated into many host crystals, such as YVO_4 [16], Y_2O_2S [75-82], Y_2O_3 [83-87] to develop red light emitting phosphors for cathode-ray televisions (CRTs). Eu^{3+} has also been investigated for X-ray detection [28, 88]. Eu^{3+} ions usually occupy the sites that have no inversion symmetry in the host crystals. The strong red emission line at around 610 to 630nm is due to the electric dipole transition of $^5D_0 \rightarrow {}^7F_2$. Eu^{3+} ions can also occupy the sites of inversion symmetry, as in $InBO_3$ [88]. If it occurs the emission line at ~ 600nm due to the magnetic dipole transition of $^5D_0 \rightarrow {}^7F_1$ becomes relatively stronger and dominates.

$YVO_4:Eu^{3+}$ was developed in 1964 [16] to meet the demands for an appropriate red phosphor for use in colour TV. This was later replaced by $Y_2O_2S:Eu^{3+}$ for better energy efficiency [75] and stability in the recycling in the screening process of CRT production. $Y_2O_3:Eu^{3+}$ has been used for a high colour rendering lamp as well as for FED displays [84, 85].

- Tb^{3+}

Figure 1.10 presents the emission bands of Tb^{3+} in Y_2O_2S under UV excitation. The complicated appearance is caused by the crystal field splitting.

The emission spectrum consist of emissions due to transitions of $^5D_3 \rightarrow {}^7F_J$, mainly in the blue region, and $^5D_4 \rightarrow {}^7F_J$ (J=0-6), mainly in the green. The blue/green ratio strongly depends on the Tb^{3+} concentration due to the cross relaxation effect between two adjacent Tb^{3+} pairs: Tb^{3+} ($^5D_3$) + Tb^{3+} ($^7F_6$) → Tb^{3+} ($^5D_4$) → Tb^{3+} ($^7F_0$). This phenomenon has been observed in many host crystals [32, 89-97].

The blue/green intensity ratio also depends on the host crystals. Host crystals affect the intensity ratio in two ways: the first is the maximum phonon energy that causes phonon-induced relaxation. The intensity ratio becomes small when the maximum phonon energy is high; the other factor is the relative position of the $4f^75d^1$ and $4f^8$ energy level. If the minimum energy of the $4f^75d^1$ is fairly low and the Frank-Condon shift is fairly large, an electron excited to the $4f^75d^1$ level can relax directly to the $^5D_4$, bypassing the $^5D_3$ and thus producing only $^5D_4$ luminescence.

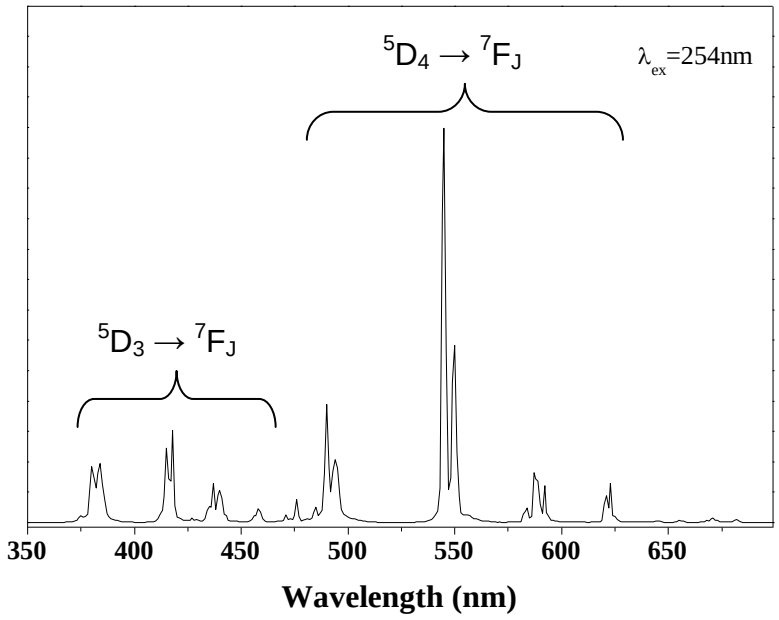

Figure 1.10 Emission spectrum of $Y_2O_2S:Tb^{3+}$.

- Dy^{3+}

The emission of Dy^{3+} has a whitish colour due to transitions of $^4F_{9/2} \rightarrow {}^6H_{15/2}$ (~470-500nm, blue) and $^4F_{9/2} \rightarrow {}^6H_{13/2}$ (~570-600nm, yellow) (Figure 1.11). The $^4F_{9/2} \rightarrow {}^6H_{13/2}$ transition has $\Delta J=2$ and is hypersensitive and decreases with a

decrease in the polarity of the neighbouring ions. Direct UV excitation of Dy^{3+} is not effective due to the relatively large energy of the CTS and $4f^8 5d^1$ energy state. However the excitation via energy transferred from the host matrix ions could be effective. Quantum yields of up to 65% have been reported for $YVO_4:Dy^{3+}$.

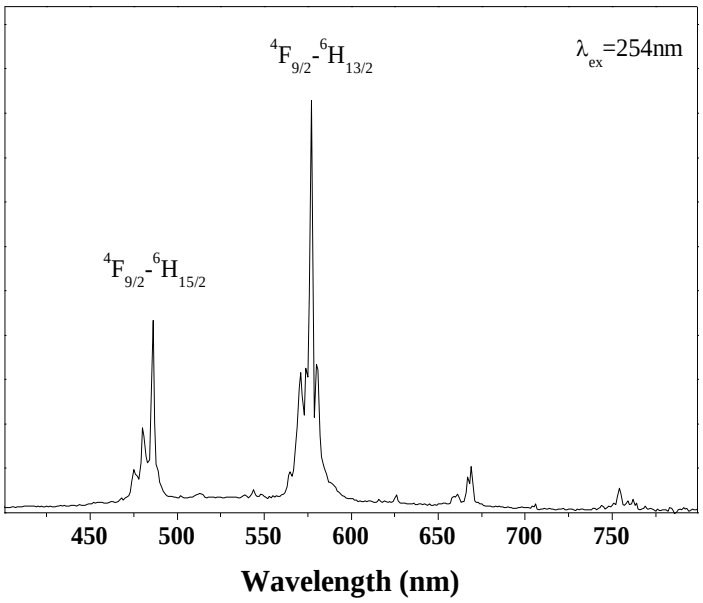

Figure 1.11 Emission spectrum of $Y_2O_2S:Dy^{3+}$.

- Er^{3+}

Er^{3+} has been extensively studied for its capability of converting low-energy photons to high-energy photons through the upconversion process [5, 98-103]. More details about Er^{3+} and upconversion will be discussed in the upconversion phosphors section. Er^{3+} ions doped into glasses function as optical amplifiers for 1.55 μm semiconductor laser light and have been employed in optical telecommunication systems [21].

1.3.2 Y_2O_2S and Gd_2O_2S

The choice of host lattice strongly influences the luminescent properties of the phosphors by determining the distance between dopant ions, their coordinate numbers, their relative spatial position and their electrical environments. Here we describe the two host crystal lattices used in this work.

The Y_2O_2S and Gd_2O_2S crystal lattices are well known wide band-gap (4.6-4.8eV) semiconductors [104]. They do not exist as natural minerals but were invented as host matrices for RE^{3+} ions by Royce [105] and Yocom [106] from the Radio Corporation of America (RCA) in 1968. Since then both lattices have been the subjects of intensive research interest.

The crystal symmetry of Ln_2O_2S (Ln=Y, Gd) is trigonal, and the space group is P3m1. Figure 1.12 shows the schematic crystal structure of Ln_2O_2S. Each Ln atom is bonded to four oxygen atoms and three sulphur atoms and has a seven-coordinate geometry. Both Ln and oxygen atoms have the same site symmetry of C_{3v} and the S site has symmetry of D_{3d}.

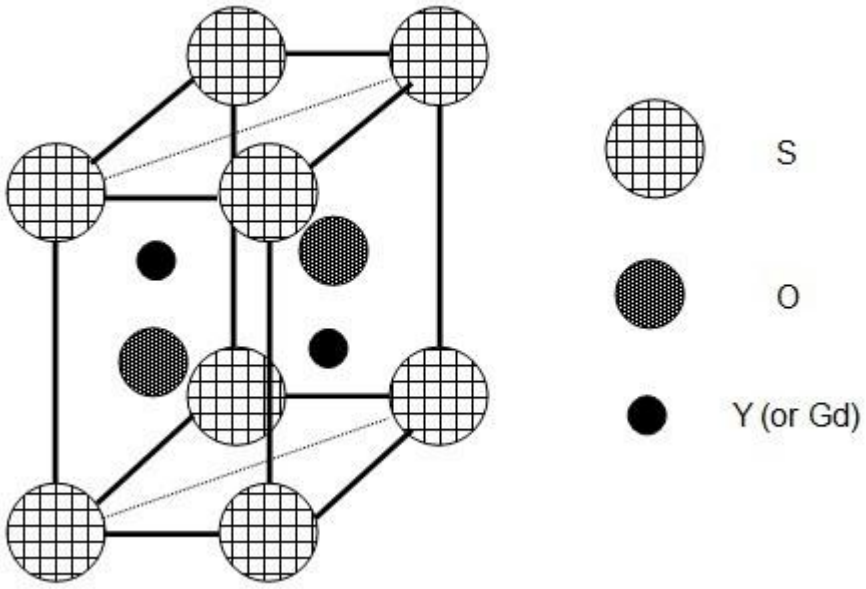

Figure 1.12 Schematic crystal structure of Ln_2O_2S (Ln=Y, Gd).

1.4 Stokes emission and anti-Stokes emission

Phosphors emit light after the absorption of energy from an incident photon. The emission photon is usually of lower energy compared to the incident photon. This kind of emission is termed Stokes emission. The energy loss is caused by lattice relaxation due to a change in the strength of the chemical bond [107]. The gap between absorption and emission energy is called the Stokes shift.

There is also the possibility that a phosphor, when excited with strong light sources, i.e. a laser, could absorb two (or several) photons at one time and emit a photon of higher energy than the incident photon. This process is called upconversion and the emission is anti-Stokes emission. Upconversion phosphors of high upconversion efficiencies are usually doped with lanthanide ions and are promising candidates for biological labelling and diagnostics. Both Stokes emission and anti-Stokes emission are illustrated in Figure 1.13.

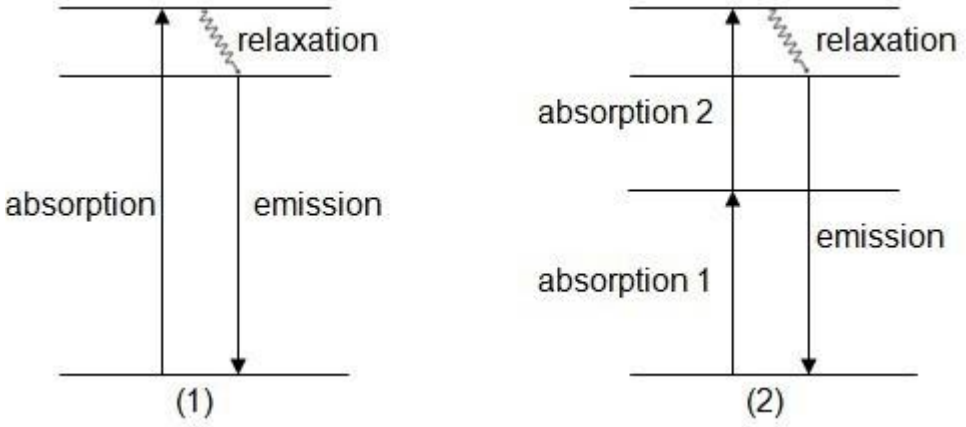

Figure 1.13 Schematic energy transfer processes for (1) Stokes emission and (2) anti-Stokes emission.

1.5 Recent developments in RE^{3+} ions activated phosphors

In 1998, developments in the field of phosphors for lighting and displays over the previous thirty years were reviewed by Justel *et al* [40]. Improvements by then had driven phosphors to work close to their physical limits. However in recent years, the classical RE^{3+} activated phosphors, to be more specific, nanometre-sized particles of narrow size distribution and designed morphology have come back into research focus. Some recent developments are introduced in this section.

RE^{3+} doped phosphors, such as $Gd_2O_2S:Tb^{3+}$, $Gd_2O_2S:Pr^{3+}$, $(Y,Gd)_2O_2S:Eu^{3+}$, and $Y_2O_2S:Tb^{3+}$, have been commonly used as scintillation materials for medical diagnostics [44, 68]. For these materials, several properties are required, such as high X-ray absorption, hard radiation stability, high conversion efficiency from X-ray to visible light, short decay times and low afterglow. Emissions from RE^{3+} 4f transitions usually have long decay times

(~ms), which is disadvantageous in medical imaging. Thus co-doping is often employed for better performance of the scintillation materials [36]. For example, the afterglow in $(Y,Gd)_2O_2S:Eu^{3+}$ is caused by thermally unstable trapped charge carriers (electrons by the Eu^{3+} ions and holes by the intrinsic trap state) and their subsequent release and eventual recombination at the luminescent centre, which could be significantly reduced by the co-doping with Pr^{3+} [28]. Thermally stable Pr^{4+} (up to 700K) formed during X-ray radiation acts as an effective hole trap and successfully competes with the intrinsic hole traps, resulting in non-radiative recombination and reduction of trap centres thus drastically reducing such afterglow at room temperature. Addition of 0.1 mol% Tb^{3+} into $Gd_2O_2S:Pr^{3+}$ improves the light output by ~15% and the incorporation of Ce^{3+} ions reduces radiation damage by controlling the generation of the colour centres with an absorption energy of 3.4 eV (~370 nm) which are generated by the X-ray irradiation and decrease the light output [29].

In modern medical imaging systems, such as computed tomography (CT), scintillation materials are usually used in conjunction with optical detectors, i.e. films, Si based photodiodes, CCD arrays. The total resolution of the system is determined by the phosphor material noise (screen noise) as well as the noise of the optical detectors [31]. Furthermore, the screen noise consists of two components: quantum noise and structure noise [108]. Quantum noise is affected by the spatial fluctuation of the absorbed X-ray quanta and dominates in low-exposure conditions [31] while the structure noise is strongly affected by the thickness and uniformity of the phosphor screen. A high degree of close packing of the phosphor particles and a thicker layer could reduce the structure noise. Thus parameters affecting particle morphology and size distribution which influence the effective filling fraction should be controlled. Decrease in particle size also causes reduction in structure noise due to less scattering of the radiation [31]. Smaller particles potentially lead to higher screen resolution and a higher screen density as well.

Recently, $Gd_2O_2S:Pr^{3+}$ has been used in detectors for water window X-ray (wavelength of 2.3-4.4nm, energy of 0.28-0.53 keV) detection in complicated electromagnetically noisy environments [33]. $Gd_2O_2S:Tb^{3+}$ is the most frequently

employed phosphor in x-ray intensifying screens [38]. $Gd_2O_2S:Tb^{3+}$ has been incorporated with polyethylene microstructures to fabricate flexible scintillators for the next-generation flexible X-ray image sensors [34]. Pixel height and fill factor are two factors that affect the sensitivities of the as-prepared scintillators with different pitch sizes.

Nanometre sized particles of uniform spherical shape have been developed for high definition TV (HDTV) [80, 81, 84-86, 109]. These phosphors are designed to operate under a low electron accelerating voltage (1-5 kV) as required in field emission display (FED) technology and luminescence efficiency comparable to [84] or even higher [85] than the commercial bulk materials can be obtained. $Y_2O_3:Eu^{3+}$ nanocrystals in the size range 70-100nm are reported to be 50% more efficient than the bulk material at 1kV accelerating voltage under electron excitation [85]. A continuous and uniform silica layer was coated to $Y_2O_2S:Eu^{3+}$ to enhance its processability [81]. $Y_2O_3:Eu^{3+}/Y_2O_3$ nanoparticles of core-shell structures were prepared and their luminescence properties were investigated [86]. In contrast to quantum dots (QDs), the peak positions of Eu^{3+} emission are not affected by the particle size: the core- shell structure reduces the Eu^{3+} emission intensity by diluting the Eu^{3+} concentration.

Classical inorganic phosphors are commonly prepared using the solid state reaction method [44, 110], often followed by grinding and milling to reach the required particle size. This usually introduces many surface defects which function as non-radiative recombination sites for charge carriers and cause a drop-off in luminescence efficiency.

Many chemical approaches have been developed to prepare monosized particles. In our work, phosphor precursor powders were prepared using the homogeneous precipitation method [84]. The homogeneous precipitation technique is based on the slow hydrolysis (or other reactions) of a solute, such as Y^{3+} for the preparation of $Y(OH)CO_3$ (the metal hydroxycarbonate precursor of the phosphor). The whole process can be simplified as the release of CO_2 and NH_3 by urea decomposition, followed by the sequential addition of the ligands OH^{-1} and CO_3^{2-} to the metal cations until the concentration of reactants reaches critical

supersaturation and then precipitation occurs. The precipitates assume a spherical shape to minimise the free energy.

The precipitation rate is controlled by the thermal decomposition of urea at over 85˚C [111], in which process the urea decomposes into CO_2 and NH_3 at a relatively slow and controllable rate [112, 113]. The decomposition of urea depends upon temperature and the reaction rate is first order with respect to urea [113]. Urea decomposed in water at a rate of 4% per hour for temperatures above 85˚C [113], which is ideal to feed the reactants into the reaction in a controlled manner.

1.6 Upconversion phosphors

1.6.1 Introduction

Upconversion (UC) is a nonlinear optical process for which the optical properties of the material depend on the radiant flux density of the exciting light and is characterized by the conversion of long-wavelength (low energy) radiation to short-wavelength (high energy) radiation [102]. Auzel summarised his pioneering work in the field of UC and proposed several mechanisms to explain the UC process [114-118]. However, the efficiencies of these UC processes are usually low and most UC phosphors for practical applications are realized through two mechanisms. One is initially called the APTE effect (addition de photon par transfers d'energie) and was later named energy transfer upconversion (ETU) [116], it has an efficiency of ~10^{-3}, the other termed excited state absorption (ESA) has an efficiency of ~10^{-5} [119]. Both mechanisms require re-absorption of a second photon by metastable, long lifetime excited states, which leads to a higher excited state from which the UC emission occurs. In the case of ESA, the luminescent centre sequentially absorbs two or more photons of appropriate energy to populate the excited state. This is in contrast to ETU, in which the population of the emitting level is achieved by subsequent energy transfer from a neighbouring ion to the excited state. Very often a co-dopant called a sensitizer is employed for higher efficiency (~10^{-1}) [119]. A schematic illustration of the ETU and ESA processes is presented in Figure 1.14.

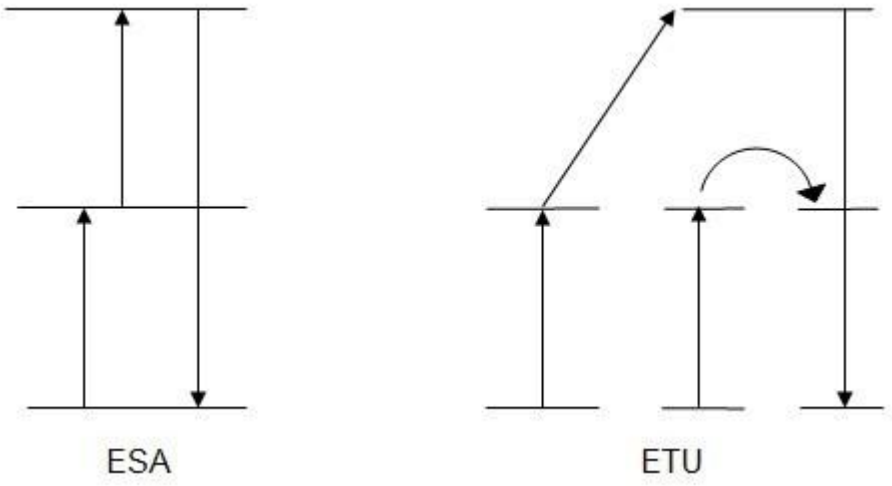

Figure 1.14 Schematic illustration on UC processes of ESA and ETU [118].

A ladder-like arrangement of energy states with similar energy gaps is required for UC, which are realized for certain ions, such as transition metal ions and rare earth ions. Transition metal ions, such as Os^{4+} [120, 121], Ni^{2+} [122], Ti^{2+} [123-125], have been reported to also manifest these properties in suitable host materials. These systems, although extensively studied, have shortcomings such as satisfying the requirement on low operating temperatures and need to improve optical properties, thus the need is still for fundamental research.

UC phosphors of high efficiencies at room temperatures are usually doped with rare earth ions. Upconversion has been observed from many RE^{3+} activated solids, such as silicates [126], oxides [103, 127-134], oxysulfides [99, 100, 135-140], fluorides [141-149]. Amongst them Yb^{3+} and Er^{3+} co-doped $NaYF_4$ of hexagonal phase is the most efficient UC phosphor to date [149], which was introduced by Menyuk *et al* in 1972 [141].

RE^{3+} ions such as Er^{3+}, Tm^{3+}, and Ho^{3+} best meet the requirements on energy state structures for UC activators and are the most commonly employed in current upconversion phosphors [102, 150]. For practical applications, the concentration of Er^{3+} and Tm^{3+} are respectively optimised to not exceed ~3% and ~0.5% to avoid concentration quenching [102]. It is a common routine to sensitize the activator ions with Yb^{3+} sensitizer for 980nm NIR excitation, usually in high concentration (18%-25%) [139, 143-145, 147-149, 151]. However, when UC

phosphors are excited with a red laser, the presence of Yb^{3+} decreases both the down-conversion and upconversion intensities [130].

Figure 1.15 shows how Yb^{3+} ions transfer energy to Er^{3+} and Tm^{3+} activators. The energy gap (~10370cm^{-1}) between the ground state ($^2F_{7/2}$) of Yb^{3+} and its $^2F_{5/2}$ excited state could bridge the transition energy (~10350cm^{-1}) between the $^4I_{11/2}$ and $^4I_{15/2}$ states as well as the $^4F_{7/2}$ and $^4I_{11/2}$ states of Er^{3+} via efficient resonant energy transfer. In the case of Yb^{3+} sensitized Tm^{3+}, the energy of four NIR incident photons is injected from Yb^{3+} into Tm^{3+}. Yb^{3+} and Er^{3+} co-doped phosphors also benefit from manifesting high saturation resistance [102].

To date, $NaYF_4$ is the most efficient host material for UC phosphors. It shows low phonon energy (ca. 350 cm^{-1}) [152] and the similar ionic radii between Na^+, Y^{3+} and RE^{3+} prevent the formation of crystal defects and lattice stress, which has been found to be advantageous over other host materials [142, 144, 153]. Crystal structures also play a role in respect to UC efficiency. Green emission in hexagonal $NaYF_4$:Yb^{3+}/Er^{3+} exhibits approximately 10 times stronger efficiency than that in cubic $NaYF_4$:Yb^{3+}/Er^{3+} [149]. The high UC efficiency of hexagonal $NaYF_4$:Yb^{3+}/Er^{3+} originates from the fact that Yb^{3+} and Er^{3+} occupy two independent lattice sites in $NaYF_4$, which guarantees an efficient resonant or near resonant energy transfer process between Yb^{3+} and Er^{3+} [154].

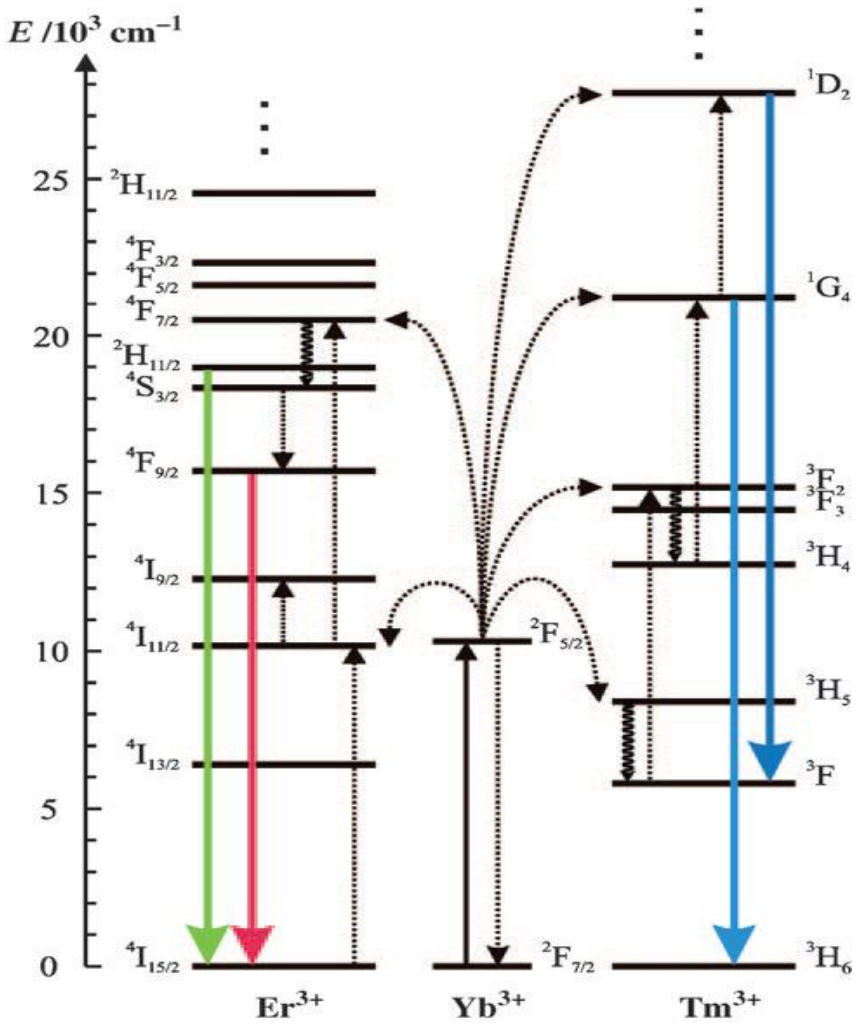

Figure 1.15 Energy transfer processes for Yb^{3+} sensitized Er^{3+} and Tm^{3+} systems [153]. Full, dotted and curly arrows indicate radiative, non-radiative energy transfer processes and multi-phonon relaxation processes, respectively.

1.6.2 Developments of RE^{3+} activated UC nanocrystals

Great progress has been achieved in the field of UC phosphors in the last few decades. There are two factors that contribute to this: on the one hand, the developments in semiconductor lasers that now provide relatively cheap exciting light sources for upconversion, such as infrared (IR) or near-infrared (NIR) lasers; and in addition, UC phosphors are considered a promising alternative for organic dyes or quantum dots in biological labelling due to low back ground noise and low toxicity [101, 155-158].

Various synthetic approaches have been explored to prepare highly efficient UC phosphors. Details have been discussed in review articles [102, 150,

159, 160]. The benefits and drawbacks of several typical synthetic routes are presented in Table 4. Using these methods, monodisperse UC nanocrystals of narrow size distribution can be obtained [128, 137, 138, 143-146, 152, 161].

Table 1.4 Typical synthetic routes to UC nanocrystals [150].

Method	Host materials	Remarks
Coprecipitation	LaF_3, $NaYF_4$, $LuPO_4$, $YbPO_4$	Fast growth rate. No need for costly equipment or complex procedures. Post-heat treatment typically required.
Thermal decomposition	LaF_3, $NaYF_4$, GdOF	Expensive, air-sensitive metal precursors. High quality, monodisperse nanocrystals. Toxic by-products.
Hydro(solvo)thermal synthesis	LaF_3, $NaYF_4$, $La_2(MoO_4)_3$	Cheap raw materials. No post-heat treatment. Excellent control ove particle size and shape. Specialised reaction vessels required.
Sol-gel processing	ZrO_2, TiO_2, $BaTiO_3$, $Lu_3Ga_5O_{12}$, YVO_4	Cheap raw materials. Calcinations at high temperatures required.
Combustion synthesis	Y_2O_3, Gd_2O_3, La_2O_2S	Time and energy saving. Considerable particle aggregation.
Flame synthesis	Y_2O_3	Time saving and readily scalable.

As mentioned above, hexagonal $NaYF_4$ is the preferred host crystal for higher UC efficiency [149]. Many efforts have been made to synthesize pure phase $NaYF_4$ UC phosphors [143, 146, 152, 153, 162, 163]. The thermal decomposition method, which is based on the thermal decomposition of trifluoroacetates in solvent mixtures of oleic acid and octadecene, was applied to generate high UC efficient $NaYF_4$:Yb^{3+}, Er^{3+} nanocrystals for the first time [162]. In this method, the decomposition of trifluoroacetates at 330˚C rapidly forms reactive fluoride compounds, which is advantageous. The shortcomings include the emission of toxic fluorinated and oxyfluorinated carbon species, the

requirement of high reaction temperature and the narrow temperature window of the decomposition [102].

In 2008 Li and Zhang proposed an alternative method for the synthesis of pure hexagonal phase $NaYF_4$:Yb^{3+},Er^{3+}/Tm^{3+} nanocrystals by replacing the metal trifluoroacetates with in situ generated rare-earth oleates from NaOH and NH_4F [147]. All the fluoride reagents are consumed to form solid-state nuclei at room temperature before the diffusion-limited growth of the nanocrystals at elevated temperature, thus providing a user-friendly synthetic condition [147]. Nanocrystals of different shapes can be obtained by tuning the ratio between the ligands (oleic acid) and a high-boiling solvent (octadecene).

High phase purity of hexagonal $NaYF_4$:Yb^{3+},Er^{3+} can be generally achieved by either sufficiently high reaction temperatures (~300˚C) or prolonged heat treatment (up to several days), which usually come together with significant particle aggregation [150].

Recently, simultaneous phase and size control of $NaYF_4$:Yb^{3+},Er^{3+} was realised through Gd^{3+} co-doping [164]. Incorporating Gd^{3+} ions with larger ionic radii into the $NaYF_4$: Yb^{3+},Er^{3+} system induces increased dipole polartizability and electron cloud distortion and favours the hexagonal phase of low-symmetry cation sites [164]. A mixture of cubic and hexagonal phases was found without the addition of Gd^{3+} under the chosen reaction conditions. Gradual transformation from the cubic to the hexagonal phase was observed with increased Gd^{3+} concentration and the pure hexagonal phase was obtained at 30 mol% of Gd^{3+}. Moreover, the size of the corresponding particles decreases. Furthermore, Tm^{3+} was introduced into the ternary system for tuning the emission colour of the UC nanocrystals [164]. The emission colour can be tuned from blue (0.2% Tm^{3+}) to green (2% Er^{3+}) by adjusting the Tm^{3+}/Er^{3+} ratio.

Wang *et al* reported a liquid-solid-solution (LSS) process to synthesize a variety of nearly monodisperse RE activated nanocrystals with narrow size distribution [159, 160]. The LSS process is based on the phase transfer induced reduction of metal ions at the liquid-solid or solution-solid interfaces at a designated temperature followed with in-situ adsorption of ligands onto the

surface of the nanocrystals. A phase separation process occurs spontaneously because of the weight of the nanocrystals (see Figure 1.16). The nanocrystals as-prepared by the LSS process are hydrophobic with the alkyl chains on the outside [160] but could be rendered hydrophilic by surface modification [165]. These nanocrystals are re-dispersible and could be used as building blocks to form 3D colloidal spheres by a bottom-up self assembly method based on a designated oil-in-water (O/W) micro-emulsion system [166, 167], in which the nanocrystals are gathered, assembled and fixed spontaneously during the controlled solvent evaporation process in a restricted micrometre-sized 3D space. More details could be found in reference [159].

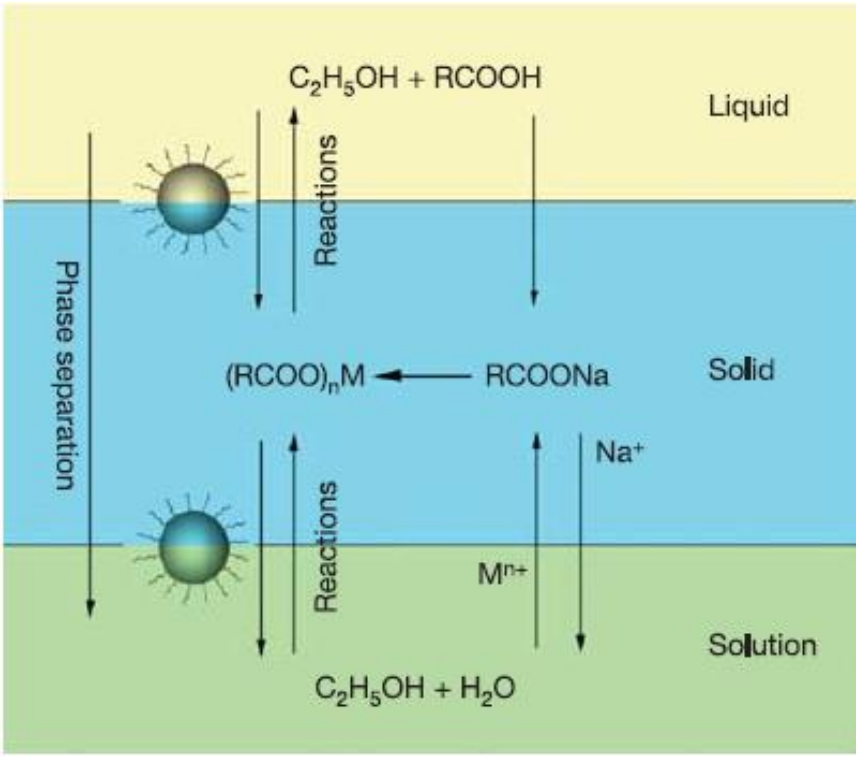

Figure 1.16 Scheme of the LSS synthetic process [160].

For UC phosphors, activators of ladder-like, well-separated energy level structures are required. So far only a few transition metal ions and RE^{3+} ions, such as Er^{3+}, Ho^{3+}, Tm^{3+}, Os^{4+}, have met these requirements and limit the achievable UC colours. Wang *et al* designed a new series of UC phosphors with core-shell structures using Tb^{3+}, Eu^{3+}, Dy^{3+}, and Sm^{3+} as emitters, respectively [168]. In their approach, the $NaGdF_4$:Yb^{3+},Tm^{3+} nanocrystals are coated with

$NaGdF_4:X^{3+}$ (X=Tb, Eu, Dy, or Sm) sublattice layers forming a well-defined core-shell structure (see Figure 1.17 a).

The energy transfer processes are illustrated in Figure 1.17 b. Yb^{3+} functions as a sensitizer to harvest pumped photons and subsequently promote a neighbouring Tm^{3+} (accumulator) to the excited states. Gd^{3+} (migrator) ions extract energy from high-lying energy states of the accumulator and randomly migrate the energy through the Gd sublattice before an activator ion, X^{3+}, traps the energy and eventually emits a photon [168]. Based on this energy migration upconversion (EMU) process, UC emissions that cover almost the entire visible spectral range could be approached with NIR excitation. Also, it has been shown that, the migration of excitation energy through the Gd sublattice can travel a substantial length (more than 5nm), or even between two separated nanoparticles. This discovery enables lanthanide-doped nanophosphors to work as acceptors since the Gd sublattice could shorten the interaction distance between the donor and the acceptor as well as tune the mismatched energy levels to the same resonant frequency [168].

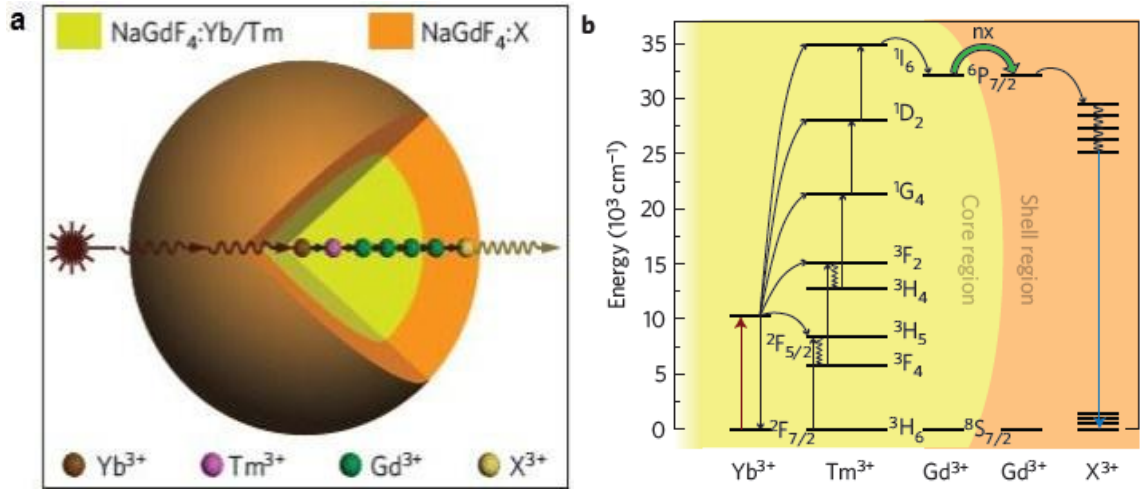

Figure 1.17 Tuning upconversion through energy migration in core-shell nanoparticles [168]. a. Scheme of the $NaGdF_4:Yb^{3+},Tm^{3+}/NaGdF_4:X^{3+}$ core-shell structure; b. Proposed energy transfer mechanisms in the core-shell nanoparticles.

1.6.3 Applications of UC phosphors

The most promising application for UC phosphors falls into the biological field [101, 102, 150, 151, 155-159, 169]. Organic dyes and quantum dots (QDs) are commonly used for biological labelling and imaging. These are usually excited with UV light and suffer from the interference of auto-fluorescence of the biological tissues. In contrast, UC phosphors are usually excited with IR or NIR light source, which means weak or even no auto-fluorescence from cells or tissues. In addition, the IR radiation penetrates deeply into biological tissues and causes minimal photo damage to the organisms being studied [144, 147]. UC phosphors also benefits from high photo-chemical stability, narrow emission bandwidths and good biocompatibility [102]. A seven order of magnitude higher visible light output has been reported for colloidal $NaYF_4:Yb^{3+}/Er^{3+}$ nanocrystals than CdSe-ZnS QDs under the same experimental geometry [153, 170]. The main challenge is that most UC nanocrystals are with sizes in the region of 20 nm, which is too large compared to most QDs.

Another interesting application for UC phosphors is volumetric three-dimensional television (3D TV). Downing *et al* presented the first three-colour 3D TV operated at room temperature using Pr^{3+}(red), Er^{3+}(green), Tm^{3+}(blue) activated UC phosphors [171]. The display is viewable under typical ambient room lighting conditions. Research efforts have been made to prepare UC phosphors of high quantum efficiency suitable for the 3D displays [164, 172].

UC phosphors have been employed to enhance the performance of solar cells [45, 47, 48, 151, 173-178]. According to Henry's detailed balance model [179], the maximum energy conversion efficiency η of an ideal solar cell with a given bandgap is competitive with the thermalization η_{therm}, sub-bandgap η_{sub}, and radiative η_{rad} efficiency losses. Under air mass 1.5 global non-concentrated conditions, $\eta + \eta_{therm} + \eta_{sub} + \eta_{rad} = 1$. UC phosphors are suggested to have the potential to increase the conversion efficiency η by reducing the sub-bandgap loss η_{sub} [48]. Both down conversion and up-conversion could be used to enhance the energy conversion efficiency [45, 46, 180]. UC phosphors are suggested for bandgaps above ~1.25eV and down-conversion phosphors for bandgaps below ~1.25eV since bandgaps below ~1.25eV have larger thermalization losses

whereas bandgaps above ~1.25eV have larger sub-bandgap losses [45]. For this application, $NaYF_4$ doped with only Er^{3+} is preferred for the relatively broad absorption band [45, 47].

UC phosphors can also be used in the security and anti-counterfeiting field. Kim *et al* designed photo-patterns based on UC nanocrystals and proposed applications in the field of security [181]. Liu *et al* designed RE^{3+} (Yb^{3+}/Er^{3+},Yb^{3+}/Tm^{3+},Er^{3+}) activated $NaYF_4$ nanocrystals with both UC and down-conversion luminescence and investigated their anti-counterfeiting performance [182]. Results suggest these nanocrystals can provide a strengthened and more reliable anti-counterfeiting effect due to their colour-tuning capability and high concealment [182].

1.7 Quantum dots

1.7.1 Introduction to quantum dots

Quantum dots are semiconductor nanocrystals with particle size of roughly 1 to 10 nm. Quantum dots bridge the gap between cluster molecules and bulk materials. Typically a QD particle consists of ~100 to ~10 000 atoms. QDs are sometimes called ‘artificial atoms’ and are utilised as building blocks in the bottom-up approach to more complicated nanostructures through self assembly processes. Some fundamental concepts and the unique, size dependent properties of QDs are explained in the following section.

In a semiconductor, photon absorption can pump an electron from valence band to conduction band and spontaneously generate a positive charged hole. The electron in the conduction band is bound to the localised hole via Coulomb force forming an exciton. The characteristic distance between the bound electron and the hole is termed the exciton Bohr radius. When the materials dimension is reduced to a size close to or even smaller than the exciton Bohr radius, the quantum size confinement occurs. When the size of a nanocrystals is roughly 3 to 10 times the exciton Bohr radius, the exciton is in a weakly confined state [183]; when the particle size is smaller than the exciton Bohr radius, the exciton is in a strong confined state [184].

When QDs are in the quantum confine regime, the bandgap increases compared with that of the bulk material, resulting in a blue shift in the absorption spectrum as well as in the emission spectrum. The continuous energy bands of the bulk materials collapse and split into several discrete, well separated energy levels (see Figure 1.18), which lead to the discrete absorption spectrum of QDs. The bandgap energy for a spherical QD can be approximately calculated using the given equation:

$$E_g(QD) \approx E_g(bulk) + \frac{\pi^2 \hbar^2}{2\mu R^2} \qquad (3)$$

where R is the particle radius and μ is the effective mass defined by:

$$\frac{1}{\mu} = \frac{1}{m_e} + \frac{1}{m_h} \qquad (4)$$

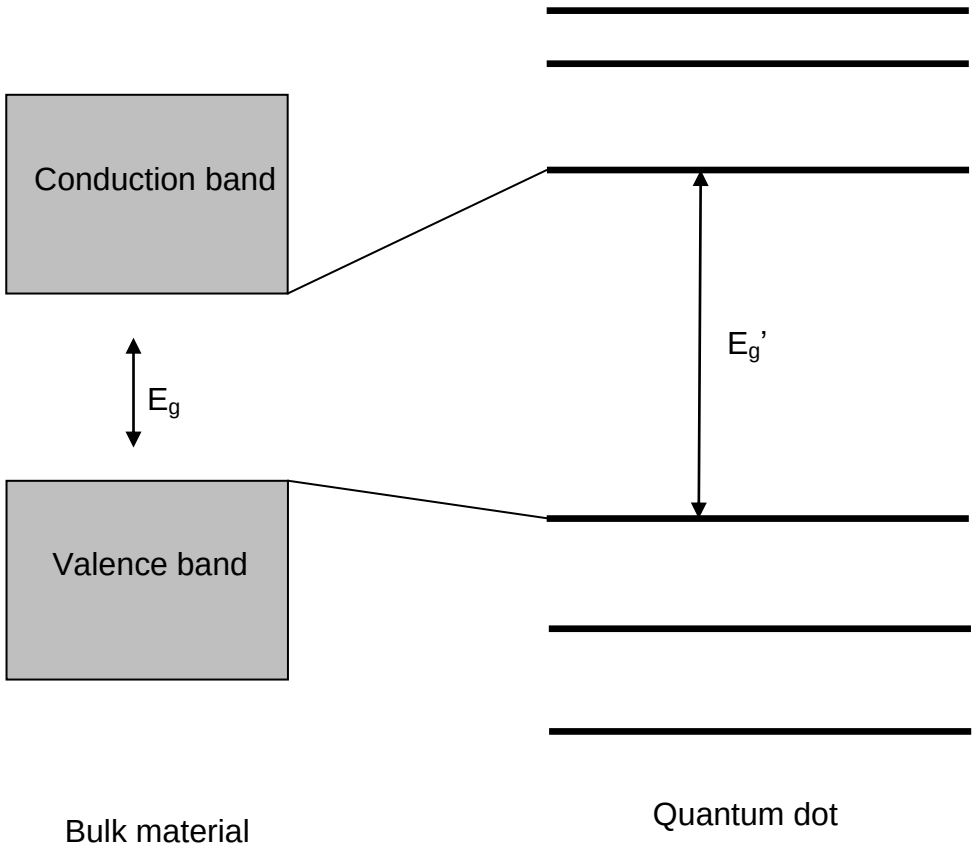

Figure 1.18 Schematic illustrations for the bandgap of the bulk material and the QD.

According to equation (3), the bandgap of the QDs is in proportion to $1/R^2$. Thus, the emission colour of the QDs is tuneable simply by tailoring the particle size to a proper value. Figure 1.19 shows the size-dependence emission colour of CdTe QDs synthesized in water with size in the 2-5nm range.

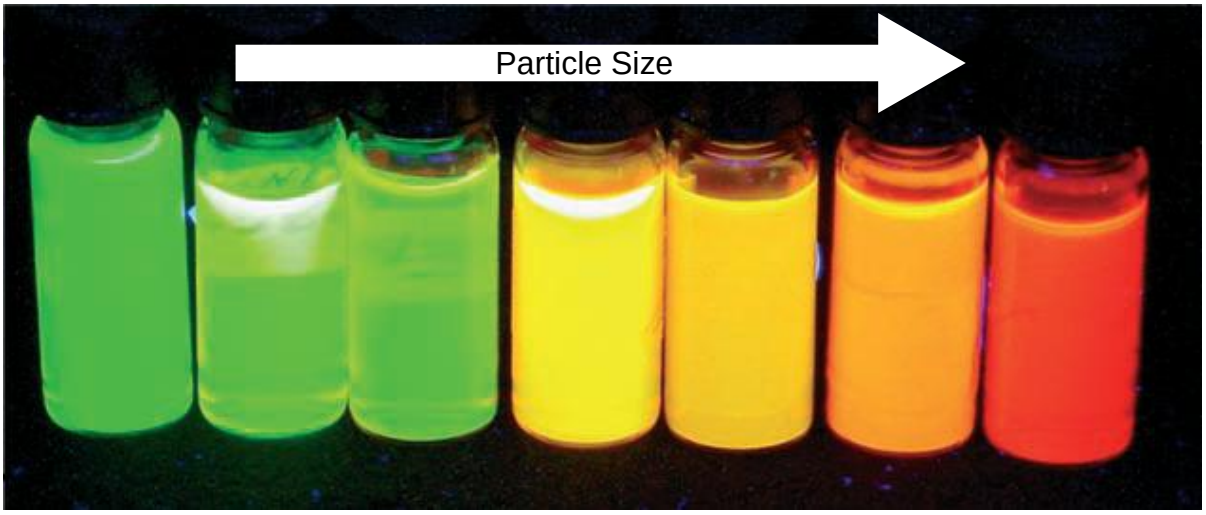

Figure 1.19 Size-dependent photoluminescence of CdTe (2-5nm size range) [185].

Reduction of the size of QDs results in an enlarged fraction of the total number of atoms on the surface and thus a high surface volume ratio. Therefore QDs exhibit physical and chemical properties in huge contrast to the bulk materials. The melting temperatures of QDs reduce with decreasing particle size [186-189]. The melting temperature of CdS decreases from 1678K (bulk) to 573K (1.6 nm in diameter) [189]. ZnS:Mn nanocrystals show reduction in phase transition temperature [190]. On the other hand, the high surface-to-volume ratio of QDs causes poor luminescence properties since surface-related non-radiative relaxation dominates in the strong confinement regime. For practical applications, QDs are usually coated with a passivation layer, either composed of organic ligands [160, 185, 191-194] or by an inorganic layer to form the core-shell structure [195-198]. The passivation layer can stabilize the QDs and enhance the luminescent efficiency by reducing the non-radiative contribution of the surface.

Many preparation methods have been explored to synthesize quantum dots, including molecular beam epitaxy (MBE), metalorganic-chemical-vapor-deposition (MOCVD), and vapour-liquid-solid (VLS) [191]. Amongst these methods, one soft chemical method, colloidal synthesis is of great research

attraction and been employed as a common routine approach to prepare QDs of narrow size distribution and tailored morphologies [191]. A typical colloidal process consists of a temporally discrete nucleation event followed by relatively rapid growth from solution-phase monomers and a slower growth termed Ostwald ripening. Particle size and shapes can be controlled by adjusting reaction conditions, such as monomer concentration, reaction temperatures, pH, and choice of solvent and surfactant. Review articles concerning the shape control mechanisms have been published [199-205]. Other benefits from colloidal synthesis include spontaneous passivation layers on the QDs and easy routes to introduce impurities.

Dopants, the intentional impurities in host crystals, strongly influence the electronic and optical properties of the host materials in a controllable manner. These doped nanocrystals exhibit some unique optical properties, such as minimized self-absorption, long excited-state lifetime narrow emission bandwidth, and good thermal stability [206]. Many applications of the nanocrystals may ultimately depend on tailoring their performance using proper dopants. Bhargava investigated Mn^{2+} and Tb^{3+} doped ZnS nanocrystals and suggested applications in displays, sensors and lasers [192, 194]. It's worth noting that the quantum yield of ZnS:Mn (~18%) was higher than the best available undoped crystals [194]. And great progress has been achieved ever since on more efficient luminescence for doped nanocrystals (greater than 50%) [207, 208]. Incorporating impurities at specific distanced from the centre of core-shell nanocrystals leads to good separation between the impurity, the surface and other impurities, thus affecting the competition between radiative and non-radiative pathways in the nanocrystals [207, 208].

Recently, Mn^{2+} was successfully incorporated into previously undopable CdSe nanocrystals [209, 210]. The doping process is governed by growth kinetics and the initial adsorption of Mn^{2+} on the nanocrystal surface is critical for this doping, (it is determined by surface morphology, nanocrystal shape, and surfactants in the growth solution) [209]. Recent progress in doped nanocrystal, theories concerning the doping process and effect of dopant on the optical and

electronic properties of the host crystals can be found in the latest review article [211].

Most recently, a new method has been developed to dope InAs QDs with metal impurities, such as Ag, Cu, and Au, enabling control of the bandgap and Fermi energy [212]. Both p-type and n-type nanocrystals were realised by respectively introducing Ag and Cu impurities into InAs QDs using this method and their optical and electronic properties were investigated [212].

1.7.2 Recent developments of ZnS:Mn^{2+} and PbS QDs

In 1994, Bhargava reported the first Mn-doped ZnS nanocrystals with a size range from 3.5 to 7.5 nm and the luminescence efficiency due to the surface passivation from UV-cured polymerization [194]. Thereafter great research effort has been attracted into this field. ZnS:Mn^{2+} nanoparticles (ca. 3.5 nm) have been prepared through aqueous reactions and are suggested as efficient low-voltage CL phosphors [213, 214]. The influence of synthesis conditions on the properties of ZnS:Mn^{2+} has been explored and an excess S^{2-} was preferred for enhanced photoluminescence performance by filling the sulfur vacancies in the nanocrystals while the particle diameters increase from 3.7 to 5.1 nm when the precursor concentration shifts from an excess of Zn^{2+} to an excess of S^{2-} [215]. Water soluble ZnS:Mn^{2+} QDs of high luminescence efficiency (up to 50% in water) has been obtained by thiol ligands exchange for applications in light emitting diodes and biomedical labels [206]. Srivastava *et al* developed a simple colloidal synthetic technique for highly luminescent (quantum yield > 50%) ZnS:Mn^{2+} QDs in gram scale [216]. Moreover, the QDs can be transferred to water by usual methodology while retaining high quantum yield (> 30%) [216].

Core-shell structures based on ZnS:Mn^{2+} core coated with different inorganic layers have been explored. Influences of UV light treatment and ZnS coating on the luminescence properties of ZnS:Mn^{2+} QDs were investigate [217]. Both UV light treatment and ZnS coating can reduce the non-radiative transition and lead to luminescence enhancement [217]. Ethiraj *et al* [218] reported enhancement on luminescence intensities of ZnS:Mn^{2+} QDs (~1.7nm) when coated with SiO_2 together with significant increase in particle diameters (up to

900nm). Karar *et al* introduced a method to synthesize ZnS:Mn^{2+} QDs with ZnO capping layers of tailored thickness and suggested the resultant stress from ZnO capping layers yields enhancement on luminescence intensity/efficiency of the ZnS:Mn^{2+} QDs (~4nm) [219].

Recent developments on PbS QDs are mostly driven by the demand for utilisation of the solar energy in the IR region (>700nm), which takes up nearly one half of the solar energy reaching earth's surface [220], to improve the performance of the photovoltaic devices [220-222]. In 2005, McDonald *et al* [223] demonstrated the first IR photovoltaic devices on the basis of solution-processible nanocomposites of PbS QDs in poly[2-methoxy-5-(2'-ethylhexyloxy-p-phenylenvinylene)] (MEH-PPV). However, the efficiency is very low (～0.006% short-circuit internal quantum effciency). In a subsequent work by Zhang et al, planar Schottky photovoltaic devices were prepared from octylamine capped PbS QDs to improve the IR photovoltaic efficiency [220]. The device shows 160 times more current at -1V bias and a thermal annealing procedure leads to respectively 200-fold and 600-fold increase in short circuit current and maximum power output, and a 10 times faster response time due to the more efficient charge separation and the improved electron transport properties [220]. Johnston *et al* [222] reported planar, stackable PbS nanocrystals photovoltaic devices with up to 4.2% IR power conversion efficiency (3-fold improvement over previous results) and 1.8% solar power conversion efficiency.

PbS QDs also find application in light-emitting diodes (LEDs). The first paper on PbS QDs based light-emitting devices appeared in 2003. Single layer devices based on mixtures of PbS QDs with MEH-PPV or poly[2-(6-cyano-6'-methylheptyloxy)-1,4-phenylene] were reported with tuneable EL spectra across the range of 1000 to 1600nm [224]. The EL intensity of the PbS QDs capped with octylamine is much higher than those capped with oleic acid due to the suppression of either Förster energy transfer or direct carrier transfer energy from the polymer to the QDs because of the longer carbon chains of oleic acid [224]. A highly efficient EL device with an external quantum efficiency of 1.15% corresponding to an internal quantum efficiency of ~5% to 12% was demonstrated on the basis of butylamine capped PbS QDs [225]. The high

quantum efficiency is attribute to the direct generation of the excited state of the nanocrystals, thus eliminating detrimental competing processes [225]. Most recently, bright IR LEDs with radiances (6.4 W sr^{-1} m^{-2}) 8-fold higher and external quantum efficiencies (2.0%) twice higher than previous results were fabricated [226]. By tuning the distance between adjacent PbS QDs good control over the exciton dissociation and recombination events were realised leading to high light output and quantum efficiency [226].

Photodiodes with infrared sensitivities were proposed for cost-effective imaging. In 2009, Rauch *et al* reported the fabrication of hybrid bulk heterojunction photodiodes containing PbS QDs as sensitizers for NIR (up to 1800 nm) detection with high external quantum efficiency (up to 51%) and demonstrated for the first time NIR imaging with hybrid photodiodes [227]. Pal *et al* fabricated p-n junction photodiodes with up to 80% external quantum efficiency and significant reduction on the dark current, in which the photoactive layer is made from PbS QDs [228].

1.7.3 QDs for white LEDs

QDs are promising candidates for creating a new generation of electroluminescence devices due to their unique optical properties, such as photo and chemical stability, narrow emission bandwidth, long lifetime, and high PL quantum efficiencies. Moreover their emission colour can be controlled not only by the material choice but also by the precise control over particle size which can be easily achieved during the synthetic procedure. The last decade has witnessed impressive progress on QDs based LEDs: the external quantum efficiency has improved by over 100-fold and high colour saturation is now the routine. Review articles concerning recent developments in the field of QDs based LEDs have been published [185, 229-231].

One of the conventional methods to approach white LEDs is the colour-conversion technique [232, 233]. The colour conversion method is based on the appropriate blend of various colours of nanocrystals, which are often of high quantum efficiency [232, 234] and usually excited with blue/UV LED chips. Jang *et al* incorporated multishell-structured CdSe/ZnS/CdSZnS (green) CdSe/CdS/ZnS/CdSZnS (red) QDs into blue LEDs and fabricated white LEDs for

display backlights, yielding high external quantum efficiency (up to 72% for the green and 34% for the red QD-LEDs) and long lifetime (>2200 hours) under ambient conditions [235]. The white LEDs with the 1931 CIE colour coordinates of (0.24, 0.21) was successfully integrated in a 46 inch LCD TV panel to demonstrate excellent colour [235].

Another benefit from the colour-conversion white LED is that the efficiency can be enhanced (up to 82% [236]) utilising non-radiative energy transfer. The mechanism was theoretically demonstrated by Basko *et al* [237] and realized in the laboratory by Achermann *et al* [238]. To allow the non-radiative energy transfer process to take place, the nanocrystal core must be in close contact with the pumping source (less than 5 nm) [237].

Doped nanocrystals show great potential to serve as light converters in white LEDs due to their low self-absorption, high thermal and chemical stability and high resistance to photo-oxidation [231]. $Zn_{1-x}Cd_xS:Mn^{2+}$/ZnS QDs with core-shell structures were investigated and employed as light converter for near-UV and blue LEDs, yielding orange and white light emission respectively [195, 239].

1.8 Current research and results

In the following chapters research carried out in the Wolfson Centre for Materials Processing at Brunel University is reported and discussed. The methodologies used to prepare the phosphor particles and characterization techniques are described in details in Chapter 2. The areas of phosphor research that are covered are listed below along with the chapter numbers:

- Chapter 3 Luminescent properties of RE^{3+} doped Y_2O_2S phosphors;
- Chapter 4 Luminescent properties of $Gd_2O_2S:RE^{3+}$ phosphors;
- Chapter 5 Upconversion luminescence of RE^{3+} activated Y_2O_2S and Gd_2O_2S phosphors;
- Chapter 6 Luminescence investigation of the novel ZnS:Mn based QDs for new applications.

Chapter 2 Experimental

2.1 Introduction

In this chapter, methodologies used to prepare nanometre-sized rare earth doped phosphor powders and quantum dots are described, respectively.

Rare earth ions (RE^{3+}) activated phosphor lattices were prepared through a typical two-step process:

Firstly, submicron spherical precursor powders were obtained using the urea homogeneous precipitation method. The spherical particle morphology is achieved because the precipitate is non-crystalline so that the material assumes a spherical shape to reduce its free energy.

Secondly, the resulting non-crystalline precipitates were converted to oxide or oxysulfide phosphors through appropriate firing treatments.

In this way, RE^{3+} (RE= Dy, Pr, Tb, Er, or Eu) ions were doped into Y_2O_2S and Gd_2O_2S phosphor lattices. Their luminescent properties were then characterised.

Quantum dots (QDs) are semiconductor nanoparticles that efficiently emit a specific colour of light when excited with radiation of the required energy. They have attracted continuing increasing interest for their unique properties [240-244]. In this chapter ZnS:Mn QDs were prepared by aqueous reactions using a surfactant induced highly ordered structure as soft template to embed into gallium nitride LEDs based on photonic crystals. $Zn_xCd_{1-x}S$:Mn QDs and PbS QDs were prepared using a similar method.

Phosphors have wide applications in many fields, which depend on both their luminescence properties and their morphology properties. Instrumentation and techniques used to characterise the resulting phosphors are also described in detail in this chapter.

2.2 Preparation of RE^{3+} doped yttrium oxides and yttrium oxysulfides

Spherical hydroxycarbonate phosphor precursor powders were prepared using the urea homogeneous precipitation method [84, 111, 245], which is a novel way to prepare ultrafine particles [112, 113, 246, 247]. Urea decomposes into ammonia and carbon dioxide at a relatively slow rate in aqueous media when the solution is heated to temperature above 85 ˚C. The precipitation process is controlled by a single nucleation event and uniform growth of the nuclei results in particles of uniform shape and size. Formation of many nuclei is ensured by rapid and constant agitation. It worth noting that to obtain fine precipitation particles it's usually preferred to heat the solution at higher temperature. For precursors of yttrium oxide and yttrium oxysulfide, the chemical reactions to obtain precursors are given below:

$$H_2NCONH_2 \rightarrow NH_4^+ + OCN^-$$

$$OCN^- + 2\ H^+ + 2\ H_2O \rightarrow H_2CO_3 + NH_4^+$$

$$[YOH(H_2O)_n]^{2+} + H_2CO_3 \rightarrow Y(OH)CO_3 \cdot H_2O + (n\text{-}1)\ H_2O$$

2.2.1 Preparation of $Y_2O_3:Dy^{3+}$ phosphor particles

Y_2O_3 (Ampere Industries (French), 99.99%) and Dy_2O_3 (Aldrich, 99.99%) were used as starting materials, both used as received with no further purification.

To make $Y(NO_3)_3$ (0.5 M) stock solution, 56.45 g Y_2O_3 was dissolved in a certain amount (~20-30 ml) of diluted nitric acid (Sigma-Aldrich, 70%) to give the rare earth nitrate solution. The solution was carefully transferred to a 1 litre volumetric flask and then the pH value was adjusted to 2-3 by carefully adding deionised water or dilute nitric acid. $Dy(NO_3)_3$ (0.01 M) stock solution was prepared using the same method.

The synthesis of $Y_2O_3:Dy^{3+}$ nanometre sized particles is a two stage process: firstly, Dy^{3+} doped yttrium hydroxycarbonate precursor $Y(OH)CO_3:Dy^{3+}$ was prepared using the urea homogeneous precipitation method and then the

following sintering treatment to convert it to oxide phosphor particles was carried out.

In a typical experiment, 25 ml of $Y(NO_3)_3$ stock solution was mixed with $Dy(NO_3)_3$ stock solution in suitable quantities (the amount used depends on the doping concentration needed) before being diluted to 500 ml in a 1 litre beaker with deionised water. 30 g urea was added to the solution and boiled on a hot plate. The solution was kept over 85˚C for 1 hour since turbidity was first observed then filtered without cooling. The precipitates were washed twice with deionised water. Soft, white powders were obtained after the precipitates were dried at 100 ˚C for 24 hours in an oven. The whole procedure is illustrated in the flow diagram in Figure 2.1.

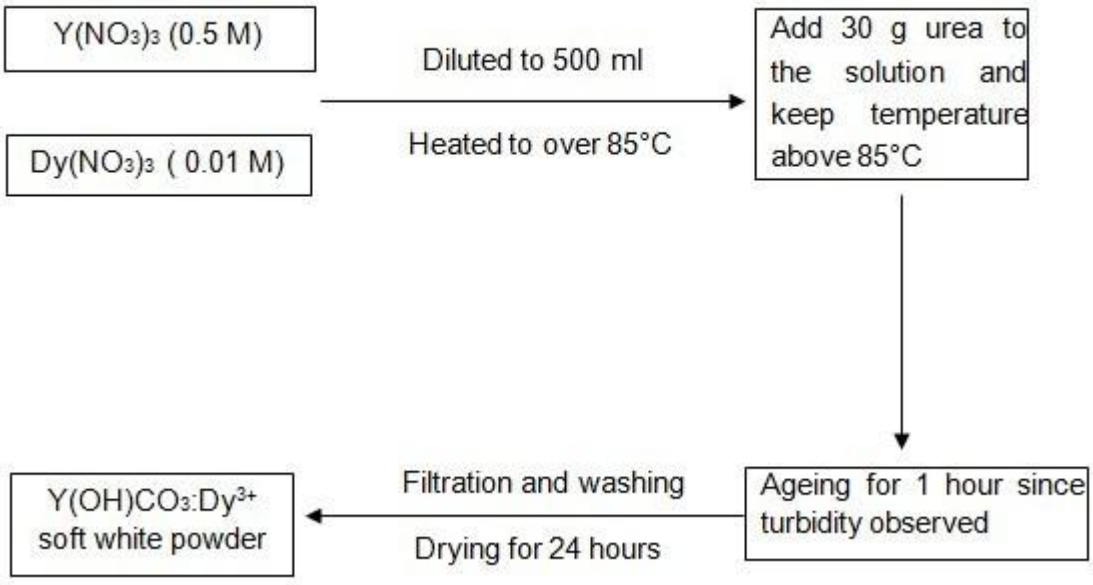

Figure 2.1 Synthesis procedure for $Y(OH)CO_3:Dy^{3+}$ precursors

To convert the precursors to $Y_2O_3:Dy^{3+}$, the precursor powders were transferred to an alumina crucible and fired at 900˚C for 1 hour. The samples were cooled in air to room temperature before washed with deionised water. White powders were obtained after drying at 100˚C for 24 hours.

2.2.2 Preparation of $Y_2O_2S:Dy^{3+}$ phosphor particles

Precursors were prepared using the same method detailed above. To obtain $Y_2O_2S:Dy^{3+}$ particles, the precursor powders were treated with a procedure previously reported by our group [17]. The procedure is as follows: precursor powders were mixed evenly with Na_2CO_3 and S before being transferred into a cylindrical crucible, then the mixture was covered with a top layer composed of Y_2O_3, Na_2CO_3 and S (mole ratio: precursor:Y_2O_3:Na_2CO_3:S=1:1:1.5:2). The top layer was used to shield the sample from oxygen and guarantee the necessary inert atmosphere to obtain oxysulfide particles [79]. The sample was fired at 900 ˚C for 1 hour. The chemical reaction of the $Y_2O_2S:Dy^{3+}$ phosphor is as follows:

$$2\ Y(OH)CO_3:Dy^{3+}\cdot H_2O + 3\ Na_2CO_3 + 4\ S$$

$$\rightarrow Y_2O_2S:Dy^{3+} + 4\ CO_2 + SO_2 + 3\ Na_2O + 2\ H_2O + H_2S$$

The crucible was cooled to room temperature in the air after the firing process. The bottom layer was separated from the top layer and put into a beaker containing 100ml deionised water. The solution was boiled on a hot plate and kept at 100˚C for 20 minutes. The solution was filtered when it was cooled down to room temperature. White powders were obtained after the precipitates were dried at 100˚C for 24 hours in an oven.

2.2.3 Preparation of $Y_2O_2S:Pr^{3+}$ phosphor particles

$Pr(NO_3)_3$ (0.01 M) stock solution was prepared using the same method described in 2.1.1 with Pr_2O_3 (Aldrich, 99.9%) as a starting material. The urea homogeneous precipitation method was used to prepare $Y(OH)CO_3:Pr^{3+}$ hydroxycarbonate sub micrometre phosphor precursor powders.

25 ml of $Y(NO_3)_3$ (0.5 M) stock solution was mixed with the appropriate amount of $Pr(NO_3)_3$ (0.01 M) stock solution and then diluted to 500 ml with deionised water. The solution was kept boiling on a hot plate before 30 g urea was added to it. After turbidity can be observed, the solution was left for 1 hour. The precipitates were filtered and washed twice with deionised water. The

precipitates were dried at 100˚C for 24 hours yielding white, soft powders which were converted to oxysulfides by the sulfurization procedure described in 2.1.2.

2.2.4 Preparation of $Y_2O_2S:Tb^{3+}$ phosphor particles

$Tb(NO_3)_3$ stock solution were obtained by dissolving Tb_2O_3 (Aldrich, 99.99%) in dilute nitric acid until the solution reached pH 3. $Y(OH)CO_3:Tb^{3+}$ hydroxycarbonate precursor powders were prepared using the urea homogeneous precipitation method: 25 ml of $Y(NO_3)_3$ (0.5 M) stock solution was mixed with a proper amount of $Tb(NO_3)_3$ (0.01 M) stock solution (the amount varies from 1.25 ml to 131.6 ml dependent on the doping concentration required) and then diluted to 500 ml with deionised water before the solution was heated on a hot plate. 30 g urea was added to the solution when it was boiling and left for 1 hour since it turned milky white, which indicates the decomposition of urea and formation of the nuclei required for precipitation. The precipitates were filtered and washed twice with deionised water and then dried at 100˚C for 24 hours yielding white, soft powders.

The precursor powders were blended with Na_2CO_3 (Sigma, ≥99.0%) and S (Aldrich, ≥99.99 %) to give an even mixture which was covered with a top layer composed of Y_2O_3, Na_2CO_3 and S. The mole ratio of the precursors/Y_2O_3/Na_2CO_3/S was 1/1/1.5/2. After firing at 900˚C for 1 hour, the top layer was discarded and the bottom layer was washed in boiled water for 20 minutes before the precipitates were filtered. The precipitates were dried at 100˚C for 24 hours to yield soft, white powders.

2.2.5 Preparation of $Y_2O_2S:Eu^{3+}$ phosphor particles

$Y_2O_2S:Eu^{3+}$ phosphor particles were prepared by a similar process. The urea homogeneous precipitation method was used to prepare $Y(OH)CO_3:Eu^{3+}$ hydroxycarbonate precursor powders: Eu_2O_3 (Aldrich, 99.99%) was used as a starting material to prepare $Eu(NO_3)_3$ (0.01 M) stock solution. 25 ml of $Y(NO_3)_3$ (0.5M) stock solution, and 25.2 ml of $Eu(NO_3)_3$ (0.01 M) stock solution were mixed in a 1 litre beaker and then diluted to 500 ml with deionised water. The solution was kept boiling on a hot plate before 30 g urea was added to it. After turbidity can be observed, the solution was left for 1 hour. The precipitates were filtered

and washed twice with deionised water. The precipitates were dried at 100˚C for 24 hours yielding white, soft powders which were converted to the oxysulfides through sulfurization treatment. The final $Y_2O_2S:Eu^{3+}$ phosphor contains 2 mol % Eu^{3+}.

2.2.6 Preparation of $Y_2O_2S:Tb^{3+}$, Er^{3+} phosphor particles

Two kinds of terbium and erbium co-doped yttrium oxysulfides were prepared using the urea homogeneous precipitation method: one is denoted $Y_{2-y-x}Tb_yEr_xO_2S$ and the other $Y_{2-x-y}Tb_xEr_yO_2S$, where x = 0.01 and y = 0.0005, 0.001 or 0.002.

In a typical experiment, 25 ml of $Y(NO_3)_3$ (0.5 M), 12.6 ml of $Tb(NO_3)_3$ (0.01 M) and 1.26 ml of $Er(NO_3)_3$ (0.01 M) were mixed and diluted to 500 ml with deionised water. The solution was stirred and heated to 100˚C before 30 g urea was added. The solution turned turbid in about 15 minutes after urea was added and was left to stand for 1 hour and then filtered without cooling. White, soft phosphor precursor powders were obtained when the precipitates were dried at 100˚C for 24 hours.

The as-prepared precursor powders were mixed with Na_2CO_3 and S to give an even blend which was covered with a top layer of Y_2O_3, Na_2CO_3 and S (mole ratio: Precursor/Y_2O_3/Na_2CO_3/S=1/1/1.5/2). After firing at 900˚C for 1 hour, the top layer was discarded while the bottom layer was washed in boiled water for 20 minutes before filtration. The precipitates were dried at 100˚C for 24 hours giving white powders.

2.3 Preparation of RE^{3+} doped gadolinium oxysulfides

2.3.1 Preparation of $Gd_2O_2S:Dy^{3+}$ phosphor particles

Gd_2O_3 (Ampere Industries (French), 99.99%) and Dy_2O_3 (Aldrich, 99.99%) were used as starting materials. $Gd(NO_3)_3$ (0.5 M) and Dy_2O_3 (0.01 M) stock solutions were prepared by respectively dissolving Gd_2O_3 and Dy_2O_3 in dilute nitric acid until the solution reached pH 3.

$Gd(NO_3)_3$ and $Dy(NO_3)_3$ solutions were mixed thoroughly in the stoichiometries needed to reach the required doping concentration of Dy^{3+}. The solution was diluted to 500 ml and heated on a hot plate with vigorous stirring. 30 g urea was added to the solution when it turned turbid and then it was left for 1 hour. The white precipitates were filtered, washed twice with deionised water and dried at 100˚C to give soft precursor powders.

The precursor powders were mixed thoroughly with Na_2CO_3 and S before being transferred to a cylindrical crucible. Then it was pressed firmly and covered with a top layer obtained by mixing Gd_2O_3, Na_2CO_3 and S. The mole ratio of the precursors/Gd_2O_3/Na_2CO_3/S is 1/1/1.5/2. After the mixed powders were fired at 900˚C for 1 hour, the crucible was cooled to room temperature in the air. The top layer was discarded and the bottom layer was washed in boiled water for 20 minutes before filtration. The precipitates were dried at 100˚C to give white phosphor powders.

2.3.2 Preparation of $Gd_2O_2S:Tb^{3+}$ phosphor particles

The urea homogeneous precipitation method was used to prepare $Gd(OH)CO_3:Tb^{3+}$ hydroxycarbonate precursor powders. 25 ml of $Gd(NO_3)_3$ (0.5 M) stock solution was mixed with a proper amount of $Tb(NO_3)_3$ (0.01 M) (the amount varies from 1.25 ml to 131.6 ml dependent on the doping concentration required) stock solution before being diluted to 500 ml with deionised water. The solution was boiled before 30 g urea was added to it under continuous stirring. When turbidity was observed the solution was left above 85˚C for 1 hour. The precipitates were filtered and washed twice with deionised water before being dried at 100˚C to yield white, soft powders.

The as-prepared precursor powders were mixed thoroughly with Na_2CO_3 and S and covered with a top layer composed of Gd_2O_3, Na_2CO_3 and S, in which the mole ratio of the precursors/Gd_2O_3/Na_2CO_3/S is 1/1/1.5/2. After sintering at 900˚C for 1 hour, the bottom layer was washed in boiled water for 20 minutes. The precipitates were filtered and washed twice with deionised water before being dried at 100˚C to give white phosphor powders.

In addition, some of the obtained phosphors were re-fired at 1100˚C. An alumina boat containing the required amount phosphor powders were placed in the bottom of a quartz tube and fired at 1100˚C for 1 hour. The quartz tube was sealed with glass wool completely to ensure an oxygen-free atmosphere and purified nitrogen gas was passed through the system at a rate of 200 cm^3 per minute during both the firing and the cooling periods.

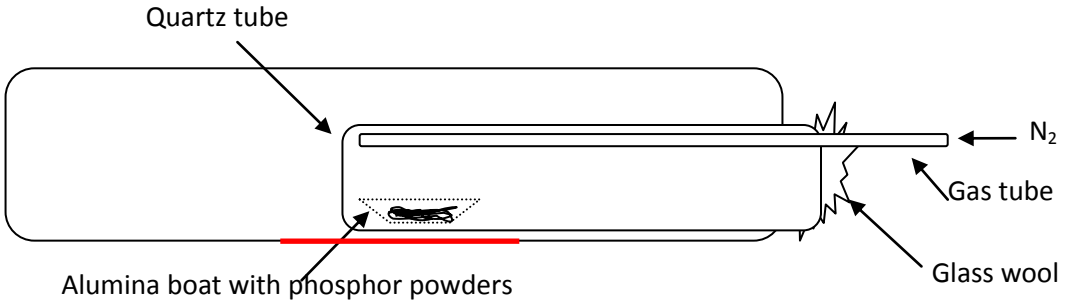

Figure 2.2 Schematic diagram of re-firing $Gd_2O_2S:Tb^{3+}$ phosphor powders. The red line indicates heated area.

2.3.3 Preparation of $Gd_2O_2S:Pr^{3+}$ phosphor particles

Nanometre-sized $Gd_2O_2S:Pr^{3+}$ phosphor powders were prepared by converting spherical $Gd(OH)CO_3:Pr^{3+}$ hydroxycarbonate precursors obtained using the urea homogeneous precipitation method [33].

To make the precursor powders, 25 ml of $Gd(NO_3)_3$ stock solution was mixed thoroughly with appropriate amounts of $Pr(NO_3)$ stock solution, which yields different doping concentrations of Pr^{3+} activators, before it was diluted to 500 ml with deionised water. The solution was heated to boiling and then 30 g urea was added. After turbidity was observed, the solution was left boiling for 1 h. The precipitates were filtered, washed twice with deionised water and then dried at 100˚C to give white soft powders.

The precursor powders were mixed thoroughly with Na_2CO_3 and S before being transferred to a cylindrical alumina crucible. The blended mixture was pressed firmly and covered with a top layer obtained by mixing Gd_2O_3, Na_2CO_3 and S. The mole ratio of the precursors/Gd_2O_3/Na_2CO_3/S is 1/1/1.5/2. After the mixture was fired at 900˚C for 1 hour, the crucible was cooled to room

temperature in the air. The top layer was discarded and the bottom layer was washed in boiled water for 20 minutes before filtration. The precipitates were dried at 100˚C, giving white phosphor powders.

The resulting $Gd_2O_2S:Pr^{3+}$ phosphor powders were also subjected to the re-firing treatment at 1100˚C using a similar method to that described in 2.2.2. A thin $Gd_2O_2S:Pr^{3+}$ phosphor layer was placed in an alumina boat and carefully pushed to the bottom of a quartz tube, which was then completely sealed with glass wool. The whole system was put in a tube furnace and fired at 1100˚C for 1 hour with nitrogen gas flowing through the system during both the firing and the cooling periods.

2.3.4 Preparation of $Gd_2O_2S:Tb^{3+}$, Er^{3+} phosphor particles

Rare earth oxides Gd_2O_3, Tb_2O_3 and Er_2O_3 were used as starting materials for the preparation of nanometre-sized $Gd_2O_2S:Tb^{3+}$, Er^{3+} phosphor particles. Stock solutions were prepared by dissolving the rare earth oxides in dilute nitric acid until the solutions reached pH 3. $Gd(NO_3)_3$ stock solution is 0.5 M while the others are 0.01 M. Two kinds of phosphors were prepared with different doping concentration of activators, specifically different ratios of Tb^{3+} and Er^{3+} cations were used, which were respectively denoted $Gd_{2-y-x}Tb_yEr_xO_2S$ and $Gd_{2-x-y}Tb_xEr_yO_2S$, where x = 0.01 and y = 0.0005, 0.001, or 0.002.

The urea homogenous precipitation method was used to prepare $Gd(OH)CO_3:Tb^{3+}$, Er^{3+} hydroxycarbonate phosphor precursor powders. In a typical experiment, 25 ml of $Gd(NO_3)_3$, 12.6 ml of $Tb(NO_3)_3$ and 1.26ml of $Er(NO_3)_3$ stock solutions were mixed and diluted to 500 ml with deionised water. The resulting solution was heated to 100˚C on a hot plate and then 30 g urea was added with continuous stirring. After turbidity was observed, it was left above 85˚C for 1 hour. The precipitates were filtered, washed twice with deionised water and dried at 100˚C to yield white soft powders.

The precursor powders were mixed thoroughly with Na_2CO_3 and S before being transferred to a cylindrical alumina crucible. The blend was pressed firmly and covered with a top layer obtained by mixing Gd_2O_3, Na_2CO_3 and S. The mole ratio of the precursors/Gd_2O_3/Na_2CO_3/S is 1/1/1.5/2. After the mixture was fired at

900˚C for 1 hour, the crucible was cooled to room temperature in the air. The top layer was discarded and the bottom layer was washed in previously boiled water for 20 minutes before filtration. The precipitates were dried at 100˚C giving white phosphor powders.

2.4 Preparation of quantum dots (QDs)

An amphiphilic compound contains two immiscible hydrophobic parts (tails) and hydrophilic parts (heads) within the same molecule. When dissolved in water or other proper solvents such as methanol, toluene, amphiphilic compounds could self-assemble into highly ordered crystal structures through micro-segregation of the two incompatible components on a nanometre scale. Israelachvili defines the packing parameter of an amphiphilic molecule as p = v/la, in which a is the surface area of the head-group and v and l are the volume and length of the hydrophobic chains, respectively [248]. Amphiphilic molecules with p≤1/2 will spontaneously assembled into micellar aggregates upon dispersal in water. A spherical morphology which is thermodynamically stable will be formed as the concentration increases. A cubic phase could be formed by these spheres in some systems. The spheres may also be connected to one another, forming a bicontinuous cubic phase (BCP).

QDs are synthesized using the bicontinuous cubic phases as nanometre sized reactors [213, 214, 249, 250]. Some surfactants could self-assemble into a mesoporous BCP of long-range 3D periodicity when mixed with water or non-aqueous solvents. Specifically, the aqueous pores in the BCP are interconnected with neighbouring ones, which allow ions to diffuse from pore to pore without passing through the surfactant membrane barrier, making it an ideal choice for making mono-dispersed nanometre sized particles.

2.4.1 Preparation of manganese doped zinc sulfide

Nanoparticles of ZnS:Mn were synthesized using a similar method previously reported using $ZnCl_2$ (BDH AnalaR, ≥96.0%) and $MnCl_2{\cdot}4H_2O$ (BDH AnalaR, ≥98.0%) as starting materials. 0.2 M of $ZnCl_2$ and 1.6×10^{-3} M of $MnCl_2$

aqueous solution were obtained by respectively dissolving $ZnCl_2$ and $MnCl_2{\cdot}4H_2O$ in deionised water.

5 ml of $ZnCl_2$ and 5 ml of $MnCl_2$ aqueous solutions were mixed with sodium dioctyl sulfosuccinate (AOT, ≥99.0%, Sigma) in the ratio of 40 wt% aqueous solution and 60 wt% AOT. A transparent, viscous paste was formed after 24 hours incubation, which was then injected into a 150 ml solution of 0.2 M $Na_2S{\cdot}9H_2O$ (≥99.99%, Aldrich) and 0.1 M NaCl (≥99.0%, Aldrich) through a 5 ml syringe. The supernatant was discarded 1h later. The specimen was washed with deionised water by centrifugation then twice with methanol (Sigma, 99.9%) before being dried in a vacuum oven at 50˚C for 24 hours.

2.4.2 Preparation of lead sulfide

PbS nanoparticles were prepared using a BCP as a matrix [249]. $Pb(NO_3)_3$ (Aldrich, ≥99.99 %) was used as received. In a typical synthesis procedure, about 1.5 g mixture of aqueous Na_2S solution (21.5 wt %) and AOT (78.5 wt %) was prepared in a centrifugation tube followed by centrifugation. After a period of occasional stirring, it was left to incubate at room temperature for 24 hours giving a transparent but extreme viscous mixture. The mixture was taken up in a 5 ml syringe and extruded into aqueous 0.4 M $Pb(NO_3)_3$ solution in the shape of a cylinder of 2 mm in diameter. After 1 h, the cylinder was transferred to a clean centrifugation tube and washed with once with deionised water and twice with methanol by centrifugation, resulting in the precipitation of a dark brown PbS powder.

2.4.3 Preparation of manganese doped zinc cadmium sulfide

The $Zn_{1-x}Cd_xS$:Mn particles were synthesized using a similar method previously reported in literature [213]. $ZnCl_2$ (0.2 M), $Cd(CH_3COO)_2$ (0.2 M) and $MnCl_2$ (1.6×10^{-3} M) aqueous solutions were prepared by dissolving $ZnCl_2$, $(CH_3COO)_2Cd{\cdot}2H_2O$ (BDH AnalaR, 99%) and $MnCl_2{\cdot}4H_2O$ in deionised water, respectively. All the solutions were used straight after preparation.

8ml 0.1 M of $ZnCl_2$, 2 ml of 0.1 M $Cd(CH_3COO)_2$ (or with other proper Zn/Cd mole ratio) and 10 ml of 0.0016 M $MnCl_2$ aqueous solutions were mixed

with sodium dioctyl sulfosuccinate (AOT) in the ratio of 40 wt% aqueous solution and 60 wt% AOT. A transparent, viscous paste was formed after 24 hours incubation. The paste was injected to a 150 ml solution of 0.2 M $Na_2S \cdot 9H_2O$ and 0.1M NaCl. 1 hour later the supernatant liquid was discarded and the specimen was washed once with water by centrifugation, and then twice with methanol before it was dried in a vacuum oven at 50˚C for 24 hours.

2.5 Instruments and sample preparation methodologies

Phosphor powders were characterized with X-ray powder diffraction, scanning electron microscopy, transmission electron microscopy, Raman spectroscopy, photoluminescence and cathodoluminescence spectroscopy. Details about the instruments and sample preparation methodologies are described in the following sections:

2.5.1 X-ray Powder diffraction

X-ray powder diffraction (XRPD) was used to determine the crystal phase of the phosphor powders. Diffraction patterns of the samples were recorded using a Bruker D8 ADVANCE X-ray powder diffractometer using a copper source and LynxEye^{TM} silicon strip detector (Figure 2.3). The diffractometer was previously calibrated using an aluminium oxide line position standard from Bruker and the LaB_6 NIST SRM 660a line profile standard. The emission of the nickel filtered Cu source, and hence the instrumental line broadening, was determined by fitting the NIST standard using Bruker TOPAS (total pattern analysis solution) version 3. The resulting XRPD patterns were refined and average size of crystallites were calculated using the TOPAS computer program.

For all the rare earth doped phosphors, the powders were pressed in the middle of the sample holder to make a flat surface before put into the scanning chamber. All data were collected from 5˚ to 100˚ (2θ) for 35 minutes in the step scan mode. As for the QD samples, since the diffracted intensities from such nanocrystallites are generally weak, all data were collected from 20˚ to 65˚ (2θ) for 6 hours in the step scan mode.

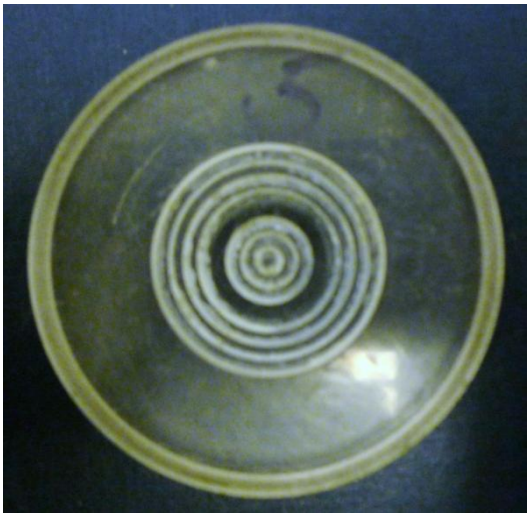

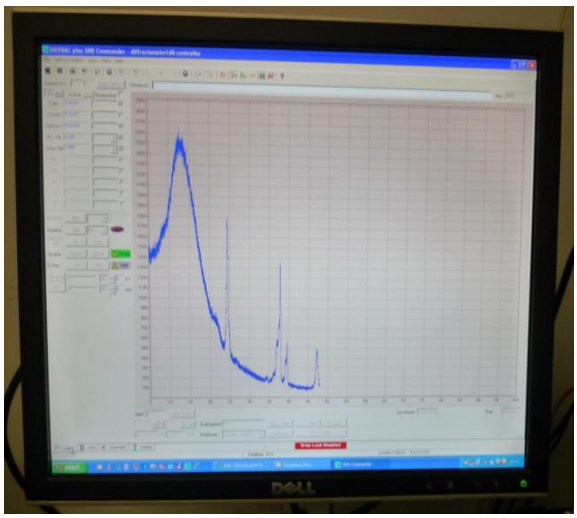

Figure 2.3 Top: Bruker D8 ADVANCE X-ray powder diffractometer; Bottom left: Sample holder; Bottom right: sample scan.

2.5.2 Scanning electron microscopy

Scanning electron microscopy (SEM) is applied to characterise the micro-morphologies of the RE^{3+} doped phosphors. An ultra high performance field emission scanning electron microscope, ZEISS SUPRA 35VP (Figure 2.4), was used to observe the microstructures of the surfaces of the phosphor powders and to record the images. The microscope is equipped with both high-vacuum and variable operating pressure capability. The field emission source and Gemini column in this instrument result in a very high resolution capability while the variable pressure system enables imaging and analysis of samples in their natural state which allows non-destructive examination of environmentally sensitive samples as well as insulating samples.

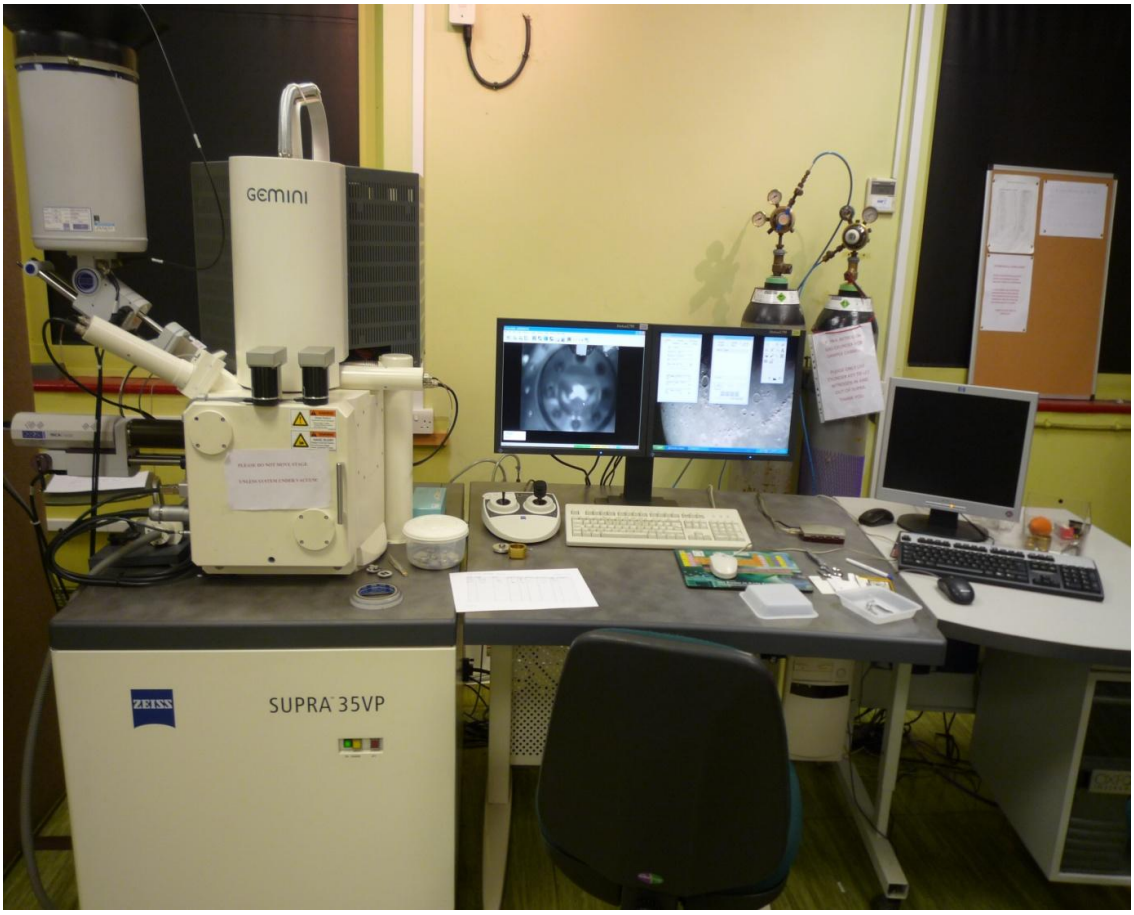

Figure 2.4 ZEISS SUPRA 35 VP scanning electron microscope

The SEM samples were prepared as follows: A tiny amount of phosphor powder was dispersed in isopropyl alcohol (IPA) by ultra-sonication. A few drops of the solution were spread on the surface of aluminium stub before it was dried

for about 10 min to give a clean and dry phosphor layer. Samples are coated with gold nanoparticles using a POLARON SPUTTER coater (see Figure 2.5) before being placed in the chamber for observation. The standard coating procedure is as follows: Ensure argon gas supply was on before placing the samples in the vacuum chamber. Shut the coater lid and press the manual button. Set coating time and voltage as 30 seconds and 1.5 kV respectively before starting the pump by pressing Start Sequence button. Once the leak valve LED which will flash initially is lit, press the start on timer to start coating. The coating is completed when the end LED lights up. On completion, press the red VENT/STOP and keep it pressed in, which will automatically stop the pump. Wait for the chamber to pressurize. Remove samples, shut chamber lid and switch off the argon gas.

Figure 2.5 POLARAN SPUTTER coater

2.5.3 Transmission electron microscopy

Transmission electron microscopy (TEM) was carried out with a JEOL JEM-2000FX electron microscope equipped with a CCD camera (see Figure 2.6).

The instrument uses LaB_6 as the electron gun and the applied accelerating voltages could be up to 200kV.

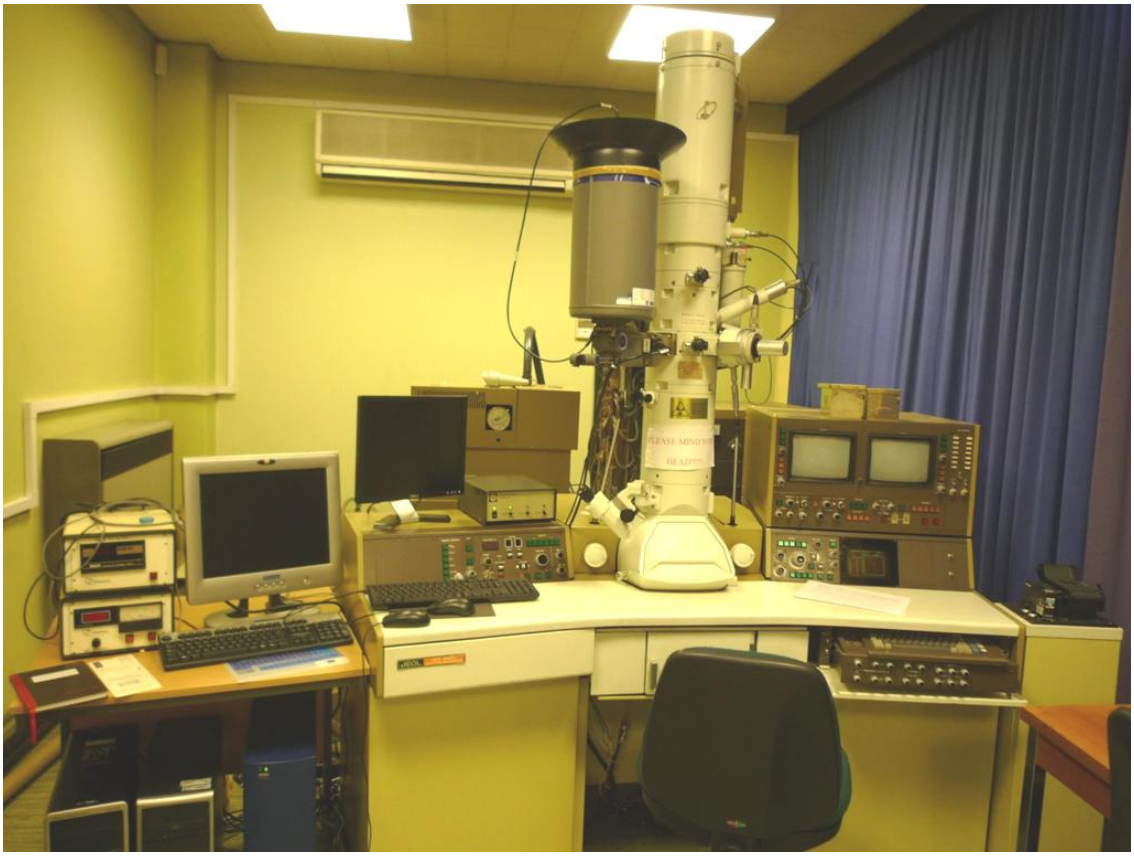

Figure 2.6 JEOL JEM-2000FX transmission electron microscope.

Samples for TEM were prepared using the same method described as follows except for the PbS QDs: a tiny amount of the QD particles was dispersed in methanol by ultra-sonication and a drop of the solution was spread on the surface of a carbon-coated copper grid. When the methanol was completely vaporised the grid was gently put into the chamber for characterization.

As for the PbS QDs, The Langmuir-Blodgett technique [249] was used to prepare monolayers of PbS nanocrystals for the TEM studies: Freshly made PbS QDs powders were dispersed in methanol by ultra-sonication before an excess *n*-dodecanethiol solution was added with vigorous shaking. After around 10 minutes, dark PbS powder was recovered through centrifugation and washed twice with methanol by centrifugation. To obtain the monolayers needed, a few drops of thiol-capped PbS QDs in chloroform were spread on the surface of deionised

water. Patches of thin film formed on the surface of the water were then carefully transferred onto the copper grids.

2.5.4 Raman spectroscopy

Raman spectroscopy was obtained using a HORIBA JOBIN YVON LabRAM HR800 spectrometer (Figure 2.7). The instrument has a built-in He-Ne 20 mW laser of 632.8 nm wavelength, which is polarized at 500:1. Also there are two external lasers available: an Ar^+ green laser of 514.5 nm wavelength and infrared laser of 1064 nm wavelength. One air-cooled CCD detector is set for collecting signals in the visible light region and one liquid nitrogen cooled CCD detector for those in the infrared region.

The 1064 nm infrared laser is chosen as exciting source to obtain Raman spectra of QD nanoparticles to avoid disturbance of luminescent emissions. The 632.8 nm red laser is used to observe upconversion emissions from rare earth doped phosphors. Before recording a spectrum, some preparation procedures are carried out as follows: Select the right laser by changing the mirror positions and enter the wavelength value in the LabSPEC software. Choose a suitable grating and position the spectrometer to collect in the suitable Raman/PL emission range.

A standard silicon sample is used for calibration: the vision image function in the LabSPEC is used to help focus the laser. Correct focus is reached when the reflected spot on the sample is the most concentrated. Then click the 'autocalibration' button within LabSPEC, the calibration would be automatically done. The Si $\nu 1$ line should centre at 520.7 cm^{-1} for a good calibration.

Phosphor powders were placed on a silica slide with slight pressure to give a flat surface before it was placed on the microscope stage. Once calibration was carried out, the laser was focused on the sample. Multi-window accumulation mode was used to record the spectra. For Raman spectra, data are collected from 100 cm^{-1} to 1000 cm^{-1}. For upconversion PL emission spectra, data are collected from 400 nm to 900 nm.

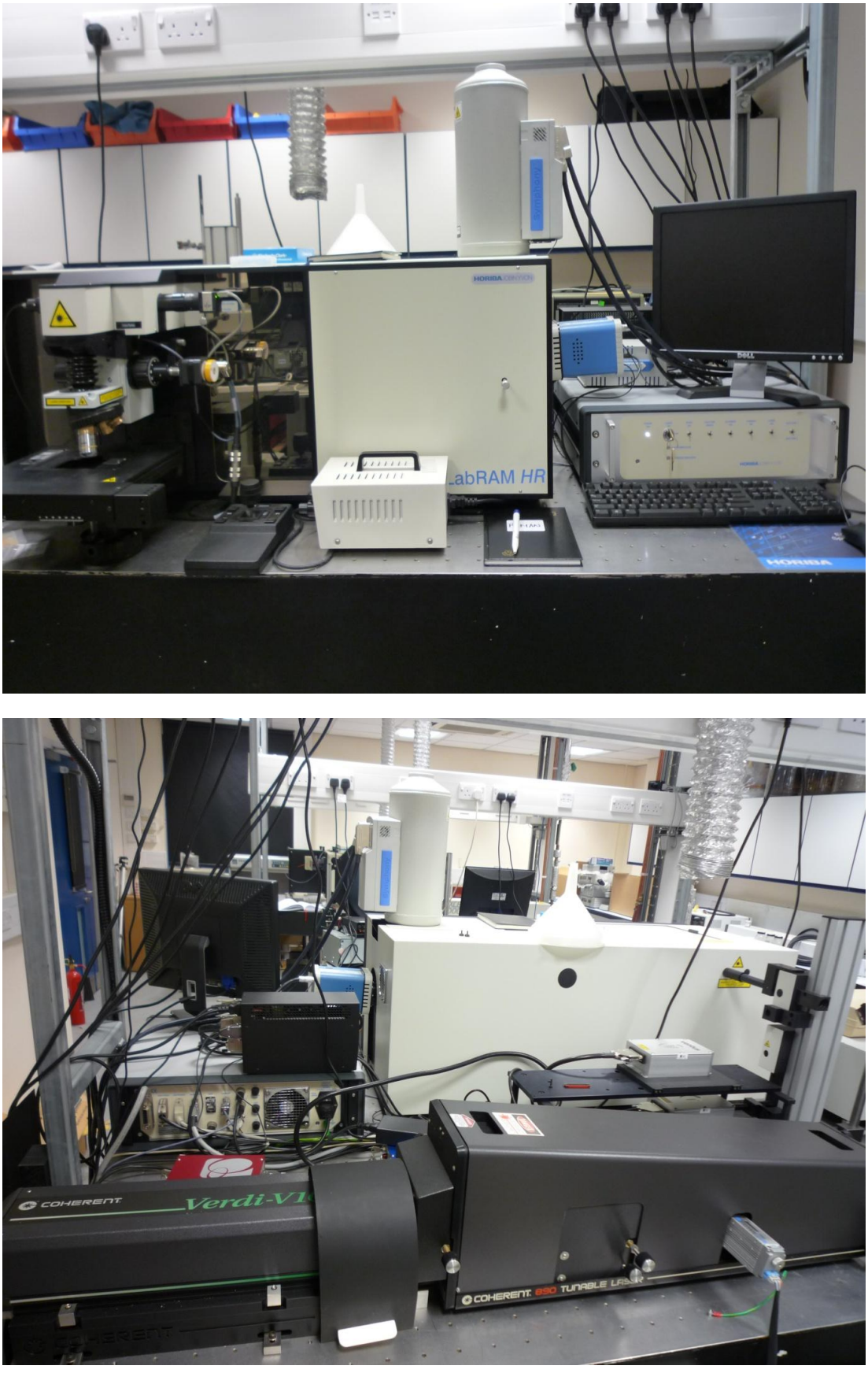

Figure 2.7 HORIBA JOBIN YVON LabRAM HR800 Raman microscope. Top: Front view; Bottom: External green and infrared lasers.

2.5.5 Photoluminescence spectroscopy

Photoluminescence (PL) spectroscopy is used to study the luminescence properties of both rare earth doped phosphors and QDs.

PL excitation and emission spectra of rare earth doped phosphors were recorded using a Bentham phosphor research spectrometer incorporated with BenWin+ software (Figure 2.8). Emission spectra were recorded from 300 nm to 800 nm using 254 nm UV light as exciting source while the excitation spectra for each phosphor were recorded by monitoring the dominant emission peak.

Figure 2.8 Bentham phosphor research spectrometer.

PL emission and excitation spectra of QDs were recorded using a HORIBA YOBIN YVON Flurolog®-3 spectroflurometer (Figure 2.9). QD suspensions were prepared by dispersing QDs particles in methanol. In order to improve the dispersion, the suspensions were vibrated in an ultrasonic bath for several minutes. Data were collected by the FluroEssence software.

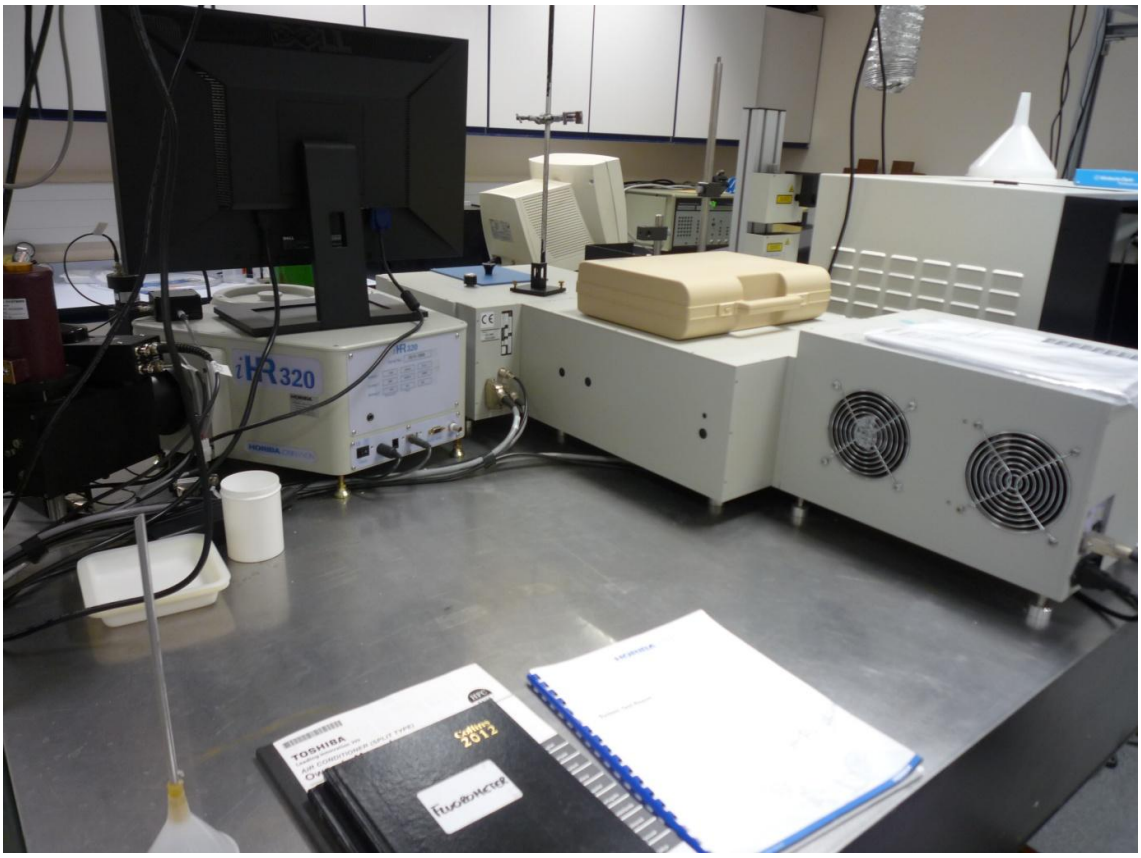

Figure 2.9 HORIBA YOBIN YVON Flurolog®-3 spectroflurometer.

2.5.6 Cathodoluminescence instrument and measurments

Cathodoluminescence (CL) spectroscopy was also used to study the luminescent properties of the rare earth doped phosphors. The samples for CL measurement were prepared using electrophoresis to coat the phosphor particles onto aluminium stubs [84]. Isopropanol (IPA) with 5×10^{-4} M $Mg(NO_3)_2$ was used as an electrolyte solution. Phosphor suspensions were made by dispersing small amounts of phosphor powders (~0.5g/50mL) into the electrolyte solution through ultrasonication. The electrophoresis voltage used was 150 V and coating time was varied from 2-10 minutes to guarantee a choice coating thickness of 3 mg/cm^2.

In order to collect the low voltage (up to 5kV) CL data, the coated Al stubs were placed into a chamber, which was evacuated to a pressure of approximately 10^{-6} torr. An EGPS-7H electron gun from Kimbal Physics Inc. (Walton, NH, Figure 2.10) was used as excitation source. For the luminance measurement, the E-beam was controlled by a pulse generator Thandar TG503, the E-beam size was set at 1.41 mm in diameter. A Photo Research Prichard PR800 photometer was used to measure luminance. In order to record the CL spectra, a 10 mm in diameter defocused beam was used. A Bentham monochromator detector system (Figure 2.11) was used to record CL spectra and calculate the CIE coordinates (The CIE 1931 standard for colorimetry).

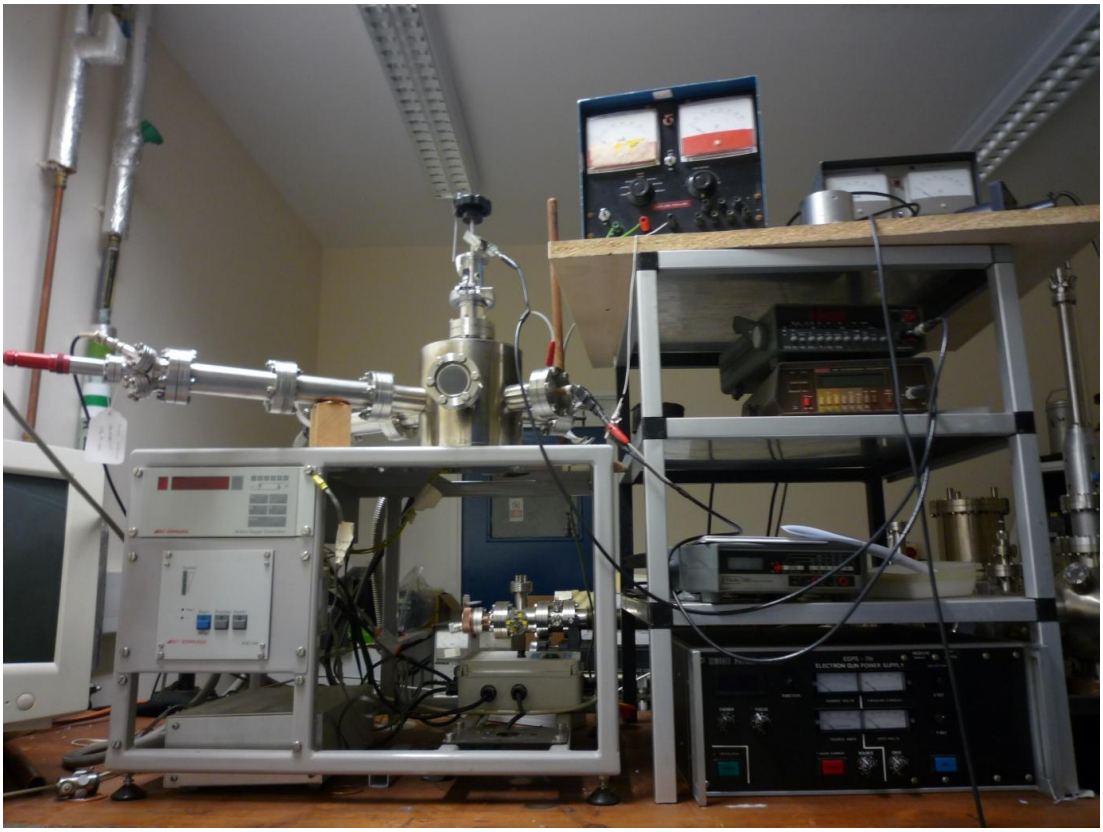

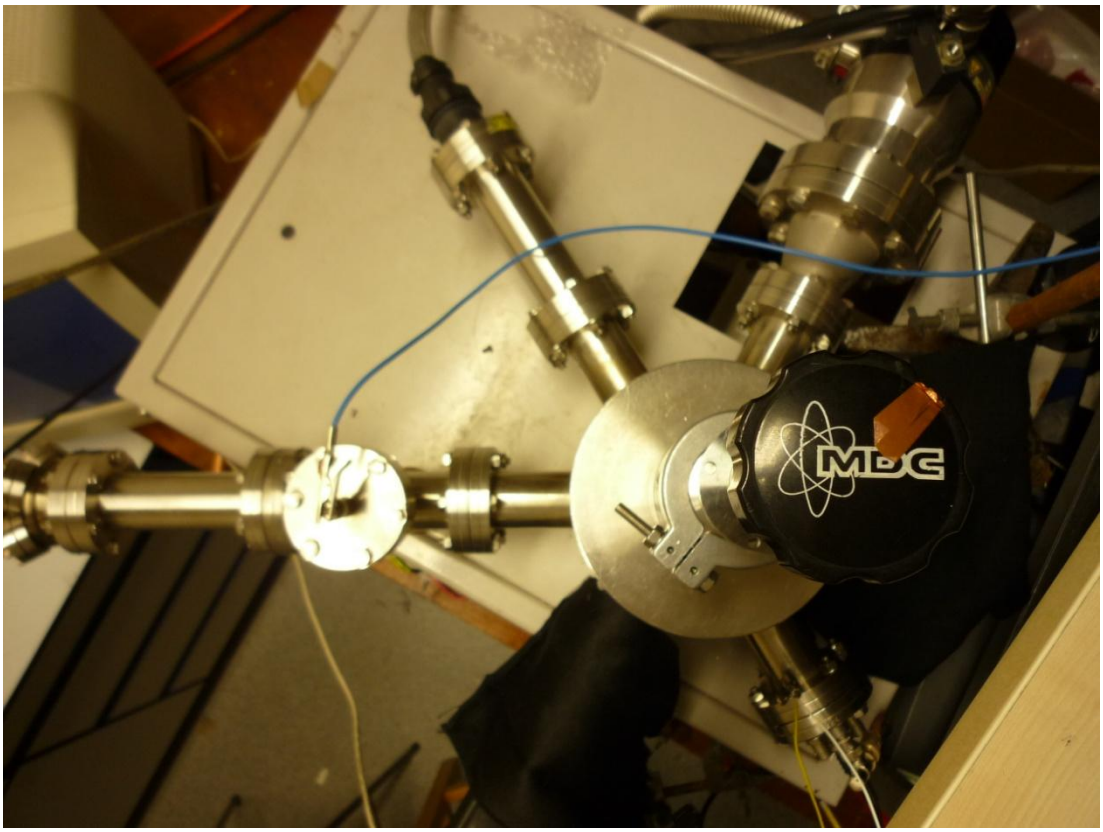

Figure 2.10 Kimbal Physics Inc. EGPS-7H electron gun (bottom).

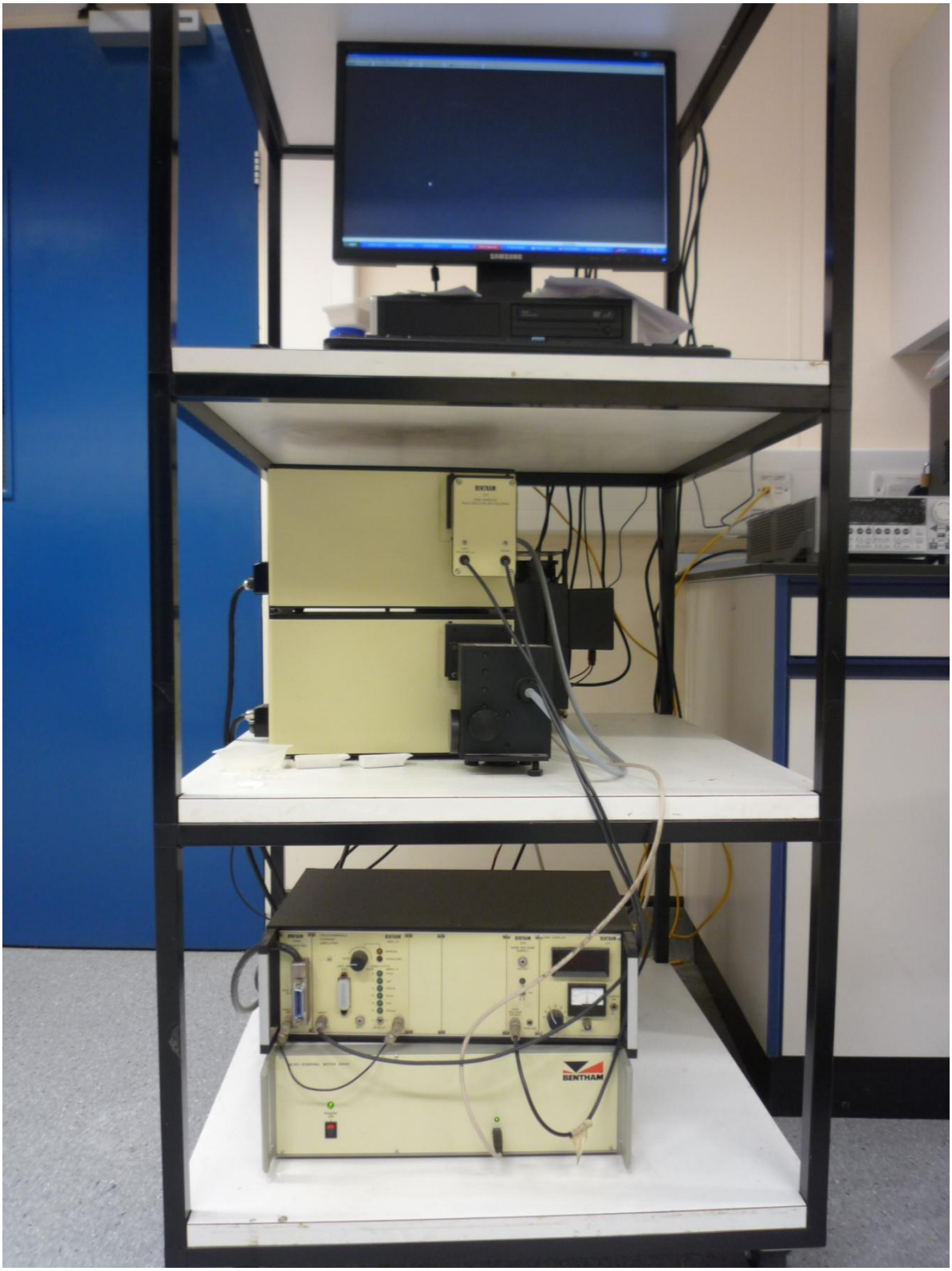

Figure 2.11 Bentham monochromator detector system.

Chapter 3 Luminescent properties of RE^{3+} doped Y_2O_2S phosphors

3.1 Introduction

In the last few decades the Y_2O_2S lattice has attracted increasing interest from both theoretical scientists and industrial researchers. Struck and Fonger estimated the band gap energy E_g to be 4.6 eV through the study of charge transfer states of certain rare earth activators in the oxysulfide system [251]. Mikami and Oshiyama calculated the electronic structure and intrinsic point defects of Y_2O_2S using first-principle methodologies [104, 252]. Itoh and Inabe proposed a much higher estimated band gap of 6.77 eV compared to previous measurements of 4.6-4.8 eV after measuring reflectivity spectra of single crystals of Y_2O_2S in the energy range of up to 30 eV using synchrotron radiation [253]. Li and Ahuja calculated the electronic structure, elastic constants and dielectric function of Y_2O_2S by means of an accurate first-principles method using the full potential linear muffin-tin orbital method [254]. The calculated band gap of 3.0 eV is consistent with that from Mikami and Oshiyama.

In general practice, europium doped Y_2O_2S has been widely used in cathode ray tubes (CRTs) since phosphorescence was discovered in europium doped materials [105, 255].

In this chapter, the luminescent properties of $Y_2O_2S:RE^{3+}$ (RE= Dy, Pr, Tb) nanometre sized phosphor particles are presented and discussed for the further understanding of the Y_2O_2S host matrix. X-ray powder diffraction (XRPD) and scanning electron microscopy (SEM) results are examined to discuss effects of various doping concentration on crystal structure and micro morphologies of the resulting phosphors. PL and CL spectra were recorded for luminescence study. Effects of various doping concentration on luminescent properties are discussed.

3.2 Crystal structures

The crystal structure of Y_2O_2S is trigonal and the space group determined by X-ray diffraction is P3m1 [69]. The lattice parameters are a = 0.37 nm and c =

0.65 nm, respectively. There is one molecule per unit cell, each yttrium atom is coordinated by four oxygen atoms and three sulfur atoms as its nearest neighbours (see Figure 3.1). The site symmetry of the Y^{3+} cations is C_{3v} (3m) [76]. When doped with rare-earth ions, the Y^{3+} sites are usually occupied with rare-earth ions [82, 256, 257], which probably results from the fact that the ionic radii of RE^{3+} cations are slightly greater than those of the Y^{3+} cations.

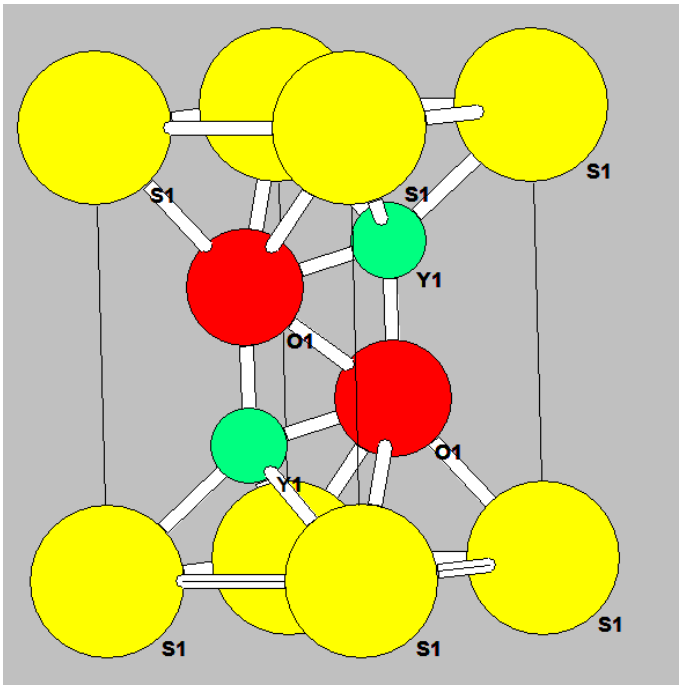

Figure 3.1 Schematic diagrams of the Y_2O_2S crystal unit cell.

X-ray powder diffraction (XRPD) was used to identify the crystal structure of the $Y_2O_2S:RE^{3+}$ phosphor powders. Diffraction data over 2θ range from 5 ˚ to 100 ˚ (5˚ to 70˚ for $Y_2O_2S:Dy^{3+}$) were recorded using an X-ray diffactometer. XRPD patterns of the $Y_2O_2S:RE^{3+}$ particles fired at 900˚C are shown in Figure 3.2. The XRPD patterns are identical to the hexagonal $Y_2O_2S:Eu^{3+}$ crystal phase previously reported in the literature [256], which indicates the Y^{3+} cations were substituted by RE^{3+} cations in $Y_2O_2S:RE^{3+}$ particles. It is also worth noting that occasionally extra peaks assigned to Y_2O_3 crystallites could be observed in the XRPD patterns, which are a natural result from the residual Y_2O_3 particles used in top layers while converting as-prepared precursor powders to oxysulfides.

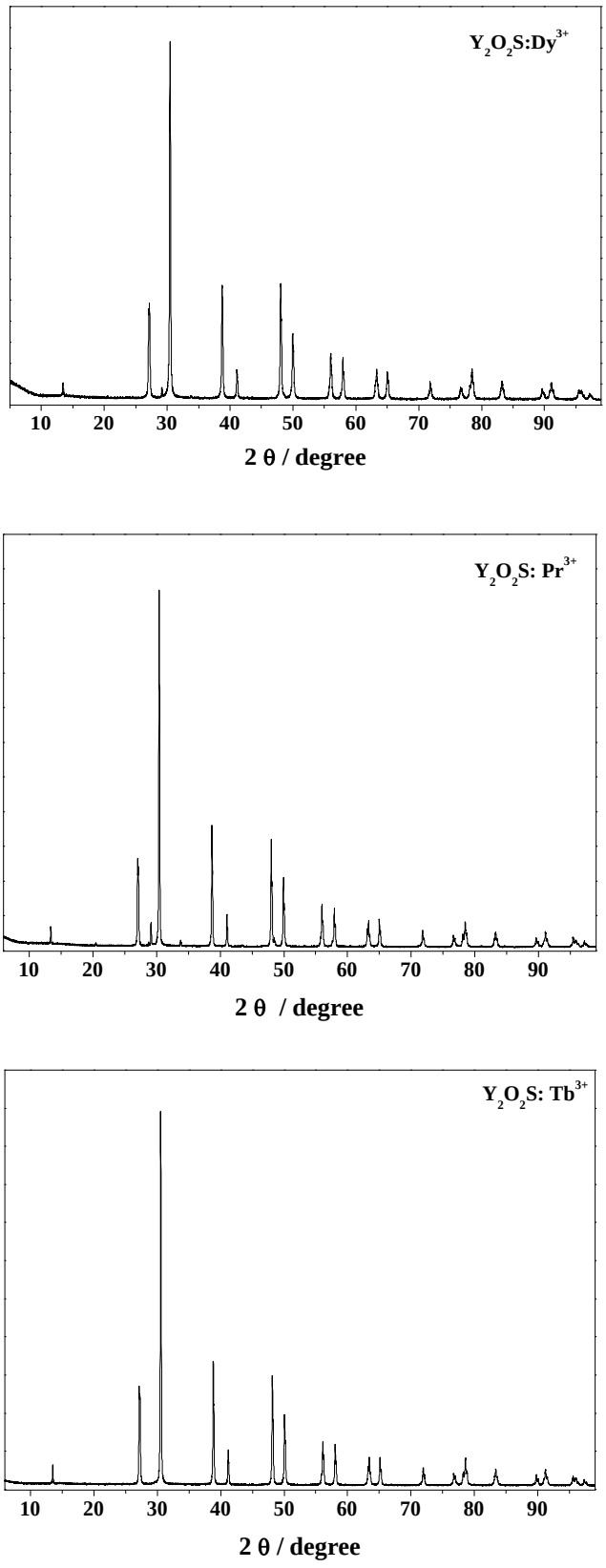

Figure 3.2 XRPD patterns for the $Y_2O_2S:RE^{3+}$ (RE=Dy, Pr, and Tb) particles fired at 900˚C.

The effective doping concentration for the RE^{3+} ions is up to 10%. Yet no peak shift in XRPD patterns could be observed, indicating that various doping concentration of RE^{3+} cations at this level has no detectable effect on the crystal structure of $Y_2O_2S:RE^{3+}$ nanocrystals. This phenomenon could be fairly reasonable considering the closely similar ionic radii of Y^{3+} cation and RE^{3+} cations (ionic radii of Y^{3+}, Dy^{3+}, Pr^{3+} and Tb^{3+} are 0.104 nm, 0.1052 nm, 0.113 nm, 0.1063 nm, respectively). Structural parameters were calculated from XRPD data using the TOPAS analysis system and the estimated results are listed in Table 3.1.

Table 3.1 Structural parameters of $Y_2O_2S:RE^{3+}$ calculated from XRPD data.

RE^{3+}	*a* (Å)	*c* (Å)	crystal size (nm)
Dy^{3+}	3.7859	6.5892	117.8
Pr^{3+}	3.7867	6.5910	145.1
Tb^{3+}	3.7856	6.5880	128.2
Y_2O_2S [104]	3.750	6.525	—

3.3 Morphological Characterizations

The morphologies of the $Y_2O_2S:RE^{3+}$ nanocrystals were examined using a field emission scanning electron microscope (FE-SEM). The morphologies of the $Y_2O_2S:Dy^{3+}$ nanocrystals fired at 900˚C are demonstrated by SEM images as shown in Figure 3.3. It can be observed in Figure 3.3 (a) that most of the $Y_2O_2S:Dy^{3+}$ phosphor powders are of roughly spherical shapes and some particles are agglomerated into larger size particles. Some well-separated $Y_2O_2S:Dy^{3+}$ particles are shown in Figure 3.3 (b), suggesting that the crystallites of most particles are around 100 nm, which is consistent with the estimated structural parameters from the XRPD results.

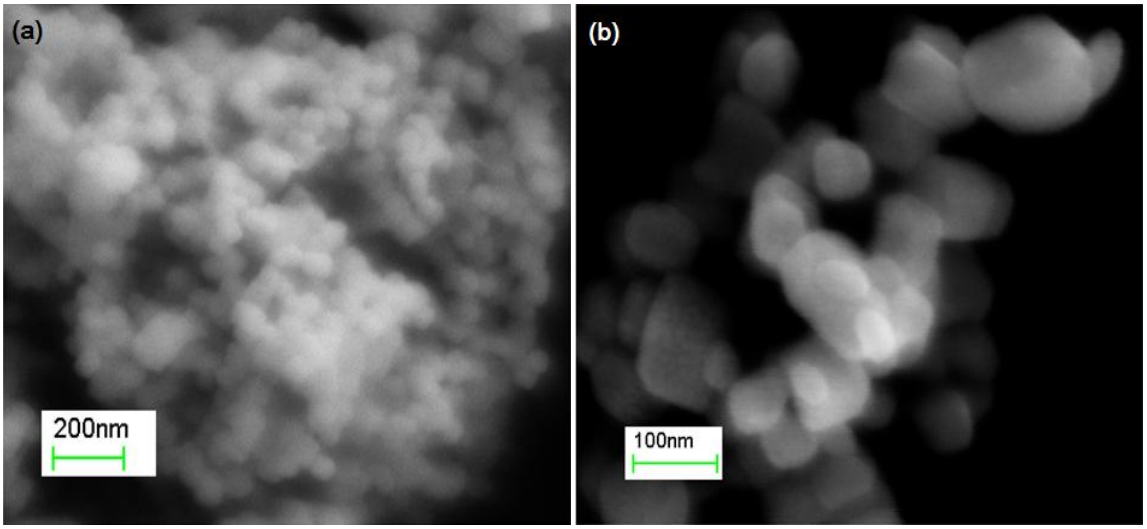

Figure 3.3 SEM images of $Y_2O_2S:Dy^{3+}$ particles fired at 900˚C.

Crystallite sizes of most $Y_2O_2S:Pr^{3+}$ particles are between 100 nm and 150 nm as can be seen in Figure 3.4 (b) although some agglomeration can be observed in some regions in Figure 3.4 (a). Clear differences from those of the $Y_2O_2S:Dy^{3+}$ particles are apparent, the shapes of $Y_2O_2S:Pr^{3+}$ crystallites are more irregular. Crystallites of plates, column and quasi-spherical shapes can be observed, which must result from the combustion process for converting precursor powders to oxysulfide phosphors and partial aggregation of Na_2CO_3 in the blend mixture [258, 259].

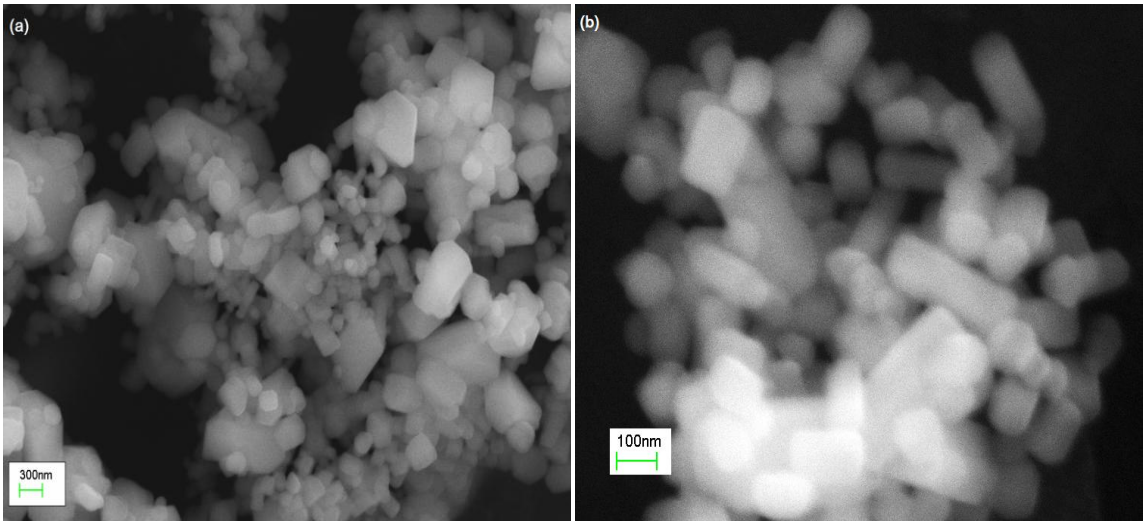

Figure 3.4 SEM images of $Y_2O_2S:Pr^{3+}$ particles fired at 900˚C.

From the SEM images presented in Figure 3.5(a) of the $Y_2O_2S:Tb^{3+}$ phosphor particles, it can be seen that they exhibit smooth and well-formed crystalline forms although there is obviously some agglomeration. Most of the particles have sphere-like shapes except for some pillar-like particles. Crystallite sizes of $Y_2O_2S:Tb^{3+}$ phosphor powders are in line with those of $Y_2O_2S:Dy^{3+}$ and $Y_2O_2S:Pr^{3+}$ phosphors obtained using the same preparation method. Most of them are around 100 nm.

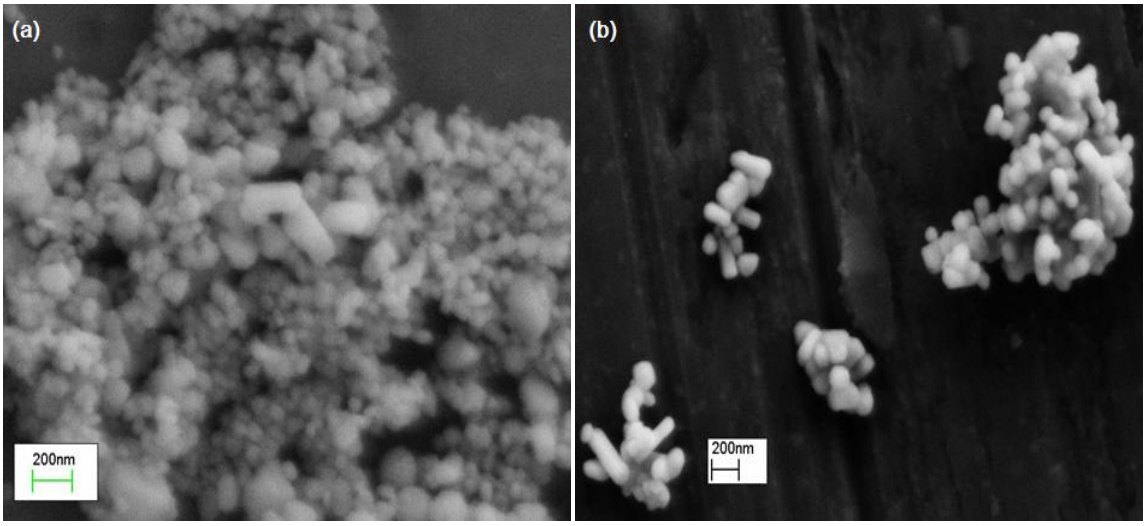

Figure 3.5 SEM images of $Y_2O_2S:Tb^{3+}$ particles fired at 900˚C.

3.4 Photoluminescence properties of $Y_2O_2S:RE^{3+}$

PL emission spectra were collected over the range from 400 nm to 800 nm for 1 mol% RE^{3+} (RE= Dy, Pr) doped Y_2O_2S and for $Y_2O_2S:Tb^{3+}$ in the range from 300 nm to 700 nm at room temperature and are presented in Figure 3.6. The assignments for the RE^{3+} transitions were made by comparisons with data from the literature for RE^{3+} ions [70]. Four emission bands from the $Y_2O_2S:Dy^{3+}$ particles can be observed in Figure 3.6 (a). The predominant yellow emission band centred at 577 nm originates from the transition of $^4F_{9/2} \rightarrow {}^6H_{13/2}$, the blue emission band centred at 486 nm could be assigned to transition of $^4F_{9/2} \rightarrow {}^6H_{15/2}$, and two weak emission bands at 669 nm and 754 nm to $^4F_{9/2} \rightarrow {}^6H_{11/2}$ and $^4F_{9/2} \rightarrow {}^6H_{5/2}$ transitions respectively. The blue to yellow intensity ratio (I_{486}/I_{577}) falls in the region of 0.44 - 0.51 for all samples, which is argued as a promising feature of $Y_2O_2S:Dy^{3+}$ to achieve soft white light emission when co-doped with other

appropriate RE^{3+}/transition metal ions for suitable control over the blue/yellow intensity ratio [260]. The CIE coordinates (the CIE 1931 standard for colorimetry) were calculated from the spectra to evaluate the colorimetric performance of $Y_2O_2S:Dy^{3+}$. Figure 3.7 displays the CIE chromaticity diagram of $Y_2O_2S:Dy^{3+}$ at various Dy^{3+} concentrations. The calculated CIE coordinates for $Y_2O_2S:Dy^{3+}$ phosphors shift over the range of x from 0.37 to 0.39 and y from 0.40 to 0.44, which lie on the boundary line of the CIE white domain.

The emission spectrum of $Y_2O_2S:Pr^{3+}$ consists of five main emission bands at 514 nm, 548 nm, 641 nm, 670 nm and 770 nm, as shown in Figure 3.6 (b). These could be attributed to transitions from $^3P_0$ to $^3H_4$, $^3H_5$, $^3H_6$, $^3F_2$ and $^3F_4$, respectively. Also, the strong emission band from $^3P_0 \rightarrow {}^3H_4$ transition is evidence that the Pr^{3+} cations occupy the Y^{3+} cations sites in $Y_2O_2S:Pr^{3+}$ phosphors. Because the transition between $^3P_0$ and $^3H_4$ is an electric dipole transition [69, 261], which is only allowed when the Pr^{3+} ion occupies a lattice site lacking a symmetrical centre, thus the Pr^{3+} cations are expected to occupy the Y^{3+} cation sites in the Y_2O_2S crystals so that the $^3P_0 \rightarrow {}^3H_4$ transition is allowed.

The CIE colour coordinate is also employed to analyze the luminescence colour of $Y_2O_2S:Pr^{3+}$ samples. Figure 3.8 displays the CIE chromatic coordinate diagram for $Y_2O_2S:Pr^{3+}$ phosphors. The colour of $Y_2O_2S:Pr^{3+}$ falls in the green region and the CIE coordinates shift over a range of x from 0.19 to 0.21, y from 0.62 to 0.65 when the Pr^{3+} concentration changes. The integrated intensity ratio of the green (514 nm) and the red (670 nm) emission bands varies for different Pr^{3+} doping concentrations. The results are presented in Table 3.2.

The PL emission spectrum of the $Y_2O_2S:Tb^{3+}$ particles excited at 254 nm is shown in Figure 3.6 (c). The emission bands are attributable to transitions of $^5D_3$ and $^5D_4$ excited energy levels to the ^7F_J (J=0-6) ground state levels. Emission bands at 384 nm, 418 nm, 437nm and 458 nm could be respectively assigned to the transitions of $^5D_3 \rightarrow {}^7F_6$, $^5D_3 \rightarrow {}^7F_5$, $^5D_3 \rightarrow {}^7F_4$ and $^5D_3 \rightarrow {}^7F_3$ while the emission bands at 490 nm, 545 nm, 587 nm and 623 nm correspond to $^5D_4 \rightarrow {}^7F_J$ (J=6, 5, 4, 3) transitions.

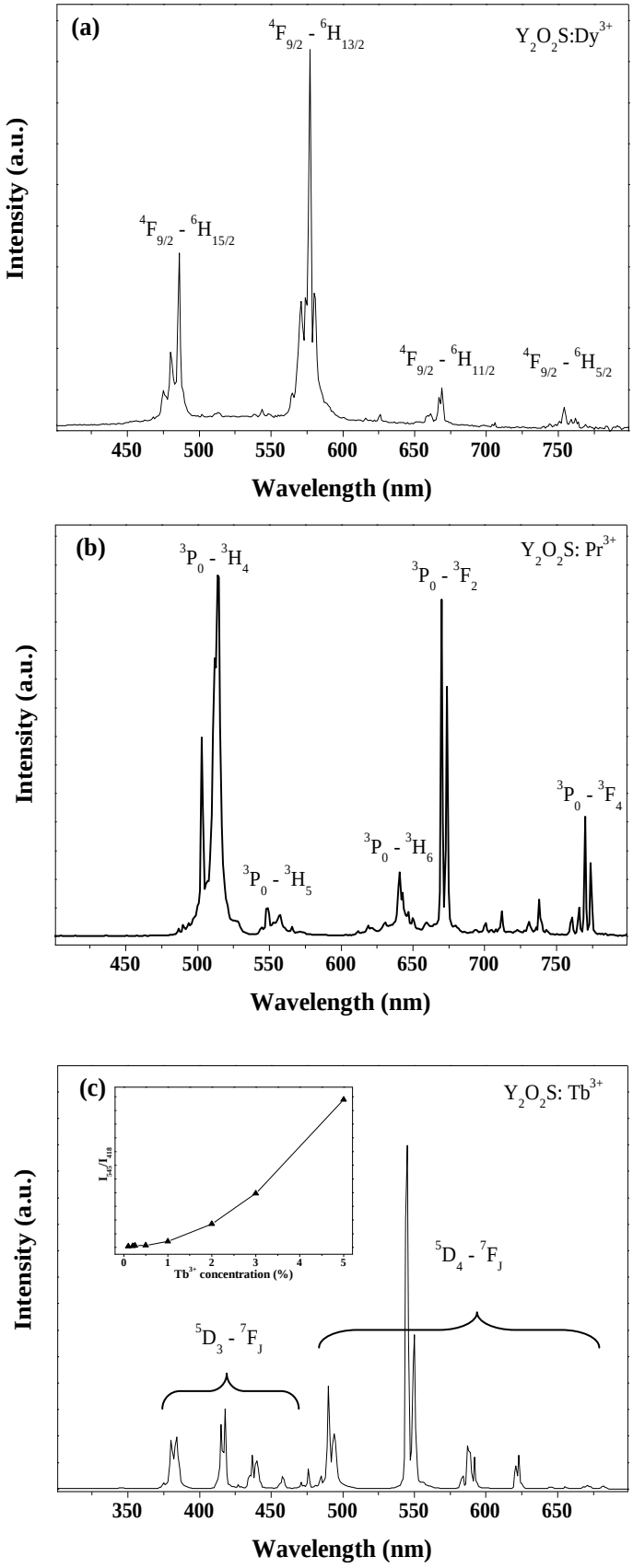

Figure 3.6 PL emission spectra (λ_{ex}=254 nm) of 1 mol% RE^{3+} (RE=Dy, Pr, Tb) doped Y_2O_2S phosphors.

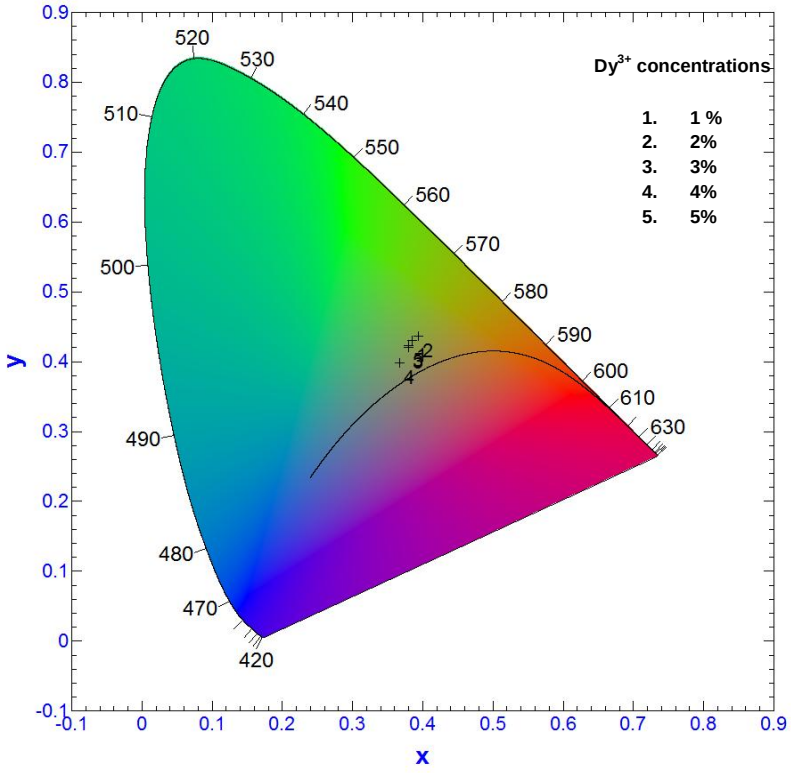

Figure 3.7 CIE chromaticity diagram of $Y_2O_2S:Dy^{3+}$ at various Dy^{3+} concentrations.

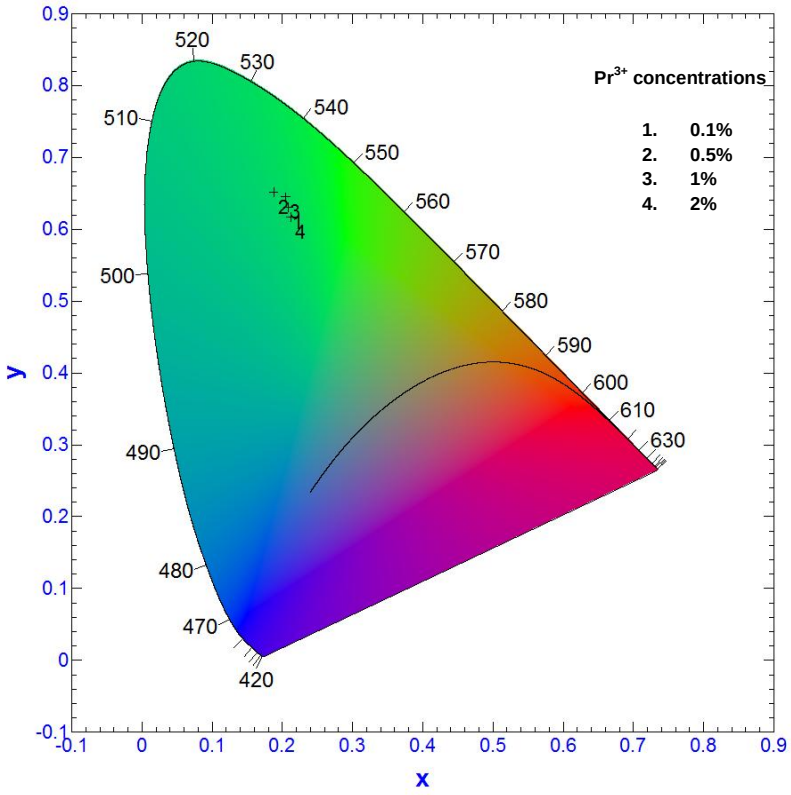

Figure 3.8 CIE chromaticity diagram of $Y_2O_2S:Pr^{3+}$ at various Pr^{3+} concentrations.

Table 3.2 Optical properties of $Y_2O_2S:Pr^{3+}$ phosphors.

Pr^{3+} concentration	CIE coordinate (x)	CIE coordinate (y)	Colour temperature (K)	I_{514}/I_{670}
0.1%	0.2178	0.2431	7632	1.672
0.5%	0.2469	0.3449	7915	1.620
1%	0.2829	0.4748	7632	1.070
2%	0.3064	0.5638	7624	1.162

Although for the 1 mol% Tb^{3+} activated Y_2O_2S phosphor the green emission band at 545 nm is the most intense one, the intensity ratio between the $^5D_4 \rightarrow {}^7F_J$ and $^5D_3 \rightarrow {}^7F_J$ transitions is dependent on the doping concentration of Tb^{3+} cations. This is due to the cross relaxation process happened between two adjacent Tb^{3+} cation pairs as illustrated in the following equation [68]: Tb^{3+} ($^5D_3$) + Tb^{3+} ($^7F_6$) → Tb^{3+} ($^5D_4$) → Tb^{3+} ($^7F_0$).The inset of Figure 3.6 (c) shows the intensity ratio of green/blue emission (I_{545}/I_{418}) as a function of Tb^{3+} concentration. The intensity ratio of green/blue emission grows exponentially with Tb^{3+} concentration, which is in good agreement with the previous report [89].

The cross relaxation effect due to the Tb^{3+} concentration on phosphor colour emission could be analysed in a CIE chromaticity diagram which shows the emission colour composition. The CIE chromaticity diagram for $Y_2O_2S:Tb^{3+}$ phosphor is presented in Figure 3.9 and the calculated CIE coordinates are listed in Table 3.2 together with other optical properties. The emission colour of $Y_2O_2S:Tb^{3+}$ shifts from blue to yellowish-green with increasing Tb^{3+} concentration, which means that the colour of $Y_2O_2S:Tb^{3+}$ is tuneable by simply controlling the doping concentration of Tb^{3+} cations.

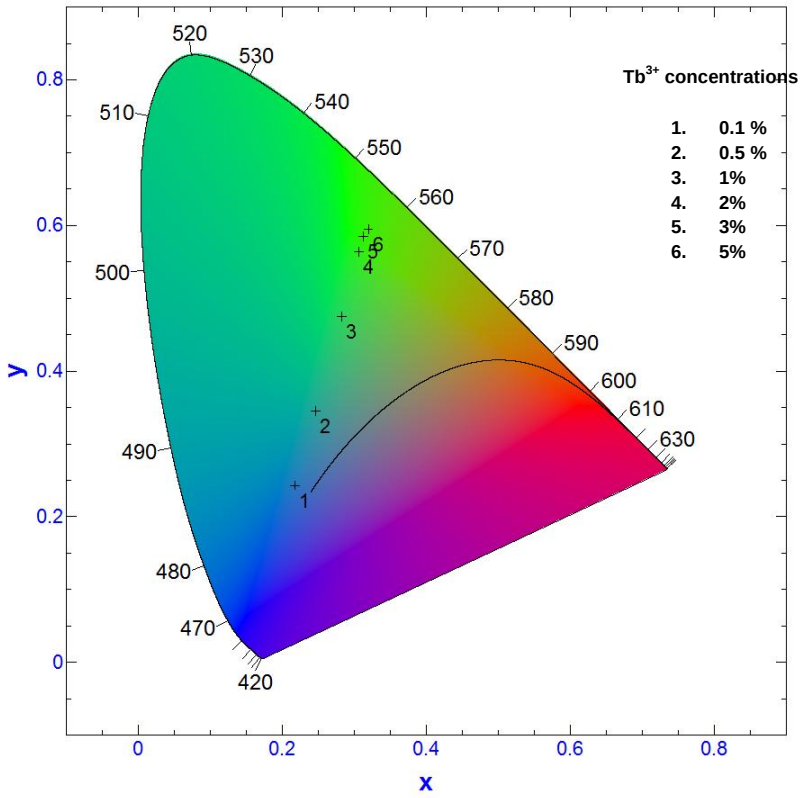

Figure 3.9 CIE chromaticity diagram of $Y_2O_2S:Tb^{3+}$ at various Tb^{3+} concentrations.

Table 3.3 CIE coordinates of $Y_2O_2S:Tb^{3+}$ phosphors.

Tb^{3+} concentration	CIE coordinate(x)	CIE coordinate(y)	Colour temperature /K
0.1%	0.2178	0.2431	Not defined
0.5%	0.2469	0.3449	10350
1%	0.2829	0.4748	6757
2%	0.3064	0.5638	6000
3%	0.3123	0.5849	5872
5%	0.3197	0.5945	5742

Moreover, the overlay of the PL emission spectra of $Y_2O_2S:Tb^{3+}$ is presented in Figure 3.10 and Figure 3.11 (the emission band to which the spectra were normalised is not shown in the figure) for further understanding of the Tb^{3+} concentration effect on emission intensity. At low Tb^{3+} concentration, the blue emissions of $^5D_3 \rightarrow {}^7F_J$ (J=6, 5, 4, 3) transitions are dominant. The emission intensity of the $^5D_3 \rightarrow {}^7F_J$ (J=6, 5, 4, 3) transitions decreases as the Tb^{3+} doping concentration is increased as shown Figure 3.10 while that of $^5D_4 \rightarrow {}^7F_J$ (J=6, 5, 4,

3) transitions grows with increasing Tb^{3+} doping concentration, which is clearly presented in Figure 3.11. This behaviour of Tb^{3+} ions is in good agreement with that observed in other host lattices [89, 94-96, 262].

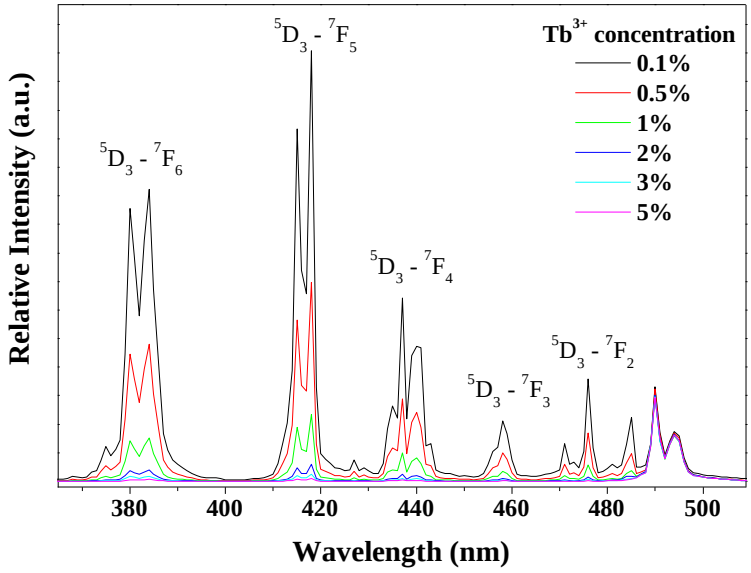

Figure 3.10 Overlay emission spectra of $Y_2O_2S:Tb^{3+}$ phosphors. All emission intensity values were normalised to that of the 545 nm emission peak.

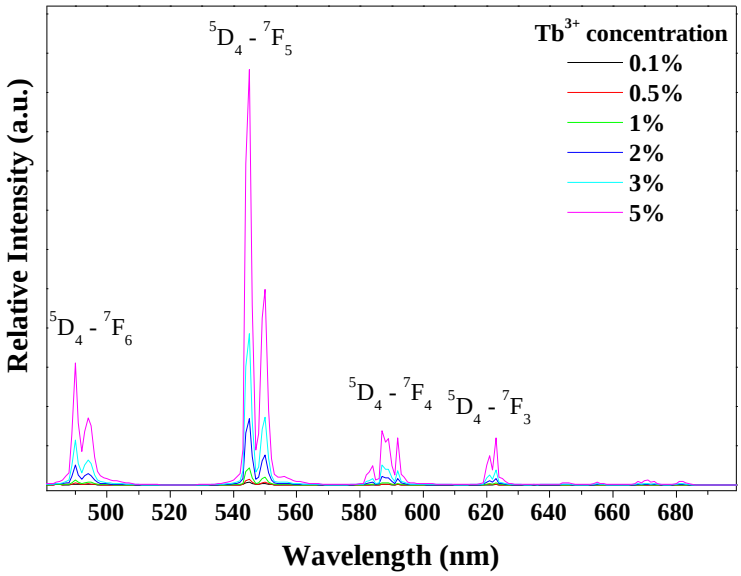

Figure 3.11 Overlay emission spectra of $Y_2O_2S:Tb^{3+}$ phosphors. All emission intensity values were normalised to that of the 418 nm emission peak.

3.5 Cathodoluminescence properties of $Y_2O_2S:RE^{3+}$

Cathodoluminescence (CL) properties were measured with an electron gun in a high vacuum chamber. The samples were excited by an electron beam with controlled accelerating voltage of 5 kV. CL spectra were collected over the range of 300-800 nm. Figure 3.12 displays CL spectra of 1 mol% RE^{3+} doped $Y_2O_2S:Tb^{3+}$. The emission bands in the CL spectra are slightly different from those in the PL spectra.

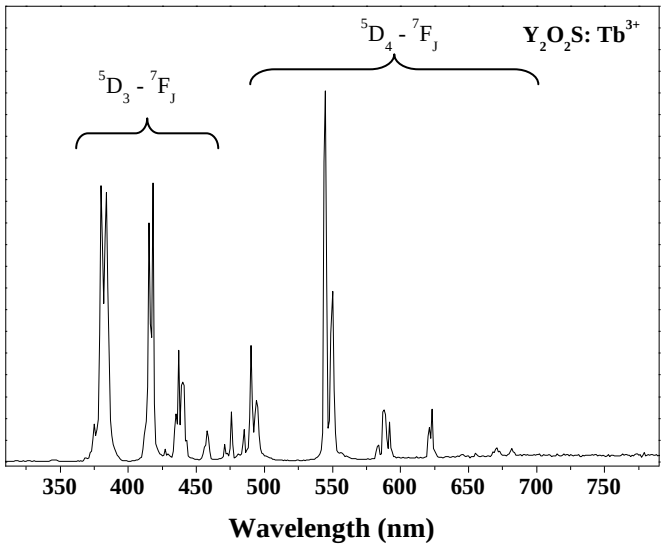

Figure 3.12 CL emission spectra of $Y_2O_2S:Tb^{3+}$ phosphors.

This difference could result from the two different excitation processes for PL and CL. For the PL of RE^{3+} activated Y_2O_2S, the RE^{3+} ions could be excited from ground energy level to higher excited energy level by directly absorbing photons of incident light. PL excitation spectra of $Y_2O_2S:RE^{3+}$ (RE= Dy, Pr, Tb) were collected by monitoring the most intense emission band and presented in Figure 3.13. Characteristic broad band emission corresponding to transitions of ground energy state to excited energy states could be observed. The weak, broad band maximum at 264 nm was due to the host excitation of Y_2O_2S [69]. While for CL excitation, these RE^{3+} luminescence centres are predominantly excited by recombination of pairs of electrons and holes that are generated inside the crystal by the incident electron beam [110]. It's also suggested that the sulphur ion in Y_2O_2S rather than the crystal structure is probably responsible for the indirect CL excitation of the luminescence centres in $Y_2O_2S:RE^{3+}$ (RE= Dy, Pr, Tb) phosphors.

Also, it's noticeable that the emission bands in CL spectra are more intense than their counterparts in PL spectra, which results from the higher quantum efficiency of the CL process.

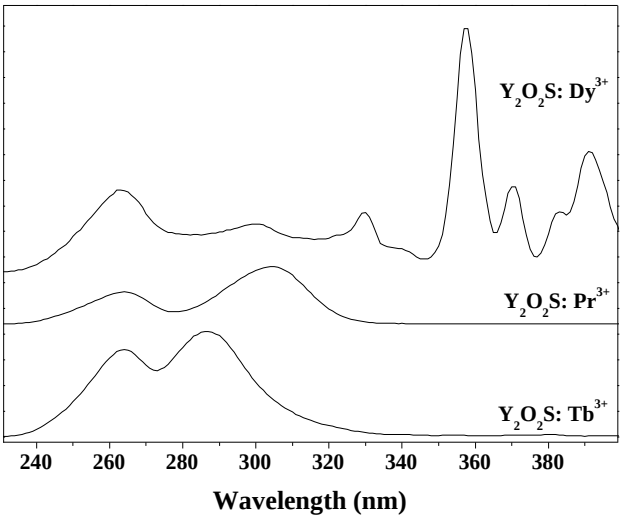

Figure 3.13 PL excitation spectra of $Y_2O_2S:RE^{3+}$ phosphors.

Figure 3.14 displays the overlay CL emission spectra of $Y_2O_2S:Tb^{3+}$ in the visible light region. The intensity of the emission bands from the $^5D_3 \rightarrow {}^7F_J$ transitions decreases with increasing Tb^{3+} concentration. This phenomenon is caused by the cross relaxation process. Inset Figure 3.14 displays the luminance of $Y_2O_2S:Tb^{3+}$ as a function of the Tb^{3+} concentration. The highest radiance was obtained at 545 nm blue emission from the 5 mol% Tb^{3+} doped $Y_2O_2S:Tb^{3+}$ which also possesses the highest luminance. This might result from the cross relaxation effects, making $Y_2O_2S:Tb^{3+}$ a promising candidate for green phosphors in field emission display devices.

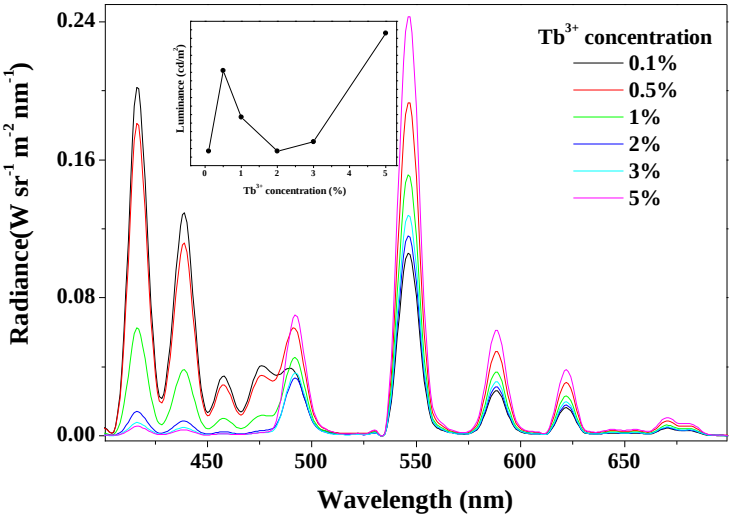

Figure 3.14 Overlay CL emission spectra of $Y_2O_2S:Tb^{3+}$ at various Tb^{3+} concentrations. Inset: CL luminance variation with Tb^{3+} concentration.

3.6 Conclusions

To sum up, the conclusions are demonstrated as follows:

1. Nanometre sized phosphor particles were obtained using the urea homogeneous precipitation method. The average crystal size varies from 117.8 nm to 145.1 nm depending on the different RE^{3+} cations. $Y_2O_2S:Dy^{3+}$ and $Y_2O_2S:Tb^{3+}$ particles have roughly spherical shape while $Y_2O_2S:Pr^{3+}$ ones are more irregular.
2. The dependence of the luminescence properties on the dopant concentrations was studied. The results indicate that the optimum doping concentration for $Y_2O_2S:Dy^{3+}$ and $Y_2O_2S:Pr^{3+}$ were 1 mol% and 0.1 mol%, respectively. The results also suggest that $Y_2O_2S:Dy^{3+}$ is a promising candidate for UV-based white light emission devices.
3. The cross relaxation effect was observed in both the PL and CL spectra of Y_2O_2S: Tb^{3+} phosphors, indicating that the emission colour of $Y_2O_2S:Tb^{3+}$ could be tuneable by simply varying Tb^{3+} doping concentration.
4. The cross relaxation effect might be responsible for the highest luminance of $Y_2O_2S:Tb^{3+}$ at 5 mol%.

Chapter 4 Luminescence of $Gd_2O_2S:RE^{3+}$ phosphors

4.1 Introduction

Field emission displays (FEDs) are a display technology that reproduces images using large area field electron emission arrays of electron sources to excite the phosphor pixel on the screen. FEDs have many advantages over other display systems, including high contrast ratios with true black reproduction, fast response time, less power consumption, wide viewing angle and lifelike colour. The last few decades have witnessed a fast development on FEDs, which was specifically stimulated by the progressive researches on using carbon nanotubes (CNTs) as highly efficient field emitters [263-266].

Developments on FEDs generated a growing demand for fine phosphor powders that could be used to achieve improved resolution and efficiency. This has created interest in developing phosphors that operate at low voltages (500 to 5000V) for FEDs that require phosphor particles which are sub-micrometer, mono-sized and have a regular morphology. Such small phosphor particles would be expected to self-organise and close-pack to form thin, dense layers on the screen, giving improved resolution and brightness over much larger conventional commercial phosphors [267]. In addition they could be easily incorporated into ink formulations for printing directly on to the anode substrate. Previous studies in these laboratories on spherical cubic $Y_2O_3:Eu^{3+}$ phosphors have suggested that a comparable CL luminescence to a commercial standard sample could be reached from the sub-micrometer particles [84]. Small particles (100nm) display 60% of the luminance of a commercial standard phosphor (3 μm). A green emitting Y_2O_2S: Tb^{3+} phosphor of submicrometer size was also reported, which had a luminous efficiency of 34.6 lm/W at an electron beam accelerating voltage of 5000V [17].

The same demands for phosphor particles of sub-micrometre size and regular morphology are made for high quality low energy X-ray medical imaging systems. Kalivas pointed out that the inherent physical properties of phosphor

materials have a significant effect on the image detector transfer characteristics [31]. In both types of radiographic photodetector systems, traditional screen film or digital (where phosphors are coupled with CCD arrays), total image noise has a detrimental effect on the quality of the resulting image. The total image noise is composed of screen noise from the phosphor which is the main component and to a lesser degree by photodetector noise. Screen noise has contributions from both quantum and structure noise. Quantum noise has been shown to be a consequence of the statistical nature of the spatial fluctuations of the x-ray quanta that have been absorbed and it dominates in a low exposure environment. Significant structure noise is a consequence of an inhomogeneous phosphor coating creating fluctuations of the absorbed x-ray quanta in high exposure conditions. The thickness and uniformity of the phosphor screen has been found to be critical for a low level of structure noise in high exposure conditions. A thicker phosphor layer and a high degree of close packing of the phosphor particles can reduce structure noise. Thus the phosphor particle morphology and size will influence the effective filling fraction, particles that are similar in size and morphology will result in a high effective filling fraction. There is also a reduction in structure noise with a decrease in particle size, due to a higher degree of particle packing and lower scattering of radiation [268]. The spatial resolution achievable with a phosphor-based detector is also directly related to the phosphor grain size, and so the smaller grain sizes of the custom produced phosphors will be superior to commercial phosphors in this respect [31, 268].

In this chapter, results are presented from studies on Pr^{3+} and Tb^{3+} activated Gd_2O_2S X-ray phosphors. CL luminescent properties of $Gd_2O_2S:Pr^{3+}$ phosphors were compared with those of commercial phosphor particles which are much larger and have a wider size distribution. The effect of doping concentration and firing temperature on the emission properties of the resulting phosphors were studied and reported in this chapter. Green and red emission lines were observed in the $Gd_2O_2S:Pr^{3+}$ CL spectra and their intensity ratio were shown to be dependent on both Pr^{3+} activator concentration and firing temperature. This work was published at the 16th International Displays Workshop (IDW ’09) and presented as a poster.

$Gd_2O_2S:Tb^{3+}$ phosphor has a green emission line at 545 nm, which is convenient for coupling to silicon photodiodes in X-ray scintillators. In this chapter the PL spectra and CL data from $Gd_2O_2S:Tb^{3+}$ phosphor particles at low accelerating voltage (1000V to 5000V) are also reported. Blue and green emission lines were observed in the CL spectra of $Gd_2O_2S:Tb^{3+}$ and their intensity ratio are shown to be dependent on both Tb^{3+} activator concentration and firing temperature.

4.2 Crystal structures and morphological analysis

X-ray powder diffraction (XRPD) is used to determine the crystal phase of the resulting phosphors. Figure 4.1 displays the XRPD patterns of 0.5 mol% RE^{3+} activated Gd_2O_2S samples fired at 900˚C and 1100˚C respectively, both showed good agreement with the hexagonal phase of the Gd_2O_2S structure (previously reported in literature [27]). Crystal size and lattice parameters were calculated using TOPAS software and the results are presented in Table 4.1, which shows a slight growth in crystallite size when the phosphor particles were re-fired at 1100˚C.

It's well known that the properties of X-ray medical imaging systems have a strong dependence on the particle size and morphology of the X-ray phosphors [36]. SEM images of $Gd_2O_2S:RE^{3+}$ fired at different temperatures are shown in Figure 4.2 to Figure 4.5. All the samples exhibit discrete particles of roughly spherical shape with smooth surface. Most of the particles are smaller than 150 nm, which is more than 20 times smaller in diameter than the commercially available materials, although larger particles or agglomeration could be observed as well. The particles fired at 1100˚C show no significant growth in size compared with their counterparts fired at 900˚C.

It also can be seen from the SEM images that samples re-fired at 1100˚C start melting into each other while the 900˚C samples are well separated. The particle size observed from the SEM images is highly consistent from the calculated data from XRPD pattern, indicating our phosphor particles are nearly single crystals.

Table 4.1 Crystal size and lattice parameters of $Gd_2O_2S:RE^{3+}$ phosphor particles.

	crystal size (nm)	*a* (Å)	*c* (Å)
$Gd_2O_2S: Pr^{3+}$ (900˚C)	119.8 (23)	3.8556(9)	6.6692(4)
$Gd_2O_2S: Pr^{3+}$ (1100˚C)	123.3(14)	3.8569(0)	6.6731(3)
$Gd_2O_2S: Tb^{3+}$ (900˚C)	157.0(11)	3.8539(0)	6.6668(9)
$Gd_2O_2S: Tb^{3+}$ (1100˚C)	118.48(87)	3.8542(6)	6.6677(1)
Bulk Gd_2O_2S [269]	—	3.8514(5)	6.667(2)

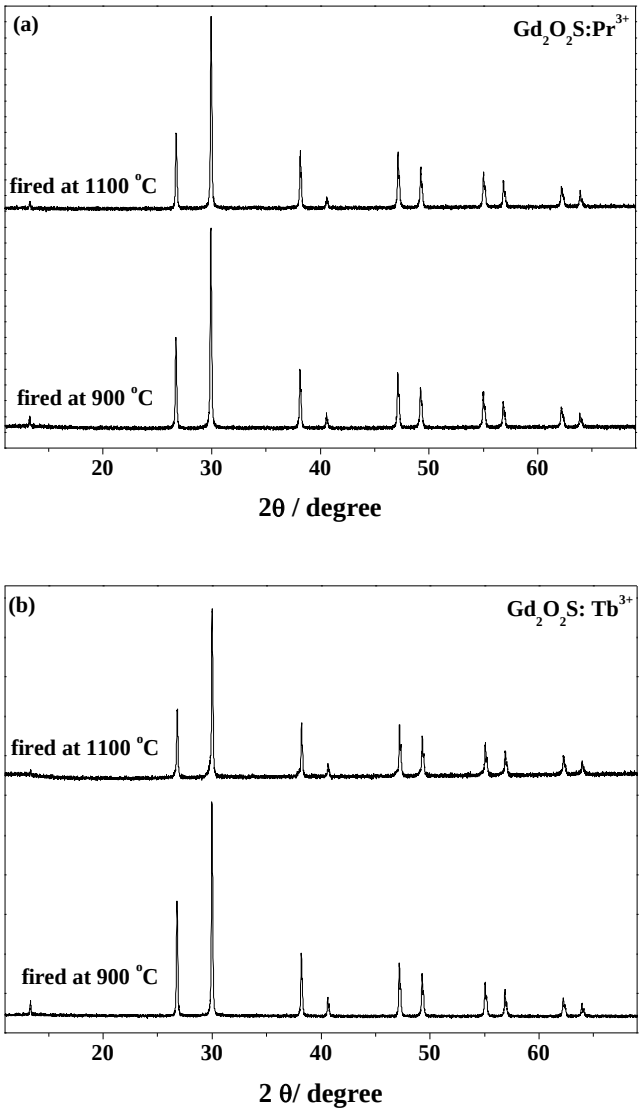

Figure 4.1 XRPD patterns of $Gd_2O_2S:RE^{3+}$ samples fired at 900˚C and 1100˚C.

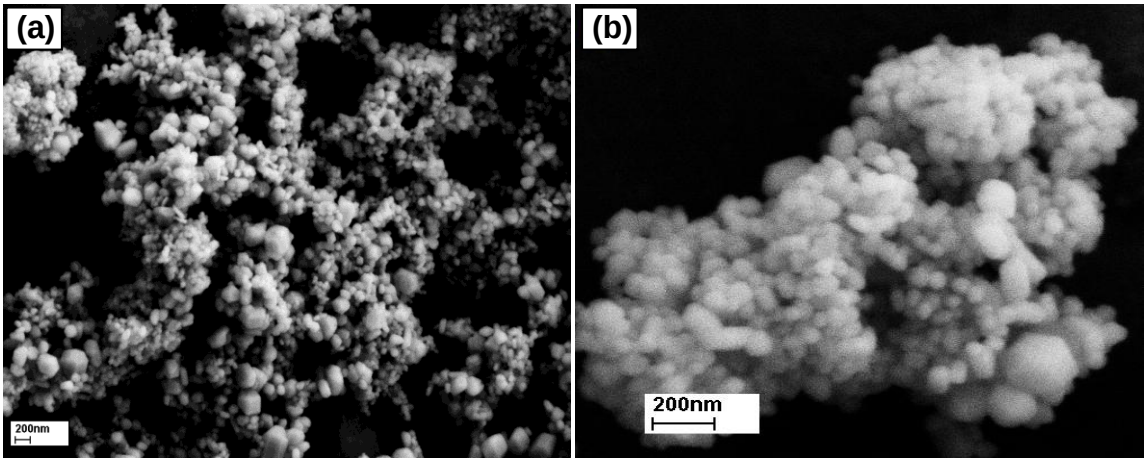

Figure 4.2 SEM images of $Gd_2O_2S:Pr^{3+}$ fired at 900˚C.

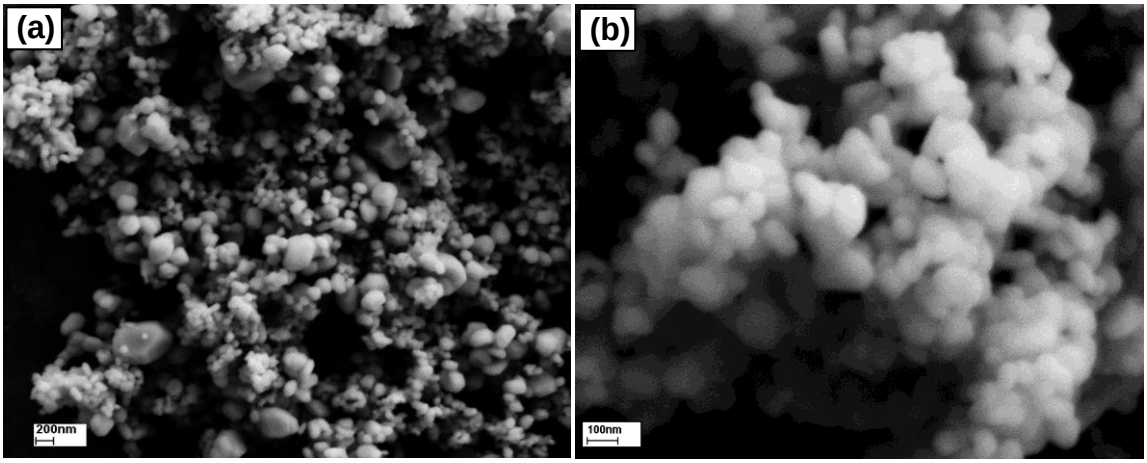

Figure 4.3 SEM images of $Gd_2O_2S:Pr^{3+}$ fired at 1100˚C.

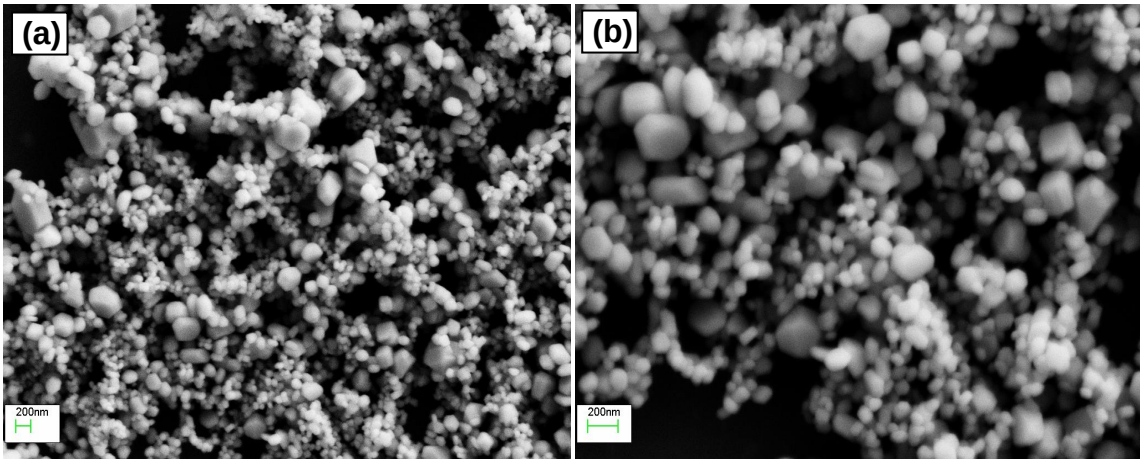

Figure 4.4 SEM images of $Gd_2O_2S:Tb^{3+}$ fired at 900˚C.

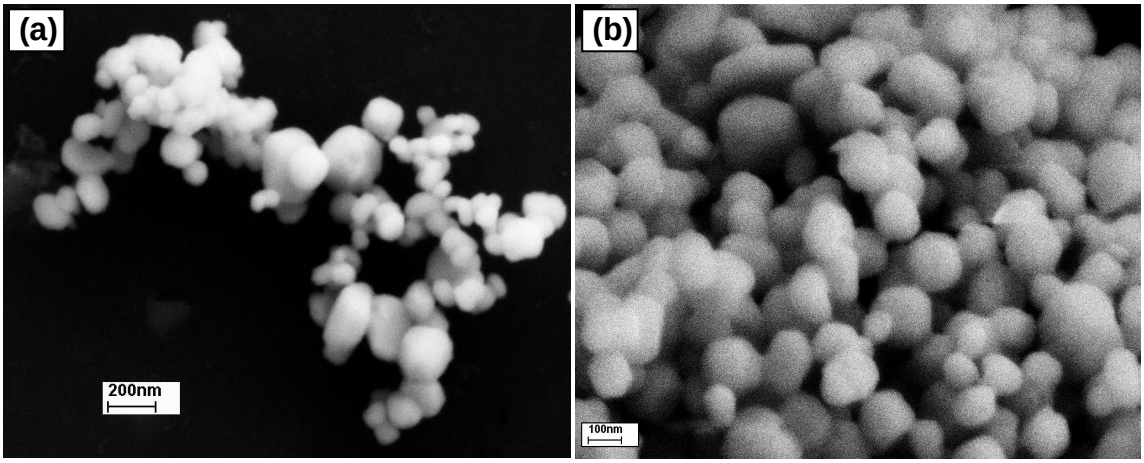

Figure 4.5 SEM images of $Gd_2O_2S:Tb^{3+}$ fired at 1100˚C.

4.3 PL measurement of $Gd_2O_2S:RE^{3+}$ phosphors

Figure 4.6 (a) displays the PL spectra of 0.1 mol% Pr activated $Gd_2O_2S:Pr^{3+}$ phosphors fired at 900˚C and 1100˚C under the excitation of 254 nm. The assignments for the RE^{3+} transitions were made by comparisons with data from the literature for RE^{3+} ions [71]. The emission bands could be assigned to transitions from $^3P_0$ to $^3H_4$, $^3H_5$, $^3H_6$, $^3F_2$ and $^3F_4$, respectively. The intensities of the emission bands from samples fired at 1100˚C are about twice as high as those of the emission bands from samples fired at 900˚C, which indicates the firing temperature has a dramatic influence on the luminescence intensity of the resulting phosphors. Similar phenomenon could also be observed from the PL spectra of 0.1 mol% Tb activated $Gd_2O_2S:Tb^{3+}$ phosphors (see Figure 4.6b). The higher firing temperature should largely reduce the surface defects of the phosphor crystals, which have often been blamed for the decreasing luminescence efficiency with decreasing particle size in conventional phosphors [270]. Thus energy resonance transformation of luminescence centres is limited within the single nanocrystals (due to their size and small number of activation sites per crystal), which could enhance the luminescence intensity.

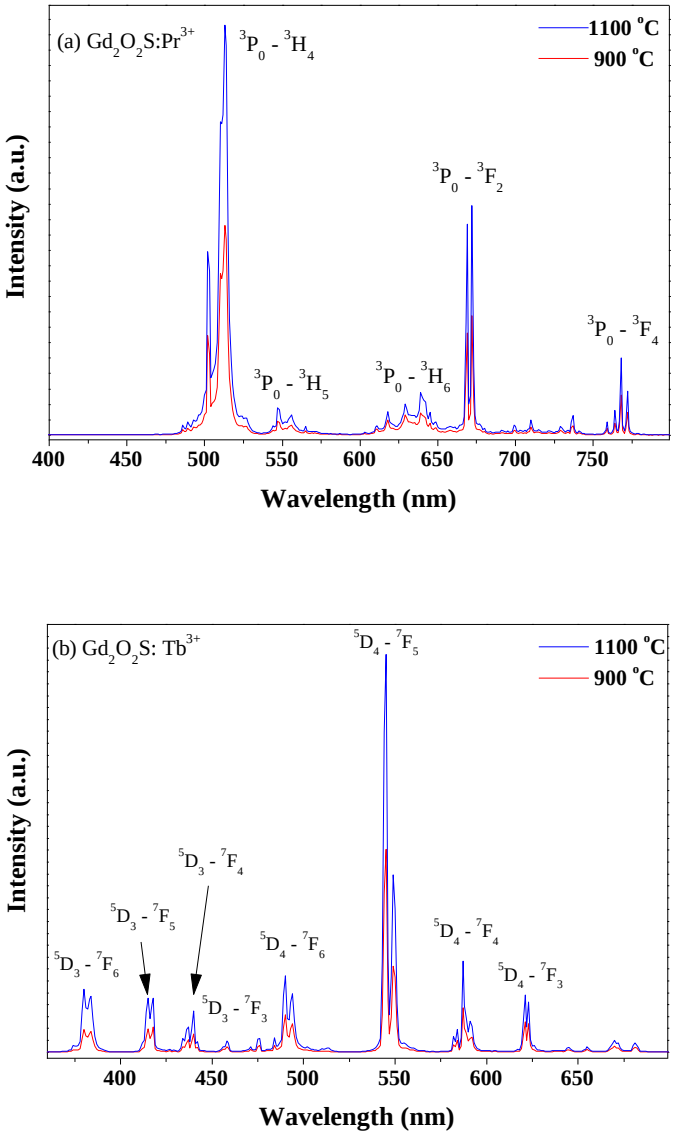

Figure 4.6 PL spectra of 0.1 mol% RE^{3+} activated $Gd_2O_2S:RE^{3+}$ fired at 900˚C and 1100˚C.

As described in chapter 3, at lower Tb^{3+} concentration, blue emissions from $^5D_3 \rightarrow {}^7F_J$ (J=6, 5, 4, 3) transitions are dominant in the PL spectra of $Y_2O_2S:Tb^{3+}$ phosphors. The blue emissions decrease with increasing Tb^{3+} concentration whereas the green emissions attributed to the $^5D_4 \rightarrow {}^7F_J$ transitions increase simultaneously. This is due to the cross relaxation process that takes place between two adjacent Tb^{3+} cation pairs as illustrated in the following equation [68]:

$$Tb^{3+}(^5D_3) + Tb^{3+}(^7F_6) \rightarrow Tb^{3+}(^5D_4) + Tb^{3+}(^7F_0).$$

However, the spectra of the $Gd_2O_2S:Tb^{3+}$ phosphors show different properties. As shown in Figure 4.6 (b), the green emission band at 545 nm assigned to $^5D_4 \rightarrow {}^7F_5$ is still of the highest intensity even when the Tb^{3+} concentration is as low as 0.1 mol%, this behaviour is different to that found in the spectrum of $Y_2O_2S:Tb^{3+}$. This is related to the different position of the charge transfer states (CTS) of the host crystals [44] and could be explained with the aid of Fonger and Struck's configurational coordinate model, which was proposed to explain that there was no emission from the $^5D_2 \rightarrow {}^7F$ transition in $La_2O_2S:Eu^{3+}$ at room temperature due to the thermally excited quenching transitions from the characteristic $^5D_2$ states of Eu^{3+} to the CTS of a host crystal [271].

Ratinen *et al* [25] has reported that the bottom of the CTS in Gd_2O_2S lies close to the $^5D_3$ excited state of Tb^{3+} while the CTS in Y_2O_2S is higher. Therefore most of the electrons on the $^5D_3$ excited state of Tb^{3+} in Gd_2O_2S are activated to the CTS and eventually fed to $^5D_4$ state at room temperature, thus greatly reducing the intensities of the emission bands from $^5D_3 \rightarrow {}^7F_J$ transitions. This energy transfer could hardly complete in Y_2O_2S because the CTS in Y_2O_2S lies in a higher position than in Gd_2O_2S. Therefore the blue emissions from $^5D_3 \rightarrow {}^7F_J$ transitions are predominant at lower Tb^{3+} concentration in $Y_2O_2S:Tb^{3+}$ phosphors.

The intensity of the blue emissions in $Gd_2O_2S:Tb^{3+}$ manifests the same trend as that in $Y_2O_2S:Tb^{3+}$ as the Tb^{3+} concentration increases. Figure 4.7 and Figure 4.8 displays normalised overlay spectra of $Gd_2O_2S:Tb^{3+}$ phosphors fired at 1100 ˚C with various Tb^{3+} concentration. The intensity of blue emissions decreases with increasing Tb^{3+} concentration while the intensity of green emissions increases due to cross relaxation between Tb^{3+} pairs. This observation is consistent with previous report in the literature [97].

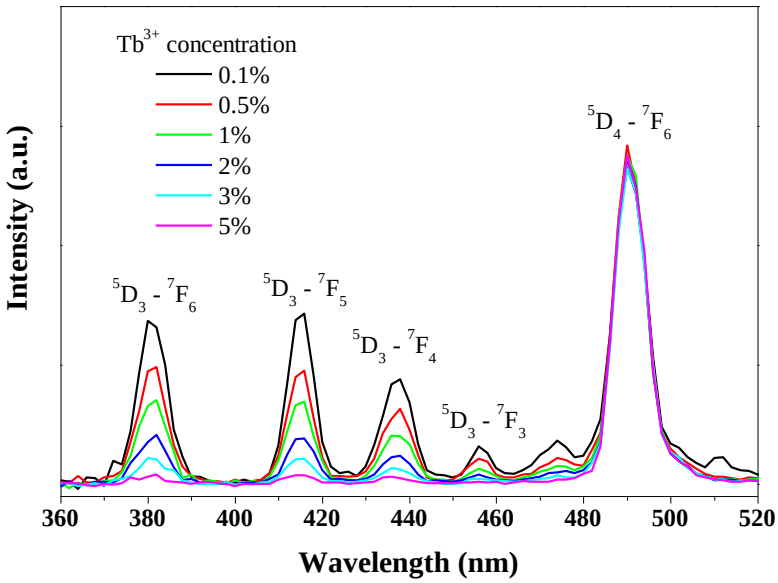

Figure 4.7 Overlay spectra of $Gd_2O_2S:Tb^{3+}$ phosphors (normalised to 545 nm).

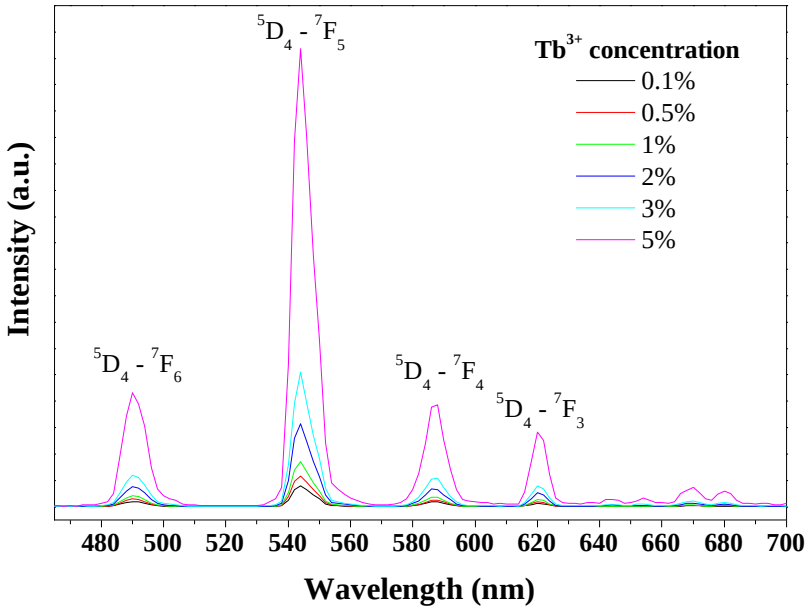

Figure 4.8 Overlay spectra of $Gd_2O_2S:Tb^{3+}$ phosphors (normalised to 380 nm).

The CIE colour coordinate is employed to analyze the luminescence colour of $Gd_2O_2S:Tb^{3+}$ samples. Figure 4.9 displays the CIE chromatic coordinate diagram for $Gd_2O_2S:Tb^{3+}$ phosphor samples re-fired at 1100˚C. The CIE coordinates and colour temperatures for all $Gd_2O_2S:Tb^{3+}$ samples are presented in Table 4.2. The results indicate that the optical properties of the $Gd_2O_2S:Tb^{3+}$ phosphors are strongly influenced by the firing temperature and the activator

concentration. The CIE coordinate values grow linearly with Tb^{3+} concentration as a consequence of the blue to green shift in the emission spectra due to cross-relaxation. The samples re-fired at 1100˚C have larger CIE coordinates and colour temperatures compared to the ones fired at 900˚C.

The increase in both x and y indicates the samples re-fired at 1100˚C emit 'greener' light under the UV excitation, suggesting the $^5D_3 \rightarrow {}^5D_4$ relaxation is more efficient due to the perfection of the crystal structure since non-radiative relaxation causing energy loss is often linked with defects in crystals.

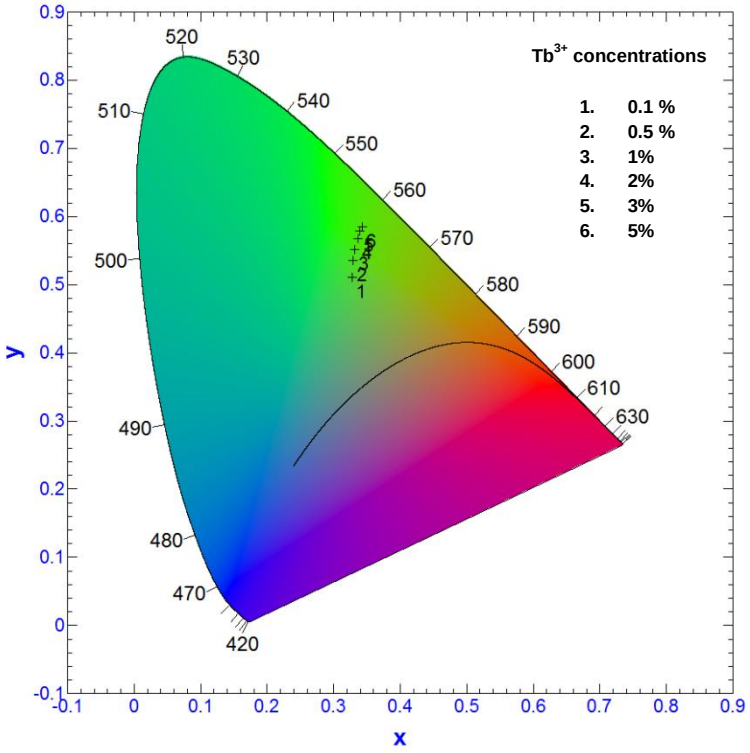

Figure 4.9 CIE chromatic diagram for $Gd_2O_2S:Tb^{3+}$ phosphor samples fired at 1100˚C.

Table 4.2 Optical properties of $Gd_2O_2S:Tb^{3+}$ phosphor samples.

Tb concentration	CIE x	CIE y	Colour temperature /K	Fired temperature /˚C
0.1 mol%	0.3279	0.5112	5620	1100
0.5 mol%	0.3285	0.5360	5604	1100
1 mol%	0.3316	0.5512	5546	1100
2 mol%	0.3367	0.5673	5438	1100
3 mol%	0.3388	0.5786	5426	1100
5 mol%	0.3426	0.5846	5367	1100
0.1 mol%	0.3199	0.4945	5802	900
0.5 mol%	0.3271	0.5197	5635	900

4.4 CL measurement of $Gd_2O_2S:RE^{3+}$ phosphors

The CL spectra of all $Gd_2O_2S:Pr^{3+}$ phosphor samples were similar to the CL spectrum of the Pr^{3+} 0.5 mol% concentration sample that had been fired at 900 ˚C (see Figure 4.10). The green/red ratio of the 513 nm and 672 nm peak intensities were listed in table 4.3. The ratio varies for different Pr activator concentrations annealed at 900˚C, whereas the CL spectra of the two samples re-fired at 1100˚C have identical peak ratios.

The CIE coordinates, dominant wavelengths and colour temperatures for all $Gd_2O_2S:Pr^{3+}$ phosphor samples are presented in Table 4.3. It can be seen that the differences in the CIE coordinates, dominant wavelengths and colour temperatures of the samples annealed at 900°C for the 1 to 5 mol% Pr concentrations are a consequence of the larger 513/668 nm peak intensity ratios when compared to the smaller peak intensity ratios of the 10 mol% Pr concentration as a direct consequence of concentration quenching [69]. The samples re-fired at 1100˚C have smaller peak intensity ratios, larger CIE coordinates and higher dominant wavelengths, indicating that the firing temperature affects the optical properties of the $Gd_2O_2S:Pr^{3+}$ phosphors. In contrast to the $Gd_2O_2S:Tb^{3+}$ samples, the $Gd_2O_2S:Pr^{3+}$ samples increase in x but decrease in y, which might result from the different excitation mechanism for PL and CL [110]: in the case of PL, the luminescent centre is excited by adsorption of the incident light while for the CL, the luminescent centre is excited by the

recombination of electrons and holes generated by the high-energy electron beam.

Luminance and luminous efficacies of the $Gd_2O_2S:RE^{3+}$ phosphor samples show strong dependence on the RE^{3+} activator concentration. Optimisation of the Pr^{3+} activator concentration by CL measurements indicated that a 1.0 mol% Pr concentration gave the highest luminance values for both 900 ˚C and 1100 ˚C samples at accelerating voltages between 1000 V and 5000 V and a range of emission currents between 1.46 μA and 8.6 μA, using a defocused e-beam. The luminance and luminous efficacies as a function of accelerating voltage are presented in Figure 4.11 and Figure 4.12, respectively, for an emission current of 8.6 μA.

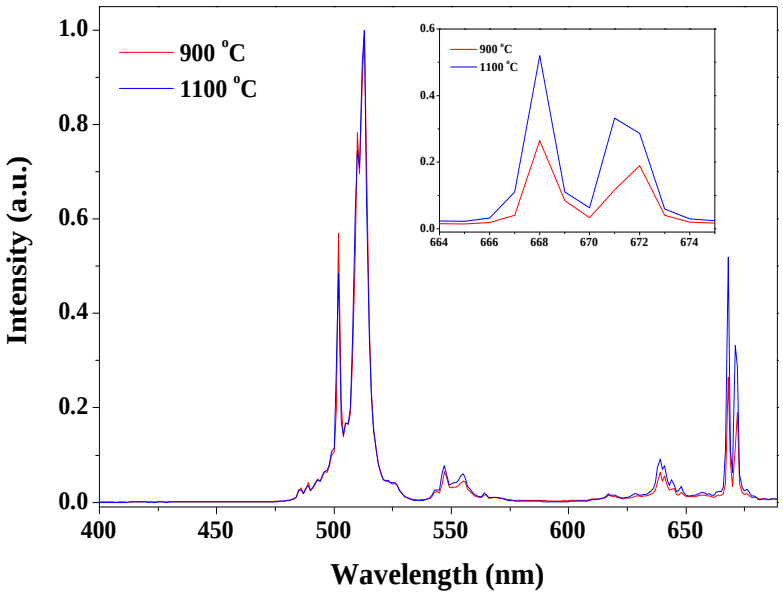

Figure 4.10 CL spectra of $Gd_2O_2S:Pr^{3+}$ (normalised to 513 nm) using an accelerating voltage of 5000 V and 8.6 μA emission current, defocused e-beam. Inset shows the expansion of 664 to 675 nm region.

The sRGB HDTV CCIR 709 colour triangle (dot line on the CIE chromaticity diagram in Figure 4.13) is compared with a colour triangle that has been produced from the same red and blue colour points, along with that of the $Gd_2O_2S:Pr^{3+}$ phosphor after firing to 1100 ˚C (solid line in Figure 4.13). This

shows that the latter phosphor has the potential to improve the colour gamut by expanding the colour space.

Table 4.3 The optical properties of $Gd_2O_2S:Pr^{3+}$ phosphors measured using an accelerating voltage of 5000 V and 8.6 μA emission current, defocused e-beam.

Pr concentration	CIE x	CIE y	Dominant λ/nm	Colour temperature/K	Fired temperature/˚C	Intensity ratio§
1 mol%	0.1496	0.6606	519	8568	900	2.80
2 mol%	0.1465	0.6603	518	8682	900	3.79
3 mol%	0.1519	0.6618	519	8566	900	3.05
5 mol%	0.1519	0.6618	519	8566	900	2.50
10 mol%	0.1594	0.6609	521	8408	900	1.78
1 mol%	0.1673	0.6523	521	8308	1100	1.92
2 mol%	0.1654	0.6530	521	8344	1100	1.92

§ Intensity ratio of the green (513 nm)/red (672 nm) emission bands

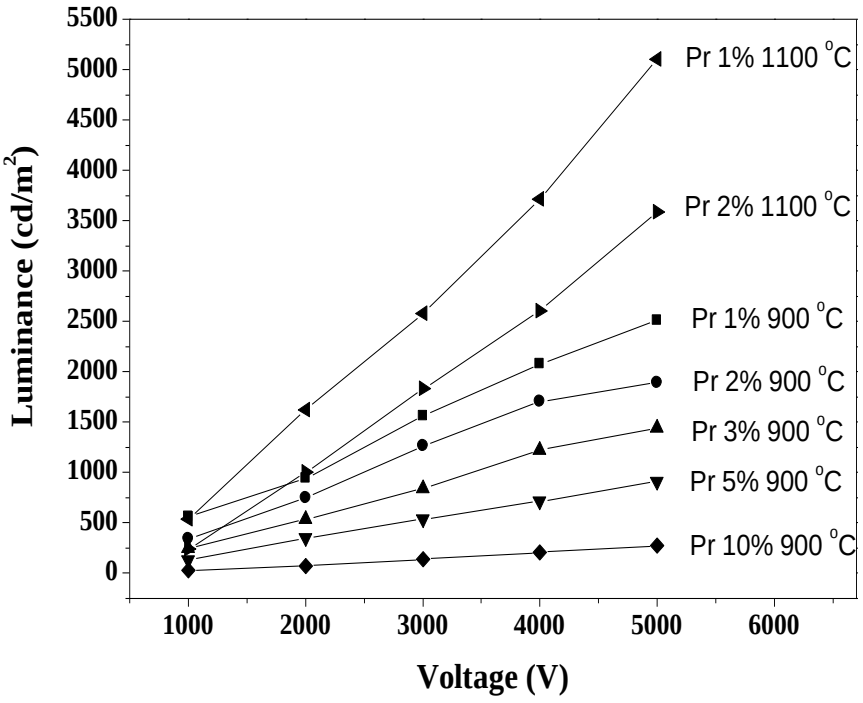

Figure 4.11 CL luminance of $Gd_2O_2S:Pr^{3+}$ phosphor samples at various accelerating voltages using 8.6 μA emission current and a defocused e-beam.

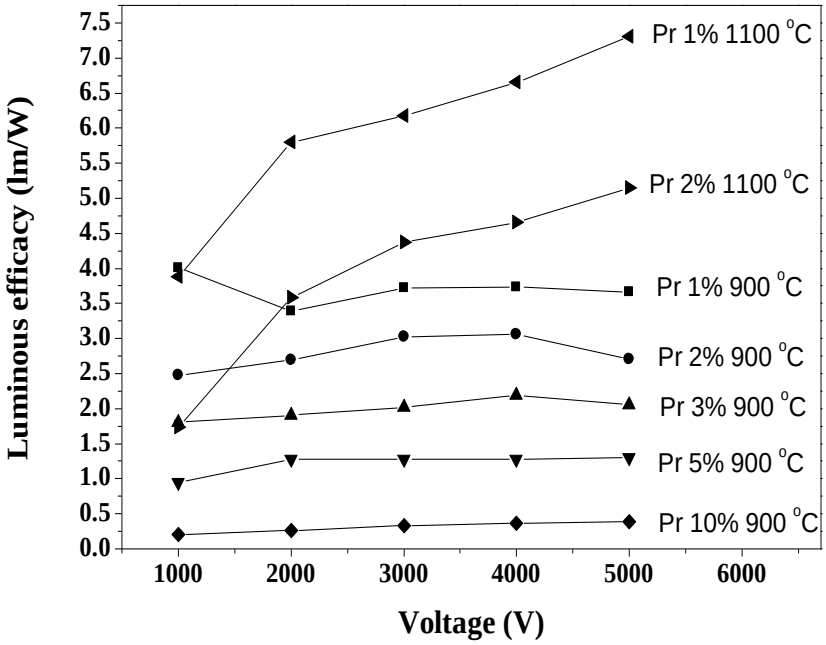

Figure 4.12 Luminous efficacy of $Gd_2O_2S:Pr^{3+}$ samples at various accelerating voltages using 8.6 μA emission current and a defocused e-beam.

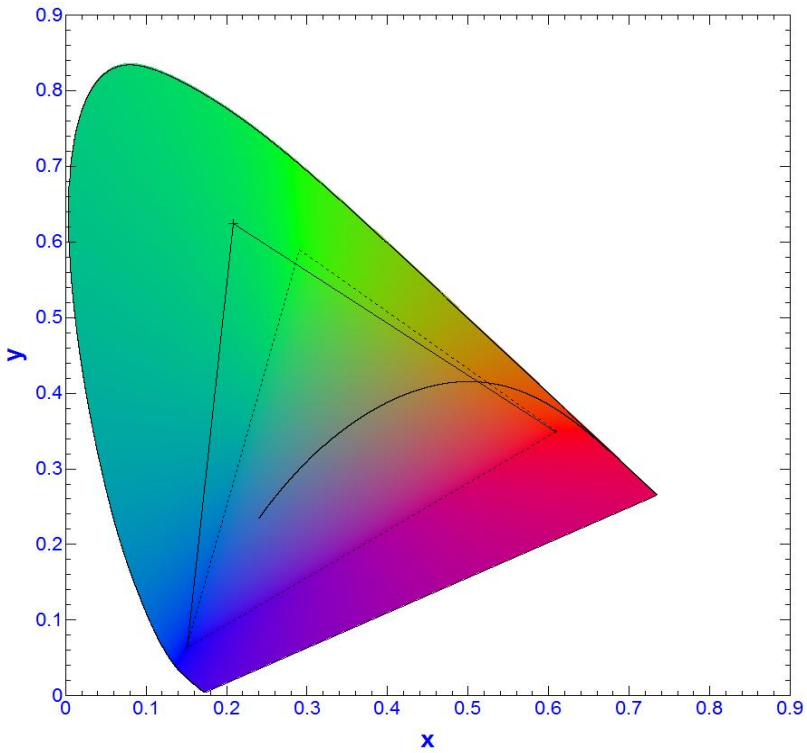

Figure 4.13 Colour triangle of HDTV sRGB triad (dot line) compared with a similar colour triangle in which the green colour point is that of the $Gd_2O_2S:Pr^{3+}$ phosphor (solid line).

Optimisation of the Tb^{3+} activator concentration by CL measurements indicated that a 2 mol% Tb^{3+} concentration gave the highest luminance. The luminance of the $Gd_2O_2S:Tb^{3+}$ phosphor samples are plotted against accelerating voltage for an emission current of 8.6 μA in Figure 4.14. The inset displays the luminance as a function of Tb^{3+} concentration at 5 kV accelerating voltage. It can be seen that the luminance grows as Tb^{3+} concentration increases from 0.5 mol% to 2 mol% and then decreases as it increases from 2 mol% to 5 mol%.

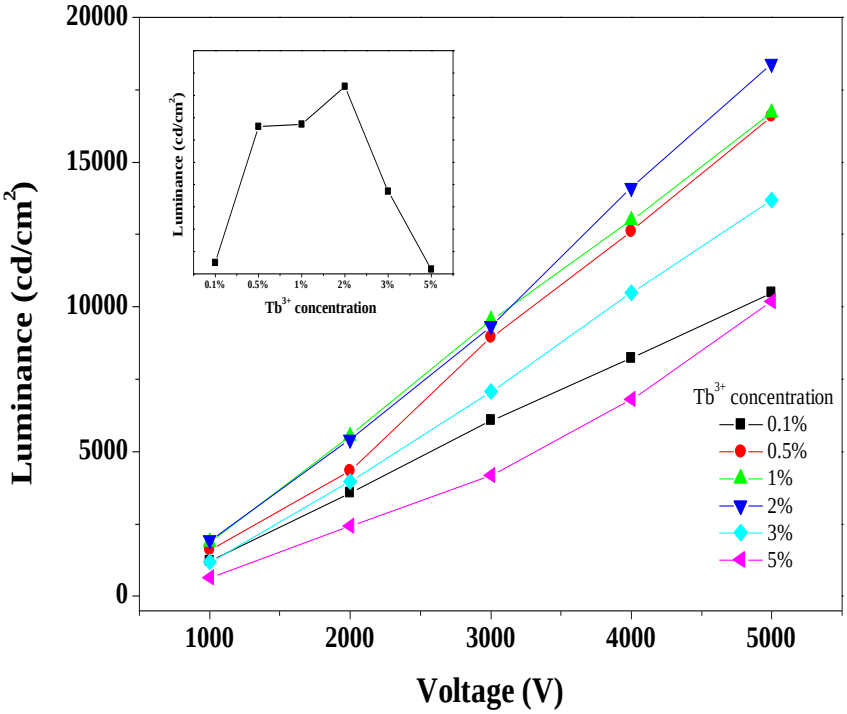

Figure 4.14 CL luminance of $Gd_2O_2S:Tb^{3+}$ samples at various accelerating voltages using 8.6 μA emission current and a defocused e-beam. Inset: The luminance as a function of Tb^{3+} concentration at 5 kV accelerating voltage.

4.5 Conclusions

1. The luminescent properties of nanometre sized $Gd_2O_2S:RE^{3+}$ phosphor samples have been investigated. Characteristic emission spectra of Pr^{3+} and Tb^{3+} have been observed. And the intensity of emission bands was shown to be dependent on both the activator concentration and the firing temperature.

2. It has been shown that for low voltage CL applications, $Gd_2O_2S:Pr^{3+}$ phosphor particles with a 1 mol% Pr^{3+} activator concentration fired at 1100 ˚C exhibit the highest luminance and luminous efficacy for this material whereas the optimised activator concentration for all of the examined $Gd_2O_2S:Tb^{3+}$ phosphor particles is 2 mol%.
3. The green colour point of the $Gd_2O_2S:Pr^{3+}$ phosphor expands the colour space of the sRGB HDTV CCIR 709 triad.
4. Cross-relaxation of Tb^{3+} cations could be observed in the spectra of $Gd_2O_2S:Tb^{3+}$ phosphor which reduces the intensity of emission bands from $^5D_3 \rightarrow {}^7F_J$ (J= 6, 5, 4, 3) transitions and enhances that of emission bands from $^5D_4 \rightarrow {}^7F_J$ (J= 6, 5, 4, 3) transitions.
5. The green emissions at 545 nm from $^5D_4 \rightarrow {}^7F_5$ transition are the most intense bands in every spectrum of $Gd_2O_2S:Tb^{3+}$ phosphor in the Tb^{3+} concentration range studied herein. This results from the fact that the bottom of the CTS in Gd_2O_2S lies close to the $^5D_3$ energy level of Tb^{3+}, and that the resulting thermal quenching between these greatly reduces the electron population in the $^5D_3$ level.

Chapter 5 Upconversion luminescence of RE^{3+} activated Y_2O_2S and Gd_2O_2S phosphors

5.1 Introduction

Upconversion (UC) phosphors emit a photon of high energy by the sequential absorption of two or more incident low-energy photons. In 1959, Bloembergen described a possible upconversion process which later became known as excited state absorption (ESA) in rare earth ion or transition metal ion doped crystals [272]. However ESA process was not very efficient as the reported in 1969 [273]. Most of the pioneering work on upconversion was carried out by Auzel [119]. In 1966, Auzel reported the first example of upconversion for the dopant couple of Yb^{3+}, Er^{3+} in $CaWO_4$ and described the energy transfer process from Yb^{3+} ion to the Er^{3+} ion, which he named as “additional de photon par transfers d’energie” (APTE effect) [114], also later termed as ETU for energy transfer upconversion [115]. Although there are several other mechanisms for the upconversion process, ESA and ETU are the ones used in practice for considering energy transfer efficiencies [116, 118].

Table 5.1 Typical examples of the UC mechanisms.

Mechanism	Typical example	Efficiency
Anti-Stokes Raman	Silicon crystals	$\sim 10^{-13}$
2-Photon excitation	CaF_2: Eu^{2+}	$\sim 10^{-12}$
Second harmonic generation	KH_2PO_4 crystals	$\sim 10^{-11}$
Cooperative luminescence	$YbPO_4$: Yb^{3+}	$\sim 10^{-8}$
Cooperative sensitization	YF_3: Yb^{3+}, Tb^{3+}	$\sim 10^{-6}$
ESA	SrF_2: Er^{3+}	$\sim 10^{-5}$
ETU	YF_3: Er^{3+}	$\sim 10^{-3}$
Sensitized ETU	$NaYF_4$: Er^{3+}, Yb^{3+}	$\sim 10^{-1}$

The optical properties of luminescent materials strongly depend on the host crystal lattice as well as nature and concentration of the dopant (the intentional impurity ions in the host lattices). Rare earth ions are one of the most common active components in many UC phosphors due to their well separated

energy state structures. The inner 4f shell in RE^{3+} contains the spectroscopically relevant electronic states, (which have long lifetimes (~ms) for UC absorption since they are well shielded from external electric environments by the outer 5s and 5p electrons). Some transition metal ions, such as Os^{4+}, Ti^{2+}, have also shown UC luminescence [120-122, 124, 125], in which the d orbitals of transition metals are strongly influenced by the local crystal field, allowing for chemical variation of the photophysical characteristics [119].

Amongst all of the known upconversion phosphors, Yb^{3+} and Er^{3+} co-doped hexagonal $NaYF_4$ has been shown to be one of the most efficient UC phosphors [143, 147, 149, 152, 162, 163], as reported by Menyuk in 1972 [141]. There have been reports on UC for rare earth ions in different host crystals, for example silicates [98], zirconium oxides [127], silica [129], yttrium oxides [100, 103, 130-134, 274], oxysulfides [135, 138, 139].

Many applications have been suggested for UC phosphors because of their unique emission properties. For example, UC phosphors with excitation in the near infrared (NIR) region have several advantages over organic dyes and fluorescent proteins for imaging biological tissues and cells [101, 102, 150, 155-158]. These advantages include the absence of photo-damage to living organisms, low auto-fluorescence, high light penetration depth in biological tissues, high detection sensitivity.

Also, UC phosphors could be used to reduce the sub-band-gap transmission losses in conventional solar cells by up-converting the transmitted low-energy photons from the solar spectrum to higher-energy photons, which can then be utilised by the solar cell. A relevant review has been published by Shalav [45]. Other applications include solid-state three-dimensional displays [164, 171, 172], upconversion lasers [22, 23], fibre optic amplifiers that operate at wavelengths of 1.55, 1.46 and 1.31 μm [20, 21].

In this chapter, results on the UC luminescence and down-conversion luminescence studies of RE^{3+} (RE=Tb, Er, Eu) doped Y_2O_2S and Gd_2O_2S are presented. Both upconversion and downconversion can be observed in the spectra of Tb^{3+} and Er^{3+} co-doped Y_2O_2S and Gd_2O_2S, which are denoted Y(or

Gd)$_{2-y-x}$Tb$_y$Er$_x$O$_2$S and Y(or Gd)$_{2-x-y}$Tb$_x$Er$_y$O$_2$S, where x = 0.01 and y = 0.0005, 0.001, or 0.002, respectively. The influences of dopant concentration and host cations on the optical properties are investigated. And to further understand the particle properties, the down-conversion emission of Tb^{3+} and Er^{3+} co-doped Y_2O_2S was compared to that of $Y_{2-x}Tb_xO_2S$ (where x value varies from 0.001 to 0.05). Furthermore the UC properties of $Y_2O_2S:Eu^{3+}$ and $Gd_2O_2S:Eu^{3+}$ nanoparticles were investigated and the effect of host crystal lattices on the UC luminescence was studied.

5.2 Crystallography analysis and morphological studies

Figure 5.1 presents the XRPD patterns of the Tb^{3+} and Er^{3+} co-doped Y_2O_2S and Gd_2O_2S samples, respectively. All of the patterns are consistent with the hexagonal phase of the host crystals that was previously reported [27, 256], indicating that this level of doping does not affect the microstructure of the host lattice in the particles. The extra peaks in the $Y_{1.9895}Tb_{0.01}Er_{0.0005}O_2S$ XRPD pattern can be assigned to cubic Y_2O_3 crystal phase, which is fairly reasonable since it was employed as a top layer component in the firing process converting precursor powders to oxysulfide particles.

The cell sizes of the hexagonal $Y_{2-y-x}Tb_yEr_xO_2S$ phosphors are very similar (see Table 5.2) as is expected where the dopant atoms are smaller than the Y^{3+} cations they replace. These findings are not unexpected as the ionic radii for Y^{3+}, Tb^{3+}, Er^{3+} are respectively 0.90 Å, 0.92 Å and 0.89 Å, so replacing Y^{3+} with tiny amounts of Tb^{3+} and Er^{3+} would be expected to have little or no effect on the lattice cell sizes in these materials. Y_2O_2S crystallizes in the trigonal space group $P\bar{3}m1$, as previously reported [139]. In this structure both Y and O atoms have the same symmetry site, C_{3v}. Each metal atom Y is coordinated to four oxygen atoms and three sulphur atoms (as its nearest neighbours). The Y atoms are thereby experiencing weaker crystal fields than in Y_2O_3; this means the Er^{3+} cation dopants on the Y sites will experience a weaker crystal field in Y_2O_2S than in Y_2O_3. Similar findings arise in the case of the Gd_2O_2S host lattice since it is isostructural with Y_2O_2S.

Figure 5.2 – Figure 5.5 presents the SEM images of the morphologies of Tb^{3+} and Er^{3+} co-doped Y_2O_2S and Gd_2O_2S samples, respectively. The phosphor particles are well separated from each other and exhibit smooth surfaces and most of the particles in the observation region are roughly spherical, although plate- and pillar-like particles can also be observed. This results from the firing process converting precursor powders to oxysulfides phosphors and partial aggregation of Na_2CO_3 in the blend mixture [258]. Most particles in the SEM images have sizes that are less than 100 nm. The mean crystallite size was calculated from XRPD data using a preferred orientation method introduced by Jarvinen [275] and the calculated data are in good agreement with the SEM observation (see table 5.2).

Table 5.2 Structural Parameters for $Y_{2-y-x}Tb_yEr_xO_2S$ (where y = 0.01, and x = 0.0005, 0.001 or 0.002), from XRPD data from XRPD data.

x	Phase*	a (Å)	c (Å)	Crystal Size (nm)	Occupancy of Y atom		
					M(1)	M(2)	% Moles
0.0005	I	3.7828(1)	6.5826(1)	88.92(33)	1.9896		94.342(38)
	II	10.5976(1)		434(12)	8	24.0	5.658(38)
0.001	I	3.7830(1)	6.5827(3)	97.86(44)	1.9896		86.153(61)
	II	10.5990(7)		170.2(26)	8	24.0	13.847(61)
0.002	I	3.7829(1)	6.5827(7)	98.22(37)	1.9896		89.346(54)
	II	10.5979(2)		198.7(31)	8	24.0	10.654(54)

*Phase I = Hexagonal phase II = cubic

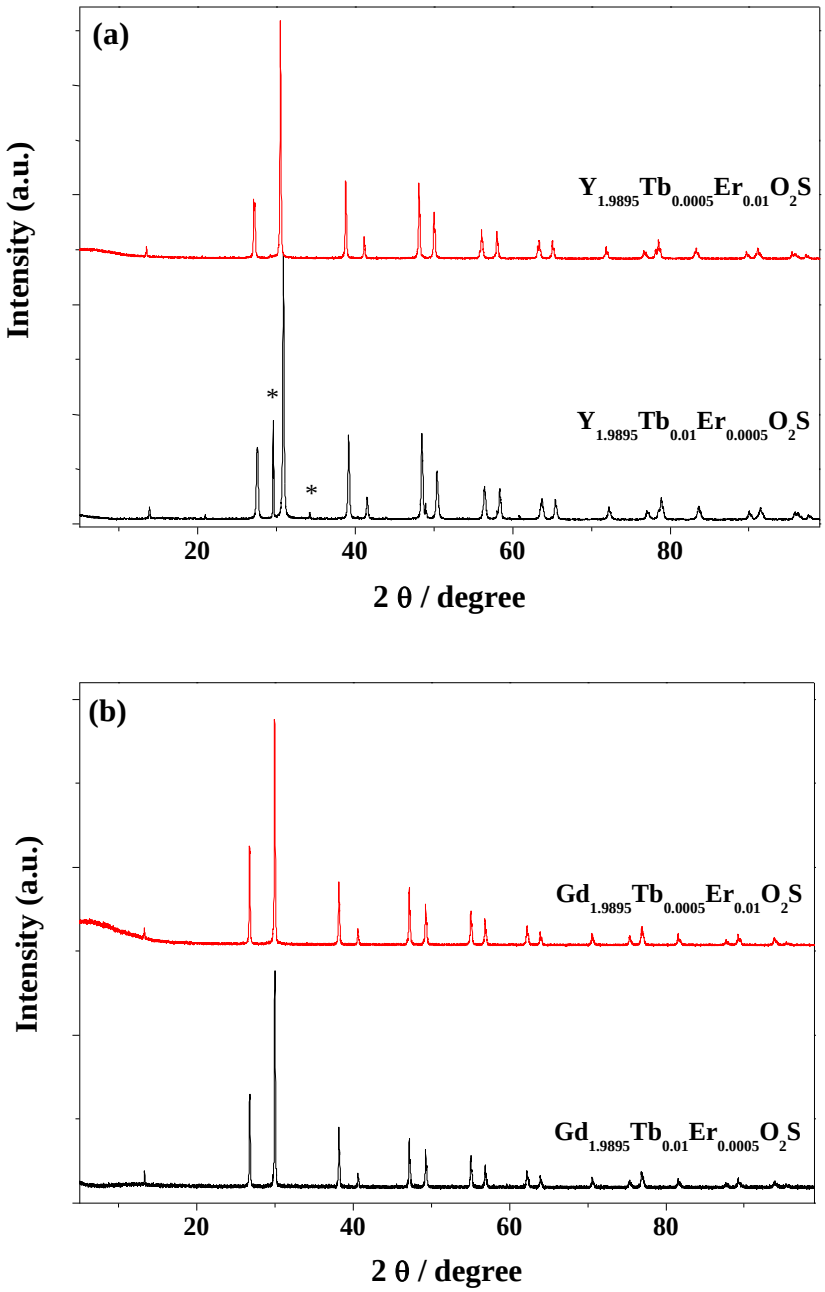

Figure 5.1 XRPD patterns of Tb^{3+} and Er^{3+} co-doped Y_2O_2S (a) and Gd_2O_2S (b) samples. * denotes peaks arising from the cubic Y_2O_3 crystal phase.

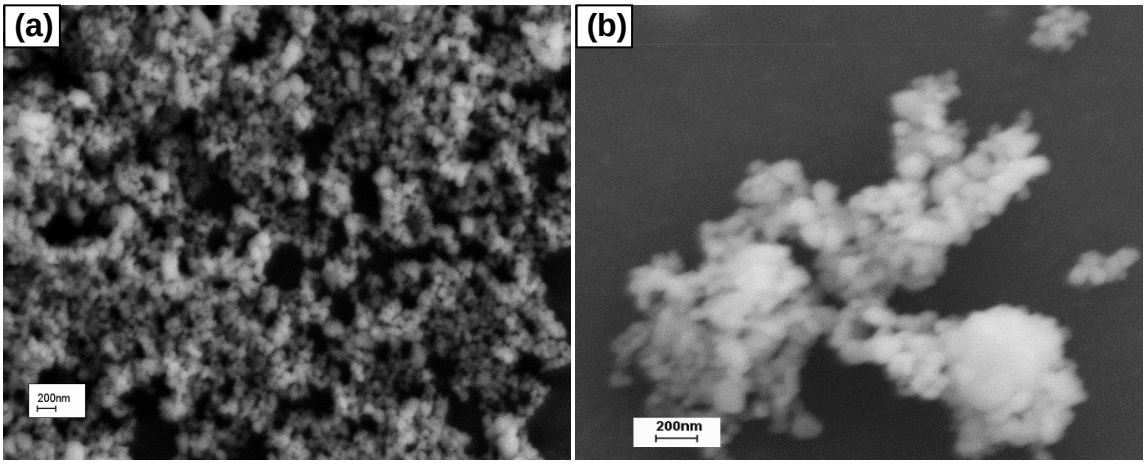

Figure 5.2 SEM images of $Y_{1.9895}Tb_{0.01}Er_{0.005}O_2S$ phosphor particles.

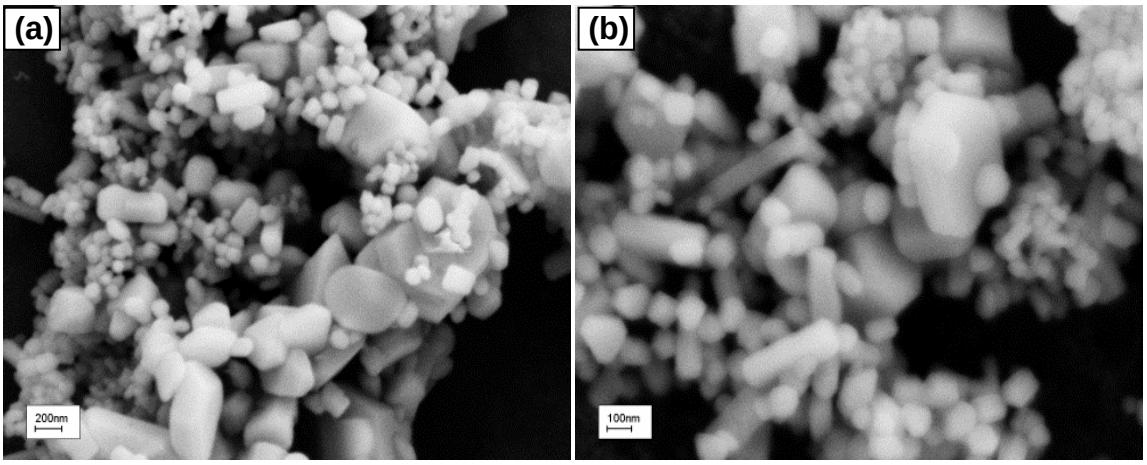

Figure 5.3 SEM images of $Y_{1.9895}Tb_{0.0005}Er_{0.01}O_2S$ phosphor particles.

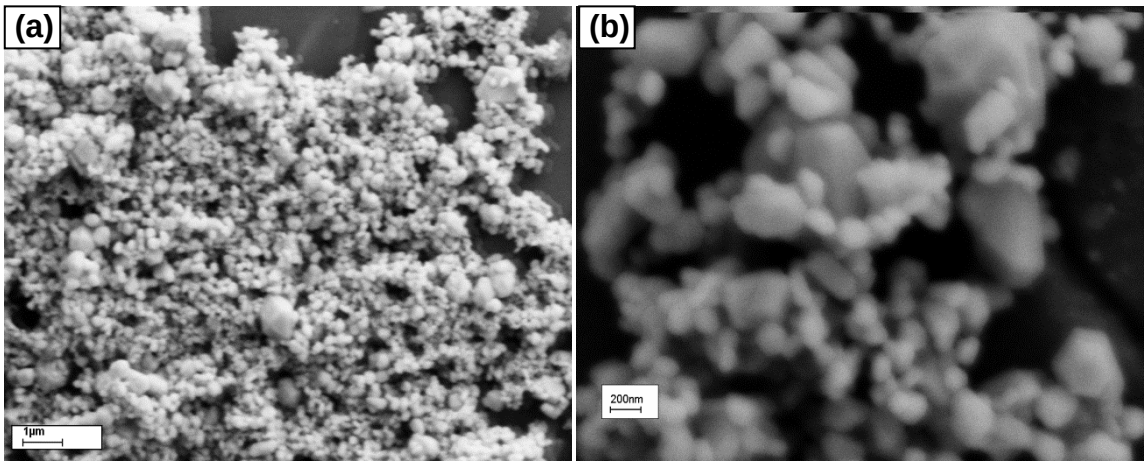

Figure 5.4 SEM images of $Gd_{1.9895}Tb_{0.01}Er_{0.005}O_2S$ phosphor particles.

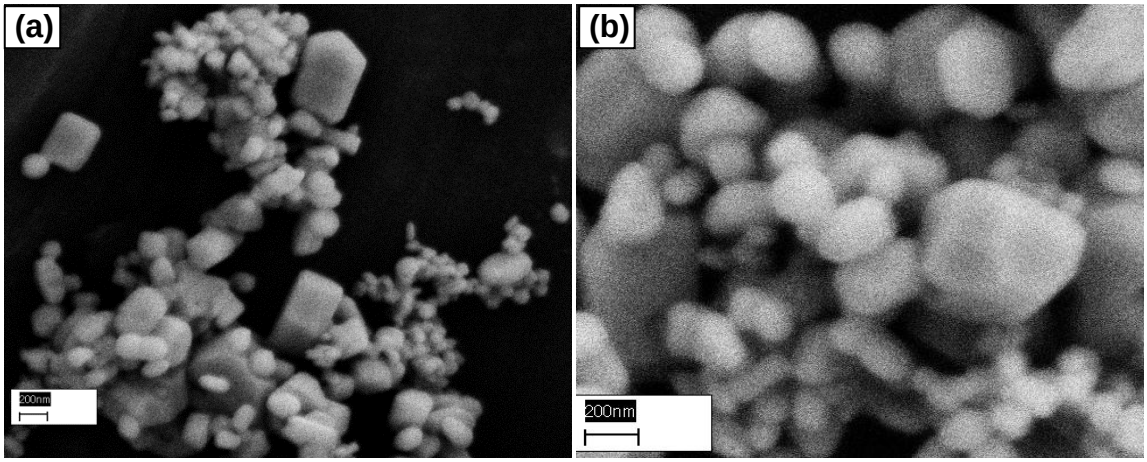

Figure 5.5 SEM images of $Gd_{1.9895}Tb_{0.005}Er_{0.01}O_2S$ phosphor particles.

5.3 Luminescence measurement

5.3.1 UC spectra for Tb^{3+} and Er^{3+} co-doped Y_2O_2S phosphor

Luminescence spectroscopy was used to investigate the upconversion properties of the Tb^{3+} and Er^{3+} co-doped Y_2O_2S samples. Spectra for all of the samples are similar to that of $Y_{1.9895}Tb_{0.01}Er_{0.0005}O_2S$ under 632.8 nm red laser excitation. UC spectra of $Y_{1.9895}Tb_{0.01}Er_{0.0005}O_2S$ and $Y_{1.989}Tb_{0.001}Er_{0.01}O_2S$ are shown in Figure 5.6 and Figure 5.7. For the $Y_{1.989}Tb_{0.001}Er_{0.01}O_2S$ sample, filters were applied to the detector to obtain the best spectrum. The emission manifold can be assigned to transitions to the Er^{3+} ground state ($^4I_{15/2}$) from the following excited-state levels $^2H_{9/2}$, $^4F_{5/2}$, $^4F_{7/2}$, $^2H_{11/2}$ and $^4S_{3/2}$, respectively (see Table 5.3). The emission manifolds are in very similar positions to those found for the Er^{3+} cations in Y_2O_3:Er^{3+},Yb^{3+} [130], but are sufficiently different both in emission wavelength and in intensity patterns to be worthy of further comment. It can be seen from the spectra the green emission bands between 520 nm and 560 nm, assigned to transitions of $^2H_{11/2} \rightarrow {}^4I_{15/2}$ and $^4S_{3/2} \rightarrow {}^4I_{15/2}$, are the most intense ones amongst all the emission bands.

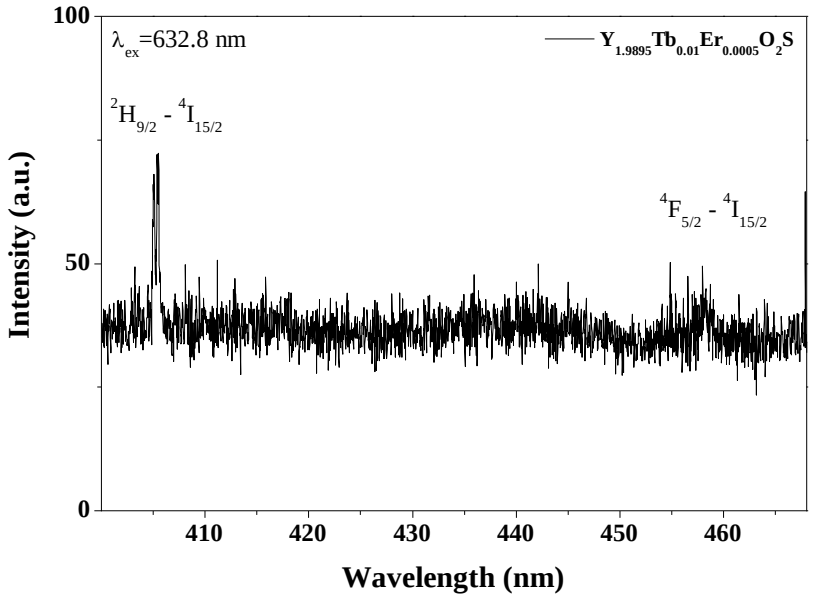
100
50
0
Intensity (a.u.)
410
420
430
440
450
460
Wavelength (nm)
λex=632.8 nm
Y1.9895Tb0.01Er0.0005O2S
2H9/2 - 4I15/2
4F5/2 - 4I15/2

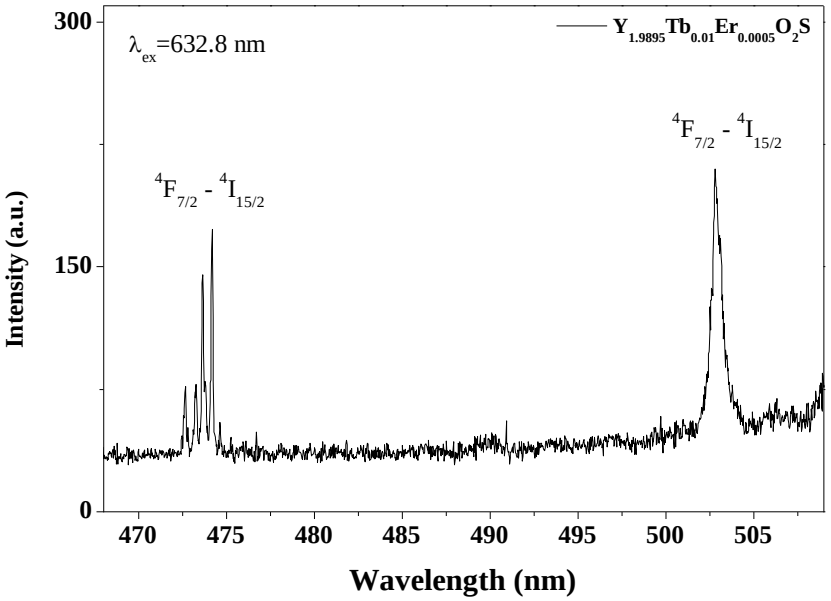
300
150
0
Intensity (a.u.)
470
475
480
485
490
495
500
505
Wavelength (nm)
λex=632.8 nm
Y1.9895Tb0.01Er0.0005O2S
4F7/2 - 4I15/2
4F7/2 - 4I15/2

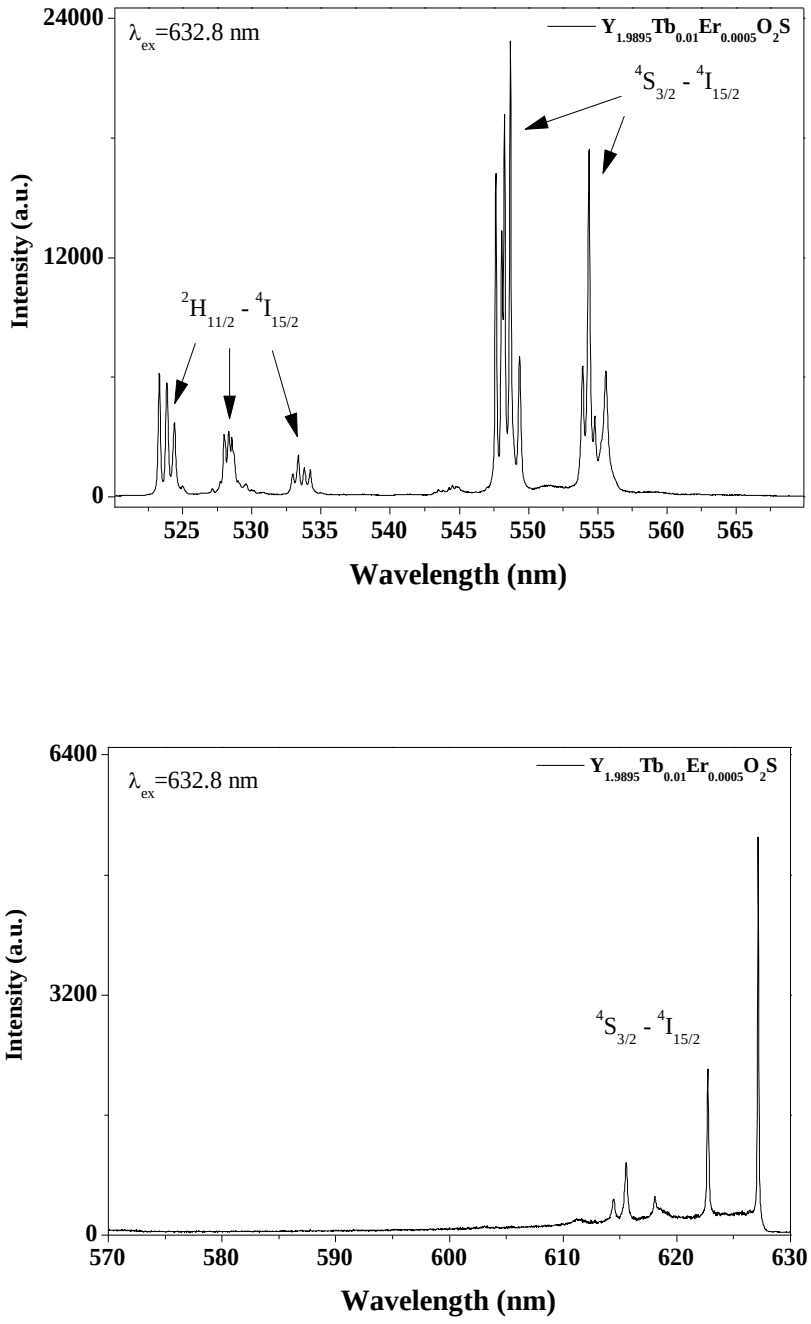

Figure 5.6 Anti-Stokes emission spectra of $Y_{1.9895}Tb_{0.01}Er_{0.0005}O_2S$ under 632.8 nm red laser excitation. Relative intensities are shown in arbitrary units and cannot be compared to each other.

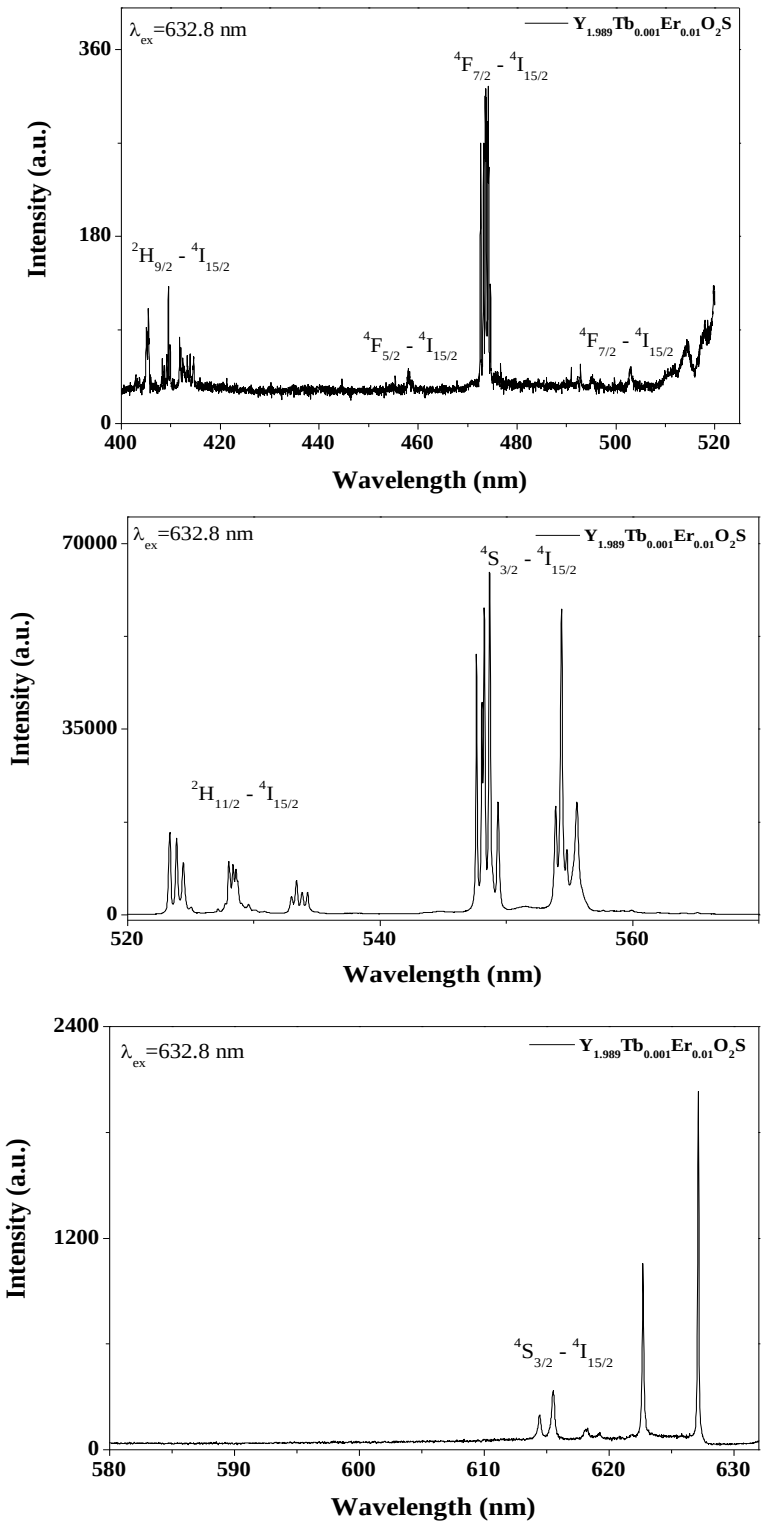

Figure 5.7 Anti-Stokes emission spectra of $Y_{1.989}Tb_{0.001}Er_{0.01}O_2S$ under 632.8 nm red laser excitation. Relative intensities are shown in arbitrary units and cannot be compared to each other.

Table 5.3 Assignments of the anti-Stokes and Stokes emission bands of $Y_{1.9895}Tb_{0.01}Er_{0.0005}O_2S$ under 632.8 nm red laser excitation.

emission assignment	emission bands range		width of emission bands range
	nm	cm^{-1}	cm^{-1}
$^2H_{9/2}\rightarrow{}^4I_{15/2}$	~404 to 406	~24752 to 24630	122
$^4F_{5/2}\rightarrow{}^4I_{15/2}$	~453 to 460	~22075 to 21739	336
$^4F_{7/2}\rightarrow{}^4I_{15/2}$	~472 to 476	~21186 to 21008	178
	~501 to 505	~19960 to 19801	159
$^2H_{11/2}\rightarrow{}^4I_{15/2}$	~520 to 535	~19230 to 18691	539
$^4S_{3/2}\rightarrow{}^4I_{15/2}$	~542 to 562	~18450 to 17793	657
	~610 to 624	~16393 to 16026	367
$^4F_{9/2}\rightarrow{}^4I_{15/2}$	~638 to 685	~15674 to 14598	1076
	~750 to 780	~13333 to 12820	513
$^4I_{9/2}\rightarrow{}^4I_{15/2}$	~801 to 830	~12484 to 12048	436
$^4I_{11/2}\rightarrow{}^4I_{15/2}$	~850 to 905	~11765 to 11050	715

Figure 5.8 illustrates the energy diagram of a free Er^{3+} ion and some proposed excitation and emission processes. Silver *et al* [130] proposed two possible energy transfer processes: one is called two-photon excitation. Two incident photons have a combined energy of 31606 cm^{-1} and are capable of populating the $^2P_{3/2}$ excited state. This then decays nonradiatively to lower energy levels such as the $^2H_{9/2}$, $^4F_{5/2}$, $^4F_{7/2}$, $^2H_{11/2}$, and the $^4S_{3/2}$ levels before it returns to the ground state and emit upconversion photons. The other possible energy process is excited state absorption (ESA), which involves nonradiative relaxation from the $^4F_{9/2}$ excited state to other lower lying levels, such as $^4H_{9/2}$, $^4H_{11/2}$, and $^4H_{13/2}$, and absorption of a second 632.8 nm (~15803 cm^{-1}) photon resulting in excitation to $^4G_{7/2}$, $^4G_{11/2}$, and $^4F_{7/2}$. Both processes are presented in Figure 5.7. The UC emissions are indicated with coloured solid lines. No UC emissions from Tb^{3+} ions were observed while Tb^{3+} cations usually give out bright green down-converting emission when excited with ultraviolet (UV) radiation, although indeed these particles gave good down-conversion emission, which will be discussed later.

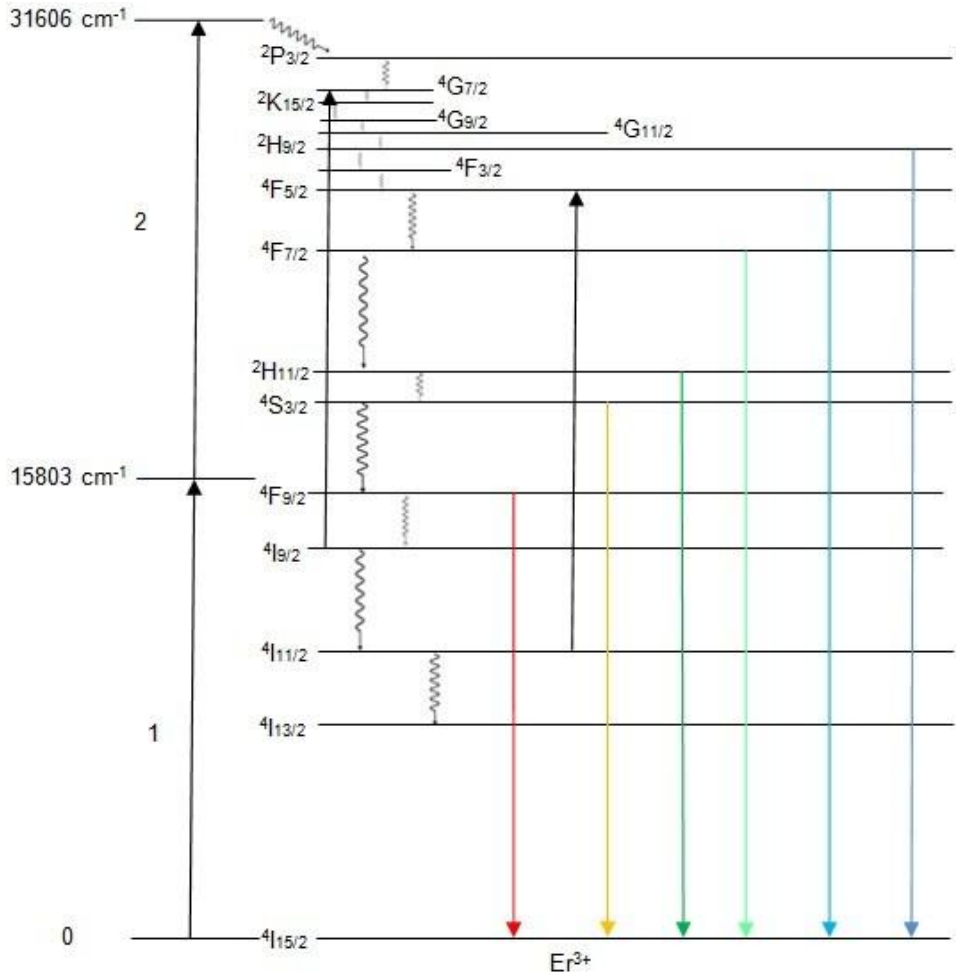

Figure 5.8 Schematic energy level diagram of a free Er^{3+} cation and some proposed excitation and emission processes.

The overlay of the anti-Stokes emission spectra of the $Y_{2-y-x}Tb_yEr_xO_2S$ in the range between 520 nm and 560 nm is presented in Figure 5.9. The Raman band at a wavenumber shift of 256 cm^{-1}, which originates from Y_2O_2S, could be observed on both Stokes and anti-Stokes sides of the excitation line and was used as a standard to compare the UC emission intensities. For the $Y_{2-y-x}Tb_yEr_xO_2S$ samples, the emission bands of $Y_{1.9895}Tb_{0.01}Er_{0.0005}O_2S$ sample have the lowest intensity and the intensity increases with Er^{3+} concentration, which is different finding from the previous report. Happanen [276] observed upconversion luminescence from $Y_2O_2S:Yb^{3+},Er^{3+}$ nanophosphors using 970 nm infrared laser excitation and found that the intensity decreases with increasing Er^{3+} concentration due to concentration quenching.

There are several effects that contribute to these different phenomena: firstly, for $Y_2O_2S:Yb^{3+}$, Er^{3+} nanophosphors, the Yb^{3+} ions (the sensitizers) are excited with the infrared laser and transfers energy to the Er^{3+} ions resulting in UC emission. In our case, Er^{3+} cations were directly excited using red laser and no evidence indicates energy transfer processes to Tb^{3+} cations so we observe that the UC luminescence increasing with Er^{3+} concentration;

Secondly, our particles have an average diameter of around 100 nm, allowing the Er^{3+} cations to be more evenly distributed in the host lattice compared to the nanophosphors, which could minimise cross relaxation processes that are responsible for the emission quenching [135]. In addition, there is no UC emission from Tb^{3+}, indicating no energy transfer occur between Tb^{3+} and Er^{3+} cations in the UC process. Thus the presence of the Tb^{3+} cations act just like the optically inactive Y^{3+} cations and help separate/dilute the effective concentration of Er^{3+} cations. The cross-relaxation process is therefore suppressed during upconversion and luminescence intensity then increases with Er^{3+} cation concentration, at least in the range studied in this work.

Figure 5.10 depicts the overlay of UC emissions of the $Y_{2-x-y}Tb_xEr_yO_2S$ sample in the range from 520 to 560 nm. When x was increased from 0.0005 to 0.001, a great enhancement on UC emission intensity could be observed; however when x was increased on from 0.001 to 0.002, the UC emission intensity decreases with increasing Tb^{3+} concentration. This can be explained as follows: both Tb^{3+} and Er^{3+} would take Y^{3+} sites in the host lattice and there's no energy transfer processes between Tb^{3+} and Er^{3+} in the UC process. The presence of the Tb^{3+} cations acts just like the Y^{3+} cations and virtually increases the critical Er-Er distance, separate/dilute the effective concentration of Er^{3+} cations.

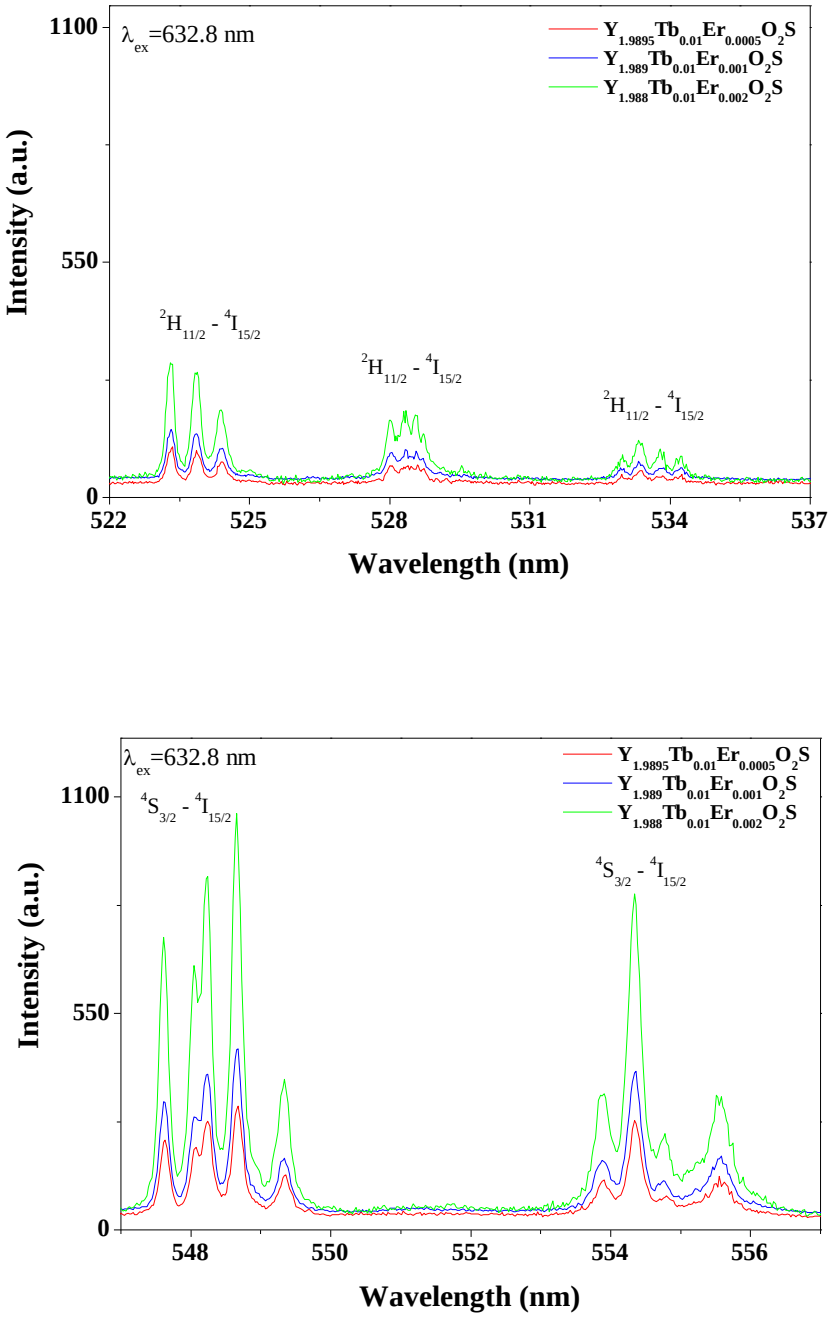

Figure 5.9 Overlay of anti-Stokes emission spectra of the $Y_{2-y-x}Tb_yEr_xO_2S$ sample, where y=0.01, x=0.0005, 0.001, or 0.002.

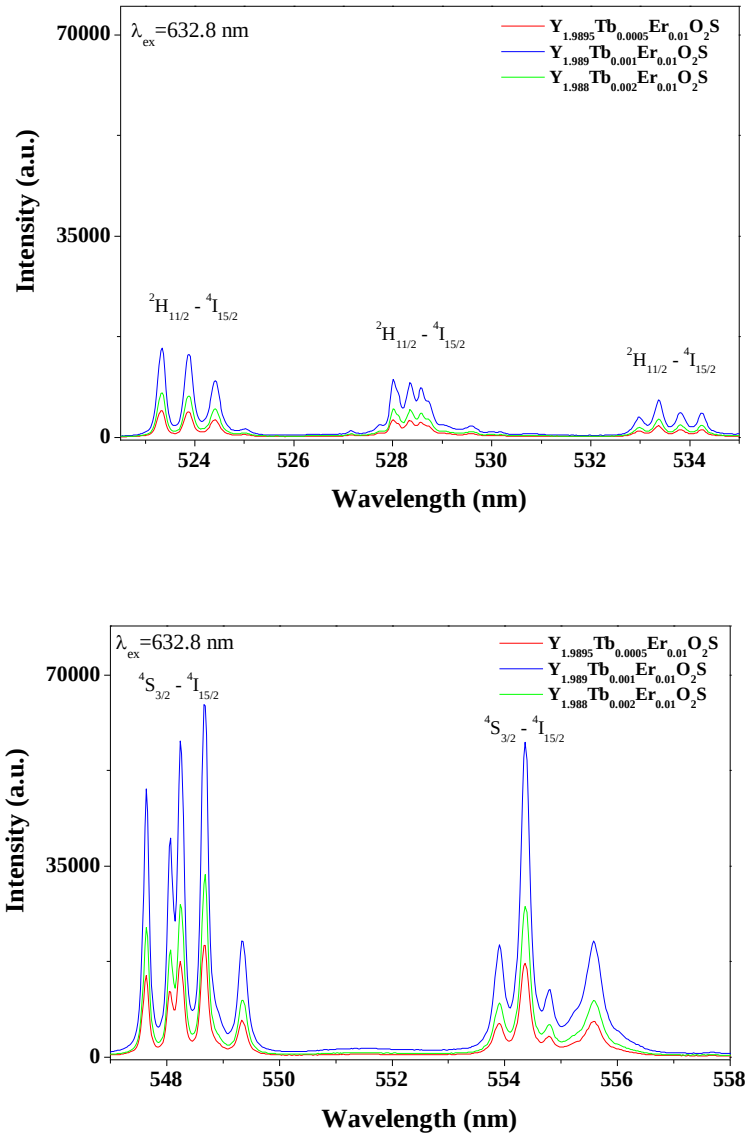

Figure 5.10 Overlay of anti-Stokes emission spectra of the $Y_{2-x-y}Tb_xEr_yO_2S$ sample, where y=0.01, x=0.0005, 0.001, or 0.002.

5.3.2 Down-conversion for Tb^{3+} and Er^{3+} co-doped Y_2O_2S phosphor

The down conversion emission spectra of the $Y_{2-y-x}Tb_yEr_xO_2S$ samples are shown in Figure 5.11. Bright green emission from Tb^{3+} cations can be observed, also weak emission bands from Er^{3+} cations was observed (indicated by arrows). The intensity of Er^{3+} emission increases with Er^{3+} concentration. This is a surprise as in Figure 5.11 (b) (which presents the emission spectra of $Y_{1.99}Er_{0.01}O_2S$ NPs) there is very poor down conversion emissions from the Er^{3+} cations. Clearly the

intensity of the emission from the Er^{3+} cations observed in Figure 5.11(a) (where the concentration of the Er^{3+} is much lower than in figure 5.11(b) yet the intensity is increasing with concentration) is not from a straight downconversion process and must involve the Tb^{3+} cations.

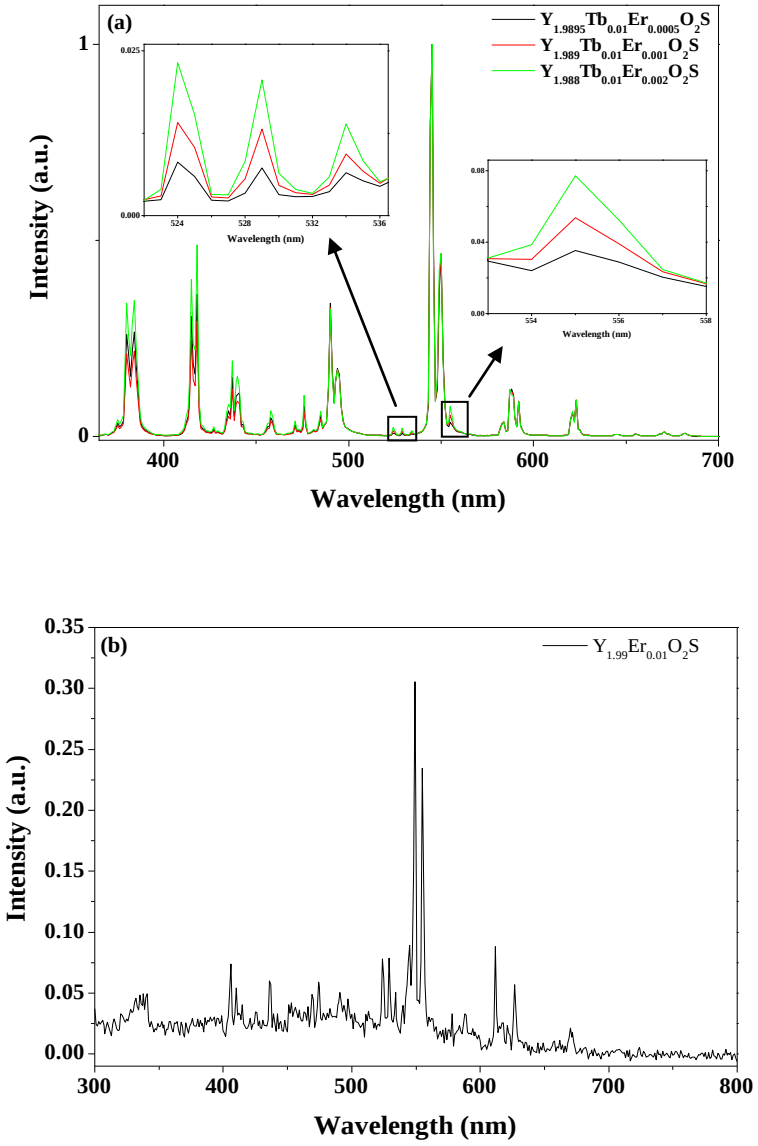

Figure 5.11 (a) Downconversion emission spectra (λ_{ex}=254 nm) of the $Y_{2-y-x}Tb_yEr_xO_2S$ samples; (b) PL emission spectrum (λ_{ex}=254 nm) of the $Y_{1.99}Er_{0.01}O_2S$ sample shows no emission band.

To further understand the role of the Er^{3+} cations we present the spectra of the $Y_{2-x}Tb_xO_2S$ phosphors (where x varies from 0.001 to 0.05) in Figure 5.12. It is clearly shown that the intensity of the blue emissions, which are assigned to

transitions of $^5D_3 \rightarrow {}^7F_J$, decrease as the Tb^{3+} concentration goes up. With the increase of Tb^{3+} concentration, more $^5D_3$ levels quench to $^5D_4$, and the intensity of the blue emissions are decreased. This has been well described and discussed in Chapter 3. However, the presence of Er^{3+} has caused differences in the present materials. Firstly, emission from the Er^{3+} cations can be observed, which is not from a straight downconversion process and must involve the Tb^{3+} cations since the intensity is increasing with concentration yet no emission could be observed in Figure 5.11 (b) where the Er^{3+} concentration is much higher.

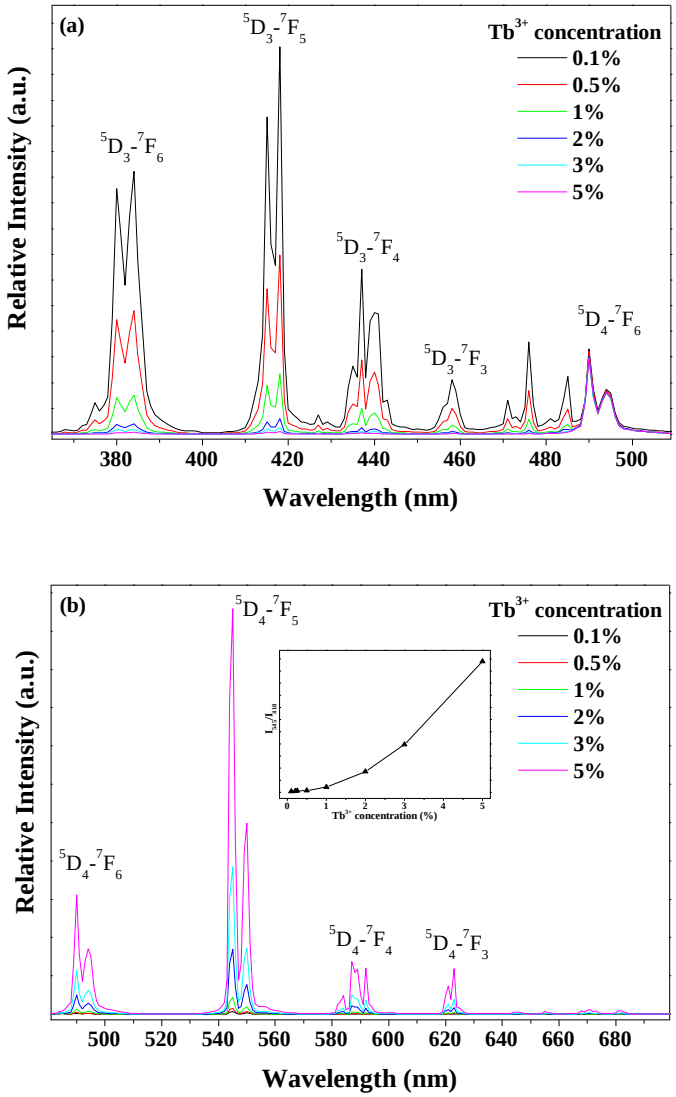

Figure 5.12 PL spectra of the $Y_{2-x}Tb_xO_2S$ phosphors (where x varies from 0.001 to 0.05) normalised to 545 nm (a) and 385 nm (b), respectively. Inset displays the blue/green ratio as a function of Tb^{3+} concentration.

Firm evidence for this is presented in figure 5.13, where blue emissions from $Y_{1.9895}Tb_{0.01}Er_{0.0005}O_2S$ are stronger than those of $Y_{1.989}Tb_{0.01}Er_{0.001}O_2S$ yet weaker than those of $Y_{1.988}Tb_{0.01}Er_{0.002}O_2S$. As stated above, we observed some extra emission bands at 525 nm, 528 nm, 535 nm and 554 nm, which could be attributed to $^2H_{11/2}\rightarrow{}^4I_{15/2}$ of Er^{3+} cations, with their intensities increasing with Er^{3+} cations concentration linearly. In figure 5.14 the order of intensity for the green emission at 550 nm is opposite to that of the blue: $Y_{1.989}Tb_{0.01}Er_{0.001}O_2S$ is stronger than $Y_{1.9895}Tb_{0.01}Er_{0.0005}O_2S$ which is itself stronger than $Y_{1.988}Tb_{0.01}Er_{0.002}O_2S$.

It is worthy of note that the energy between $^5D_3\rightarrow{}^7F_5$ of Tb^{3+} and $^2H_{9/2}\rightarrow{}^4I_{15/2}$ of Er^{3+} cations is very close. It is very likely that energy transfer takes place between Tb^{3+} and Er^{3+} cations. An electron in the ground state of Er^{3+} could absorb an emission photon from $^5D_3\rightarrow{}^7F_5$ and pump itself to $^2H_{9/2}$ followed by a non-radiative relaxation to $^2H_{11/2}$ then emit a photon. Such a process would rob intensity from the Tb^{3+} green emission and at the same time by effectively cancelling some of the Tb^{3+} cations the remaining unaffected Tb^{3+} cation concentration is “effectively” reduced. Hence the blue emission is stronger than expected for the $Y_{2-y-x}Tb_yEr_xO_2S$ phosphors. Hence in the downconversion there is energy transfer between the Tb^{3+} and Er^{3+} cations.

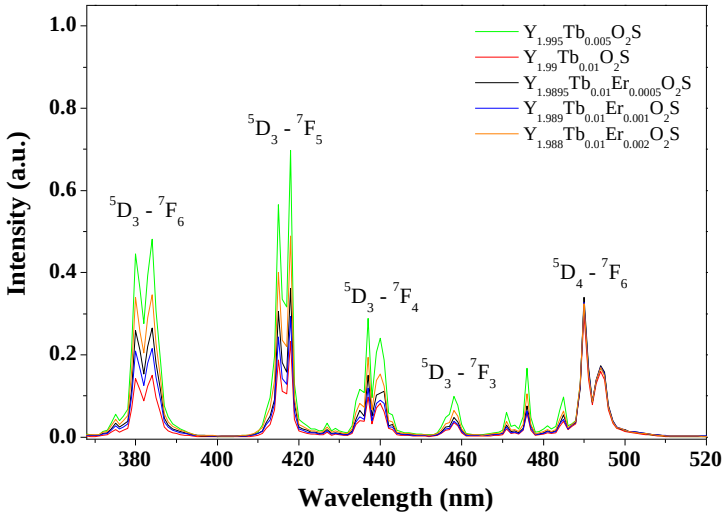

Figure 5.13 PL emission spectra of $Y_{2-y-x}Tb_yEr_xO_2S$ normalized to the green 545 nm.

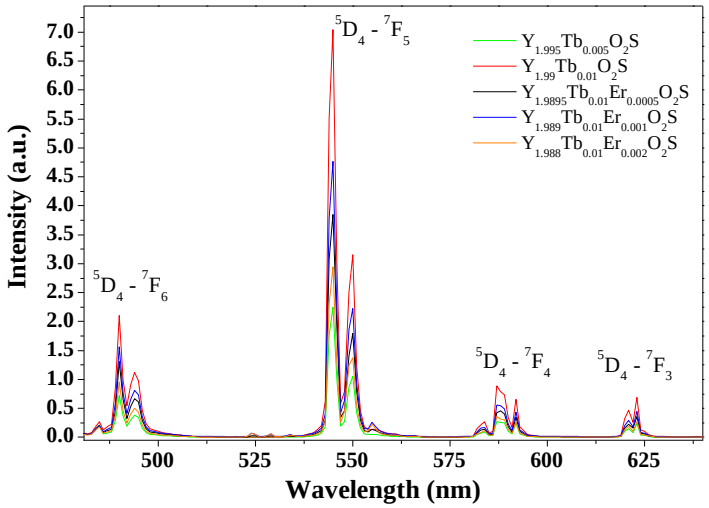

Figure 5.14 PL emission spectra of $Y_{2-y-x}Tb_yEr_xO_2S$ normalised to the UV 385 nm.

5.3.3 UC spectra for Tb^{3+} and Er^{3+} co-doped Gd_2O_2S phosphor

To further understand the effect of the host lattice on the UC properties, Tb^{3+} and Er^{3+} co-doped Gd_2O_2S phosphors were prepared and their UC properties were characterised and studied. UC emission bands and relative intensities are presented in Figure 5.15 and Figure 5.16. Assignments are listed in Table 5.4. UC spectra of the Tb^{3+} and Er^{3+} co-doped Gd_2O_2S phosphors are similar to those of Y_2O_2S except for the emission bands at 440 nm of $^2H_{5/2} \rightarrow {}^4I_{15/2}$ transitions. The emission band at 625 nm (16000 cm^{-1}) corresponds to the Raman shift of Gd_2O_2S at 194 cm^{-1} from the 632.8 nm (15803 cm^{-1}) laser line, which could also be observed at the other side of the excitation line (not shown in the UC spectra, see Figure 5.17). The UC emission intensities for the Tb^{3+} and Er^{3+} co-doped Gd_2O_2S of varying composition are compared to each other using the intensity of the 625 nm emission band as a standard.

Table 5.4 Assignments of anti-Stokes and Stokes emission bands of $Gd_{1.9895}Tb_{0.01}Er_{0.0005}O_2S$.

emission assignment	emission bands range		width of emission bands range
	nm	cm^{-1}	cm^{-1}
$^2H_{9/2}\rightarrow{}^4I_{15/2}$	~408 to 418	~24510 to 23923	587
$^2H_{5/2}\rightarrow{}^4I_{15/2}$	~432 to 443	~23148 to 22573	575
$^4F_{5/2}\rightarrow{}^4I_{15/2}$	~453 to 460	~22075 to 21739	336
$^4F_{7/2}\rightarrow{}^4I_{15/2}$	~470 to 478	~21276 to 20920	356
	~482 to 505	~20747 to 19801	946
$^2H_{11/2}\rightarrow{}^4I_{15/2}$	~520 to 535	~19230 to 18691	539
$^4S_{3/2}\rightarrow{}^4I_{15/2}$	~542 to 562	~18450 to 17793	657
	~614 to 617	~16287 to 16207	80
$^4F_{9/2}\rightarrow{}^4I_{15/2}$	~644 to 680	~15528 to 14706	822
$^4I_{9/2}\rightarrow{}^4I_{15/2}$	~800 to 832	~12500 to 12019	481
$^4I_{11/2}\rightarrow{}^4I_{15/2}$	~849 to 865	~11778 to 11561	218

The overlay of the anti-Stokes emission spectra of the Er^{3+} and Tb^{3+} co-doped Gd_2O_2S samples in the range between 520 nm and 560 nm is illustrated in Figure 5.18. For the $Gd_{2-x-y}Tb_yEr_xO_2S$ samples (where y=0.01, x=0.0005, 0.001, or 0.002), the emission intensities increase with Er^{3+} concentration while for the $Gd_{2-x-y}Tb_xEr_yO_2S$ samples (where y=0.01, x=0.0005, 0.001, or 0.002), the emission intensities decrease with increased Tb^{3+} concentration. Liu *et al* [168] reported that Tb^{3+} ions work as acceptors/emitters by accepting indirect excitation energy through an adjacent Gd^{3+} super lattice on the 980 nm near-infrared excitation. However in our experiment no Tb^{3+} emission could be observed in the UC emission spectra, which could exclude the possibility of the energy transfer process between Gd^{3+} and Tb^{3+} or between Er^{3+} and Tb^{3+}. So the presence of Tb^{3+} virtually increases the Er-Er inter-ionic distance and suppresses the energy transfer process between Er^{3+} ion pairs. So this could suppress the cross-relaxation effect of the Er^{3+} ions, yielding nearly linearly growth in UC emission intensity. It could also be regarded that it lowers the effective Er^{3+} concentration although the real concentration was kept the same.

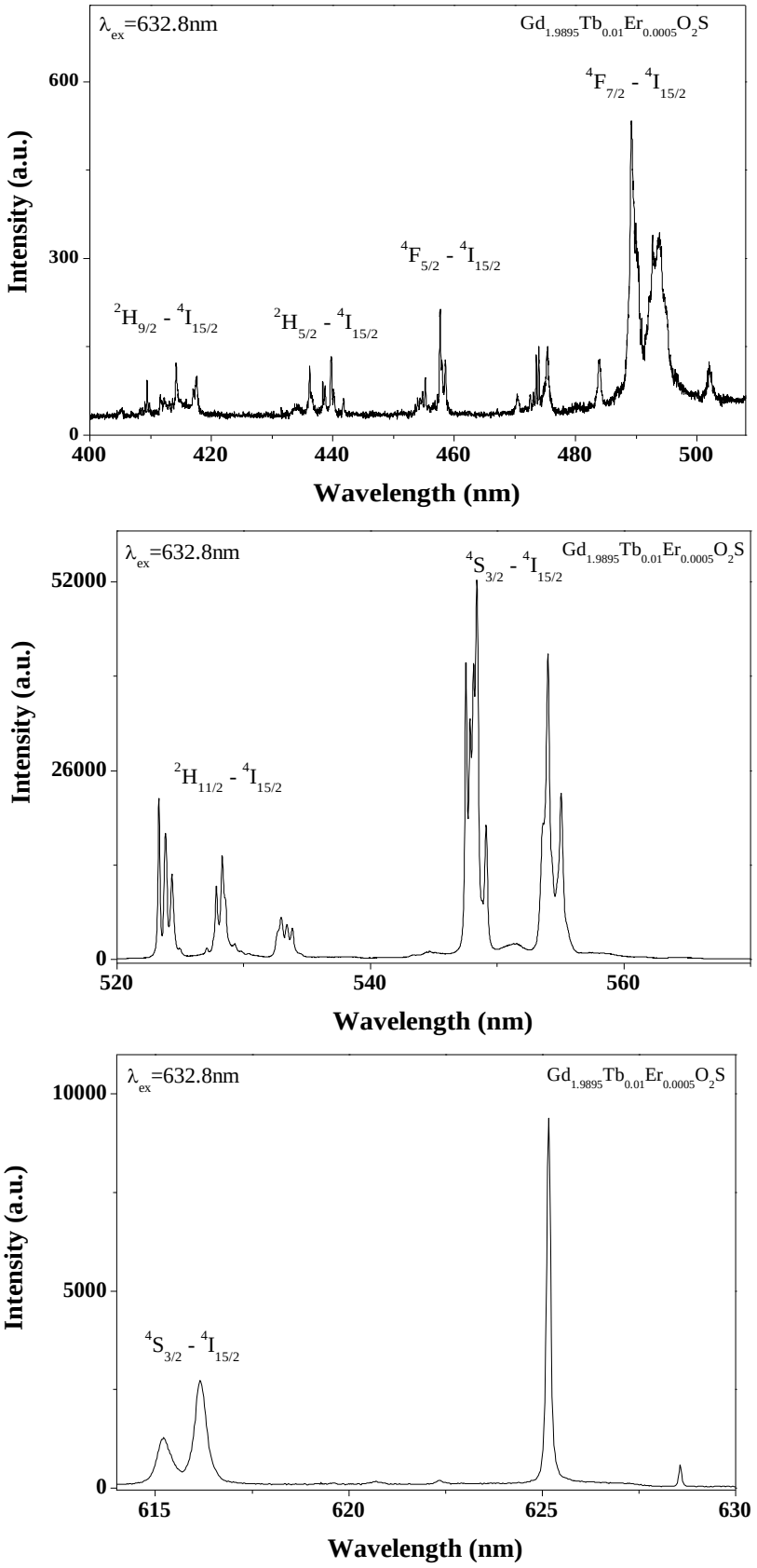

Figure 5.15 Anti-Stokes emission spectra of $Gd_{1.9895}Tb_{0.01}Er_{0.0005}O_2S$. Intensities are shown in arbitrary units and cannot be compared to each other.

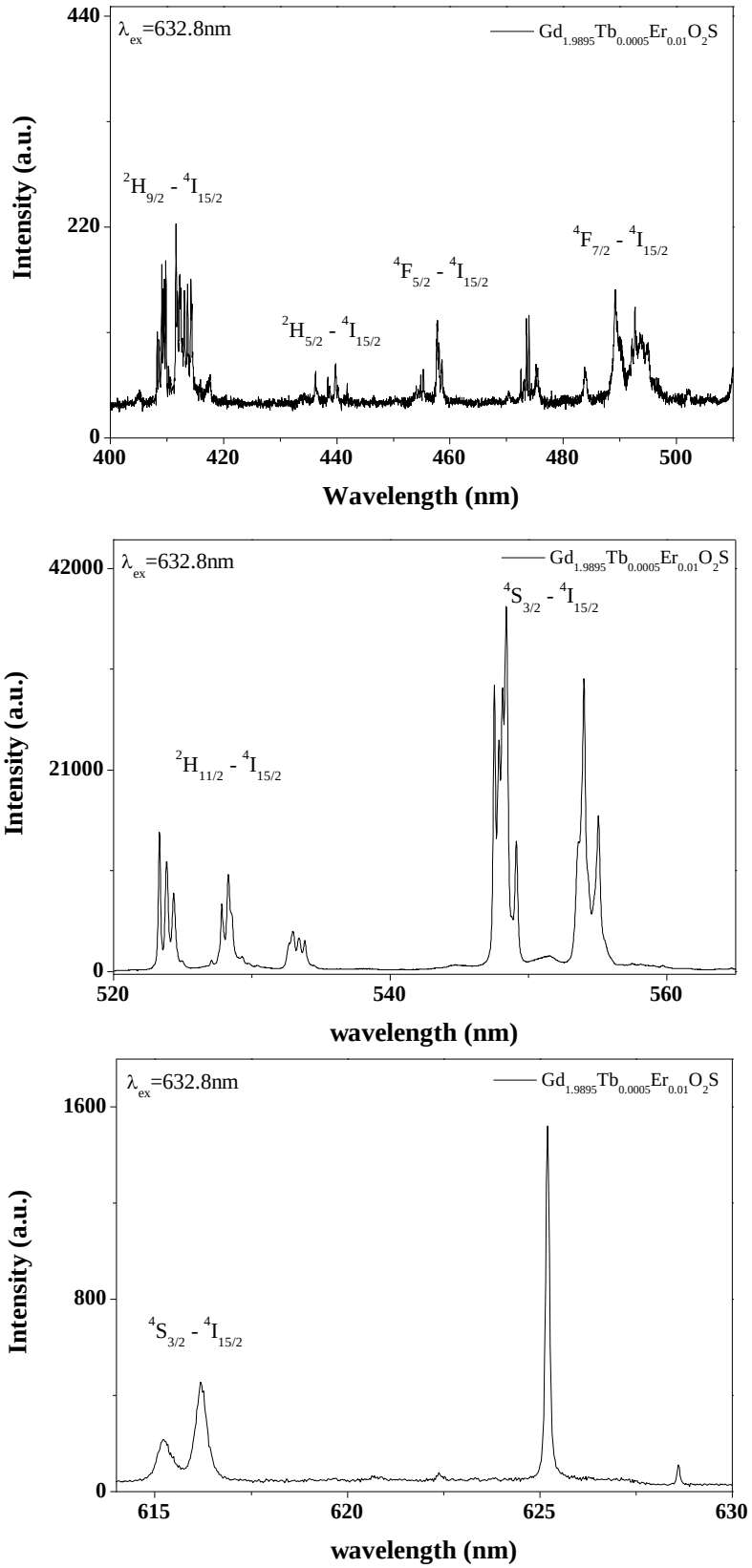

Figure 5.16 Anti-Stokes emission spectra of $Gd_{1.9895}Tb_{0.005}Er_{0.01}O_2S$. Intensities are shown in arbitrary units and cannot be compared to each other.

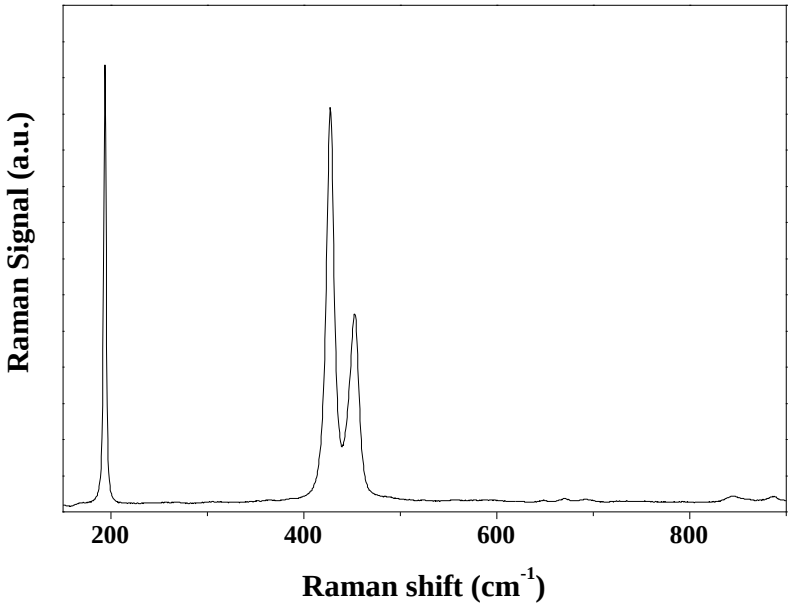

Figure 5.17 Raman spectrum of the Gd_2O_2S host crystals.

The overlaid UC emission bands of Er^{3+} and Tb^{3+} co-doped Y_2O_2S and Gd_2O_2S show different trends as the dopant concentration is varied. This must be caused by the host cations. In contrast to Y^{3+}, which is optically inactive, Gd^{3+} has energy states that lie close to the excited state of Er^{3+}. There is a possibility that energy transfer can happen between two adjacent Gd^{3+} and Er^{3+} cations in the UC process, which means in Er^{3+} and Tb^{3+} co-doped Gd_2O_2S, Er^{3+} can get certain energy compensation from the host crystals. Thus the UC emission intensities increase nearly linearly with Er^{3+} concentration.

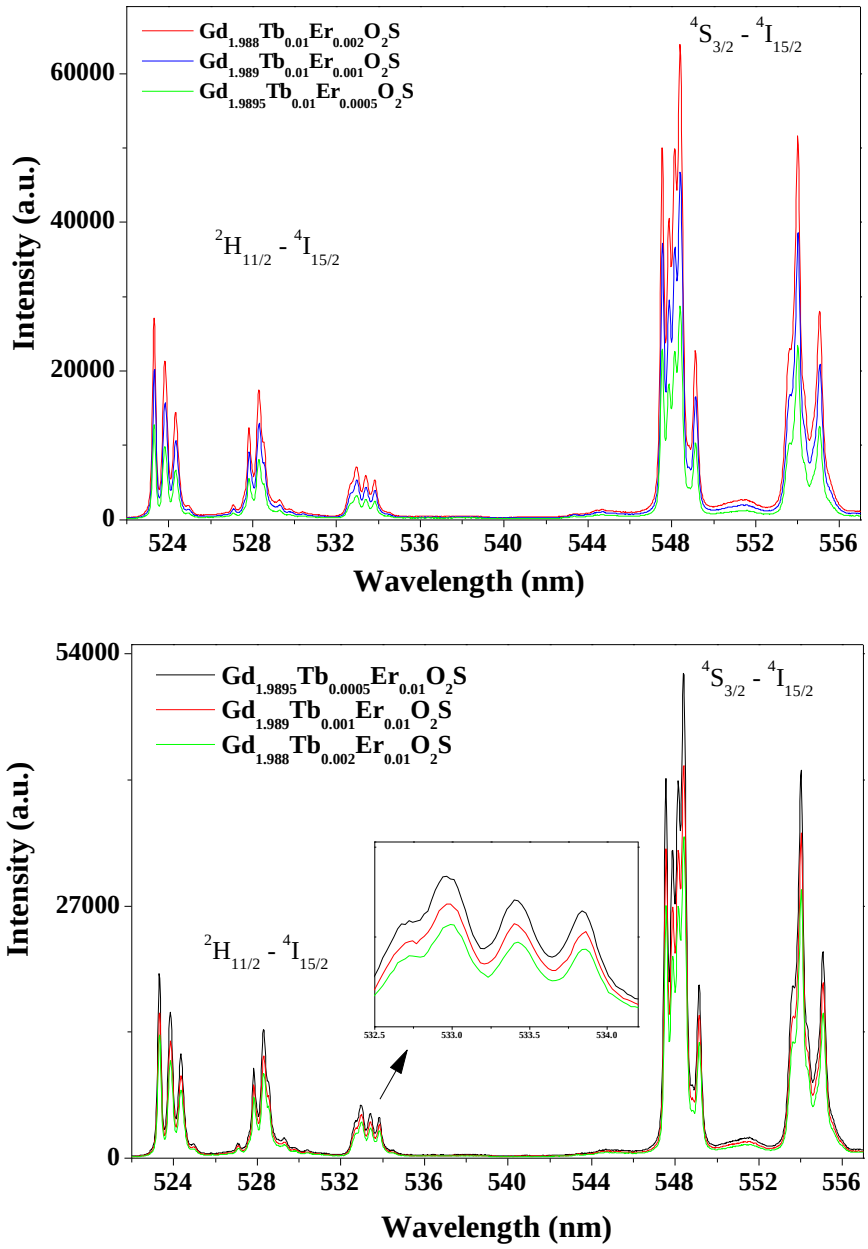

Figure 5.18 Overlay of anti-Stokes emission spectra of the Er^{3+} and Tb^{3+} co-doped Gd_2O_2S sample.

5.4 UC investigation of Eu^{3+} doped Y_2O_2S and Gd_2O_2S

SEM micrographs of Eu^{3+} doped Y_2O_2S and Gd_2O_2S fired at 900˚C are shown in Figure 5.19. All fired particles exhibited smooth surfaces and roughly spherical shapes. XRPD patterns showed good agreement with the literature reported hexagonal phases of Y_2O_2S and Gd_2O_2S, respectively.

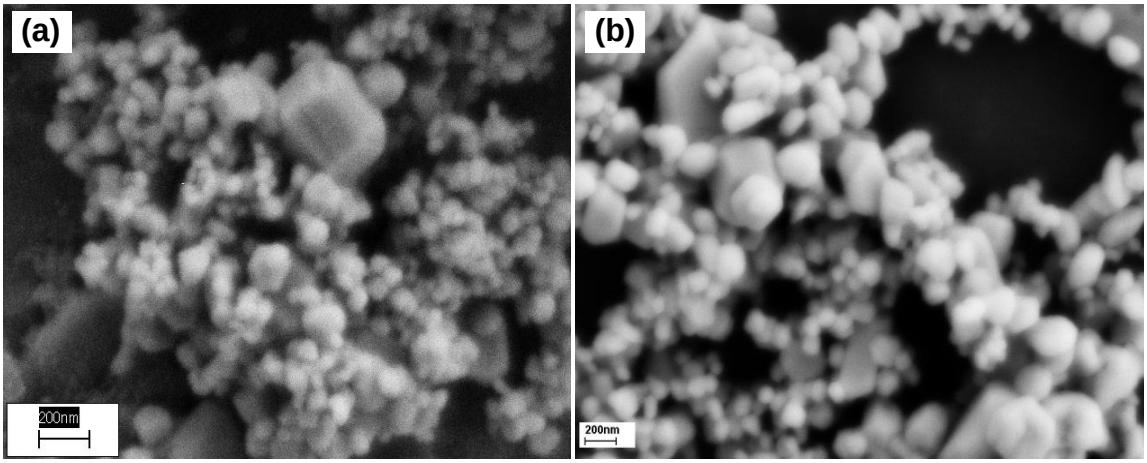

Figure 5.19 SEM images of (a) $Y_2O_2S:Eu^{3+}$ and (b) $Gd_2O_2S:Eu^{3+}$ fired at 900˚C.

Anti-Stokes and Stokes emission spectra of $Y_2O_2S:Eu^{3+}$ and $Gd_2O_2S:Eu^{3+}$ on the 632.8 nm excitation are shown in Figure 5.20. The assignments of the emission bands were made by comparing with the reported spectra in the literature [131]. It's worth noting that there is no energy gap between the ground state and excited states of Eu^{3+} that is similar to that of a 632.8 nm photon, which means Eu^{3+} ions can't be directly excited by the 632.8 nm laser. However, the ^7F energy state could be thermally populated at room temperature. The population of the thermally excited electrons can be calculated from the Bolzmann equation,

$$\frac{N_n}{N_m} = \frac{g_n}{g_m} \exp\left[-\frac{E_n - E_m}{kT}\right]$$

where, N is the number of electrons, g is the degeneracy of the energy levels, E_n-E_m is the energy gap between the two energy levels, k is the Boltzmann's constant, T is the temperature.

When the sum of the thermal energy and the energy of an incident 632.8 nm photon is equal to bridge the $^5D_0 \rightarrow {}^7F_0$ energy gap, excitation to the $^5D_0$ energy state could occur. This excitation process is responsible for the Stokes emission bands in the range of 640-900 nm. Also the excited Eu^{3+} could absorb another incident photon and be populated to higher energy states (ESA process), which is responsible for the anti-Stokes emission bands [131].

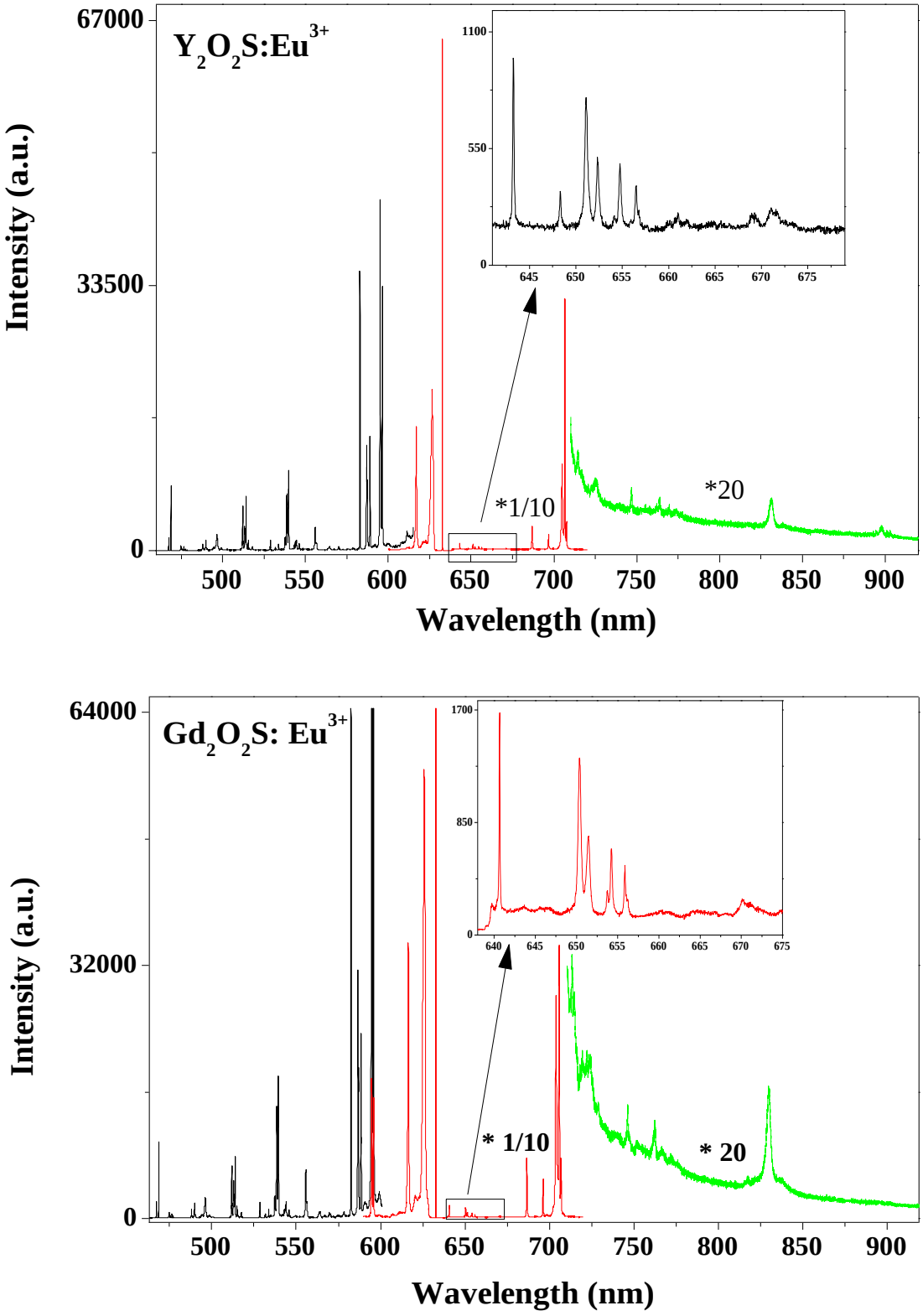

Figure 5.20 Anti-Stokes and Stokes emission spectra of $Y_2O_2S:Eu^{3+}$ and $Gd_2O_2S:Eu^{3+}$ under 632.8 nm red laser excitation.

5.5 Conclusions

The following conclusions can be made from the work reported in this chapter:

1. UC emissions from the Tb^{3+} and Er^{3+} co-doped Y_2O_2S and Gd_2O_2S nanometre-sized particles at varying doping concentration using 632.8 nm red laser as the excitation source were observed and studied.
2. UC emissions can be assigned to transitions of Er^{3+} cations, no UC emission from Tb^{3+} can be observed under the red laser excitation.
3. The intensities of UC emission were affected by both doping concentration and host lattices. For the $Y_{2-x-y}Tb_yEr_xO_2S$ and $Gd_{2-x-y}Tb_yEr_xO_2S$ samples (where y=0.01, x=0.0005, 0.001, or 0.002), the intensities of UC emissions increase with Er^{3+} concentration; for the $Y_{2-x-y}Tb_xEr_yO_2S$ sample, when x was increased from 0.0005 to 0.001, the intensity was greatly enhanced while when x was increased on from 0.001 to 0.002, the UC emission intensity decreases with increasing Tb^{3+} concentration. For the $Gd_{2-x-y}Tb_xEr_yO_2S$ sample, the intensity decreases with increasing Tb^{3+} concentration.
4. For the $Y_{2-x-y}Tb_yEr_xO_2S$ sample (where y=0.01, x=0.0005, 0.001, or 0.002), the presence of the Er^{3+} cations directly affects the Tb^{3+} down-converting properties by acting as centres for energy transfer.
5. UC emissions were observed for the $Y_2O_2S:Eu^{3+}$ and $Gd_2O_2S:Eu^{3+}$ phosphors under the 632.8 nm red laser excitation.

Chapter 6 Luminescence investigation of the novel ZnS:Mn based QDs for new applications

6.1 Introduction

Quantum dots (QDs) are nanoscale semiconductor particles with sizes less than ~10 nm, which exhibit unique optical properties arising from quantum confinement. When the particle size corresponds to the regime of quantum confinement, the energy gap increases compared to bulk materials and splits up to discrete states. In addition the thermodynamics of the QDs are usually heavily influenced by surface effects due to the large surface ratio to bulk size. For example, CdSe QDs exhibit size-dependent electronic band gap energies [277, 278] and CdS QDs reduces the melting temperature with decreasing particle size [189, 279]. Mn doped ZnS nanocrystals have been reported to show a size-induced solid-solid phase transition temperature reduction [190].

Although QDs could be prepared by a variety of physical and chemical process, such as molecular beam epitaxy (MBE) [280, 281] and metal-organic chemical vapor deposition (MOCVD) [281], the colloidal chemical synthesis has proved to be a more convenient approach to fabricate QDs; especially when considering the relatively low-cost and easy introduction of doping elements the method offers [194, 202, 282-284]. Mechanisms and factors contributing to particle size and morphology have been extensively studied, further details can be found in reference [191].

Their exclusive optical and electrical properties have led to QDs finding applications in a variety of fields including biological imaging and sensing [170, 285-287], solar cells [221, 240, 288-299], lighting devices and displays [11, 185, 226, 230, 231, 233, 235, 236, 239, 241, 244, 300-304]. Compared to other display technologies, QD-based displays have advantages such as fast response time, narrow emission bands, exquisite colour purities, high luminescence efficiency, low energy consumption, and relatively easy approach to scale-up products compared to organic light-emitting diodes (OLEDs).

Over the last five years, demand has grown for phosphor powders that can be used to achieve improved resolution and efficiency in converting blue LED light to other colors for backlighting applications in, for instance, LED backlit LCD displays. Recently, CdSe quantum dots have been used as the phosphors for such displays [235]. We anticipate similar demand in the future for conversion of UV LED light into visible wavelengths.

ZnS:Mn nanocrystals emit orange light and may soon find applications in lighting by converting UV LED light into the visible region of the electromagnetic spectrum. The orange emission from the $^4T_1$ — $^6A_1$ transition of Mn^{2+} has been extensively studied. Bhargava *et al* [194] reported the luminescence enhancement and life shortening of Mn^{2+} emissions from microsecond in bulk to nanosecond in ZnS:Mn nanocrystals. The high external quantum efficiency (~18%) was suggested to be a direct consequence of fast energy transfer of excited electron-hole pairs into the Mn^{2+} impurity and a subsequent efficient and fast radiative recombination, which resulted from the high-degree of hybridization of the s-p states of the ZnS host and the d states of the Mn^{2+} dopant [194].

As part of a program of research to incorporate phosphor materials into LEDs based on Photonic Crystals (PC) we prepared ZnS:Mn quantum dots (QDs). The PC was constructed by etching nanometer sized holes within the LED layers. The presence of the photonic crystal grown through the LED layers (buried photonic crystals) causes increased efficiency by enhancing light extraction. The aim of the work was to show that the quantum dots could be incorporated into the PC holes in the LED. The long term goal of the program is to use nanophosphors (NP)/quantum dots (QD) for colour conversion when they are incorporated into the PC holes in the LED. It has been reported that the structure facilitates non-radiative energy transfer of excitons if the NPQDs and the quantum wells (QWs) are in close proximity [238] resulting in an increase in NPQD emission. However it requires the NPQDs to be sub-surface in the holes of the buried photonic crystal [236]. It is envisaged that such structures could be used to produce white light very efficiently, but control of the filling of the holes is very important.

6.2 Crystallography analysis and morphological studies

Figure 6.1 shows TEM images of the ZnS:Mn QDs. It could be seen in the TEM images that the QD particles are aggregated when removed from solution with an average particle size of 20 nm (i.e. more than 200 times smaller in diameter than the commercially available material). Moreover, X-ray powder diffraction (XRPD) data (see Figure 6.2) indicate a mean crystal size of 3.3(1) nm for this material which is in good agreement with the values measured by TEM observation. In addition the calculated crystallites size data obtained from TOPAS software are slightly smaller than the 3.5 nm particles prepared using the same method previously reported by Dinsmore *et al* [213].

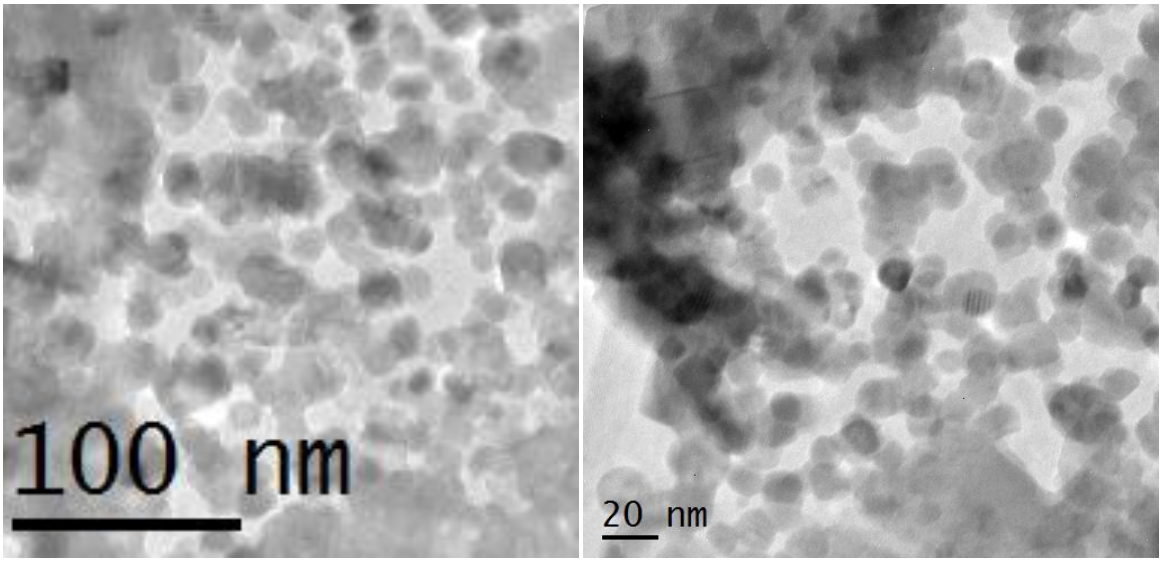

Figure 6.1 TEM images of ZnS:Mn QDs.

XRPD patterns obtained from the ZnS:Mn phosphor showed good agreement with the published zinc-blende ZnS structure, although the cell size is different in agreement with the previous study; it fits best to a tetragonally distorted cubic structure (a = 5.4208(82)Å, c = 5.326(25)Å). The cell size is also slightly larger than that of the slightly larger particles reported previously in reference [213].

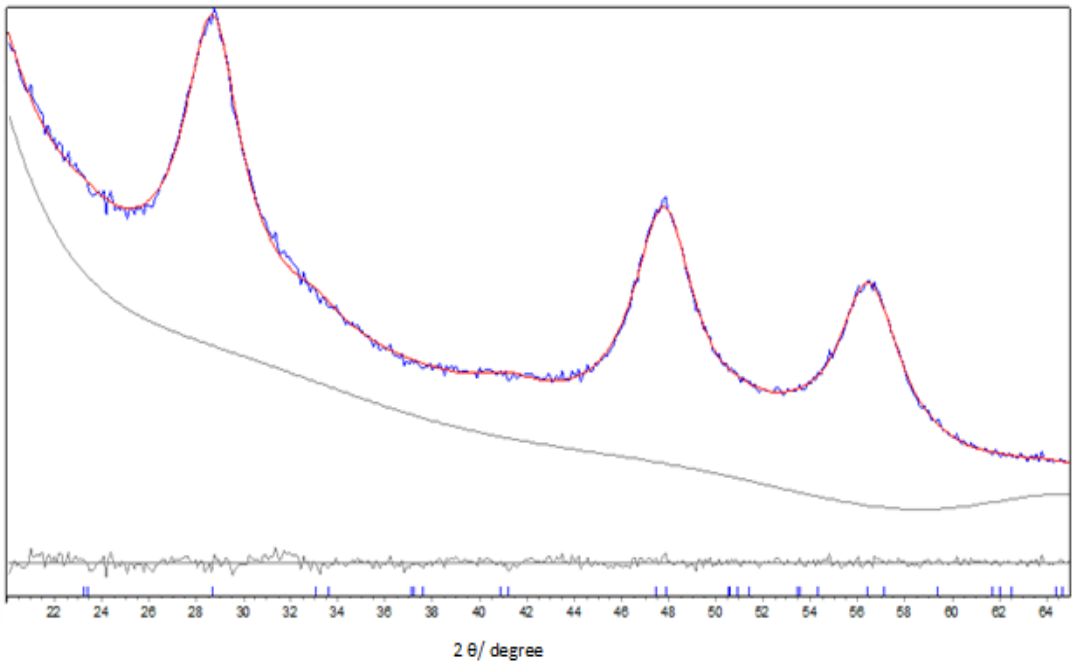

Figure 6.2 XRPD pattern of ZnS:Mn QDs. The red line indicates the fitting using TOPAS software.

6.3 Optical properties of ZnS:Mn QDs

The luminescent properties of ZnS:Mn QDs were measured using a Horiba Yobin Yvon Flurolog spectroflurometer. Figure 6.3 shows the photoluminescence excitation (PLE) and photoluminescence emission (PL) spectra of ZnS:Mn QDs. In the PLE spectrum the maximum is at 327 nm while in the PL spectrum the maximum at 587 nm, which is close to the bulk value of 590 nm from the $^4T_1$ — $^6A_1$ transition of Mn^{2+}. These findings are similar to those in the literature [213], indicating the particle size doesn't significantly affect the emission wavelength. The PLE spectrum of ZnS:Mn QDs is asymmetric [238], and is different from the symmetric one of the bulk material [213]. Small blue shifts were observed in both excitation and emission spectra due to quantum confinement effects.

This asymmetry is on the blue side and spans the wavelength range of those shown previously [213]. The greater asymmetry recorded in the present work may be due to the average crystallite size being a little smaller. The blue shift has been attributed to the quantum confinement effect which increases the

band gap energy [193, 194, 213, 305, 306]. It has been suggested that the blue shift may be associated with distortion of the ZnS lattice [213].

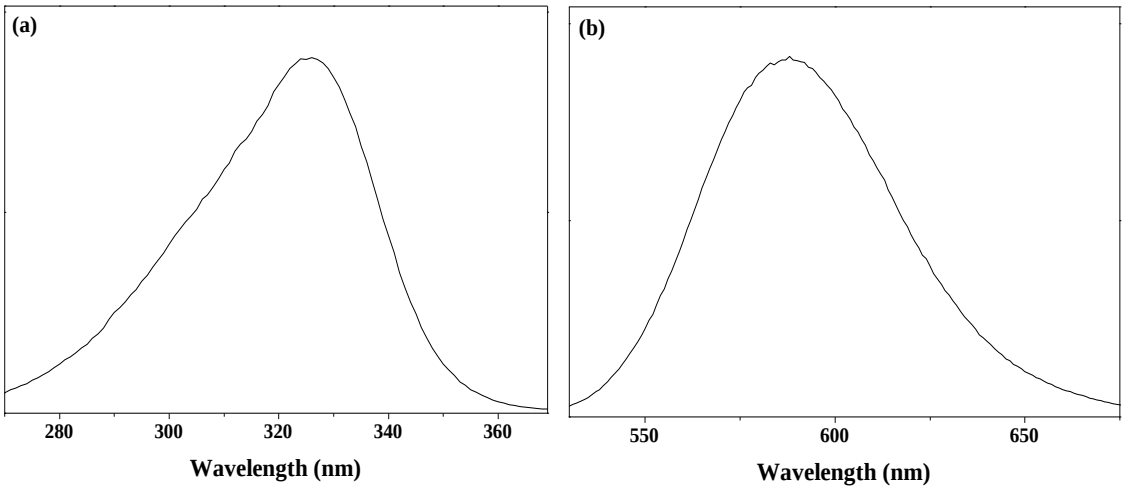

Figure 6.3 PLE (a) and PL (b) spectra of ZnS:Mn QDs.

The Raman spectra of ZnS:Mn QDs was characterised with a HORIBA JOBIN YVON LabRAM HR800 spectrometer using 632.8 nm red laser as exciting source. The Raman spectrum of the nanometre sized particles is presented in Figure 6.4. The Raman bands at 262 cm^{-1} and 345 cm^{-1} come close to bands reported at 271 and 352 cm^{-1} for bulk cubic ZnS, which were assigned to transverse optical (TO) and longitudinal optical (LO) Zn-S phonons of the cubic phase ZnS:Mn QDs, respectively [307]. Raman bands at 417 cm^{-1} and 658 cm^{-1} are assigned to the C-C-O bending and O-C=O bending vibration, respectively, indicating there are still residual surfactant AOT present in the samples after washing.

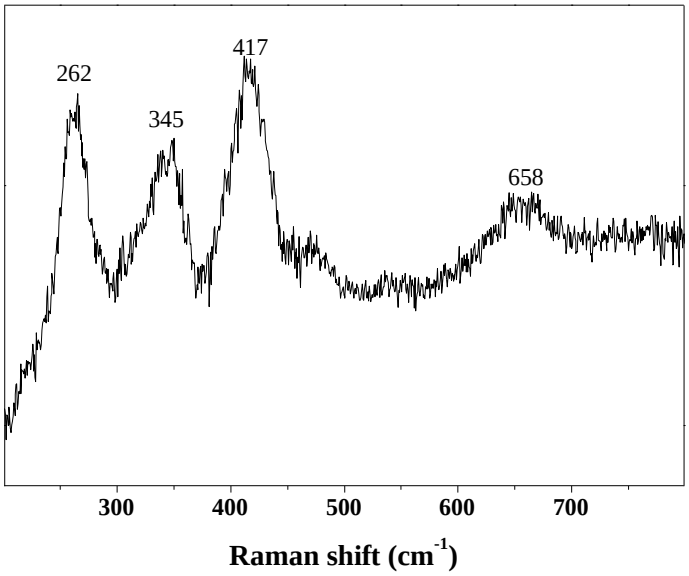

Figure 6.4 Raman shift of ZnS:Mn QDs.

6.4 Embedding ZnS:Mn QDs into GaN LED-based on PCs

The PCs used in this work were provided by our collaborators at University of Bath. The PCs were prepared by etching nanometre sized holes within the LED layers, which were grown on a sapphire substrate. Figure 6.5 shows TEM images of side views of the GaN based PC samples. Figure 6.5 (top) shows side views of nanometre sized PC columns grown into a GaN substrate and also presents a side view (Figure 6.5 bottom) of a buried PC in an LED crystal in the form of nanometre sized holes. The presence of the photonic crystal grown through the LED layers (buried photonic crystals) causes increased efficiency by enhancing light extraction. The aim of this work was to show that the quantum dots could be incorporated into the PC holes in the LED. It has been reported that the structure facilitates non-radiative energy transfer of excitons if the NPQDs and the quantum wells (QWs) are in close proximity [238] resulting in enhancement in NPQD emission. However, it requires the NPQDs to be sub-surface in the holes of the buried photonic crystal [236].

A typical section of such a PC crystal formed from holes in a GaN structure on a sapphire substrate is presented in Figure 6.6. The section exhibits a nano-imprinted photonic quasi-crystal (PQC) having a pore radius of ca. 200 nm and a depth of ca. 1.4 μm. The pores have irregular openings and roughened side-walls.

To smooth the side-walls it was necessary to etch with 1 M KOH at 80 °C for 10 minutes.

The ZnS: Mn QDs were introduced into the PC holes by drop casting. The holes in the GaN grown on a sapphire substrate and partially filled with ZnS: Mn nanometre sized particles are shown in Figure 6.7. The factors affecting the filling rate of the holes were also investigated.

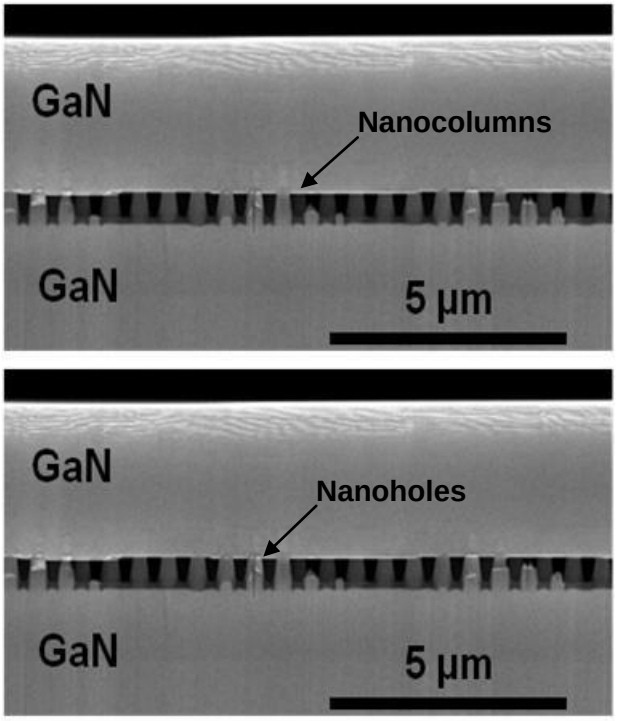

Figure 6.5 TEM images of nanometre sized column holes in GaN wafer (top) and nanometre sized holes of buried photonic crystals (bottom). Nanometre sized columns and holes were indicated with arrows.

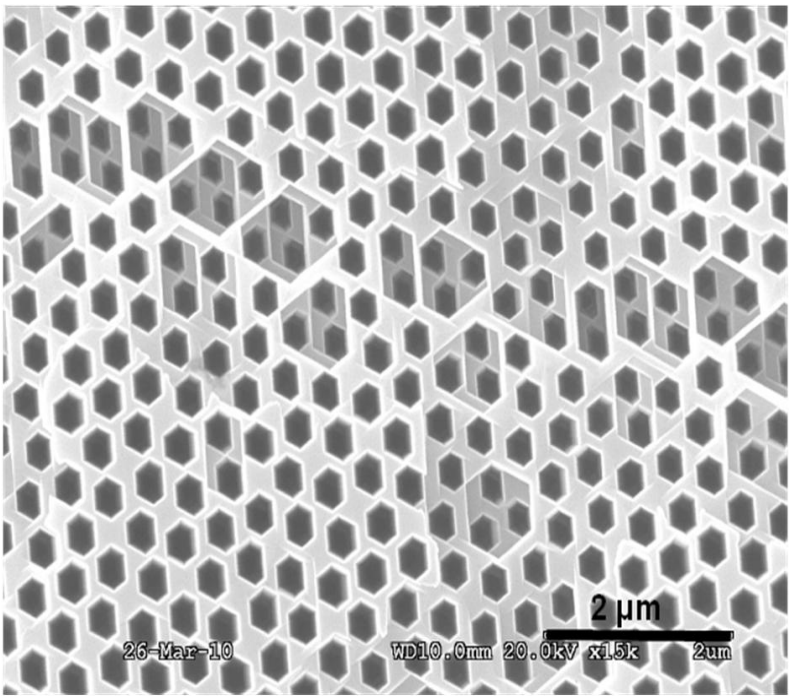

Figure 6.6 Typical PC structures made up of holes in GaN grown on a sapphire substrate.

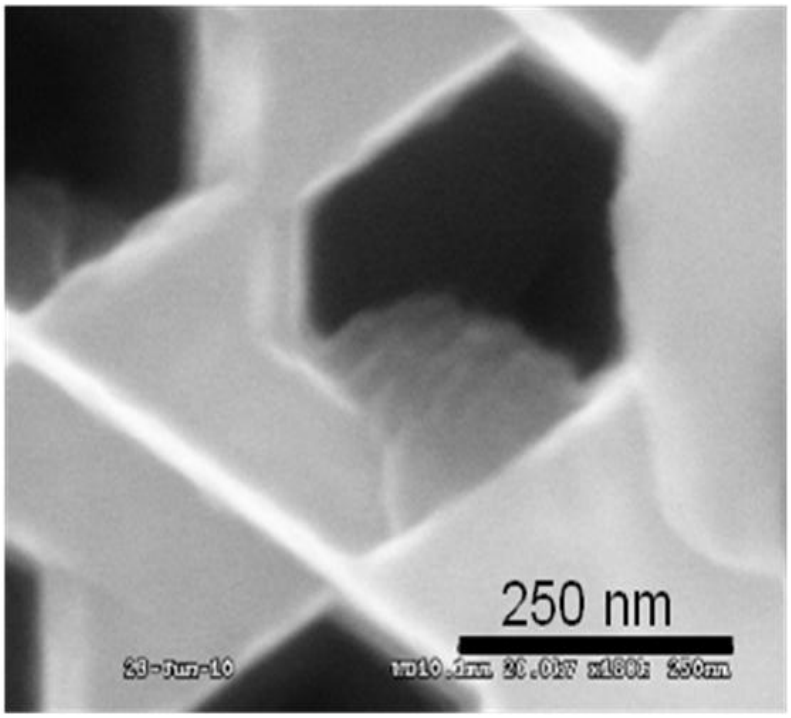

Figure 6.7 Holes in GaN grown on a sapphire substrate partially filled with ZnS:Mn QDs.

6.5 Luminescent properties of $Zn_{1-x}Cd_xS$:Mn QDs

$Zn_{1-x}Cd_xS$:Mn QDs were prepared using a similar method to that previously described by Dinsmore *et al* [213]. In this preparation method, the particles size is determined by the aqueous pore formed in the bicontinuous cubic phase (BCP), which is determined by the AOT/water/Na_2S ratio [249]. Thus it's reasonable to assume that the $Zn_{1-x}Cd_xS$:Mn QDs of different chemical composition possess approximately the same size in our experiments. This assumption was supported by the TEM observations. Typical TEM images of the $Zn_{1-x}Cd_xS$:Mn QDs are presented in Figure 6.8. The sizes of all the $Zn_{1-x}Cd_xS$:Mn QDs are similar to each other with a diameter of ~5 nm, smaller than the ZnS:Mn QDs prepared using a similar method [213].

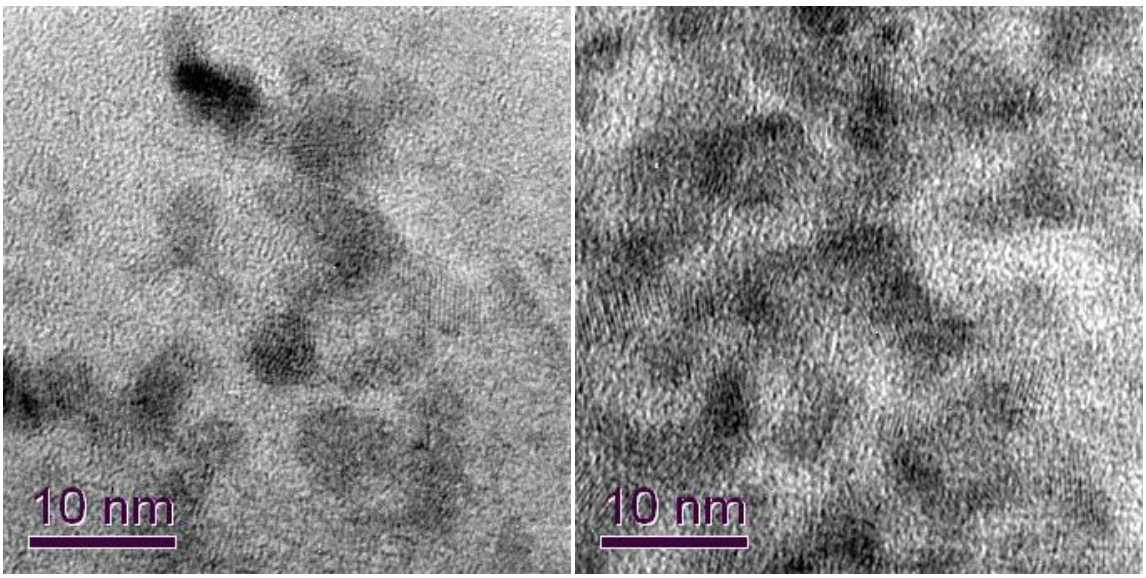

Figure 6.8 Typical TEM images of $Zn_{1-x}Cd_xS$:Mn QDs.

XRPD data for all the QDs samples were collected from 20 ˚ to 65 ˚ (2θ) for 6 h in the step scan mode since the diffracted intensities from such small nanocrystallites are generally weak. Figure 6.9 presents the XRPD patterns for all the $Zn_{1-x}Cd_xS$: Mn QDs samples. It is clear that the diffraction peaks of the QDs gradually shift to lower 2θ degrees as the Cd concentration increases the QDs. This observation is consistent with previous reports [308-310]. According to Bragg's law:

$$n\lambda = 2d \sin\theta,$$

where n is an integer determined by the order given, and λ is the wavelength, one can easily conclude that the d value increases with the Cd concentration in the QDs. This is reasonable as Cd^{2+} cations (109 pm) have a larger atomic radius than Zn^{2+} cations (88 pm). It has also been suggested that the phase transition from the zinc-blende (ZnS) structure to the wurtzite (CdS) structure has a contribution to this gradual shift [309, 310]. Furthermore, this continuous peak shifting of the QDs eliminates the possibility of phase separation or separated nucleation of CdS or ZnS nanocrystals in the $Zn_{1-x}Cd_xS$:Mn QDs.

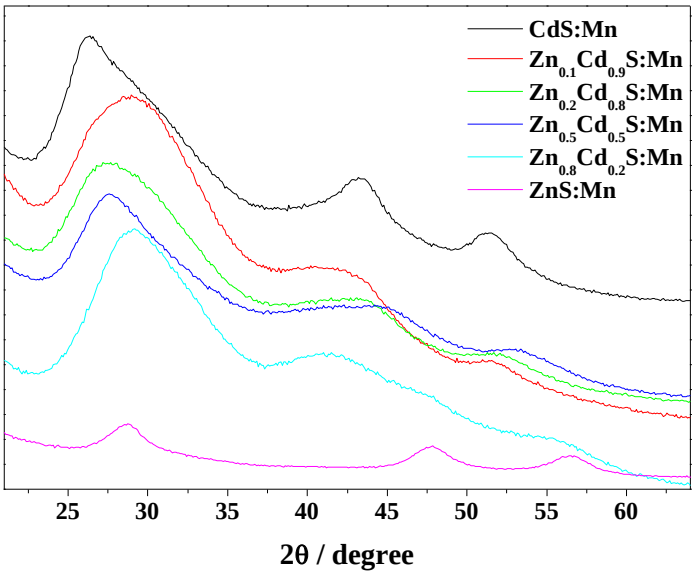

Figure 6.9 XRPD patterns of the $Zn_{1-x}Cd_xS$:Mn QDs.

The PLE and PL spectra of the $Zn_{1-x}Cd_xS$:Mn QDs with various Cd mole fractions are shown in Figure 6.10 and Figure 6.11. The intensities of the QDs are shown in arbitrary units and can't be compared to each other. For the ZnS:Mn QDs, the PLE spectra maximum value is at about 327 nm. For the $Zn_{1-x}Cd_xS$:Mn QDs, the PLE maximum value gradually shifts from about 345 nm to 410 nm as the Cd mole fraction increases from 0.2 to 0.8. When the Cd concentration increases on from 0.9 to 1, the PLE maximum value shows no change but the PLE spectra become more asymmetrical. The PL emission spectra of all the $Zn_{1-x}Cd_xS$:Mn QDs are more or less the same. All exhibit the characteristic broad orange emission from the $^4T_1$ - $^6A_1$ transition of Mn^{2+}.

To further understand how the addition of Cd cations affects the luminescent properties of the resulted QDs, the maxima for both PLE and PL spectra were plotted against the Cd mole ratio in the $Zn_{1-x}Cd_xS$:Mn compounds (see Figure 6.12). The PLE maximum shifts linearly towards lower energies as the Cd concentration is increased from 0 to 0.8 and then forms a plateau and even reversely shifts as the Cd concentration is increased up to 1. A similar trend can be observed for the PL spectra although the shift occurs in a relatively narrow range (roughly 10 nm), which is almost negligible compared to the full width at half maximum (around 65 nm).

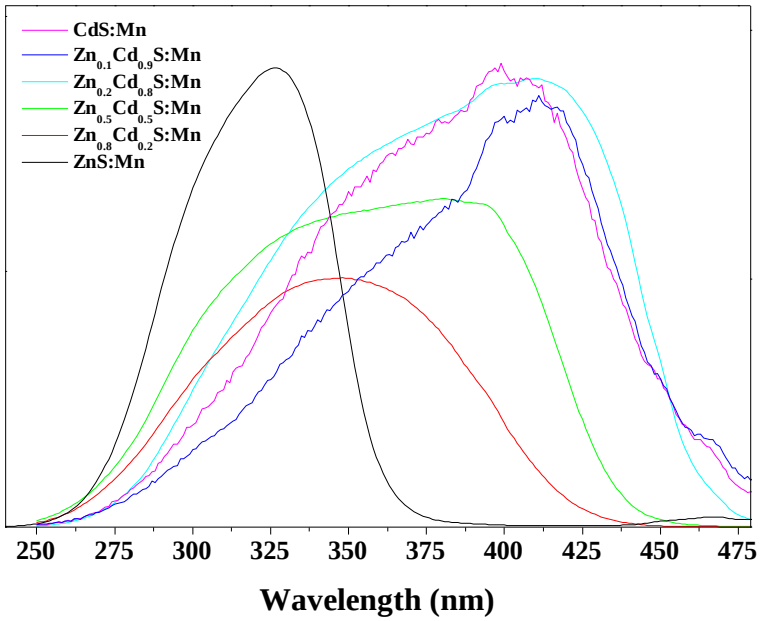

Figure 6.10 PLE spectra of the $Zn_{1-x}Cd_xS$:Mn QDs. The intensities are shown in arbitrary units and cannot be compared to each other.

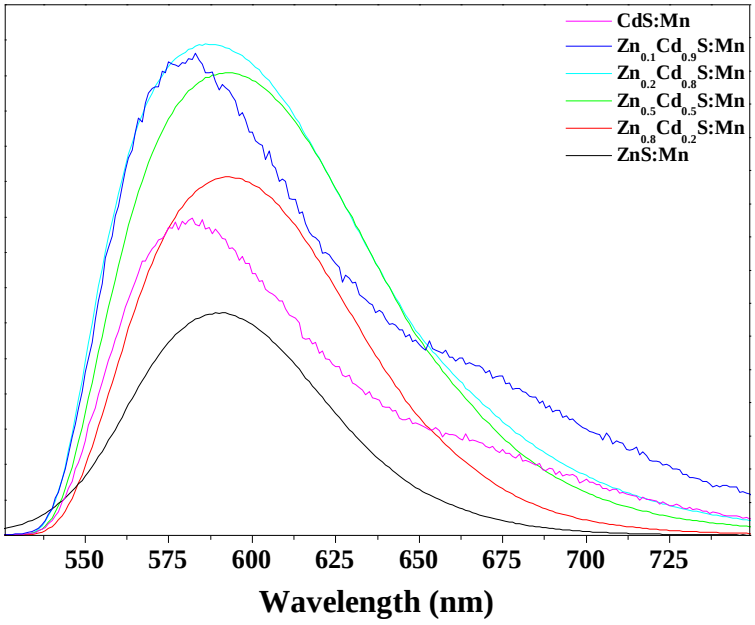

Figure 6.11 PL spectra of the $Zn_{1-x}Cd_xS$:Mn QDs. The intensities are shown in arbitrary units and cannot be compared to each other.

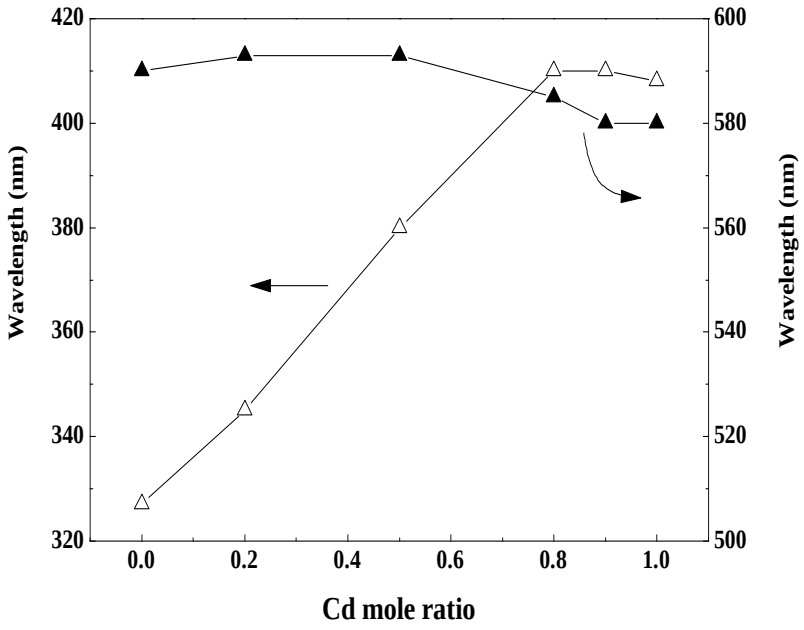

Figure 6.12 Plot of the λ maxima for PLE and PL spectra against the Cd concentration in the $Zn_{1-x}Cd_xS$:Mn QDs.

The red-shifts of the PLE peaks resulting from the addition of Cd in the $Zn_{1-x}Cd_xS$:Mn QDs yield a better overlap of the excitation spectra of these nanocrystals and the emission spectra of near-UV or blue LED. This property

makes the $Zn_{1-x}Cd_xS$:Mn QDs a promising candidate as light converter for near-UV or blue LED and might lead to a cheaper approach to white lighting [195, 239].

Raman spectroscopy was used to investigate the surface structures of the $Zn_{1-x}Cd_xS$:Mn QDs. An infrared laser of 1064 nm wavelength was applied as the excitation source to eliminate possible interference from luminescent emissions. Figure 6.13 shows the Raman spectra of the $Zn_{1-x}Cd_xS$:Mn QDs obtained at room temperature. The Raman bands at 262 cm^{-1} and 345 cm^{-1} were assigned to transverse optical (TO) and longitudinal optical (LO) Zn-S phonons of cubic phase ZnS:Mn QDs. These peaks gradually shift towards lower Raman shift values as the Cd concentration increases from 0 to 1. This must result from the phase transition from the zinc-blende structure of ZnS:Mn to the wurtzite structure of CdS:Mn as a direct consequence of the larger atomic radius of Cd^{2+} cations compared to the Zn^{2+} cations. Raman bands at 417 cm^{-1} and 658 cm^{-1} assigned to the C-C-O bending and O-C=O bending vibration could also be observed, indicating the presence of residual surfactant. It has been suggested that the polymerization of the surfactant could lead to a better surface passivation and enhance the luminescent efficiency of the ZnS:Mn nanocrystals [194]. We believe the residual surfactant here may affect the $Zn_{1-x}Cd_xS$:Mn QDs in a similar way.

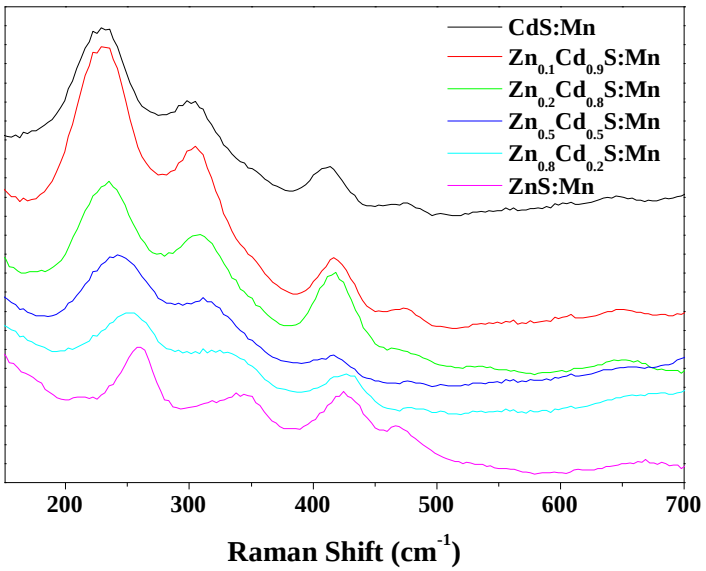

Figure 6.13 Raman spectra of the $Zn_{1-x}Cd_xS$:Mn QDs.

6.6 Results and discussions of the PbS QDs

Monodisperse PbS QDs were obtained using a similar method to that reported by Yang *et al* [249], as shown in the TEM images in Figure 6.14. The particle size from the TEM observation is ~5nm. Lattice fringes could be seen in the high-resolution TEM image, indicating good crystallinity. An amorphous layer can be seen in the high-resolution TEM image, indicating the presence of residual surfactant, and further evidence for this is found in the FT-IR spectrum. XRPD samples were prepared by evaporating the solvent of several droplets of the PbS suspension in methanol on a clean Si substrate. The XRPD data indicates that the PbS QDs exhibit the rock salt structure.

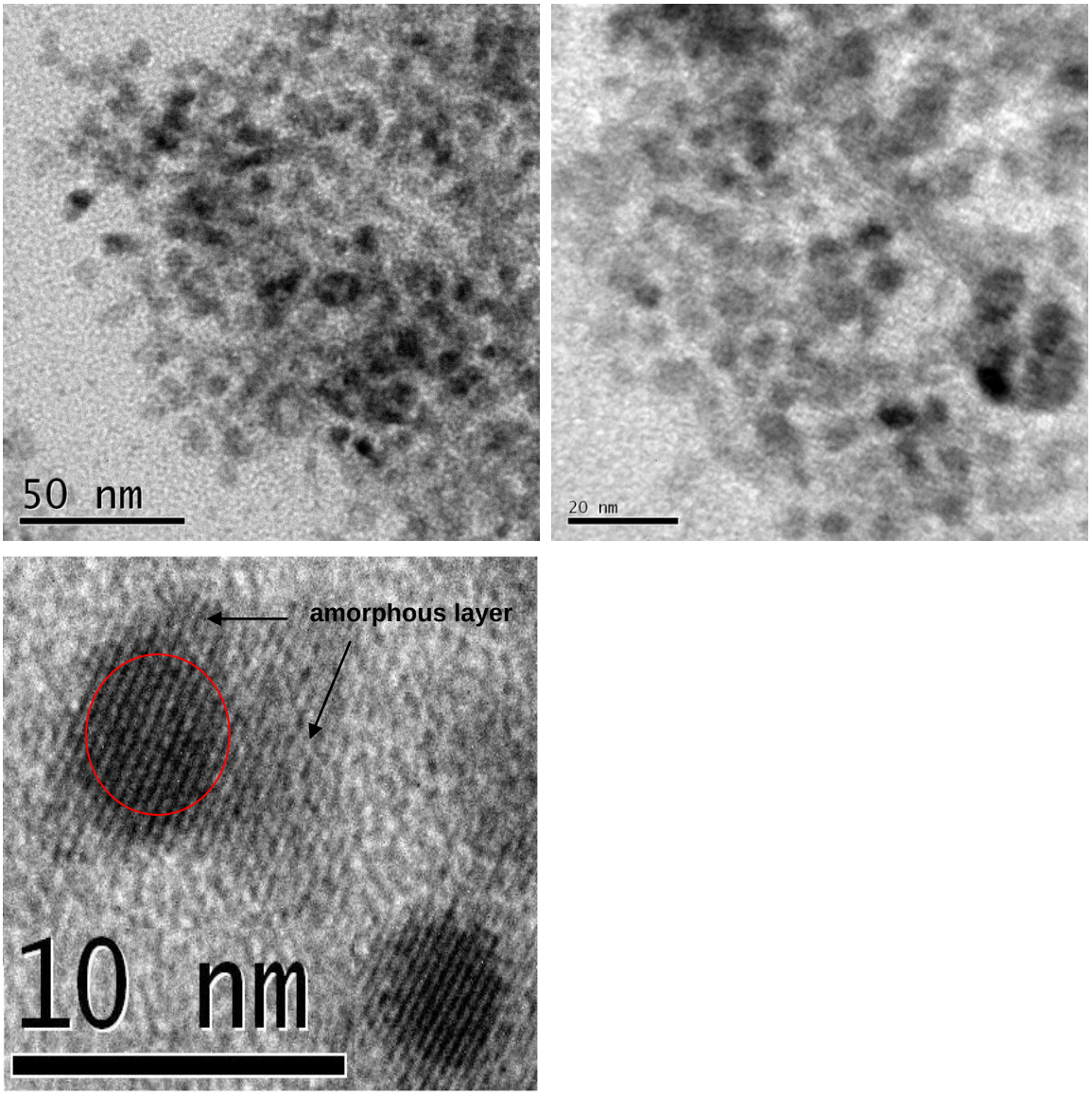

Figure 6.14 TEM images of the PbS QDs.

FTIR was used to investigate the structure of the PbS QDs. It's worth noting that the Pb-S bond is mainly a electrovalent bond so bands associated with Pb-S stretching and bending vibrations in the FTIR spectra of the samples containing PbS QDs are generally very weak [311]. Figure 6.15 shows the FTIR spectrum of the PbS QDs together with the FTIR spectrum of the residual methanol solvent. The broad peak at 3305 cm^{-1}, and the narrower ones at 1118 cm^{-1}, and 1017 cm^{-1} are attributed to the vibration of the –OH groups [311], C-O groups and $–CH_3$ groups [312], respectively. The asymmetric and symmetric stretching vibration of CH_2 at 2942 cm^{-1} and 2828 cm^{-1} are also observed [313]. The absorption peak at 1430 cm^{-1} is attributed to the deformation vibration of a CH_2- group [314]. All these peaks slightly shift towards higher frequencies in the presence of PbS QDs, which is consistent with the previous observation by Bakshi *et al* [315]. Two weak peaks at 861 cm^{-1} and 1189 cm^{-1} indicate the presence of PbS [313-315], which may arise from the interaction between Pb and $–SO_3^-$ group from the surfactant.

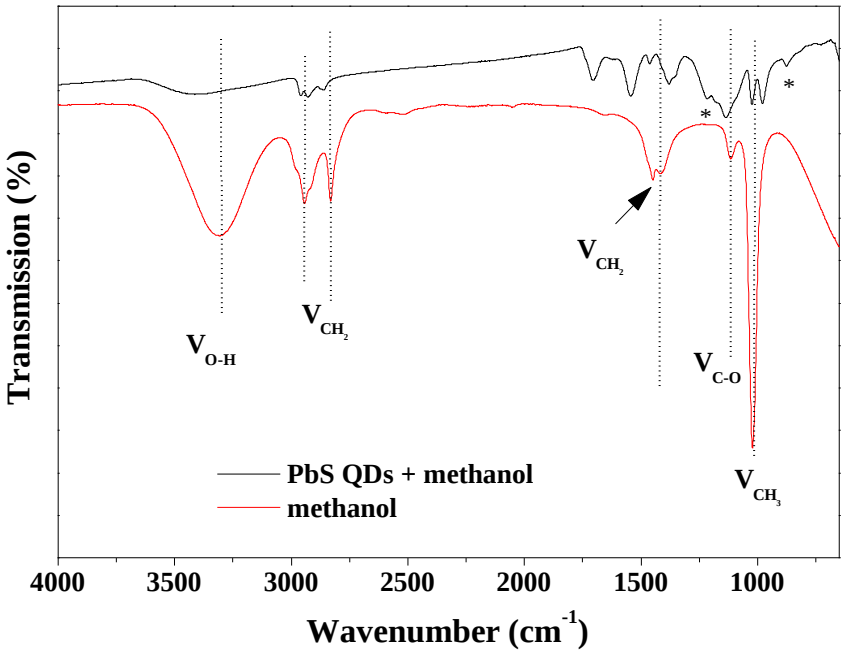

Figure 6.15 FTIR spectra of the PbS QDs and the methanol solvent. * indicates the presence of PbS QDs.

6.7 Conclusions

The main conclusions are:

1. The ZnS:Mn QDs were prepared and successfully incorporated into the holes of GaN LED based PCs. The cell size of the ZnS:Mn QDs was slightly larger and the particle size was about 6% smaller than previously published data.

2. The $Zn_{1-x}Cd_xS$:Mn QDs exhibit red shift in the PLE spectra with the addition of Cd cations. The crystal structures and surface properties were also affected. The red shifts in the PLE spectra expand the overlap between the excitation spectra and the emission spectra from blue LED, which is an advantage for white lighting applications.

3. Monodisperse PbS QDs with particles size of ~5 nm were obtained. The characteristic weak absorption peak from interaction between PbS QDs and the residual surfactant could be observed in the FTIR spectra. In our experiment no PL spectra of the PbS QDs can be observed, which may result from the strong trapping effect of the SO_3 group.

Chapter 7 Conclusions and suggestions for future work

7.1 Conclusions from downconversion studies

Trivalent rare earth cation (RE^{3+}) activated nanometre-sized oxysulfide phosphor particles were prepared by converting the precursor powders at high temperatures in a furnace. The precursor powders were prepared using urea precipitation method. Characteristic emission spectra of RE^{3+} (RE=Dy, Pr, Tb) cations were observed. Doping concentration for $Y_2O_2S:Dy^{3+}$ and $Y_2O_2S:Pr^{3+}$ were optimised at 1 mol% and 0.1 mol%. The results from $Y_2O_2S:Dy^{3+}$ studies have been interpreted to indicate that $Y_2O_2S:Dy^{3+}$ is a promising candidate for UV-based white lighting devices.

It has been found that the luminescent properties of Tb^{3+} are strongly affected by both doping concentration and host crystals. $^5D_3$-$^5D_4$ cross relaxation processes between two adjacent Tb^{3+} cation pairs were observed in both $Y_2O_2S:Tb^{3+}$ and $Gd_2O_2S:Tb^{3+}$. The intensity of the blue emissions from the $^5D_3 \rightarrow {}^7F_J$ (J= 6, 5, 4, 3) transitions decreases while the intensity of the green emissions from the $^5D_4 \rightarrow {}^7F_J$ transitions increases spontaneously with increased Tb^{3+} concentration, leading to a linear growth in both the x and the y colour coordinates. This indicates that the emission colour of Tb^{3+} is tuneable by varying the doping concentration.

The emission colour of $Y_2O_2S:Tb^{3+}$ and $Gd_2O_2S:Tb^{3+}$ at low doping concentration (0.1%) is determined by the relative position of the charge transfer state (CTS) of the host crystals. The bottom of the CTS in Gd_2O_2S lies close to the $^5D_3$ energy level of Tb^{3+}, and electrons in the $^5D_3$ energy level could non-radiatively relax to the $^5D_4$ energy level through thermal quenching, leading to a reduction of the electron population in the $^5D_3$ energy level. Thus the green emissions arising from the $^5D_4 \rightarrow {}^7F_J$ (J= 6, 5, 4, 3) transitions are predominant in the spectra for the 0.1% Tb^{3+} activated Gd_2O_2S phosphors.

The firing temperature can also influence the luminescent properties of the resulting phosphors. For the $Gd_2O_2S:Pr^{3+}$ and the $Gd_2O_2S:Tb^{3+}$ samples, the intensities of the emission bands from samples fired at 1100˚C are about twice as high as those of the emission bands from samples fired at 900˚C. This is achieved by reducing the number of crystal surface defects. The latter act as non-radiative recombination sites in the phosphors.

7.2 Conclusions from upconversion studies

UC emission spectra from the Tb^{3+} and Er^{3+} co-doped Y_2O_2S and Gd_2O_2S nanometre-sized particles at varying doping concentration using 632.8 nm red laser as the excitation source have been observed and studied. The UC emissions can be assigned to transitions of Er^{3+} cations, no UC emission from Tb^{3+} was observed under the red laser excitation.

The intensities of UC emission were affected by both doping concentration and host lattices. For the $Y_{2-x-y}Tb_yEr_xO_2S$ and $Gd_{2-x-y}Tb_yEr_xO_2S$ samples (where y=0.01, x=0.0005, 0.001, or 0.002), the intensities of UC emissions increase with Er^{3+} concentration; for the $Y_{2-x-y}Tb_xEr_yO_2S$ sample, when x was increased from 0.0005 to 0.001, the intensity was greatly enhanced while when x was increased on from 0.001 to 0.002, the UC emission intensity decreases with increasing Tb^{3+} concentration. For the $Gd_{2-x-y}Tb_xEr_yO_2S$ sample, the intensity decreases with increasing Tb^{3+} concentration.

In contrast to Y^{3+}, which is optically inactive, Gd^{3+} has energy states that lie close to the excited state of Er^{3+}. There is a possibility that energy transfer process can happen between two adjacent Gd^{3+} and Er^{3+} cations in the UC process, which means in Er^{3+} and Tb^{3+} co-doped Gd_2O_2S, Er^{3+} can benefit from energy compensation from the Gd^{3+} in the host crystals. Thus the UC emission intensities increase nearly linearly with Er^{3+} concentration.

For the $Y_{2-x-y}Tb_yEr_xO_2S$ sample (where y=0.01, x=0.0005, 0.001, or 0.002), the presence of the Er^{3+} cations directly affects the Tb^{3+} down-converting properties by acting as centres for energy transfer. Furthermore, these phosphors

exhibit both UC and down conversion luminescence and may find applications in security and anti-counterfeiting field for the high concealment.

7.3 Conclusions from quantum dots studies

ZnS:Mn QDs were prepared using an aqueous reaction method. The cell size of the ZnS:Mn QDs was slightly larger and the particle size was about 6% smaller than previously published data. Furthermore, the ZnS:Mn QDs were successfully incorporated into the nano-holes of GaN LED based photonic crystals by drop casting. Using this approach and the correct mixtures of QDs it should be possible to use RGB mixing for white light.

The aqueous reaction method was employed to prepare $Zn_{1-x}Cd_xS$:Mn QDs and monodisperse PbS QDs. The $Zn_{1-x}Cd_xS$:Mn QDs exhibit a red shift in the PLE spectra with the addition of Cd cations. The crystal structures and surface properties were also affected. The red shifts in the PLE spectra expand the overlap between the excitation spectra and the emission spectra from blue LED, which is an advantage for white lighting applications. The monodisperse PbS QDs have particles size of ~5 nm. A characteristic weak adsorption peak could be observed in the FTIR spectra.

7.4 Future work

White-light LEDs have been considered suitable light source for homes and offices due to their numerous advantages (such as high efficiency, small size, fast switching and long operating lifetime) over conventional incandescent light bubbles and fluorescent lamps. Impressive progress has been achieved in the last two decades in the terms of energy conversion efficiency and emission colour quality. However, it is still a challenge to produce warm white light with low colour temperature together with high colour rendering. Future work leading on from this thesis could be directed to the discovery of high-performance conversion phosphors for blue and near UV LEDs.

In this thesis, the ZnS:Mn and $Zn_{1-x}Cd_xS$:Mn QDs have been investigated for potential applications as conversion phosphors for white-light LEDs. The excitation spectra of the $Zn_{1-x}Cd_xS$:Mn QDs have shown good overlap with the

emission spectra of the blue LED, indicating the $Zn_{1-x}Cd_xS$:Mn QDs a promising candidate for these applications. However, cadmium is a well-known highly toxic component and any potential release is considerably harmful to the environment and mankind. Future work could be carried out on the discovery of non-toxic, cadmium-free nanocrystals, such as ZnSe and ZnO QDs.

References:

1. Morkoc, H., *et al*., *Large-band-gap SiC, III-V nitride, and II-VI ZnSe-based semiconductor device technologies.* Journal of Applied Physics, 1994. **76**(3): p. 1363-1398.
2. Huang, M.H., *et al*., *Room-temperature ultraviolet nanowire nanolasers.* Science, 2001. **292**(5523): p. 1897-1899.
3. Tang, Z.K., *et al*., *Room-temperature ultraviolet laser emission from self-assembled ZnO microcrystallite thin films.* Applied Physics Letters, 1998. **72**(25): p. 3270-3272.
4. Faist, J., *et al*., *Quantum cascade laser.* Science, 1994. **264**(5158): p. 553-556.
5. Stouwdam, J.W. and F. van Veggel, *Near-infrared emission of redispersible Er^{3+}, Nd^{3+}, and Ho^{3+} doped LaF_3 nanoparticles.* Nano Letters, 2002. **2**(7): p. 733-737.
6. Bailey, R.E. and S.M. Nie, *Alloyed semiconductor quantum dots: Tuning the optical properties without changing the particle size.* Journal of the American Chemical Society, 2003. **125**(23): p. 7100-7106.
7. Hines, M.A. and G.D. Scholes, *Colloidal PbS nanocrystals with size-tunable near-infrared emission: Observation of post-synthesis self-narrowing of the particle size distribution.* Advanced Materials, 2003. **15**(21): p. 1844-1849.
8. Barone, P.W., *et al*., *Near-infrared optical sensors based on single-walled carbon nanotubes.* Nature Materials, 2005. **4**(1): p. 86-92.
9. Hung, L.S. and C.H. Chen, *Recent progress of molecular organic electroluminescent materials and devices.* Materials Science and Engineering:R:Reports, 2002. **39**(5-6): p. 143-222.

10. Kelley, T.W., *et al*., *Recent progress in organic electronics: Materials, devices, and processes.* Chemistry of Materials, 2004. **16**(23): p. 4413-4422.
11. Burn, P.L., S.-C. Lo, and I.D.W. Samuel, *The development of light-emitting dendrimers for displays.* Advanced Materials, 2007. **19**(13): p. 1675-1688.
12. So, F., *et al*., *Recent progress in solution processable organic light emitting devices.* Journal of Applied Physics, 2007. **102**(9): p. 091101.
13. Blasse, G., *New luminescent materials.* Chemistry of Materials, 1989. **1**(3): p. 294-301.
14. Auffray, E., *et al*., *Test beam results of a cerium fluoride crystal matrix.* Nuclear Physics B - Proceedings Supplements, 1995. **44**(1–3): p. 57-62.
15. Verwey, J.W.M. and G. Blasse, *Luminescence efficiency of ions with broad-band excitation in lithium lanthanum phosphate glass.* Chemistry of Materials, 1990. **2**(4): p. 458-463.
16. Levine, A.K. and F.C. Palilla, *A new, highly efficient red-emitting cathodoluminescent phosphor (YVO_4:Eu) for color television.* Applied Physics Letters, 1964. **5**(6): p. 118-120.
17. Silver, J., *et al*., *A new oxide/oxysulfide based phosphor triad and high-efficiency green-emitting $(Y,Gd)_2O_2S$:Tb phosphor for FED applications.* SID Symposium Digest of Technical Papers, 2005. **36**(1): p. 594-597.
18. Ronda, C.R., T. Justel, and H. Nikol, *Rare earth phosphors: fundamentals and applications.* Journal of Alloys and Compounds, 1998. **275**: p. 669-676.
19. Xie, R.-J. and N. Hirosaki, *Silicon-based oxynitride and nitride phosphors for white LEDs-A review.* Science and Technology of Advanced Materials, 2007. **8**(7-8): p. 588-600.
20. Tick, P.A., *et al*., *Transparent glass ceramics for 1300 nm amplifier applications.* Journal of Applied Physics, 1995. **78**(11): p. 6367-6374.
21. Tanabe, S., *Optical transitions of rare earth ions for amplifiers: how the local structure works in glass.* Journal of Non-Crystalline Solids, 1999. **259**(1–3): p. 1-9.
22. Jiang, S., M. Myers, and N. Peyghambarian, *Er^{3+} doped phosphate glasses and lasers.* Journal of Non-Crystalline Solids, 1998. **239**(1–3): p. 143-148.

23. Joubert, M.F., *Photon avalanche upconversion in rare earth laser materials.* Optical Materials, 1999. **11**(2-3): p. 181-203.
24. Jayasimhadri, M., *et al*., *Optical properties of Dy^{3+} ions in alkali tellurofluorophosphate glasses for laser materials.* Journal of Physics D-Applied Physics, 2006. **39**(4): p. 635-641.
25. Ratinen, H., *X-ray-excited optical fluorescence of ten rare earth ions in Y_2O_2S, La_2O_2S, and Gd_2O_2S.* physica status solidi (a), 1972. **12**(2): p. 447-451.
26. Alves, R.V. and R.A. Buchanan, *Properties of Y_2O_2S:Tb X-ray intensifying screens.* IEEE Transactions on Nuclear Science, 1973. **20**(1): p. 415-419.
27. Issler, S.L. and C.C. Torardi, *Solid state chemistry and luminescence of X-ray phosphors.* Journal of Alloys and Compounds, 1995. **229**(1): p. 54-65.
28. Köstler, W., *et al*., *Effect of Pr-codoping on the X-ray induced afterglow of $(Y,Gd)_2O_3$:Eu.* Journal of Physics and Chemistry of Solids, 1995. **56**(7): p. 907-913.
29. Nakamura, R., *Improvements in the X-ray characteristics of Gd_2O_2S:Pr ceramic scintillators.* Journal of the American Ceramic Society, 1999. **82**(9): p. 2407-2410.
30. Tanaka, K., *Cathode luminescence of samarium, europium, and gadolinium ion doped scintillator $CdWO_4$ single crystals studied with x-ray photoelectron spectroscopy.* Journal of Applied Physics, 2001. **89**(10): p. 5449-5453.
31. Kalivas, N., *et al*., *Modeling quantum and structure noise of phosphors used in medical X-ray imaging detectors.* Nuclear Instruments and Methods in Physics Research Section a-Accelerators Spectrometers Detectors and Associated Equipment, 2002. **490**(3): p. 614-629.
32. Tian, Y., *et al*., *Preparation and luminescence property of Gd_2O_2S:Tb X-ray nano-phosphors using the complex precipitation method.* Journal of Alloys and Compounds, 2007. **433**(1-2): p. 313-317.
33. Fern, G., *et al*., *Characterisation of Gd_2O_2S:Pr phosphor screens for water window X-ray detection.* Nuclear Instruments and Methods in Physics Research Section a-Accelerators Spectrometers Detectors and Associated Equipment, 2009. **600**(2): p. 434-439.

34. Jung, I.D., *et al*., *Flexible Gd_2O_2S:Tb scintillators pixelated with polyethylene microstructures for digital x-ray image sensors.* Journal of Micromechanics and Microengineering, 2009. **19**(1): p. 015014.
35. Zhang, J., *et al*., *Color tunable phosphorescence in KY_3F_{10}:Tb^{3+} for x-ray or cathode-ray tubes.* Journal of Applied Physics, 2009. **106**(3): p. 034915-6.
36. Blasse, G., *Scintillator Materials.* Chemistry of Materials, 1994. **6**(9): p. 1465-1475.
37. Greskovich, C. and S. Duclos, *Ceramic scintillators.* Annual Review of Materials Science, 1997. **27**: p. 69-88.
38. van Eijk, C.W.E., *Inorganic scintillators in medical imaging.* Physics in Medicine and Biology, 2002. **47**(8): p. R85-R106.
39. Srivastava, A.M., *Inter- and intraconfigurational optical transitions of the Pr^{3+} ion for application in lighting and scintillator technologies.* Journal of Luminescence, 2009. **129**(12): p. 1419-1421.
40. Justel, T., H. Nikol, and C. Ronda, *New developments in the field of luminescent materials for lighting and displays.* Angewandte Chemie-International Edition, 1998. **37**(22): p. 3085-3103.
41. Bunzli, J.C.G. and C. Piguet, *Taking advantage of luminescent lanthanide ions.* Chemical Society Reviews, 2005. **34**(12): p. 1048-1077.
42. Ekambaram, S., K.C. Patil, and M. Maaza, *Synthesis of lamp phosphors: facile combustion approach.* Journal of Alloys and Compounds, 2005. **393**(1-2): p. 81-92.
43. Eliseeva, S.V. and J.-C.G. Buenzli, *Lanthanide luminescence for functional materials and bio-sciences.* Chemical Society Reviews, 2010. **39**(1): p. 189-227.
44. Shionoya, S., W.M. Yen, and H. Yamamoto, eds. *Phosphor Handbook. Second Edition*. 2006, CRC press: Boca Rotan.
45. Shalav, A., B.S. Richards, and M.A. Green, *Luminescent layers for enhanced silicon solar cell performance: Up-conversion.* Solar Energy Materials and Solar Cells, 2007. **91**(9): p. 829-842.
46. Richards, B.S., *Luminescent layers for enhanced silicon solar cell performance: Down-conversion.* Solar Energy Materials and Solar Cells, 2006. **90**(9): p. 1189-1207.

47. Shalav, A., *et al*., *Application of $NaYF_4:Er^{3+}$ up-converting phosphors for enhanced near-infrared silicon solar cell response.* Applied Physics Letters, 2005. **86**(1): p. 013505.
48. Trupke, T., M.A. Green, and P. Wurfel, *Improving solar cell efficiencies by up-conversion of sub-band-gap light.* Journal of Applied Physics, 2002. **92**(7): p. 4117-4122.
49. Wei, T.-C., *et al*. *Research on angle-selective filters of phosphor color wheel for LED projectors*. 2010. San Diego, California, USA: SPIE.
50. Bachmann, V., *et al*., *Color point tuning for $(Sr,Ca,Ba)Si_2O_2N_2:Eu^{2+}$ for white light LEDs.* Chemistry of Materials, 2009. **21**(2): p. 316-325.
51. Jung, K.Y., H.W. Lee, and H.K. Jung, *Luminescent properties of $(Sr, Zn)Al_2O_4:Eu^{2+},B^{3+}$ particles as a potential green phosphor for UV LEDs.* Chemistry of Materials, 2006. **18**(9): p. 2249-2255.
52. Hoeppe, H.A., *Recent developments in the field of inorganic phosphors.* Angewandte Chemie-International Edition, 2009. **48**(20): p. 3572-3582.
53. Valeur, B. and M.r.N. Berberan-Santos, *A brief history of fluorescence and phosphorescence before the emergence of quantum theory.* Journal of Chemical Education, 2011. **88**(6): p. 731-738.
54. Baylor, D., *Colour Mechanisms of the Eye*, in *Colour: Art & Science*, T. Lamb and J. Bourriau, Editors. 1995, Cambridge University Press: Cambridge.
55. Sommerdijk, J.L., A. Bril, and A.W. de Jager, *Luminescence of Pr^{3+}-activated fluorides.* Journal of Luminescence, 1974. **9**(4): p. 288-296.
56. Sommerdijk, J.L., A. Bril, and A.W. de Jager, *Two photon luminescence with ultraviolet excitation of trivalent praseodymium.* Journal of Luminescence, 1974. **8**(4): p. 341-343.
57. Piper, W.W., J.A. DeLuca, and F.S. Ham, *Cascade fluorescent decay in Pr^{3+}-doped fluorides: Achievement of a quantum yield greater than unity for emission of visible light.* Journal of Luminescence, 1974. **8**(4): p. 344-348.
58. Srivastava, A.M. and W.W. Beers, *Luminescence of Pr^{3+} in $SrAl_{12}O_{19}$: Observation of two photon luminescence in oxide lattice.* Journal of Luminescence, 1997. **71**(4): p. 285-290.

59. Srivastava, A.M., D.A. Doughty, and W.W. Beers, *Photon cascade luminescence of Pr^{3+} in $LaMgB_5O_{10}$.* Journal of The Electrochemical Society, 1996. **143**(12): p. 4113-4116.
60. van der Kolk, E., *et al*., *Vacuum ultraviolet excitation and emission properties of Pr^{3+} and Ce^{3+} in MSO_4 (M=Ba, Sr, and Ca) and predicting quantum splitting by Pr^{3+} in oxides and fluorides.* Physical Review B, 2001. **64**(19): p. 195129.
61. Zhang, Q.Y. and X.Y. Huang, *Recent progress in quantum cutting phosphors.* Progress in Materials Science, 2010. **55**(5): p. 353-427.
62. Feldmann, C., *et al*., *Quantum efficiency of down-conversion phosphor $LiGdF_4$:Eu.* Journal of Luminescence, 2001. **92**(3): p. 245-254.
63. Oskam, K.D., *et al*., *Downconversion: a new route to visible quantum cutting.* Journal of Alloys and Compounds, 2000. **300–301**: p. 421-425.
64. Wegh, R.T., *et al*., *Visible quantum cutting in $LiGdF_4$:Eu^{3+} through downconversion.* Science, 1999. **283**(5402): p. 663-666.
65. Liu, B., *et al*., *Visible quantum cutting in BaF_2:Gd,Eu via downconversion.* Journal of Luminescence, 2003. **101**(1–2): p. 155-159.
66. Broadbent, A.D., *A critical review of the development of the CIE1931 RGB color-matching functions.* Color Research and Application, 2004. **29**(4): p. 267-272.
67. Borbély, Á., Á. Sámson, and J. Schanda, *The concept of correlated colour temperature revisited.* Color Research and Application, 2001. **26**(6): p. 450-457.
68. Blasse, G. and B.C. Grabmaier, *Luminescent Materials*. 1994, Berlin: Springer-Verlag.
69. Ozawa, L. and P.M. Jaffe, *Luminescence of Pr^{+3} activated Y_2O_2S.* Journal of The Electrochemical Society, 1970. **117**(10): p. 1297-1301.
70. Dieke, G.H. and H.M. Crosswhite, *The spectra of the doubly and triply Ionized rare earths.* Applied Optics, 1963. **2**(7): p. 675-686.
71. Carnall, W.T., *et al*., *A systematic analysis of the spectra of the lanthanides doped into single crystal LaF_3.* Journal of Chemical Physics, 1989. **90**(7): p. 3443-3457.

72. Struck, C.W. and W.H. Fonger, *Thermal quenching of Tb^{+3}, Tm^{+3}, Pr^{+3}, and Dy^{+3} $4f^n$ emitting states in La_2O_2S.* Journal of Applied Physics, 1971. **42**(11): p. 4515-4516.
73. Diallo, P.T., *et al*., *Red luminescence in Pr^{3+}-doped calcium titanates.* Physica Status Solidi a-Applied Research, 1997. **160**(1): p. 255-263.
74. Boutinaud, P., *et al*., *UV-to-red relaxation pathways in $CaTiO_3:Pr^{3+}$.* Journal of Luminescence, 2005. **111**(1-2): p. 69-80.
75. Haynes, J.W. and J.J.J. Brown, *Preparation and Luminescence of selected Eu^{3+}-activated rare earth-oxygen-sulfur compounds.* Journal of The Electrochemical Society, 1968. **115**(10): p. 1060-1066.
76. Sovers, O.J. and T. Yoshioka, *Fluorescence of trivalent-europium-doped yttrium oxysulfide.* The Journal of Chemical Physics, 1968. **49**(11): p. 4945-4954.
77. Sovers, O.J. and T. Yoshioka, *Host cation effects on the fluorescence spectrum of Eu^{3+} in oxysulfides.* The Journal of Chemical Physics, 1969. **51**(12): p. 5330-5336.
78. Webster, G. and H.G. Drickamer, *High-pressure studies of luminescence efficiency and lifetime in $La_2O_2S:Eu$ and $Y_2O_2S:Eu$.* Journal of Chemical Physics, 1980. **72**(6): p. 3740-3747.
79. da Vila, L.D., E.B. Stucchi, and M.R. Davolos, *Preparation and characterization of uniform, spherical particles of Y_2O_2S and $Y_2O_2S:Eu$.* Journal of Materials Chemistry, 1997. **7**(10): p. 2113-2116.
80. Lo, C.L., J.G. Duh, and B.S. Chiou, *Low-voltage cathodoluminescence properties of the $Y_2O_2S:Eu$ red light emitting phosphor screen in field-emission environments.* Journal of The Electrochemical Society, 2002. **149**(7): p. H129-H133.
81. Chung, C.C. and J.H. Jean, *Aqueous synthesis of $Y_2O_2S:Eu$/silica core-shell particles.* Journal of the American Ceramic Society, 2005. **88**(5): p. 1341-1344.
82. Guo, C., *et al*., *Preparation of $Y_2O_2S:Eu^{3+}$ phosphors by a novel decomposition method.* Materials Letters, 2008. **62**(4-5): p. 600-602.
83. Kim Anh, T., *et al*., *Energy transfer between Tb^{3+} and Eu^{3+} in Y_2O_3 crystals.* Journal of Luminescence, 1988. **39**(4): p. 215-221.

84. Jing, X., *et al*., *Control of Y_2O_3:Eu spherical particle phosphor size, assembly properties, and performance for FED and HDTV.* Journal of The Electrochemical Society, 1999. **146**(12): p. 4654-4658.
85. Wakefield, G., *et al*., *Luminescence properties of nanocrystalline Y_2O_3:Eu.* Advanced Materials, 2001. **13**(20): p. 1557-1560.
86. Singh, L.R., *et al*., *Luminescence study on Eu^{3+} doped Y_2O_3 nanoparticles: particle size, concentration and core-shell formation effects.* Nanotechnology, 2008. **19**(5).
87. Jones, S.L., *et al*., *Luminescence of pulsed laser deposited Eu doped yttrium oxide films.* Applied Physics Letters, 1997. **71**(3): p. 404-406.
88. Avella, F.J., O.J. Sovers, and C.S. Wiggins, *Rare earth cathodoluminescence in $InBO_3$ and related orthoborates.* Journal of The Electrochemical Society, 1967. **114**(6): p. 613-616.
89. Berdowski, P.A.M., M.J.J. Lammers, and G. Blasse, *$^5D_3$-$^5D_4$ cross relaxation in Tb^{3+} pairs in $CsCdBr_3$ crystals.* The Journal of Chemical Physics, 1985. **83**(2): p. 476-479.
90. Okamoto, K., T. Yoshimi, and S. Miura, *Brightness degradation and its mechanism in Tb doped ZnS thin film.* Journal of Applied Physics, 1989. **65**(4): p. 1690-1693.
91. Ronda, C.R., *et al*., *The degradation behavior of LaOBr:Tb under cathode-ray excitation.* Journal of Applied Physics, 1994. **75**(9): p. 4636-4641.
92. Boutinaud, P., R. Mahiou, and J.C. Cousseins, *Effect of one-dimensional structure on Tb^{3+} $^5D_3$-$^5D_4$ cross-relaxation in K_2YF_5.* Journal of Luminescence, 1997. **72**: p. 318-320.
93. Kim, G.C., H.L. Park, and T.W. Kim, *Emission color tuning from blue to green through cross-relaxation in heavily Tb^{3+}-doped $YAlO_3$.* Materials Research Bulletin, 2001. **36**(9): p. 1603-1608.
94. Lawrence, T.A., K.A. Murra, and P.S. May, *Temperature dependence of rate constants for Tb^{3+}($^5D_3$) cross relaxation in symmetric Tb^{3+} pairs in Tb-doped $CsCdBr_3$, $CsMgBr_3$, $CsMgCl_3$.* Journal of Physical Chemistry B, 2003. **107**(17): p. 4002-4011.
95. Zhang, J.J., *et al*., *A novel synthesis of phase-pure ultrafine YAG:Tb phosphor with different Tb concentration.* Materials Letters, 2003. **57**(20): p. 3077-3081.

96. Ji, Y.M., D.Y. Jiang, and J.L. Shi, *Preparation and spectroscopic properties of $La_2Hf_2O_7$:Tb.* Materials Letters, 2005. **59**(8-9): p. 868-871.
97. da Silva, A.A., M.A. Cebim, and M.R. Davolos, *Excitation mechanisms and effects of dopant concentration in Gd2O2S:Tb^{3+} phosphor.* Journal of Luminescence, 2008. **128**(7): p. 1165-1168.
98. Hehlen, M.P., *et al*., *Spectroscopic properties of Er^{3+}- and Yb^{3+}-doped soda-lime silicate and aluminosilicate glasses.* Physical Review B, 1997. **56**(15): p. 9302-9318.
99. Liu, G.K., *et al*., *Confinement of electron-phonon interaction on luminescence dynamics in nanophosphors of Er^{3+}:Y_2O_2S.* Journal of Solid State Chemistry, 2003. **171**(1-2): p. 123-132.
100. Georgobiani, A.N., *et al*., *Infrared luminescence $Y_2O_2S:Er^{3+}$ and$Y_2O_3:Er^{3+}$.* Inorganic Materials, 2004. **40**(8): p. 840-844.
101. Fischer, L.H., G.S. Harms, and O.S. Wolfbeis, *Upconverting nanoparticles for nanoscale thermometry.* Angewandte Chemie-International Edition, 2011. **50**(20): p. 4546-4551.
102. Haase, M. and H. Schaefer, *Upconverting nanoparticles.* Angewandte Chemie-International Edition, 2011. **50**(26): p. 5808-5829.
103. Lu, S., *et al*., *Upconversion and infrared luminescences in Er^{3+}/Yb^{3+} codoped Y_2O_3 and $(Y_{0.9}La_{0.1})_2O_3$ transparent ceramics.* Optical Materials, 2011. **33**(5): p. 746-749.
104. Mikami, M. and A. Oshiyama, *First-principles study of intrinsic defects in yttrium oxysulfide.* Physical Review B, 1999. **60**(3): p. 1707-1715.
105. Royce, M.R. and P. Lancaster, *Rare erath activated yttrium and gadolinium oxy-chalcogenide phosphors*, U.P. 3418246, Editor. 1968.
106. Yocom, P.N., *Rare earth activated lanthanum and lutetium oxy-chalcogenide phosphors*, U.S.P. Office, Editor. 1968.
107. Ronda, C., *Luminescence loss mechanisms.* Journal of Luminescence, 2009. **129**(12): p. 1824-1826.
108. Nishikawa, R.M. and M.J. Yaffe, *Effect of various noise sources on the detective quantum efficiency of phosphor screens.* Medical Physics, 1990. **17**(5): p. 887-893.
109. Jean, J.H. and S.M. Yang, *Y_2O_2S:Eu red phosphor powders coated with silica.* Journal of the American Ceramic Society, 2000. **83**(8): p. 1928-1934.

110. Ozawa, L., *Cathodoluminescence and photoluminescence: Theories and practical applications*. 2007, CRC Press: Boca Raton.
111. Sordelet, D. and M. Akinc, *Preparation of spherical, monosized Y_2O_3 precursor particles.* Journal of Colloid and Interface Science, 1988. **122**(1): p. 47-59.
112. Willard, H.H. and N.K. Tang, *A study of the precipitation of aluminum basic sulfate by urea.* Journal of the American Chemical Society, 1937. **59**(7): p. 1190-1196.
113. Shaw, W.H.R. and J.J. Bordeaux, *The decomposition of urea in aqueous media.* Journal of the American Chemical Society, 1955. **77**(18): p. 4729-4733.
114. Auzel, F., *Compteur quantique par transfert d' energie entre deux ions de terres rares dans un tungstate mixte et dans un verre.* Comptes Rendus Hebdomadaires Des Seances De L Academie Des Sciences Serie B, 1966. **262**: p. 1016-1019.
115. Auzel, F., *Computeue quantique par transfert d' energie de Yb^{3+} & Tm^{3+} dans un tungastate mixte et dans un verre germanate.* Comptes Rendus Hebdomadaires Des Seances De L Academie Des Sciences Serie B, 1966. **263**: p. 819-821.
116. Auzel, F.E., *Materials and devices using double-pumped-phosphors with energy transfer.* Proceedings of the IEEE, 1973. **61**(6): p. 758-786.
117. Auzel, F., *Upconversion processes in coupled ion systems.* Journal of Luminescence, 1990. **45**(1–6): p. 341-345.
118. Auzel, F., *Upconversion and anti-stokes processes with f and d ions in solids.* Chemical Reviews, 2004. **104**(1): p. 139-173.
119. Suijver, J.F., *Upconversion Phosphors*, in *Luminescence: From Theory to Applications*, C.R. Ronda, Editor. 2007, Wiley-VCH Verlag GmbH & Co. KGaA: Weinheim. p. 133-177.
120. Wermuth, M. and H.U. Gudel, *Photon avalanche in $Cs_2ZrCl_6:Os^{4+}$.* The Journal of Chemical Physics, 2001. **114**(3): p. 1393-1404.
121. Wermuth, M. and H.U. Güdel, *Upconversion luminescence in a 5d transition-metal ion system: $Cs_2ZrCl_6:Os^{4+}$.* Chemical Physics Letters, 1997. **281**(1–3): p. 81-85.

122. Wenger, O.S., R. Valiente, and H.U. Gudel, *Optical spectroscopy of the Ni^{2+}-doped layer perovskites Rb_2MCl_4 (M = Cd, Mn): Effects of Ni^{2+}-Mn^{2+} exchange interactions on the Ni^{2+} absorption, luminescence, and upconversion properties.* Physical Review B, 2001. **64**(23): p. 235116.
123. Tang, Y., S. Dai, and Y. Fang, *Electron structure and photoluminescence behavior of $Ti_{0.09}Y_{1.91}O_2S$.* Journal of Applied Physics, 2009. **105**(3).
124. Wenger, O.S., *et al*., *Luminescence upconversion under hydrostatic pressure in the 3d-metal systems Ti^{2+}: NaCl and Ni^{2+}: $CsCdCl_3$.* Physical Review B, 2002. **65**(21): p. 212108.
125. Wenger, O.S., G.M. Salley, and H.U. Gudel, *Effects of high pressure on the luminescence and upconversion properties of Ti^{2+}-doped NaCl.* Journal of Physical Chemistry B, 2002. **106**(39): p. 10082-10088.
126. Diamente, P.R., M. Raudsepp, and F.C.J.M. van Veggel, *Dispersible Tm^{3+}-doped nanoparticles that exhibit strong 1.47 mm photoluminescence.* Advanced Functional Materials, 2007. **17**(3): p. 363-368.
127. de la Rosa, E., *et al*., *Blue-green upconversion emission in ZrO_2:Yb^{3+} nanocrystals.* Journal of Applied Physics, 2008. **104**(10): p. 103508.
128. Bai, Y., *et al*., *Enhance upconversion photoluminescence intensity by doping Li^+ in Ho^{3+} and Yb^{3+} codoped Y_2O_3 nanocrystals.* Journal of Alloys and Compounds, 2009. **478**(1-2): p. 676-678.
129. Hanna, D.C., *et al*., *Frequency upconversion in Tm- and Yb:Tm-doped silica fibers.* Optics Communications, 1990. **78**(2): p. 187-194.
130. Silver, J., *et al*., *The effect of particle morphology and crystallite size on the upconversion luminescence properties of erbium and ytterbium co-doped yttrium oxide phosphors.* The Journal of Physical Chemistry B, 2001. **105**(5): p. 948-953.
131. Silver, J., *et al*., *Yttrium oxide upconverting phosphors. 3. Upconversion luminescent emission from europium-doped yttrium oxide under 632.8 nm light excitation.* The Journal of Physical Chemistry B, 2001. **105**(38): p. 9107-9112.
132. Silver, J., *et al*., *Yttrium oxide upconverting phosphors. Part 2: Temperature dependent upconversion luminescence properties of erbium in yttrium oxide.* The Journal of Physical Chemistry B, 2001. **105**(30): p. 7200-7204.

133. Matsuura, D., *Red, green, and blue upconversion luminescence of trivalent-rare-earth ion-doped Y_2O_3 nanocrystals.* Applied Physics Letters, 2002. **81**(24): p. 4526-4528.
134. Silver, J., *et al*., *Yttrium oxide upconverting phosphors. Part 4: Upconversion luminescent emission from thulium-doped yttrium oxide under 632.8-nm light excitation.* The Journal of Physical Chemistry B, 2003. **107**(7): p. 1548-1553.
135. Hirai, T. and T. Orikoshi, *Preparation of yttrium oxysulfide phosphor nanoparticles with infrared-to-green and -blue upconversion emission using an emulsion liquid membrane system.* Journal of Colloid and Interface Science, 2004. **273**(2): p. 470-477.
136. Lei, B.F., *et al*., *Upconversion of Y_2O_2S:Tm, Mg, Ti phosphor and its long-lasting phosphorescence.* Electrochemical and Solid State Letters, 2004. **7**(10): p. G225-G227.
137. Pires, A.M., *et al*., *Er, Yb doped yttrium based nanosized phosphors: Particle size, "host lattice" and doping ion concentration effects on upconversion efficiency.* Journal of Fluorescence, 2006. **16**(3): p. 461-468.
138. Luo, X.-x. and W.-h. Cao, *Upconversion luminescence of holmium and ytterbium co-doped yttrium oxysulfide phosphor.* Materials Letters, 2007. **61**(17): p. 3696-3700.
139. Pires, A.M., O.A. Serra, and M.R. Davolos, *Yttrium oxysulfide nanosized spherical particles doped with Yb and Er or Yb and Tm: efficient materials for up-converting phosphor technology field.* Journal of Alloys and Compounds, 2004. **374**(1-2): p. 181-184.
140. Liu, G.K., H.Z. Zhuang, and X.Y. Chen, *Restricted phonon relaxation and anomalous thermalization of rare earth ions in nanocrystals.* Nano Letters, 2002. **2**(5): p. 535-539.
141. Menyuk, N., J.W. Pierce, and K. Dwight, *$NaYF_4$:Yb, Er-an efficient upconversion phosphor.* Applied Physics Letters, 1972. **21**(4): p. 159-161.
142. Yan, R.X. and Y.D. Li, *Down/Up conversion in Ln^{3+}-doped YF_3 nanocrystals.* Advanced Functional Materials, 2005. **15**(5): p. 763-770.
143. Boyer, J.C., *et al*., *Synthesis of colloidal upconverting $NaYF_4$ nanocrystals doped with Er^{3+}, Yb^{3+} and Tm^{3+}, Yb^{3+} via thermal decomposition of*

lanthanide trifluoroacetate precursors. Journal of the American Chemical Society, 2006. **128**(23): p. 7444-7445.

144. Li, Z. and Y. Zhang, *Monodisperse silica-coated polyvinylpyrrolidone/$NaYF_4$ nanocrystals with multicolor upconversion fluorescence emission.* Angewandte Chemie-International Edition, 2006. **45**(46): p. 7732-7735.
145. Wang, F., *et al*., *Synthesis of polyethylenimine/$NaYF_4$ nanoparticles with upconversion fluorescence.* Nanotechnology, 2006. **17**(23): p. 5786-5791.
146. Schaefer, H., *et al*., *Lanthanide-doped $NaYF_4$ nanocrystals in aqueous solution displaying strong up-conversion emission.* Chemistry of Materials, 2007. **19**(6): p. 1396-1400.
147. Li, Z. and Y. Zhang, *An efficient and user-friendly method for the synthesis of hexagonal-phase $NaYF_4$:Yb, Er/Tm nanocrystals with controllable shape and upconversion fluorescence.* Nanotechnology, 2008. **19**(34): p. 345606.
148. Shan, J., *et al*., *Anomalous Raman scattering of colloidal Yb^{3+},Er^{3+} codoped $NaYF_4$ nanophosphors and dynamic probing of the upconversion luminescence.* Advanced Functional Materials, 2010. **20**(20): p. 3530-3537.
149. Krämer, K.W., *et al*., *Hexagonal sodium yttrium fluoride based green and blue emitting upconversion phosphors.* Chemistry of Materials, 2004. **16**(7): p. 1244-1251.
150. Wang, F. and X. Liu, *Recent advances in the chemistry of lanthanide-doped upconversion nanocrystals.* Chemical Society Reviews, 2009. **38**(4): p. 976-989.
151. Chen, Z., *et al*., *980-nm laser-driven photovoltaic cells based on rare-earth up-converting phosphors for biomedical applications.* Advanced Functional Materials, 2009. **19**(23): p. 3815-3820.
152. Suyver, J.F., *et al*., *Upconversion spectroscopy and properties of $NaYF_4$ doped with Er^{3+},Tm^{3+} and/or Yb^{3+}.* Journal of Luminescence, 2006. **117**(1): p. 1-12.
153. Heer, S., *et al*., *Highly efficient multicolour upconversion emission in transparent colloids of lanthanide-doped $NaYF_4$ nanocrystals.* Advanced Materials, 2004. **16**(23-24): p. 2102-2105.

154. Aebischer, A., *et al*., *Structural and spectroscopic characterization of active sites in a family of light-emitting sodium lanthanide tetrafluorides.* Angewandte Chemie-International Edition, 2006. **45**(17): p. 2802-2806.
155. Hilderbrand, S.A., *et al*., *Upconverting luminescent nanomaterials: application to in vivo bioimaging.* Chemical Communications, 2009(28): p. 4188-4190.
156. Lim, S.F., *et al*., *Upconverting nanophosphors for bioimaging.* Nanotechnology, 2009. **20**(40).
157. Mader, H.S., *et al*., *Upconverting luminescent nanoparticles for use in bioconjugation and bioimaging.* Current Opinion in Chemical Biology, 2010. **14**(5): p. 582-596.
158. Wang, F., *et al*., *Upconversion nanoparticles in biological labeling, imaging, and therapy.* Analyst, 2010. **135**(8): p. 1839-1854.
159. Wang, G., Q. Peng, and Y. Li, *Lanthanide-doped nanocrystals: Synthesis, optical-magnetic properties, and applications.* Accounts of Chemical Research, 2011. **44**(5): p. 322-332.
160. Wang, X., *et al*., *A general strategy for nanocrystal synthesis.* Nature, 2005. **437**(7055): p. 121-124.
161. Yi, G.-S. and G.-M. Chow, *Colloidal LaF_3:Yb,Er, LaF_3:Yb,Ho and LaF_3:Yb,Tm nanocrystals with multicolor upconversion fluorescence.* Journal of Materials Chemistry, 2005. **15**(41): p. 4460-4464.
162. Yi, G.S. and G.M. Chow, *Synthesis of hexagonal-phase $NaYF_4$:Yb,Er and $NaYF_4$:Yb,Tm nanocrystals with efficient up-conversion fluorescence.* Advanced Functional Materials, 2006. **16**(18): p. 2324-2329.
163. Zeng, J.H., *et al*., *Synthesis and upconversion luminescence of hexagonal-phase $NaYF_4$:Yb, Er^{3+} phosphors of controlled size and morphology.* Advanced Materials, 2005. **17**(17): p. 2119-2123.
164. Wang, F., *et al*., *Simultaneous phase and size control of upconversion nanocrystals through lanthanide doping.* Nature, 2010. **463**(7284): p. 1061-1065.
165. Mahalingam, V., *et al*., *Colloidal Tm^{3+}/Yb^{3+}-doped $LiYF_4$ nanocrystals: Multiple luminescence spanning the UV to NIR regions via low-energy excitation.* Advanced Materials, 2009. **21**(40): p. 4025-4028.

166. Bai, F., *et al*., *A versatile bottom-up assembly approach to colloidal spheres from nanocrystals.* Angewandte Chemie-International Edition, 2007. **46**(35): p. 6650-6653.
167. Li, P., Q. Peng, and Y. Li, *Dual-mode luminescent colloidal spheres from monodisperse rare-earth fluoride nanocrystals.* Advanced Materials, 2009. **21**(19): p. 1945-1948.
168. Wang, F., *et al*., *Tuning upconversion through energy migration in core-shell nanoparticles.* Nature Materials, 2011. **10**(12): p. 968-973.
169. van de Rijke, F., *et al*., *Up-converting phosphor reporters for nucleic acid microarrays.* Nature Biotechnology, 2001. **19**(3): p. 273-276.
170. Larson, D.R., *Water-soluble quantum dots for multiphoton flurescence imaging in vivo.* Science, 2003. **300**(5624): p. 1434-1436.
171. Downing, E., *et al*., *A three-color, solid-state, three-dimensional display.* Science, 1996. **273**(5279): p. 1185-1189.
172. Hinklin, T.R., S.C. Rand, and R.M. Laine, *Transparent, polycrystalline upconverting nanoceramics: Towards 3-D displays.* Advanced Materials, 2008. **20**(7): p. 1270-1273.
173. Li, Z.Q., *et al*., *Core/shell structured $NaYF_4$:Yb^{3+}/Er^{3+}/Gd^{+3} nanorods with Au nanoparticles or shells for flexible amorphous silicon solar cells.* Nanotechnology, 2012. **23**(2): p. 025402.
174. Zhao, S.L., *et al*., *Er^{3+}/Yb^{3+} codoped oxyfluoride borosilicate glass ceramic containing $NaYF_4$ nanocrystals for amorphous silicon solar cells.* Materials Letters, 2011. **65**(15-16): p. 2407-2409.
175. Lahoz, F., *et al*., *Upconversion mechanisms in rare-earth doped glasses to improve the efficiency of silicon solar cells.* Solar Energy Materials and Solar Cells, 2011. **95**(7): p. 1671-1677.
176. de Wild, J., *et al*., *Upconverter solar cells: materials and applications.* Energy & Environmental Science, 2011. **4**(12): p. 4835-4848.
177. Fischer, S., *et al*., *Enhancement of silicon solar cell efficiency by upconversion: Optical and electrical characterization.* Journal of Applied Physics, 2010. **108**(4).
178. de Wild, J., *et al*., *Towards upconversion for amorphous silicon solar cells.* Solar Energy Materials and Solar Cells, 2010. **94**(11): p. 1919-1922.

179. Henry, C.H., *Limiting efficiencies of ideal single and multiple energy gap terrestrial solar cells.* Journal of Applied Physics, 1980. **51**(8): p. 4494-4500.
180. Strümpel, C., *et al*., *Modifying the solar spectrum to enhance silicon solar cell efficiency—An overview of available materials.* Solar Energy Materials and Solar Cells, 2007. **91**(4): p. 238-249.
181. Won Jin, K., N. Marcin, and N.P. Paras, *Color-coded multilayer photopatterned microstructures using lanthanide (III) ion co-doped $NaYF_4$ nanoparticles with upconversion luminescence for possible applications in security.* Nanotechnology, 2009. **20**(18): p. 185301.
182. Liu, Y., K. Ai, and L. Lu, *Designing lanthanide-doped nanocrystals with both up- and down-conversion luminescence for anti-counterfeiting.* Nanoscale, 2011. **3**(11): p. 4804-4810.
183. Bukowski, T.J. and J.H. Simmons, *Quantum dot research: Current state and future prospects.* Critical Reviews in Solid State and Materials Sciences, 2002. **27**(3-4): p. 119-142.
184. Efros, A.L. and M. Rosen, *The electronic structure of semiconductor nanocrystals.* Annual Review of Materials Science, 2000. **30**: p. 475-521.
185. Rogach, A.L., *et al*., *Light-emitting diodes with semiconductor nanocrystals.* Angewandte Chemie-International Edition, 2008. **47**(35): p. 6538-6549.
186. Lubashenko, V., *Size-dependent melting of nanocrystals: A self-consistent statistical approach.* Journal of Nanoparticle Research, 2010. **12**(5): p. 1837-1844.
187. Zhang, Z., M. Zhao, and Q. Jiang, *Melting temperatures of semiconductor nanocrystals in the mesoscopic size range.* Semiconductor Science and Technology, 2001. **16**(6): p. L33-L35.
188. Shi, F.G., *Size-dependent thermal vibrations and melting in nanocrystals.* Journal of Materials Research, 1994. **9**(5): p. 1307-1313.
189. Goldstein, A.N., C.M. Echer, and A.P. Alivisatos, *Melting in semiconductor nanocrystals.* Science, 1992. **256**(5062): p. 1425-1427.
190. Qadri, S.B., *et al*., *Size-induced transition-temperature reduction in nanoparticles of ZnS.* Physical Review B, 1999. **60**(13): p. 9191-9193.
191. Hollingsworth, J.A. and V.I. Klimov, *'Soft' Chemical Synthesis and Manipulation of Semiconductor Nanocrystals*, in *Nanocrystal Quantum*

Dots, Second Edition, V.I. Klimov, Editor. 2010, CRC Press: Boca Ratan. p. 1-61.

192. Bhargava, R.N., *Doped nanocrystalline materials - Physics and applications.* Journal of Luminescence, 1996. **70**: p. 85-94.
193. Bol, A.A. and A. Meijerink, *Long-lived Mn^{2+} emission in nanocrystalline ZnS:Mn^{2+}.* Physical Review B, 1998. **58**(24): p. R15997-R16000.
194. Bhargava, R.N., *et al*., *Optical properties of manganese-doped nanocrystals of ZnS.* Physical Review Letters, 1994. **72**(3): p. 416-419.
195. Chen, Z.-Q., *et al*., *Greatly enhanced and controlled manganese photoluminescence in water-soluble ZnCdS:Mn/ZnS core/shell quantum dots.* Chemical Physics Letters, 2010. **488**(1-3): p. 73-76.
196. Chen, O., *et al*., *Excitation-intensity-dependent color-tunable dual emissions from manganese-doped CdS/ZnS core/shell nanocrystals.* Angewandte Chemie-International Edition, 2010. **49**(52): p. 10132-10135.
197. Jing, P., *et al*., *Temperature-dependent photoluminescence of CdSe-core CdS/CdZnS/ZnS-multishell quantum dots.* Journal of Physical Chemistry C, 2009. **113**(31): p. 13545-13550.
198. Reiss, P., M. Protière, and L. Li, *Core/Shell Semiconductor Nanocrystals.* Small, 2009. **5**(2): p. 154-168.
199. Xia, Y.N., *et al*., *Shape-controlled synthesis of metal nanocrystals: Simple chemistry meets complex physics?* Angewandte Chemie-International Edition, 2009. **48**(1): p. 60-103.
200. Jun, Y.W., J.S. Choi, and J. Cheon, *Shape control of semiconductor and metal oxide nanocrystals through nonhydrolytic colloidal routes.* Angewandte Chemie-International Edition, 2006. **45**(21): p. 3414-3439.
201. Yin, Y. and A.P. Alivisatos, *Colloidal nanocrystal synthesis and the organic-inorganic interface.* Nature, 2005. **437**(7059): p. 664-670.
202. Peng, X., *Mechanisms for the Shape-Control and Shape-Evolution of Colloidal Semiconductor Nanocrystals.* Advanced Materials, 2003. **15**(5): p. 459-463.
203. Puntes, V.F., K.M. Krishnan, and A.P. Alivisatos, *Colloidal nanocrystal shape and size control: The case of cobalt.* Science, 2001. **291**(5511): p. 2115-2117.

204. Petroski, J.M., *et al*., *Kinetically controlled growth and shape formation mechanism of platinum nanoparticles.* Journal of Physical Chemistry B, 1998. **102**(18): p. 3316-3320.
205. Pileni, M.P., *Nanosized particles made in colloidal assemblies.* Langmuir, 1997. **13**(13): p. 3266-3276.
206. Zheng, J., *et al*., *Enhanced photoluminescence of water-soluble Mn-doped ZnS quantum dots by thiol ligand exchange.* Chemical Physics Letters, 2012. **519-20**: p. 73-77.
207. Pradhan, N., *et al*., *An alternative of CdSe nanocrystal emitters: Pure and tunable impurity emissions in ZnSe nanocrystals.* Journal of the American Chemical Society, 2005. **127**(50): p. 17586-17587.
208. Yang, Y., *et al*., *Radial-position-controlled doping in CdS/ZnS core/shell nanocrystals.* Journal of the American Chemical Society, 2006. **128**(38): p. 12428-12429.
209. Erwin, S.C., *et al*., *Doping semiconductor nanocrystals.* Nature, 2005. **436**(7047): p. 91-94.
210. Galli, G., *Solid-state physics - Doping the undopable.* Nature, 2005. **436**(7047): p. 32-33.
211. Norris, D.J., A.L. Efros, and S.C. Erwin, *Doped nanocrystals.* Science, 2008. **319**(5871): p. 1776-1779.
212. Mocatta, D., *et al*., *Heavily doped semiconductor nanocrystal quantum dots.* Science, 2011. **332**(6025): p. 77-81.
213. Dinsmore, A.D., *et al*., *Structure and luminescence of annealed nanoparticles of ZnS:Mn.* Journal of Applied Physics, 2000. **88**(9): p. 4985-4993.
214. Dinsmore, A.D., *et al*., *Mn-doped ZnS nanoparticles as efficient low-voltage cathodoluminescent phosphors.* Applied Physics Letters, 1999. **75**(6): p. 802-804.
215. Suyver, J.F., *et al*., *Synthesis and photoluminescence of nanocrystalline ZnS:Mn^{2+}.* Nano Letters, 2001. **1**(8): p. 429-433.
216. Srivastava, B.B., *et al*., *Highly luminescent Mn-doped ZnS nanocrystals: Gram-scale synthesis.* Journal of Physical Chemistry Letters, 2010. **1**(9): p. 1454-1458.

217. Cao, L.X., *et al*., *Luminescence enhancement of core-shell ZnS:Mn/ZnS nanoparticles.* Applied Physics Letters, 2002. **80**(23): p. 4300-4302.
218. Ethiraj, A.S., *et al*., *Enhancement of photoluminescence in manganese-doped ZnS nanoparticles due to a silica shell.* Journal of Chemical Physics, 2003. **118**(19): p. 8945-8953.
219. Karar, N., H. Chander, and S.M. Shivaprasad, *Enhancement of luminescent properties of ZnS:Mn nanophosphors by controlled ZnO capping.* Applied Physics Letters, 2004. **85**(21): p. 5058-5060.
220. Zhang, S., *et al*., *Enhanced infrared photovoltaic efficiency in PbS nanocrystal/semiconducting polymer composites: 600-fold increase in maximum power output via control of the ligand barrier.* Applied Physics Letters, 2005. **87**(23): p. 233101.
221. Nozik, A.J., *et al*., *Semiconductor quantum dots and quantum dot arrays and applications of multiple exciton generation to third-generation photovoltaic solar cells.* Chemical Reviews, 2010. **110**(11): p. 6873-6890.
222. Johnston, K.W., *et al*., *Schottky-quantum dot photovoltaics for efficient infrared power conversion.* Applied Physics Letters, 2008. **92**(15): p. 151115.
223. McDonald, S.A., *et al*., *Solution-processed PbS quantum dot infrared photodetectors and photovoltaics.* Nature Materials, 2005. **4**(2): p. 138-142.
224. Bakueva, L., *et al*., *Size-tunable infrared (1000-1600 nm) electroluminescence from PbS quantum-dot nanocrystals in a semiconducting polymer.* Applied Physics Letters, 2003. **82**(17): p. 2895-2897.
225. Bourdakos, K.N., *et al*., *Highly efficient near-infrared hybrid organic-inorganic nanocrystal electroluminescence device.* Applied Physics Letters, 2008. **92**(15).
226. Sun, L., *et al*., *Bright infrared quantum-dot light-emitting diodes through inter-dot spacing control.* Nature Nanotechnology, 2012. **7**: p. 369-373.
227. Rauch, T., *et al*., *Near-infrared imaging with quantum-dot-sensitized organic photodiodes.* Nature Photonics, 2009. **3**(6): p. 332-336.
228. Pal, B.N., *et al*., *High-sensitivity p-n junction photodiodes based on PbS nanocrystal quantum dots.* Advanced Functional Materials, 2012. **22**(8): p. 1741-1748.

229. Li, Y., *et al*., *White-light-emitting diodes using semiconductor nanocrystals.* Microchimica Acta, 2007. **159**(3-4): p. 207-215.
230. Banin, U., *Light-emitting diodes: Bright and stable.* Nature Photonics, 2008. **2**(4): p. 209-210.
231. Dai, Q.Q., C.E. Duty, and M.Z. Hu, *Semiconductor-nanocrystals-based white light-emitting diodes.* Small, 2010. **6**(15): p. 1577-1588.
232. Smet, P.F., A.B. Parmentier, and D. Poelman, *Selecting conversion phosphors for white light-emitting diodes.* Journal of The Electrochemical Society, 2011. **158**(6): p. R37-R54.
233. Ye, S., *et al*., *Phosphors in phosphor-converted white light-emitting diodes: Recent advances in materials, techniques and properties.* Materials Science & Engineering R-Reports, 2010. **71**(1): p. 1-34.
234. Chen, L., *et al*., *Light converting inorganic phosphors for white light-emitting diodes.* Materials, 2010. **3**(3): p. 2172-2195.
235. Jang, E., *et al*., *White-light-emitting diodes with quantum dot color converters for display backlights.* Advanced Materials, 2010. **22**(28): p. 3076-3080.
236. Chanyawadee, S., *et al*., *Increased color-conversion efficiency in hybrid light-emitting diodes utilizing non-radiative energy transfer.* Advanced Materials, 2010. **22**(5): p. 602-606.
237. Basko, D., *et al*., *Forster energy transfer from a semiconductor quantum well to an organic material overlayer.* European Physical Journal B, 1999. **8**(3): p. 353-362.
238. Achermann, M., *et al*., *Energy-transfer pumping of semiconductor nanocrystals using an epitaxial quantum well.* Nature, 2004. **429**(6992): p. 642-646.
239. Kim, J.-U., M.-H. Lee, and H. Yang, *Synthesis of $Zn_{1-x}Cd_xS$:Mn/ZnS quantum dots and their application to light-emitting diodes.* Nanotechnology, 2008. **19**(46): p. 465605.
240. Huynh, W.U., J.J. Dittmer, and A.P. Alivisatos, *Hybrid nanorod-polymer solar cells.* Science, 2002. **295**(5564): p. 2425-2427.
241. Schlamp, M.C., X. Peng, and A.P. Alivisatos, *Improved efficiencies in light emitting diodes made with CdSe(CdS) core/shell type nanocrystals and a*

semiconducting polymer. Journal of Applied Physics, 1997. **82**(11): p. 5837-5842.

242. Klein, D.L., *et al*., *A single-electron transistor made from a cadmium selenide nanocrystal.* Nature, 1997. **389**(6652): p. 699-701.
243. Greenham, N.C., X. Peng, and A.P. Alivisatos, *Charge separation and transport in conjugated-polymer/semiconductor-nanocrystal composites studied by photoluminescence quenching and photoconductivity.* Physical Review B, 1996. **54**(24): p. 17628-17637.
244. Colvin, V.L., M.C. Schlamp, and A.P. Alivisatos, *Light-emitting diodes made from cadmium selenide nanocrystals and a semiconducting polymer.* Nature, 1994. **370**(6488): p. 354-357.
245. Matijević, E. and W.P. Hsu, *Preparation and properties of monodispersed colloidal particles of lanthanide compounds: I. Gadolinium, europium, terbium, samarium, and cerium(III).* Journal of Colloid and Interface Science, 1987. **118**(2): p. 506-523.
246. de Azevedo, F.G. and W.A. de Oliveira, *Ebulliometric study of the decomposition of urea in aqueous media.* International Journal of Chemical Kinetics, 1984. **16**(7): p. 793-799.
247. Matijevic, E., *Monodispersed metal (hydrous) oxides-A fascinating field of colloid science.* Accounts of Chemical Research, 1981. **14**(1): p. 22-29.
248. Israelachvili, J.N., S. Marelja, and R.G. Horn, *Physical principles of membrane organization.* Quarterly Reviews of Biophysics, 1980. **13**(02): p. 121-200.
249. Yang, J.P., S.B. Qadri, and B.R. Ratna, *Structural and morphological characterization of PbS nanocrystallites synthesized in the bicontinuous cubic phase of a lipid.* The Journal of Physical Chemistry, 1996. **100**(43): p. 17255-17259.
250. Yang, J.P., *et al*., *Nanocrystalline phosphors.* Journal of the Society for Information Display, 1998. **6**(3): p. 139-142.
251. Struck, C.W. and W.H. Fonger, *Dissociation of Eu^{+3} charge-transfer state in Y_2O_2S and La_2O_2S into Eu^{+2} and a free hole.* Physical Review B, 1971. **4**(1): p. 22-34.
252. Mikami, M. and A. Oshiyama, *First-principles band-structure calculation of yttrium oxysulfide.* Physical Review B, 1998. **57**(15): p. 8939-8944.

253. Itoh, M. and Y. Inabe, *Optical properties and electronic structure of yttrium oxysulfide.* Physical Review B, 2003. **68**(3).
254. Li, S. and R. Ahuja, *Electronic, elastic, and optical properties of Y_2O_2S.* Journal of Applied Physics, 2005. **97**(10).
255. Trond, S.S., *et al*., *Properties of some selected europium-activated red phosphors.* Journal of The Electrochemical Society, 1969. **116**(7): p. 1047-1050.
256. Abdel-Kader, A. and M.M. Elkholy, *Cathodoluminescence emission spectra of trivalent europium-doped yttrium oxysulphide.* Journal of Materials Science, 1992. **27**(11): p. 2887-2895.
257. Tseng, Y.H., *et al*., *Spectral properties of Eu^{3+}-activated yttrium oxysulfide red phosphor.* Thin Solid Films, 1998. **330**(2): p. 173-177.
258. Ozawa, L., *Preparation of Y_2O_2S:Eu phosphor particles of different sizes by a flux method.* Journal of The Electrochemical Society, 1977. **124**(3): p. 413-417.
259. Lo, C.L., *et al*., *Synthesis of Eu^{3+}-activated yttrium oxysulfide red phosphor by flux fusion method.* Materials Chemistry and Physics, 2001. **71**(2): p. 179-189.
260. Jayasimhadri, M., *et al*., *Greenish-yellow emission from Dy^{3+}-doped Y_2O_3 nanophosphors.* Journal of the American Ceramic Society, 2010. **93**(2): p. 494-499.
261. Dieke, G.H. and R. Sarup, *Fluorescence Spectrum of $PrCl_3$ and the Levels of the Pr^{+++} Ion.* The Journal of Chemical Physics, 1958. **29**(4): p. 741-745.
262. van der Weg, W.F. and M.W. van Tol, *Saturation effects of cathodoluminescence in rare-earth activated epitaxial $Y_3Al_5O_{12}$ layers.* Applied Physics Letters, 1981. **38**(9): p. 705-707.
263. De Heer, W.A., A. Chatelain, and D. Ugarte, *A carbon nanotube field-emission electron source.* Science, 1995. **270**(5239): p. 1179-1180.
264. Choi, W.B., *et al*., *Fully sealed, high-brightness carbon-nanotube field-emission display.* Applied Physics Letters, 1999. **75**(20): p. 3129-3131.
265. Wang, Q.H., *et al*., *A nanotube-based field-emission flat panel display.* Applied Physics Letters, 1998. **72**(22): p. 2912-2913.
266. Baughman, R.H., A.A. Zakhidov, and W.A. de Heer, *Carbon nanotubes - the route toward applications.* Science, 2002. **297**(5582): p. 787-792.

267. Martinez-Rubio, V.M.I., *et al*., *Factors affecting efficiency in submicron phosphors: Implications for screens for high definition displays, LEDs.* Digest of Technical Papers - SID International Symposium, 2000. **35**: p. 15-17.
268. Kalivas, N., *et al*., *Effect of intrinsic-gain fluctuations on quantum noise of phosphor materials used in medical X-ray imaging.* Applied Physics A, 1999. **69**(3): p. 337-341.
269. Eick, H.A., *The preparation, lattice parameters and some chemical properties of the rare earth mono-thio oxides.* Journal of the American Chemical Society, 1958. **80**(1): p. 43-44.
270. Hase, T., *et al*., *Phosphor materials for cathode-ray tubes.* Advances in Electronics and Electron Physics, 1990. **79**: p. 271-373.
271. Fonger, W.H. and C.W. Struck, *Eu^{+3} ^5D resonance quenching to the charge-transfer states in Y_2O_2S, La_2O_2S, and LaOCl.* The Journal of Chemical Physics, 1970. **52**(12): p. 6364-6372.
272. Bloembergen, N., *Solid state infrared quantum counters.* Physical Review Letters, 1959. **2**(3): p. 84-85.
273. Brown, M.R., *et al*., *Experiments on Er^{3+} in SrF_2. III. Coupled-Ion Effects.* The Journal of Chemical Physics, 1969. **51**(8): p. 3321-3327.
274. Wittke, J.P., I. Ladany, and P.N. Yocom, *Y_2O_3:Yb:Er New red-emitting infrared-excited phosphor.* Journal of Applied Physics, 1972. **43**(2): p. 595-600.
275. Jarvinen, M., *Application of symmetrized harmonics expansion to correction of the preferred orientation effect.* Journal of Applied Crystallography, 1993. **26**(4): p. 525-531.
276. Hyppänen, I., *et al*., *Up-conversion luminescence properties of Y_2O_2S:Yb^{3+},Er^{3+} nanophosphors.* Optical Materials, 2009. **31**(12): p. 1787-1790.
277. Norris, D.J., *et al*., *Size dependence of exciton fine structure in CdSe quantum dots.* Physical Review B, 1996. **53**(24): p. 16347-16354.
278. Norris, D.J. and M.G. Bawendi, *Measurement and assignment of the size-dependent optical spectrum in CdSe quantum dots.* Physical Review B, 1996. **53**(24): p. 16338-16346.

279. Davies, J.H., *The Physics of Low-dimensional Semiconductors: An Introduction.* 1998, Cambridge: Cambridge University Press.
280. Stangl, J., V. Holý, and G. Bauer, *Structural properties of self-organized semiconductor nanostructures.* Reviews of Modern Physics, 2004. **76**(3): p. 725-783.
281. Yoffe, A.D., *Semiconductor quantum dots and related systems: Electronic, optical, luminescence and related properties of low dimensional systems.* Advances in Physics, 2001. **50**(1): p. 1-208.
282. Murray, C.B., C.R. Kagan, and M.G. Bawendi, *Synthesis and characterization of monodisperse nanocrystals and close-packed nanocrystals assemblies.* Annual Review of Materials Science, 2000. **30**(1): p. 545-610.
283. Jain, P.K., *et al*., *Highly luminescent nanocrystals from removal of impurity atoms residual from ion-exchange synthesis.* Angewandte Chemie, 2012. **124**(10): p. 2437-2440.
284. Yu, I., T. Isobe, and M. Senna, *Optical properties and characteristics of ZnS nano-particles with homogeneous Mn distribution.* Journal of Physics and Chemistry of Solids, 1996. **57**(4): p. 373-379.
285. Chan, W.C.W. and S. Nie, *Quantum dot bioconjugates for ultrasensitive nonisotopic detection.* Science, 1998. **281**(5385): p. 2016-2018.
286. Medintz, I.L., *et al*., *Quantum dot bioconjugates for imaging, labelling and sensing.* Nature Materials, 2005. **4**(6): p. 435-446.
287. Michalet, X., *et al*., *Quantum dots for live cells, in vivo imaging, and diagnostics.* Science, 2005. **307**(5709): p. 538-544.
288. O'Regan, B. and M. Gratzel, *A low-cost, high-efficiency solar cell based on dye-sensitized colloidal TiO_2 films.* Nature, 1991. **353**(6346): p. 737-740.
289. Santra, P.K. and P.V. Kamat, *Mn-doped quantum dots sensitised solar cells: A strategy to boost efficiency over 5%.* Journal of the American Chemical Society, 2012. **134**(5): p. 2508-2511.
290. Hillhouse, H.W. and M.C. Beard, *Solar cells from colloidal nanocrystals: Fundamentals, materials, devices, and economics.* Current Opinion in Colloid & Interface Science, 2009. **14**(4): p. 245-259.
291. Luther, J.M., *et al*., *Schottky solar cells based on colloidal nanocrystal films.* Nano Letters, 2008. **8**(10): p. 3488-3492.

292. Kumar, S. and G.D. Scholes, *Colloidal nanocrystal solar cells.* Microchimica Acta, 2008. **160**(3): p. 315-325.
293. Kamat, P.V., *Quantum dot solar cells. Semiconductor nanocrystals as light harvesters.* Journal of Physical Chemistry C, 2008. **112**(48): p. 18737-18753.
294. Beek, W.J.E., M.M. Wienk, and R.A.J. Janssen, *Hybrid solar cells from regioregular polythiophene and ZnO nanoparticles.* Advanced Functional Materials, 2006. **16**(8): p. 1112-1116.
295. Gur, I., *et al*., *Air-stable all-inorganic nanocrystal solar cells processed from solution.* Science, 2005. **310**(5747): p. 462-465.
296. Beek, W.J.E., *et al*., *Hybrid solar cells using a zinc oxide precursor and a conjugated polymer.* Advanced Functional Materials, 2005. **15**(10): p. 1703-1707.
297. Beek, W.J.E., M.M. Wienk, and R.A.J. Janssen, *Efficient hybrid solar cells from zinc oxide nanoparticles and a conjugated polymer.* Advanced Materials, 2004. **16**(12): p. 1009-1013.
298. Huynh, W.U., *et al*., *Controlling the morphology of nanocrystal-polymer composites for solar cells.* Advanced Functional Materials, 2003. **13**(1): p. 73-79.
299. Peter, L.M., *The Grätzel Cell: Where Next?* The Journal of Physical Chemistry Letters, 2011. **2**(15): p. 1861-1867.
300. Likovich, E.M., *et al*., *High-current-density monolayer CdSe/ZnS quantum dot light-emitting devices with oxide electrodes.* Advanced Materials, 2011. **23**(39): p. 4521-4525.
301. Gopal, A., *et al*., *Multi-color colloidal quantum dot based light emitting diodes micropatterned on silicon hole transporting layers.* Nanotechnology, 2009. **20**(23): p. 235201.
302. Anikeeva, P.O., *et al*., *Quantum dot light-emitting devices with electroluminescence tunable over the entire visible spectrum.* Nano Letters, 2009. **9**(7): p. 2532-2536.
303. Sun, Q., *et al*., *Bright, multicoloured light-emitting diodes based on quantum dots.* Nature Photonics, 2007. **1**(12): p. 717-722.
304. Li, Y.Q., *et al*., *White-light-emitting diodes using semiconductor nanocrystals.* Microchimica Acta, 2007. **159**(3-4): p. 207-215.

305. Wang, Y., *et al*., *Three-dimensionally confined diluted magnetic semiconductor clusters: $Zn_{1-x}Mn_xS$.* Solid State Communications, 1991. **77**(1): p. 33-38.
306. Yu, J.Q., *et al*., *Hot luminescence of Mn^{2+} in ZnS nanocrystals.* Journal of Luminescence, 1998. **79**(3): p. 191-199.
307. Nilsen, W.G., *Raman spectrum of cubic ZnS.* Physical Review, 1969. **182**(3): p. 838-850.
308. Wang, W., I. Germanenko, and M.S. El-Shall, *Room-temperature synthesis and characterization of nanocrystalline CdS, ZnS, and $Cd_xZn_{1-x}S$.* Chemistry of Materials, 2002. **14**(7): p. 3028-3033.
309. Zhong, X., *et al*., *Alloyed $Zn_xCd_{1-x}S$ nanocrystals with highly narrow luminescence spectral width.* Journal of the American Chemical Society, 2003. **125**(44): p. 13559-13563.
310. Li, Y.C., *et al*., *Composition- and shape-controlled synthesis and optical properties of $Zn_xCd_{1-x}S$ alloyed nanocrystals.* Advanced Functional Materials, 2005. **15**(3): p. 433-441.
311. Mozafari, M. and F. Moztarzadeh, *Controllable synthesis, characterization and optical properties of colloidal PbS/gelatin core-shell nanocrystals.* Journal of Colloid and Interface Science, 2010. **351**(2): p. 442-448.
312. Zhao, Y., J. Zou, and W. Shi, *Synthesis and characterization of PbS/modified hyperbranched polyester nanocomposite hollow spheres at room temperature.* Materials Letters, 2005. **59**(6): p. 686-689.
313. Sun, Y.P., *et al*., *Buildup of composite films containing TiO_2/PbS nanoparticles and polyelectrolytes based on electrostatic interaction.* Langmuir, 1997. **13**(19): p. 5168-5174.
314. Cao, H.Q., *et al*., *Growth and photoluminescence properties of PbS nanocubes.* Nanotechnology, 2006. **17**(13): p. 3280-3287.
315. Bakshi, M.S., *et al*., *Aqueous phase surfactant selective shape controlled synthesis of lead sulphide nanocrystals.* The Journal of Physical Chemistry C, 2007. **111**(49): p. 18087-18098.

Publication Lists

- Jack silver, Xiao Yan, Robert Withnall, George Fern, Joy Summer, Philip Shields and Duncan Allsopp, *Embedding Manganese doped Zinc Sulfide Quantum Dots in Gallium Nitride LEDs based on Photonic Crystals*, Proceedings of the 18th International Display Workshop, Nagoya, Japan, pp: 1405-1408 (2011).

- Jack Silver, Robert Withnall, Terry G. Ireland, Xiao Yan, Kelly Saltoun, Jesús J. Ojeda, *Surface studies of Y_2O_3:Eu, YAG:Ge, Y_2O_2S:Pr and Gd_2O_2S:M (M= Pr or Tb) phosphors*, Proceedings of the 18th International Display Workshop, Nagoya, Japan, pp: 731-734 (2011).

- Jack Silver, Robert Withnall, Terry G. Ireland, George R. Fern and Xiao Yan, *Cathodoluminescence of Small Particle Gd_2O_2S:Pr X-ray Phosphor*, IDW '09, Proceedings of the 16th International Display Workshops, Miyazaki, Japan, pp: 355- 358 (2009).